Analysis of hybrid perovskite thin film degradation using correlative electron microscopy techniques

Salim Mejaouri

THESE DE DOCTORAT

NNT : 2023UPAST056

université PARIS-SACLAY

Analysis of hybrid perovskite thin film degradation using correlative electron microscopy techniques

Analyse de la dégradation de couches minces de pérovskite hybride à l'aide de techniques de microscopie électronique corrélatives

Thèse de doctorat de l'université Paris-Saclay

École doctorale n° 575, Electrical, optical and bio physics and engineering (EOBE)
Spécialité de doctorat : Electronique et Optoélectronique, Nano- et Microtechnologies
Graduate School : Sciences de l'ingénierie et des systèmes Référent : Faculté des sciences d'Orsay

Thèse préparée au **Centre de Nanosciences et de Nanotechnologies** (Université Paris-Saclay, CNRS),
sous la direction **de Stéphane COLLIN**, directeur de recherche (C2N-CNRS),
la co-supervision de **Jean ROUSSET**, ingénieur de recherche (EDF R&D),
et la co-supervision de **Dominique LOISNARD**, cadre technique (EDF R&D)

Thèse soutenue à Paris-Saclay, le 07 avril 2023, par

Salim MEJAOURI

Composition du Jury

Membres du jury avec voix délibérative

Mathieu KOCIAK Directeur de recherche, LPS-CNRS	Président
Caterina DUCATI Professeur, University of Cambridge	Rapporteur & Examinatrice
Nicolas MERCIER Professeur, MOLTECH-CNRS	Rapporteur & Examinateur
Solenn BERSON Directrice de recherche, CEA-INES	Examinatrice
Emilie PLANES Maître de conférences, LEPMI	Examinatrice

université PARIS-SACLAY

DOCTORAL SCHOOL
Electrical, Optical, Bio: Physics and Engineering (EOBE)

Titre : Analyse de la dégradation de couches minces de pérovskite hybride à l'aide de techniques de microscopie électronique corrélatives.

Mots clés : pérovskite, dégradation, microscopie électronique, cathodoluminescence, cellule solaire

Résumé : Les matériaux pérovskites hybrides à base d'halogène et de plomb sont prometteurs pour la fabrication de cellules solaires photovoltaïques. Bien que les cellules solaires en pérovskite (PSC) présentent déjà des rendements élevés, l'instabilité de ce matériau reste un obstacle à leur industrialisation. Afin de surmonter cette instabilité, une compréhension complète des mécanismes de dégradation interne est nécessaire.

Dans cette thèse, nous étudions les mécanismes de dégradation à l'aide de techniques de microscopie électronique corrélatives telles que la cathodoluminescence (CL), la spectroscopie de rayons X à dispersion d'énergie (EDS) et la diffraction électronique en zones sélectionnées (SAED), qui révèlent les variations compositionnelles, structurelles et optoélectroniques des échantillons à l'échelle nanométrique. Nous optimisons d'abord ces techniques pour l'analyse de films sensibles tels que les pérovskites hybrides. Des échantillons de pérovskite inorganiques à base de césium et de brome, potentiels produits de dégradation des pérovskite hybrides, sont analysés pour développer nos connaissances sur ces phases. Ensuite, nous caractérisons des films minces de pérovskite triple cations et double halogènes ($Cs_{0.05}MA_{0.45}FA_{0.5}Pb(I_{0.83}Br_{0.17})_3$) vieillis sous air à humidité relative élevée et montrons la formation de produits de dégradation inorganiques aux formes géométriques particulières que nous identifions. Leur apparition est attribuée à la migration des ions et à la volatilisation des cations organiques sous l'effet des molécules d'eau.

Des films de pérovskite de même composition, de PSCs vieillis en fonctionnement et sous illumination, sont aussi étudiés. En combinant microscopie électronique et mesures électriques, nous corrélons l'apparition de phases de dégradation dans l'absorbeur avec les pertes de courant en sortie de la cellule solaire.

Nous proposons des moyens de prévenir ces mécanismes de dégradation et d'améliorer la stabilité du film de pérovskite et de la cellule solaire.

Title : Analysis of hybrid perovskite thin film degradation using correlative electron microscopy techniques.

Keywords : perovskite, degradation, electron microscopy, cathodoluminescence, solar cells

Abstract : Hybrid lead halide perovskites are promising materials for photovoltaics. Although perovskite solar cells (PSCs) already exhibit high efficiencies, perovskite instability remains an obstacle to their industrialization. To overcome this instability, a comprehensive understanding of the internal degradation mechanisms is required.

In this thesis, we study degradation mechanisms using correlative electron microscopy techniques, including cathodoluminescence (CL), energy dispersive X-ray spectroscopy (EDS), and selected area electron diffraction (SAED), which reveal compositional, structural, and optoelectronic variations in samples at the nanoscale.

We first optimize these techniques for the analysis of sensitive hybrid perovskite films. We analyze cesium and bromine-based inorganic perovskite samples, which are potential degradation products of hybrid perovskites, to develop our knowledge of these phases.

Then, we characterize triple cation double halide perovskite thin films ($Cs_{0.05}MA_{0.45}FA_{0.5}Pb(I_{0.83}Br_{0.17})_3$) aged under high relative humidity air and show the formation of inorganic degradation products with specific geometric shapes. Their emergence is attributed to the ion migration and the volatilization of organic cations due to the water molecules effect.

PSCs made of the same perovskite films are aged in operation under 1-sun illumination are studied. By combining electron microscopy and electrical measurements, we correlate the appearance of degradation phases in the absorber with output current losses.

Finally, we propose routes to prevent these degradation mechanisms and to improve the stability of perovskite films and solar cells.

"It is so shocking to find out how many people do not believe that they can learn, and how many more believe learning to be difficult"
Frank Herbert, Dune.

Acknowledgments

Que serait un manuscrit de thèse sans les "Remerciements", le chapitre le plus lu de toutes les thèses de doctorat et qui, comme dirait mon confrère Dr Fournier, permet d'en apprendre plus sur la personnalité de l'auteur. Je ne sais pas si le lecteur percera les secrets de ma personne en lisant ces quelques lignes, mais j'espère qu'il saisira l'ineffable gratitude que j'éprouve pour les personnes qui m'ont accompagné durant cette aventure de trois années et trois mois.

Mes premiers remerciements vont à mes encadrants, Stéphane Collin, Dominique Loisnard et Jean Rousset formant le trio archangélique. Durant ce périple, ils m'ont enseigné, accompagné et soutenu à travers les chemins tortueux d'un sujet ô combien complexe ! Ils m'ont accordé leur confiance dans l'utilisation de ces monstres technologiques que sont les microscopes électroniques et m'ont appris comment les amadouer pour qu'ils deviennent mes fidèles compagnons. C'est au contact de leur rigueur scientifique, leur connaissance sans limites et leur bienveillance que j'ai pu apprendre et m'améliorer constamment.

À Stéphane, j'aimerais te remercier d'avoir accepté de diriger cette thèse. Malgré la relation conflictuelle que tu entretiens avec la pérovskite, tu es toujours resté très disponible et d'excellent conseil. Merci de m'être partagé tes vastes connaissances sur la cathodoluminescence, l'analyse de données et la science des matériaux. Mais tu m'as également largement aidé et soutenu lors des préparations de présentations orales et de rapport écrit manuscrit et oral de thèses compris bien évidemment. Ta rigueur et ton perfectionnisme m'ont permis de m'améliorer constamment au courant de ces 3 années et d'être content de mon travail final, je t'en remercie donc grandement.

Vient ensuite le tour de Dominique que je remercie pour son accueil chaleureux sur le site d'EDF les Renardières. Ce dernier se trouvant à plus de 80km de Paris, c'était très important que je m'y sente bien pour me motiver à y aller et c'est bien grâce à toi que ce fût le cas. Par ailleurs, je te remercie de m'avoir formé sur le FIB et le TEM et de m'avoir laissé rapidement en autonomie sur ces bêtes. Tu as su prendre le temps de m'expliquer chacune des fonctionnalités et tu n'as jamais hésité à reprendre la base de microscopie électronique en y ajoutant un historique détaillé de l'évolution des technologies. Travailler avec quelqu'un d'aussi calé sur le sujet m'a permis d'embrasser largement la partie expérimentale de ma thèse et pour cela je te remercie largement.

Enfin, j'aimerais remercier Jean avec qui mon histoire remonte à plus loin. Car avant de commencer cette thèse, j'ai travaillé pendant 1 an et demi en tant qu'ingénieur sur la fabrication de contact P1/P2/P3 pour les modules pérovskites. En tant que chef de projet tu m'as accompagné lors de ma montée en compétence théoriquement et expérimentalement sur les cellules solaires pérovskites et le PV en général (malgré un petit doigt immobilisé pendant plus de 6 semaines !). Avec acharnement, nous avons réussi tant bien que mal à dresser cet irréductible laser et à établir un procédé "reproductible" pour la fabrication de modules pérovskite. Du fort de cette victoire, j'ai voulu aller plus loin et tu m'as donc proposé ce sujet de thèse. Je te remercie de la confiance que tu m'as donnée à ce moment-là et durant l'ensemble de la thèse. Mais j'aimerais ajouter qu'en plus de ton encadrement et ta supervision j'ai beaucoup aimé travailler avec toi. Ton ouverture d'esprit et ta bonne humeur m'ont été très bénéfiques pendant les heures les plus noires de cette thèse et je t'en remercie également.

La personne qui ne figure pas dans les membres de mon encadrement, mais qui en a tout fait c'est Stéfania Cacovich. J'aimerais la remercier, car en plus de son accompagnement émotionnel psychologique, elle m'a franchement aidé dans toutes les étapes de cette thèse du premier jour en me donnant sa thèse et moult papiers à lire, au dernier jour en assistant à mes répétitions de soutenance et en me poussant à soumettre mon article. MERCI !

J'aimerais maintenant remercier Sébastien Jutteau et Cédric Guérard sans qui je n'aurai jamais intégré l'IPVF en tant qu'ingénieur d'abord puis ensuite en tant que thésard EDF. Plus que m'embaucher, vous avez été de bons conseils pour mon projet professionnel et si maintenant j'intègre les équipes de EDF R& D, c'est bien grâce à vous deux. Cette thèse n'aurait pas pu se faire sans le financement d'EDF et l'utilisation des infrastructures d'EDF, de l'IPVF et du C2N. Je tiens donc à remercier Matthieu Versavel et Stéphanie Muller de m'avoir accepté à EFESE puis SYSTEME et Julien Stodolna pour l'accueil à MMC aux Renardières.

J'aimerais maintenant remercier mes compagnons de labeurs a.k.a. les thésards avec qui j'ai passer ces 3 années. Il n'est pas rare pour un directeur de recherche du calibre de Stéphane d'encadrer plusieurs (moult) thèses simultanément. J'aime à penser que celles-ci arrivent par portée. Bérengère et Capucine, nous faisons partie de la même portée 2019. Ces années n'ont pas été faciles, mais les passer avec vous a contribué à les adoucir et à les rendre agréables. J'aurai toujours en tête nos riches conversations parfois sur des sujets scientifiques au bureau. Nous avons eu l'occasion de vivre des choses géniales pour donner l'exemple des Houches en 2020 et cette semaine de rédaction (la fameuse retraite monastique) dans les Alpes il y a quelques mois. Nous voilà tous trois docteurs et je suis fier de nous.

En parlant des Houches, j'ai une pensée pour Guillaume, Marie, et Élisa avec qui nous sommes partis aux Arcs les jours qui ont suivi. Merci beaucoup, Marie, de nous avoir accueillis pendant ce week-end veille de confinement où nous avons pu tisser des liens.

Merci pour votre gentillesse, et je suis content après tout ce temps passer ensemble de vous considérer comme mes amis.

Dédicace à la bande autoproclamée "les Tuches", qui m'ont habilement traquenard en thèse et avec qui les longues heures de laboratoire, les galères de manips, le traitement de données sont devenus "légères". Mention spéciale à Sophie et Olivier qui m'ont aussi aidé lors de la rédaction avec leur relecture. J'aimerais remercier Thomas Bidaud pour la formation à ta CL chérie et ton aide pour le démarrage de la thèse. Pensée pour ceux qui ont fini il y a maintenant un certain temps, "les vieux fourneaux", Romaric, Adrien, Valentin, Amadéo, Louis, Arpit, Fabien, Cécile avec qui j'ai pu travailler de (très) loin ou avec qui j'ai simplement discuté et sympathisé.

Enfin j'envoie tous mes souhaits de réussite aux futures docteur.es, Thomas Claire, Carlos, Élisa, Célia, Alexandre, Vincent, Lise. Bon courage même si je n'ai pas de doute sur votre réussite prochaine.

Au cours de cette thèse, j'ai bien évidemment travaillé en collaboration avec beaucoup de personnes de chaque laboratoire. J'aimerai ici les remercier comme il se doit.

À l'IPVF, j'aimerai remercier immensément Armelle pour les nombreux échantillons que je t'ai demandés, tous plus saugrenus les uns que les autres. Ton travail remarquable et la répétabilité de tes échantillons (la lumière qui fait naufrager les papillons de ma jeunesse) n'ont d'égales que ta gentillesse et ton humanité. C'était donc un réel plaisir de travailler avec toi. J'aimerais saluer le travail de Sophie, Julie et Valérie véritables sauveteuses en mer pour étudiant naufragé dans les méandres des laboratoires. Mention spéciale à cette super session piscine tant attendue Sophie et promis je reviendrai !

Merci à Iwan et Marion pour l'aide sur le SnO_2 CBD, les conseils de cristallographie et de réaction chimiques pour l'article et le manuscrit. Merci à Baptiste et Daniel pour les manips d'hyperspectral et l'accueil dans la salle carac laser. Merci à Karim et Jorge pour la collaboration

qui a fait naître mon 5ème chapitre de thèse. Votre disponibilité et vos conseils ont été très instructifs et prolifiques sur cette fin de thèse (et merci pour les relectures).

Au C2N, même si nous n'avons pas le même matériau nous avons la même passion PV, j'aimerais donc remercier la team SUNLIT au complet, Andréa, Amaury, Jeronimo, Maxime et Noémie pour les discussions en réunion du lundi matin et la découverte des propriétés physiques des (vrais) semi-conducteurs ! Mention spéciale à Stéfano et son aide sur le traitement de données CL à la fin de la thèse et les discussions de mélomanes.

À EDF Renardières, j'aimerais remercier l'équipe de microscopistes de choc composée de Romain, Nico, Julien, Antoine, Maxime et Fred. Merci de m'avoir aidé sur le TEM le FIB, mais aussi, et surtout, pour les discussions hilarantes à la pause café du matin, de la pause méridienne et de l'après-midi. Merci aussi de m'avoir aidé lors de la préparation de ma soutenance.

Enfin, j'aimerai ajouter quelques mots aux personnes avec qui j'ai partagé le bureau à l'IPVF. Bien évidemment, mon voisin, mon cocritique ciné, et mon référent culture geek, j'ai nommé Samuel. Merci pour ces 4 années de partage et d'être venu de ta lointaine contrée pour ma soutenance et tout ce qui a suivi. Je dis au revoir à Alexandre, Liam, Karim et Javid. Occupez-vous bien de cet endroit où j'ai passé 5 années de ma vie.

Maintenant j'aimerais remercier les personnes qui me sont proches en dehors du travail. Mes amis me sont très proches, et je le considère comme ma famille. Cependant, j'en ai beaucoup, je ne vais donc pas les énumérer et parler de chacun d'entre eux personnellement, mais je vais les regrouper en groupe d'origine ou en famille cristalline (petite blague, je ne pouvais m'en empêcher), car vous m'êtes aussi précieux que des diamants.

Les Lyonnais : l'école d'ingénieur nous a formés, mais les liens que nous avons créés vont bien au-delà du temps de notre formation. Merci d'avoir continué à être là pour moi et de m'avoir soutenu dans les moments de doutes.

Les Canadiens : en partant au Canada je ne pensais pas que je reviendrais avec des amis aussi proches et bienveillants. Merci pour tout et mention spéciale (encore ?) à Poum pour l'aide en cuisine la veille de la soutenance.

Les Parisiens : pour citer notre envoyé spécial détacher en Guadeloupe: "30 ans de vie, 18 ans d'amitié qui peut y prétendre ?" Nous sommes frères et soeurs, votre soutien indéfectible m'a été indispensable pour en arriver là. Vous pouvez être fier de ce que vous avez fait de moi.

Pour ma famille: je pense que je n'ai pas besoin de dire grand-chose pour vous dire tout ce que je ressens et je vous remercie de m'avoir soutenu à tout moment, mon père qui m'a toujours poussé, Marianne pour l'ouverture d'esprit, et Stéphane pour ton soutient et ta gentillesse, Christian et Stéphanie pour leur soutient.

Enfin il me reste deux personnes à remercier particulièrement et à qui je dédis cette thèse :

Ana nous nous sommes rencontré il y a 5 ans de l'autre côté du monde et c'est clairement une des meilleures choses qui me soient arrivées. Cette thèse comme je te l'ai dit c'est la tienne aussi, car après avoir passé la journée avec des élèves insupportables, tu en retrouvais un à la maison dont le stress et les écarts sont d'un autre niveau. Merci pour tout, je t'aime.

Je me permets de dédier cette thèse à ma mère qui n'est pas là, mais sans qui je ne serais évidemment pas là et pour qui je ne cesserai jamais de me dépasser.

À celui ou celle qui lis ces mots, le doctorat est une aventure tumultueuse, pleine de complexités, de doutes et d'incertitudes, mais aussi et heureusement d'excitation, de joie, de rigolades et de bonheur. Je ne peux qu'être à ce jour heureux de l'avoir vécu et d'en être arrivé à son terme.

Contents

Contents v

Acknowledgments viii

List of Acronyms xvi

General introduction 1

1 Stability of perovskite material in solar cells 5
1.1 Metal halide perovskites . . . 6
1.1.1 Composition and crystalline structure . . . 6
1.1.2 Optoelectronic properties . . . 8
1.1.3 Properties of triple-cation double-halide perovskite films . . . 11
1.2 Perovskite solar cells . . . 13
1.2.1 Basic concepts of thin film solar cells . . . 13
1.2.2 PSC fabrication processes and applications . . . 15
1.2.3 State-of-the-art PSCs . . . 16
1.2.4 Baseline fabrication process in this thesis . . . 17
1.3 Degradation of perovskite films and solar cells . . . 18
1.3.1 Thermal instability of perovskite films . . . 18
1.3.2 Instability of perovskite films under illumination . . . 19
1.3.3 Instability of perovskite films under atmospheric stress factors . . . 22
1.3.4 Instability of PSCs due to charge transport layers and electrodes . . . 24
1.3.5 Stability assessment based on ISOS procedures . . . 25
1.4 Summary and objectives of the thesis . . . 27

2 Electron Microscopy techniques: theory and experimental methods 29
2.1 Electron-matter interactions . . . 30
2.1.1 Basis of electron-matter interactions . . . 30
2.1.2 Electron-beam induced damages . . . 32
2.2 Scanning Electron Microscope . . . 33
2.2.1 SEM overview . . . 33
2.2.2 Energy dispersive x-ray spectroscopy in SEM . . . 34
2.3 Cathodoluminescence . . . 39
2.3.1 CL set-up overview . . . 39
2.3.2 Resolution . . . 41
2.3.3 Data treatment . . . 43
2.4 Hybrid perovskite degradation under e-beam exposure . . . 44
2.4.1 Impact of the degradation on SEM images . . . 44
2.4.2 Impact of the degradation on CL measurements . . . 46
2.5 Scanning Transmission Electron Microscope . . . 49
2.5.1 Lamella preparation . . . 49

2.5.2 (S)TEM overview . . . 50
2.5.3 Energy dispersive x-ray spectroscopy in STEM . . . 54
2.5.4 Hybrid perovskite degradation in a STEM . . . 57
2.6 Conclusions . . . 60

3 Analysis of cesium, lead, and bromide-based perovskite 63
3.1 Ternary phases of the Cs-Pb-Br material system . . . 64
3.2 Analysis of the $CsPbBr_3$ perovskite phase . . . 65
3.2.1 Optical properties . . . 65
3.2.2 Analysis of a $CsPbBr_3$ film . . . 66
3.3 Analysis of the $CsPb_2Br_5$ phase . . . 71
3.3.1 Optical properties . . . 71
3.3.2 Analysis of $CsPb_2Br_5$ micro-crystals . . . 73
3.4 Conclusions . . . 78

4 Analysis of CsMAFA perovskite degradation products 79
4.1 Aging process of the CsMAFA-based half-cell device . . . 80
4.1.1 Analysis of the morphology . . . 80
4.1.2 Analysis of the structure . . . 82
4.1.3 Analysis of the opto-electronic properties . . . 83
4.2 Formation of PbI_2 . . . 84
4.2.1 Hexagon-like degradation product . . . 84
4.2.2 Disc-like degradation product . . . 85
4.3 Formation of cesium-based inorganic perovskite . . . 87
4.3.1 Chemical analysis of the needles with SEM and STEM-EDS . . . 88
4.3.2 Structural analysis of the needles with Selected Area Diffraction . . . 89
4.3.3 Optical analysis of the needles . . . 91
4.3.4 Analysis of the "flower" . . . 96
4.4 Discussion and proposed degradation mechanisms . . . 97
4.5 Aging with other stress factors . . . 100
4.5.1 Humidity and light . . . 100
4.5.2 Humidity and nitrogen . . . 101
4.6 Conclusions . . . 102

5 Analysis of the degradation products in PSC aged under operation conditions 105
5.1 Optimization of the PSC fabrication . . . 106
5.1.1 Addition of $Pb(SCN)_2$ and optimization of its concentration . . . 106
5.1.2 Heating of precursor solution before deposition . . . 107
5.2 Material characterizations . . . 109
5.2.1 Macroscopic analysis of the aged PSC . . . 109
5.2.2 STEM analysis of three different PSCs . . . 110
5.2.3 Contact layers peeling off and perovskite film morphology . . . 111
5.2.4 Cathodoluminescence measurements of the aged perovskite film . . . 113
5.2.5 Chemical analysis of the aged perovskite film with EDS . . . 118
5.2.6 Crystalline structure of the inclusion analyzed by SAED . . . 122
5.3 Discussions about the formation of inclusions . . . 124
5.3.1 Inclusions formation . . . 124
5.3.2 Impact of changes in the perovskite film on the PSC performance . . . 127
5.4 Conclusions . . . 128

Conclusion 129

Additional figures 141

Résumé en français 141

Additional theory and methods 147

Articles and communications 152

Bibliography 178

List of acronyms

IPCC	Integovernmental Panel on Climate Chage
IEA	International Energy Agency
PV	Photovoltaic
PSC	Perovskite Solar Cell
PSM	Perovskite Solar Module
PCE	Power Conversion Efficiency
LCOE	Levelized Cost of Electricity
SEM	Scanning Electron Microscope
CL	Cathodoluminescence
TEM	Transmission Electron Microscope
STEM	Scanning Transmission Electron Microscope
EDS	Energy Dispersive X-ray Spectroscopy
HAADF	High-angle Annular Dark Field
SE	Secondary Electrons
BSE	Backscattered Electrons
PL	Photoluminescence
XRD	X-ray Diffraction Spectroscopy
SAED	Selected Area Electron Diffraction
MA	Methylammonium
FA	Formamidinium
MAPI	$MAPbI_3$
FAPI	$FAPbI_3$
CB	Conduction Band
VB	Valence Band
CTL	Charge Transport Layer

ETL	Electron Transport Layer
HTL	Hole Transport Layer
SQ	Schockely-Queisser
TCO	Transparent Conductive Oxide
GBL	γ-butyrolactone
DMF	N, N-dimethylformamide
DMSO	Dimethyl sulfoxide
NMP	N-methyl-2-pyrrolidone
PTAA	poly(triarylamine)
Spiro	Spiro-OMeTAD
FTO	Fluorine-doped Tin Oxide
ITO	Indium Tin Oxide
CsMAFA	$Cs_{0.05}(MA_{0.15}FA_{0.85})_{0.95}Pb(I_{0.83}Br_{0.17})_3$
MAFA	$MA_xFA_{1-x}Pb(I_yBr_{1-y})_3$
CsFA	$Cs_xFA_{1-x}Pb(I_yBr_{1-y})_3$
GB	Grain Boundarie
GI	Grain Interior
SAM	Self-Assembled Monolayer
PMMA	Poly(methyl methacrylate)
RH	Relative Humidity
SCN	Thiocyanate
PEDOT:PSS	poly(3,4-ethylenedioxythiophene) polystyrene sulfonate
UV	Ultraviolet
PCBM	Phenyl-C61-butyric acid methyl ester
FEG	Field Emission Gun
FOV	Field-Of-View
ISOS	International Summit On Organic Photovoltaic Stability
EM	Electron Microscope
E-beam	Electron beam
FWHM	Full Width at Half Maximum
GL	Gun Lens

CCD	Charge-Coupled Device
EELS	Electron Energy-Loss Spectroscopy
FIB	Focus-Ion-Beam
GIS	Gas Injection System
SNR	Signal-to-Noise Ratio
DP	Diffraction Pattern
ADF	Annular Dark Field
BF	Bright Field
IPVF	Institut Photovoltaïque d'Ile-de-France
DFT	Density-Functional Theory
TRCL	Time-Resolved Cathodoluminescence
TRPL	Time-Resolved Photoluminescence
TOF-SIMS	Time-Of-Flight Secondary Ion Mass Spectrometry
XPS	X-ray Photoelectron Spectroscopy
NMR	Nuclear Magnetic Resonance
LRCS	Laboratoire de Réactivité et Chimie des Solides
Cryo	Cryogenic
RT	Room Temperature
LT	Low Temperature

General introduction

In August 2021, the Intergovernmental Panel on Climate Change (IPCC) of the United Nations released the first part of their Sixth Assessment Report, which unequivocally demonstrates a correlation between human activities of the past century and global warming [1]. As concentrations of greenhouse gases continue to rise, extreme climate events are becoming more frequent and severe, posing a direct threat to life on Earth. To mitigate the effects of global warming and avoid an increase in average global temperatures above 1.5°C as compared to pre-industrial levels (target of the 2015 Paris Climate Agreement), it is necessary to reduce the emissions of greenhouse gases such as carbon dioxide, which is primarily generated by the consumption of fossil fuels as coal, gas, and oil. The utilization of these energy sources also carries an ethical cost, as these resources are finite and concentrated in specific regions of the world. With the global demand for energy increasing every year (+5% in 2022 [2]), it has become essential to transition towards cleaner, fair, and readily available energy sources.

The development of renewable energies has seen a significant surge in the past two decades. Among them, solar energy presents a great potential as it is available everywhere on the globe and is relatively unlimited. Photovoltaic technology is one way of directly converting sunlight into usable electricity. According to the International Energy Agency (IEA), solar PV accounted in 2021 for 3.6% of the global electricity production (1002.9 TWh) with 885 GW of PV capacity installed. In order to achieve the greenhouse emission levels that are implied by the 1.5°C target, it is estimated that approximately 600 GW of PV capacity must be installed each year by 2030 [3].

The cost of PV electricity has experienced a significant decline over the past decade, driven by a reduction in solar cell prices and an increase in power conversion efficiency (PCE). While device prices continue to decrease, PCE of single-junction solar cells is approaching its theoretical limit of about 30%. Silicon solar cells are currently dominating the PV market. In 2020, they accounted for 95% of PV production. However, as the limitations of silicon solar cells are becoming increasingly apparent, researchers are turning to new PV technologies with the potential for higher efficiency or lower production costs to continue driving down the cost of PV electricity.

The next generation of solar cells utilizes materials with enhanced absorption characteristics, such as CuInGaS/Se (CIGS), CdTe, III-V materials, and Perovskite materials. These materialsare direct bandgap semiconductors that allow the development of thin-film-based PV systems, enabling novel applications, such as lightweight installation, flexible substrates, and building-integrated photovoltaics. Furthermore, as these materials absorb different wavelength ranges of the solar spectrum than silicon, they can be utilized in conjunction with silicon solar cells to create multi-junction (tandem) cells, which can effectively harvest the most of the solar spectrum and surpass the theoretical limit of single-junction solar cells.

In this context, hybrid lead halide perovskites have become the forefront of current PV research. In just 13 years, the PCE of single-junction perovskite solar cells (PSCs) has increased dramatically, from 3.8% to 25.7% [4]. In addition, recent advances in perovskite-silicon tandem

devices have resulted in a PCE value of 32.5% [5], exceeding the 30% threshold and approaching the performances of expensive III-V-based multi-junction solar cells. However, in contrast to the III-V, PSCs exhibit a significant cost advantage, as their solution-based fabrication methods is remarkably inexpensive and facile. Recent techno-economic analyses have shown that PSCs possess the potential to break into the PV market with projected levelized cost of electricity (LCOE) values of 7.9 $/kWh compared to the current averaged of 5.7 $/kWh [6].

However, this promising future for the commercialization of perovskite-based PV technology comes with important assumptions regarding its scalability and reliability. Reliability issues can have a significant impact on the levelized cost of electricity (LCOE), as recently highlighted by Duan et al. [7]. The authors estimate that to be competitive with the current LCOE of silicon solar cells, a 30% efficient tandem perovskite-silicon solar cell should add no more than 0.8% annual degradation rate to that of a silicon solar cell, which is currently certified by most manufacturers at 0.8% [3]. [1] Overcoming the instability of perovskite solar cells (PSCs) is a critical challenge for the commercialization of this technology. In addition to the traditional failure mechanisms encountered in PV modules and systems, such as hot spots, delamination, and potential-induced degradation (PID), PSCs are also affected by the intrinsic instability of the perovskite layer.

The low-energy formation of perovskites is a double-edged sword, facilitating their production but also their degradation. Hybrid perovskites are particularly prone to instability when exposed to moisture, oxygen, heat, applied current and light. These factors can dramatically affect the lifetime of PSCs, making them unsuitable for PV applications. Currently, significant research efforts are focused on addressing these issues, and PSCs are beginning to demonstrate improved stability, such as meeting the damp-heat test requirements outlined in IEC 61215 [8]. However, further efforts are needed to achieve the level of stability required for commercialization of this technology.

In order to develop efficient, low-cost and stable PSCs, it is crucial to understand the mechanisms by which external stressors affect hybrid perovskite materials. The objective of this work is to gain insight into these mechanisms by analyzing the degradation products formed in perovskite films after aging processes. To this end, we have applied electron microscopy techniques such as cathodoluminescence and energy dispersive X-ray spectroscopy in a scanning electron microscope (SEM) and a scanning transmission electron microscope (STEM) on aged $Cs_{0.\ 05}(MA_{0.15}FA_{0.85})_{0.95}Pb(I_{0.83}Br_{0.17})_3$ perovskite (CsMAFA) films and solar cells. By coupling these local characterization methods and correlating the results obtained, we aim to identify the underlying causes of degradation and to propose strategies for the development of more stable PSCs.

- In Chapter 1 we introduce the context of the thesis by describing the chemical structure of metal halide perovskites and their optoelectronic properties. We then give a brief description of the concepts of solar cells, followed by the presentation of the architecture of the n-i-p PSCs studied in this thesis and their operating principle. Next, a literature review of the degradation mechanisms affecting perovskite thin films are presented. We emphasize their origin in the intrinsic properties of the perovskite materials and on the ways reported in the literature to mitigate these phenomena. Finally, the influence of charge transport layers and contact layers on the instability of PSCs is briefly discussed.
- In Chapter 2 we first describe the basic principles of electron-matter interactions. We then provide an overview of the three electron microscopes used in this thesis, namely the Zeiss

[1] This result has been estimated by considering an additional cost of $1.50 per cell related to the deposition of the PSC on the silicon solar cell.

Merlin scanning electron microscope (SEM), the Attolight Chronos Cathodoluminescence set-up (CL), and the FEI Osiris scanning transmission electron microscope (STEM). For each instrument, the specific techniques implemented during this thesis analyze perovskite thin films are detailed, including secondary and backscattered electron (SE and BSE) imaging, energy dispersive X-ray spectroscopy (EDS), cathodoluminescence (CL), and high angle annular dark field (HAADF) imaging. The challenges due to the sensitivity of perovskite films to electron beam are discussed and appropriate experimental conditions are adopted for the rest of the work.

- In Chapter 3 we study the pure inorganic cesium-, lead-, and bromine-based perovskites $CsPbBr_3$ and $CsPb_2Br_5$, as they are potential degradation products of the CsMAFA perovskite. We first present the essential information gathered from the literature on these phases (which belong to the Cs-Pb-Br system). Their atomic structure, crystalline symmetry and optical properties are described. We then present our experimental work on $CsPbBr_3$ and $CsPb_2Br_5$ samples. We correlate results obtained by photoluminescence (PL), CL, and EDS to analyze the properties of these cesium-based perovskite phases. Our results provide insight into the relationship between sample composition and optoelectronic properties. Moreover, they contribute to the ongoing debate in the literature regarding the optoelectronic properties of these phases.

- In Chapter 4 we study the degradation products of $Cs_{0.05}(MA_{0.15}FA_{0.85})_{0.95}Pb(I_{0.83}Br_{0.17})_3$ (CsMAFA) perovskite films aged under air with high relative humidity (85% RH). To this end, we performed several characterizations of the film after aging, including X-ray diffraction spectroscopy (XRD), PL, CL, SEM-EDS, STEM-EDS, and Selected Area Electron Diffraction (SAED). By correlating the results on the degradation products, we identify their composition and crystal structure. We then propose pathways for the degradation mechanisms based on known phenomena reported in hybrid perovskite materials (see chapter 1). Finally, we present preliminary results on the aging of CsMAFA perovskite films under coupled stressors such as light-heat-humidity and nitrogen-humidity.

- In Chapter 5 we study the stability of CsMAFA-based PSCs under continuous light and operating conditions. In the first part, we present modifications of the perovskite film fabrication to improve the long-term stability of the PSC. After the optimization, PSCs show improved stability in operation for more than 1000 hours. We then present measurements performed on the perovskite film of the aged PSC. It reveals the appearance of a specific degradation product, which is subsequently analyzed using similar electron microscopy techniques as in chapter 4 (CL, STEM-HAADF imaging, SEM-EDS, STEM-EDS, and SAED). From the results obtained, we estimate the composition of the degradation product. We also relate the evolution of the PSC performance during aging to the formation of this phase in the perovskite film. Finally, we propose several degradation pathways leading to the formation of the degraded features inside the film.

Contributions

This thesis was carried out in the framework of a collaboration with several people from the IPVF, the C2N, and the EDF lab (at the Material Aging Institute (MAI)). In this subsection, I detail the contributions to the work presented below.

I performed all the SEM measurements with the Merlin SEM at the IPVF, such as SE/BSE imaging and SEM-EDS measurements, presented in this thesis. I performed all the CL measurements presented here. Thomas Bidaud (former PhD student at C2N) trained me at the beginning of my PhD and helped me with the data processing. I prepared all the PSC lamellae studied in this thesis using the Helios FIB miller at EDF Lab. I also performed all the STEM

HAADF and EDS measurements with the STEM Osiris. I was trained at the beginning of my Ph.D. by Dominique Loisnard (EDF), who supervised me during all this work. We performed together the SAED measurements presented in chapter 4, he performed the ones in chapter 5.

The $CsPbBr_3$ sample analyzed in chapter 3 was prepared by Davide Cerrati (IPVF) and analyzed by PL imaging by Minjin Kim (IPVF). The $CsPb_2Br_5$ microcrystals were fabricated by collaborators from the LRCS (Laboratoire de Réactivité et Chimie des Solides - Université d'Amiens), namely Mohammad Ali Akhavan Kazemi and Frédéric Sauvage. The PEDOT:PSS was deposited on a Si wafer by Linh Nguyen (former PhD student at C2N/IPVF). PL on these microcrystals was done by Stefania Cacovich (CNRS/IPVF) on the hyperspectral PL imaging set-up at the IPVF. DFT-based calculations in Chapter 3 and 4 were realized by Philippe Baranek (EDF/IPVF).

The half PSCs studied in the chapter 4 were fabricated at the IPVF. The deposition of the SnO_2 layer on the FTO substrate was performed by Iwan Zimmermann (IPVF) according to the chemical bath method described in ref [9]. The preparation of the CsMAFA perovskite ink and its deposition was conducted by Armelle Yaiche (EDF/IPVF).

I carried out the aging of the samples at high relative humidity and their characterization by XRD, optical microscopy and electron microscopy measurements. Daniel Ory (EDF/IPVF) trained me on the aging set-up and provided it for this study. I also conducted the PL measurements with the help of Baptiste Bérenguier, who trained me on the set-up. The PL data processing was done by Stefania Cacovich.

The PSCs presented in chapter 5 were prepared by Jean Castillon (IPVF). He optimized the fabrication process (addition of PbSCN and heating of the precursor solution) and measured the crystal grain size by SEM imaging. The stability tests of the PSCs under continuous 1 sun illumination and in operation and the *in-situ* MPP measurements were performed by Karim Medjoubi (IPVF). He also performed the EQE and XRD measurements on the aged samples. I performed the peeling of the contact layers from the PSC and the subsequent electron microscopy measurements presented in this chapter.

Chapter

1 Stability of perovskite material in solar cells

Chapter content

1.1 Metal halide perovskites 6
1.1.1 Composition and crystalline structure 6
1.1.2 Optoelectronic properties 8
1.1.3 Properties of triple-cation double-halide perovskite films 11
1.2 Perovskite solar cells 13
1.2.1 Basic concepts of thin film solar cells 13
1.2.2 PSC fabrication processes and applications 15
1.2.3 State-of-the-art PSCs 16
1.2.4 Baseline fabrication process in this thesis 17
1.3 Degradation of perovskite films and solar cells 18
1.3.1 Thermal instability of perovskite films 18
1.3.2 Instability of perovskite films under illumination 19
1.3.3 Instability of perovskite films under atmospheric stress factors 22
1.3.4 Instability of PSCs due to charge transport layers and electrodes 24
1.3.5 Stability assessment based on ISOS procedures 25
1.4 Summary and objectives of the thesis 27

Over the past decade, perovskite solar cells (PSCs) have emerged as strong candidates for future PV systems. As the performance of perovskite-based solar cells and modules has increased, the interest of researchers and industrial stakeholders has grown, and perovskites have attracted worldwide attention. In addition to remarkable absorption and carrier transport properties, perovskite materials benefit from low-cost manufacturing processes. However, the instability of these materials, both intrinsic (inherent) and extrinsic (caused by exposure to external factors), remains a significant challenge that must be overcome.

In this chapter, we present a review of the literature on hybrid perovskite materials and associated solar cells that are studied in this thesis. First, the composition, crystal structure, and optoelectronic properties of hybrid perovskite materials are introduced. Then, the concept of thin film solar cells and their working principle are presented. The architecture of PSCs, their applications, and their performance are also reviewed. Finally, degradation mechanisms of perovskite materials are covered.

1.1 Metal halide perovskites

1.1.1 Composition and crystalline structure

The name "perovskite" originally refers to the mineral calcium titanate ($CaTiO_3$) discovered by Gustavus Rose in 1839 and named after the mineralogist Lev Alexievich Perovski. The term designates a vast family of materials with a composition ABX_3, in which A^+ and B^{2+} are cations (monovalent and divalent, respectively) and X^- are anions. Among the multiple existing perovskite structures, metal halide perovskites consist of a metal cation in B-site such as Pb^{2+}, Sn^{2+}, or Ge^{2+}, and halogen anions in X-sites such as I^-, Br^-, or Cl^-. The A-site can be occupied by organic cations such as methylammonium $CH_3NH_3^+$ (MA^+) or formamidinium $CH(NH_2)_2^+$ (FA^+), or by inorganic cations such as cesium (Cs^+) and rubidium (Rb^+). Due to their composition, we usually call these materials hybrid organic-inorganic perovskites. The aristotype cubic perovskite structure is presented in Figure 1.1.

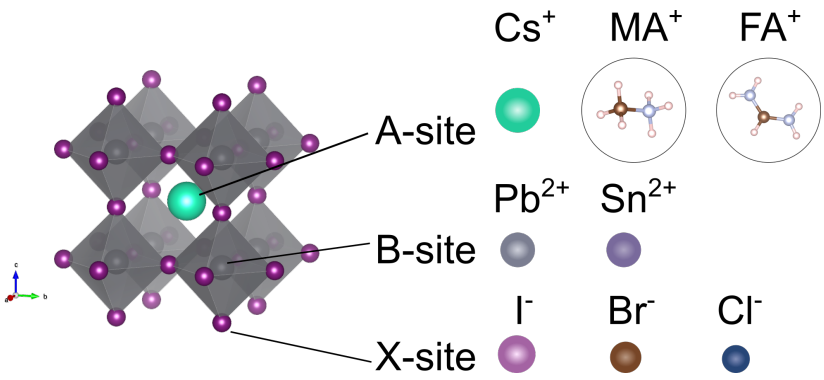

Figure 1.1: *Schematic representation of the archetypal cubic perovskite structure, denoted as ABX_3. The 3D network is composed of eight corner-sharing inorganic octahedra $[BX_6]^{4-}$, while cation A^+ occupies the cavity between them and stabilizes the structure. The typical ions present at each site are also indicated on the right.*

The X^- ions coordinate around the B^{2+} cation to form an octahedron $[BX_6]^{4-}$. Eight octahedra form a 3D network where the A^+ cation is positioned in the cuboctahedral cavity.

This specific structure involves constraints on the constituents and their ionic radii, determining whether a stable perovskite structure can be formed or not. These constraints on ions (and molecules) radius are formalized by the Goldschmidt tolerance factor t defined by the following equation:

$$t = \frac{r_A + r_X}{\sqrt{r_B + r_X}}, \tag{1.1}$$

where r_A, r_B, and r_X are the ionic radii of the A^+, B^{2+} cations, and X^- anion, respectively. t is an empirical factor historically established for oxide perovskites [10]. When it ranges between 0.9 and 1, the perovskite crystallizes at room temperature in a cubic symmetry, also called the α black phase [11]. If t is too large (> 1) or too low (< 0.7), the perovskite crystallizes in an hexagonal or orthorhombic symmetry, respectively. Such requirements significantly limit the choices of constituents for perovskite structure.

The octahedral factor μ, defined as the ratio of r_B over r_X, determines the stability of the $[BX_6]^{4-}$ octahedron. If μ is comprised between 0.4 and 0.9, the perovskite structure is stable [12].

Perovskite constituents must satisfy these conditions on t and μ to form a stable α phase at room temperature (≈ 300 K). However, these materials undergo phase transitions when the temperature varies. Let us take the example of the standard $MAPbI_3$, which is the first perovskite

composition studied for photovoltaic conversion [13]. The structure transforms from cubic (α) to tetragonal symmetry (β) at 330 K due to the rotation of the organic cation MA^+, inducing a distortion of the structure, as shown in Figure 1.2(c). At approximately 165 K, the structure undergoes a phase transition to the orthorhombic symmetry (γ), also caused by the orientation of the MA^+ cation and the rotation of the octahedra.

These transitions show that the A-site cation significantly affects the symmetry of the structure. Notably, FA-based perovskites exhibit different phase transition temperatures than MA-based composition, as shown in Figure 1.2(a). In addition, the orthorhombic phase (δ) of $FAPbI_3$, also referred to as trigonal in the literature, is significantly different from the cubic perovskite structure as the octahedra no longer share their corners (see Figure 1.2), which strongly affect the optoelectronic properties as discussed in the next Section.

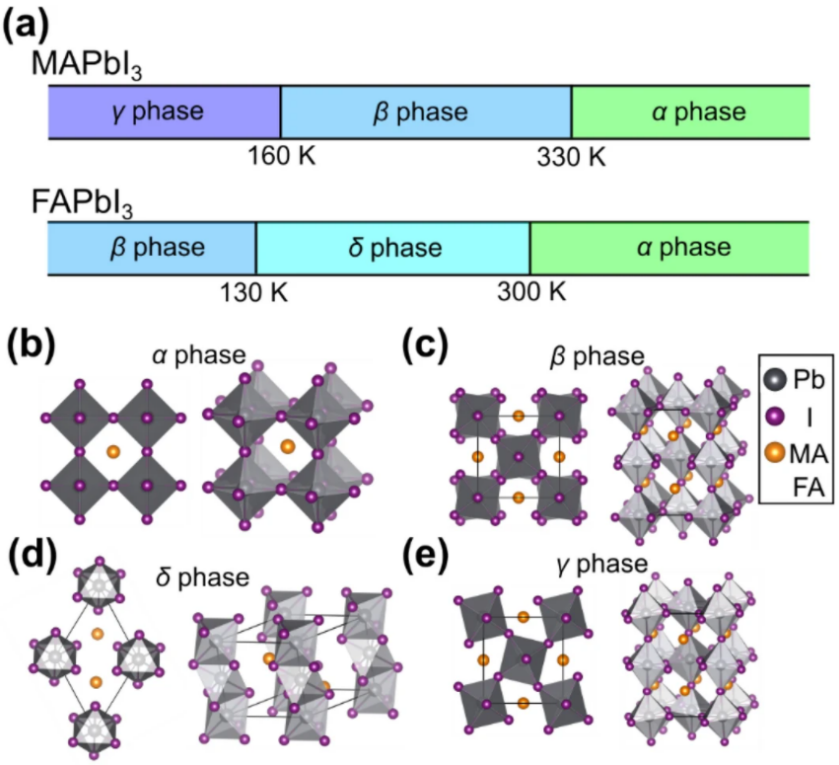

Figure 1.2: *(a) Temperature-dependent phase variations of $MAPbI_3$ and $FAPbI_3$. The four different phases are presented, including (b) the cubic (α) phase, (c) the tetragonal (β) phase, (d) the orthorhombic (δ) phase, and (e) the orthorhombic (γ) phase. In (b)–(e), gray and purple spheres represent Pb and I atoms, respectively, and orange spheres represent the MA^+ or FA^+ cations. Reprinted from [14].*

The hybrid perovskites for photovoltaic applications generally use Pb^{2+} or Sn^{2+} cations in the B-site. While Pb^{2+} cations provide a relatively stable framework for perovskite materials, they raise potential risks to human health and ecosystems [15]. The manipulation of lead requires utmost attention, limiting fabrication processes. Among several divalent cation alternatives, Sn^{2+} cations are the most promising, the properties of Sn-based perovskites being relatively similar to Pb-based ones. However, they suffer from poorer stability than their Pb-based counterparts, notably due to the facile oxidation of tin(II) in tin(IV) [16]. In a recently published work, Schileo and Grancini discussed the advantages and disadvantages of several alternatives to Pb in perovskite PV. They claimed that the limitations due to Pb are balanced by the advantages of Pb-based PSCs (performance, potential applications, and relative stability) over the alternative perovskite compositions [17].

As mentioned before, the first perovskite-based solar cells were developed with single cation and anion $MAPbI_3$ perovskite, also known as MAPI [13]. Progressively, the community turned to FA, and Cs-based perovskites such as $FAPbI_3$ [18], or $CsPbI_3$ [19], exhibiting better efficiency and stability. However, these perovskites do not crystallize at room temperature in the α phase adapted to solar applications as suggested by the tolerance factor t (see Figure 1.3(a)). This phenomenon has motivated the alloying of multiple cations to shift the tolerance factor towards the stability interval, as demonstrated by Li et al. [20] for FA^+ and Cs^+ cations and shown in Figure 1.3(a)).

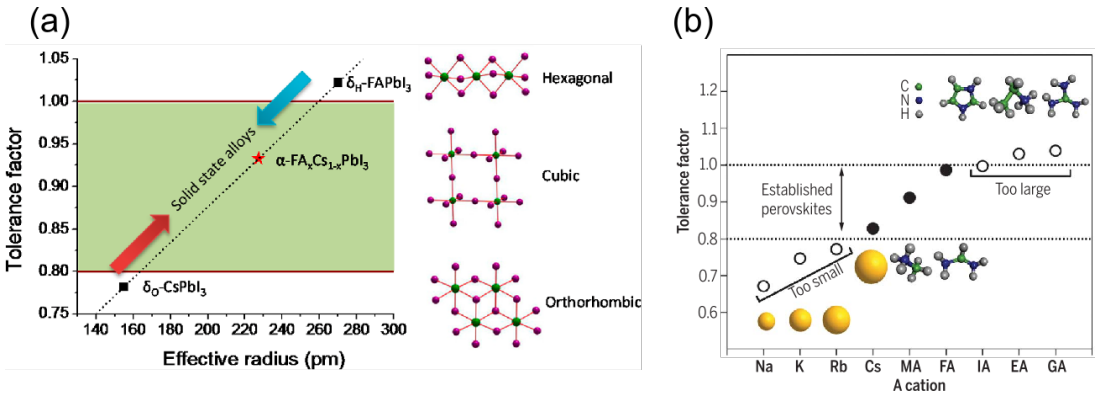

Figure 1.3: *(a) Tuning the tolerance factor through solid-state alloying of Cs^+ and FA^+ cations. Reprinted from [20]. (b) Tolerance factor of $APbI_3$ perovskites with A cations of varying size, including those that are too small (Na, K, Rb), established (Cs, MA, FA), and too large (imidazolium (IA), ethylamine (EA), guanidinium (GA)). Reprinted from [21].*

Mixing cations in A-site allows to use atoms that do not verify the t factor but further improve the performance, such as rubidium (Rb^+) [22], or guanidinium (GA^+) [23]. Mixing halides in the X-site is also a way to tune t but is mostly applied to modify the bandgap, as discussed in the following Subsection.

1.1.2 Optoelectronic properties

Band-structure

Hybrid perovskites are typically direct bandgap semiconductors meaning that the valence band (VB) maximum coincides in the Brillouin zone with the conduction band (CB) minimum. In lead iodide perovskites, the CB is mainly occupied by states from Pb(6p) orbitals, while the VB is populated by the coupling of Pb(6s) and I(5p) orbitals [24]. Hybrid perovskites are then considered as ionic materials in which electronic states of the cation define the CB, and the states of the anion define the VB [25] (see Figure 1.4).

The higher binding energies of the Br(4p) and Cl(3p) orbitals tend to decrease the VB maximum and thus increase the bandgap of the perovskite [26]. The bandgap is easily tuned by combining halides in the X-site. Figure 1.4(b) shows the evolution of the $MAPbX_3$ bandgap as a function of the halide composition mix.

This composition engineering approach is widely used to adapt the bandgap of perovskites to the aimed applications, such as tandem solar cells (see Section 1.2). Conversely, the electronic contribution of A-site cations is positioned far from the VB and the CB, making them electronically inactive or ineffective on the bandgap (see Figure 1.4(c)). They still have a structural

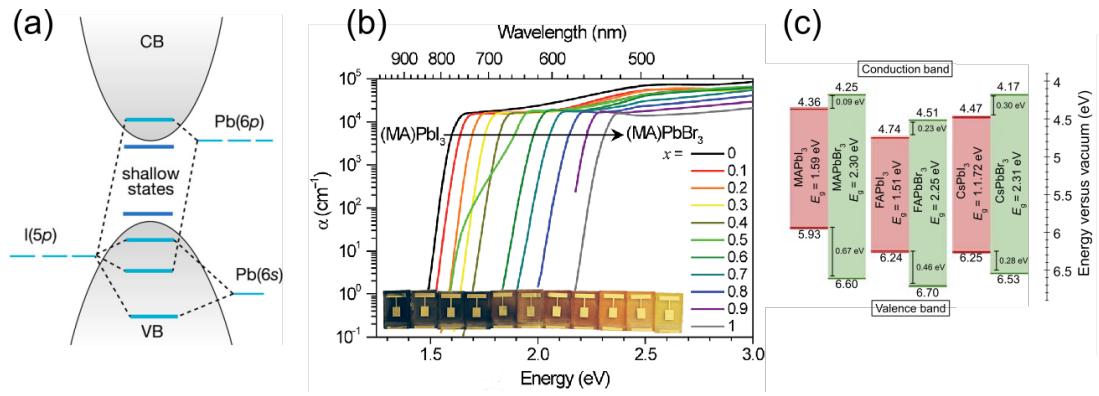

Figure 1.4: *(a) Schematic representation of the conduction band (CB) and the valence band (VB) formed by B-site and X-site ions in an ABX_3 perovskite. Adapted from [27]. (b) Absorption coefficient (α) of $MAPb(I_xBr_{1-x})_3$ perovskite films measured by spectral reflection and transmission measurements. Photographs of the $MAPb(I_xBr_{1-x})_3$-based PSCs from $x = 1$ to 0 (left to right). Reprinted from [28]. Band offset diagram for $APbX_3$ for $X = I^-$ and Br^-, and $A = MA^+$, FA^+, Cs^+. Reprinted from [29].*

effect on the Pb-X bonding distance, which indirectly impacts the bandgap of the perovskite [30].

The optical absorption of hybrid perovskites is remarkably efficient due to their direct bandgap. In contrast with monocrystalline silicon (mono-Si), the strong absorption of perovskites enables fabricating solar cells with thin (∼hundreds of nm) films acting as light absorbers [31].

Charge carrier transport

Regarding carrier transport, hybrid perovskites are ambipolar, which means they can efficiently transport both electrons and holes [32]. The carrier transport in the material is defined by their mobility μ, diffusion length L_D, and lifetime τ.

The mobility μ is inversely proportional to the effective mass of the considered carrier, which is relatively low in hybrid perovskites (∼0.1-0.2 m_e), allowing high carrier mobilities in the range of 3-25 $cm^2/V.s$ for electrons and 17-164 $cm^2/V.s$ for holes [33]. These values depend strongly on the measurement technique employed, explaining the discrepancy in values reported in the literature.

The diffusion length L_D is the distance over which a carrier can diffuse in the material before recombining. The longer is the L_D, the higher is the number of charges collected in a thin film solar cell. The L_D thus dictates the thickness of the absorber layer implemented in a photovoltaic device. It is related to the carrier lifetime τ:

$$L_D = \sqrt{\tau D}, \tag{1.2}$$

where D is the carrier diffusion coefficient expressed by $D = \mu k_B T/q$. Typically L_D reaches value up to 1 μm in hybrid perovskites while τ reaches hundreds of ns [31].

Recombination

In hybrid perovskites, the absorption of a photon with higher energy than the bandgap generates an exciton, which dissociates into a mobile electron-hole pair at room temperature (≈ 300 K)

due to its low binding energy. Eventually, without extraction, the electrons and holes recombine radiatively (i.e., with light emission) or non-radiatively (i.e., without light emission). There are several recombination processes in semiconductors, some of which are shown schematically in Figure 1.5.

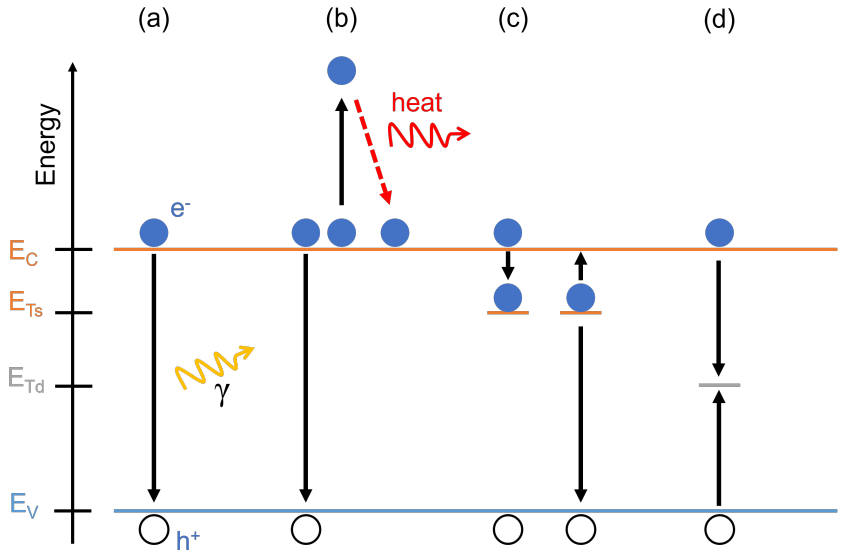

Figure 1.5: *Schematic illustration of the various recombination pathways in a semiconductor. Electrons (e^-) and holes (h^+) are represented by filled and empty circles, respectively. (a) Radiative recombination, resulting in the emission of a photon of energy $\gamma \approx E_C - E_V = E_g$. (b) Auger recombination, involving an additional free electron, which loses its energy by thermalization (red dashed arrow). (c) Trap-assisted bulk recombination through a localized trap state at energy E_{Ts}. The trapped charge can either escape the trap or recombine directly with a hole in the VB. (d) Deep trap localized at energy E_{Td} acting as a recombination site.*

Figure 1.5(a) shows a band-to-band recombination in which an electron in the CB recombines with a hole in the VB, emitting a photon with an energy close to the bandgap E_g. This recombination is faciliated in direct bandgap semiconductors such as hybrid perovskites while it is limited in indirect bandgap semiconductor such as Si.

In Auger recombination (see Figure 1.5(b)), an electron in the CB recombines with a hole in the VB, and the generated energy is transferred to another free electron of the CB. This newly excited electron accesses high energy states or loses its energy by thermalization (i.e., phonon generation). Since it requires three particles to occur, this phenomenon remains negligible in perovskites under low and moderate excitation regimes (concentrations of generated excess carriers $\Delta n < 10^{16}$ cm^{-3}) corresponding to the operating conditions of a PSC [34, 35]. However, it can arise from electronic excitation as discussed in chapter 2.

Trap-assisted recombinations occur when the charge carrier is captured in a trap state localized within the bandgap (see Figure 1.5(c,d)). The carrier is then either released or recombine in the trap state which acts as a recombination site. The charge carriers escape easier from shallow defects, i.e., localized close to the band edges, than deep defects (energy states E_{Ts} and E_{Td} in Figure 1.5, respectively). In hybrid perovskites, this mechanism is non-radiative and predominant at low excitation regime [36, 37].

Defects

Hybrid perovskites exhibit intrinsic structural defects such as lattice vacancies (V_X absence of an atom), interstitials (X_i an atom residing between lattice sites) and anti-sites (X_Y an atom oc-

cupying the position of another atom) [38]. Hybrid perovskite films also present extrinsic defects on their surfaces and grain boundaries (GBs), such as substitutional and interstitial impurities. The defects generate states within the bandgap that trap photo-generated carriers and induce non-radiative recombinations. Therefore, higher defect density can lead to higher non-radiative recombination density and reduction of carrier lifetime [39].

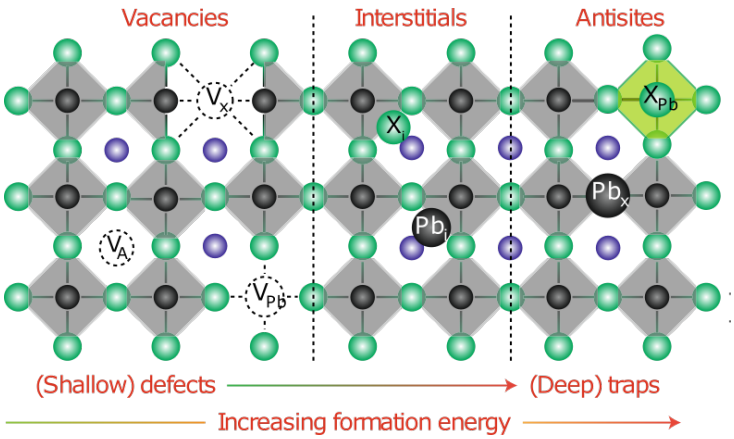

Figure 1.6: *Schematic of point defects in hybrid perovskites, such as vacancies (V_X, V_A, and V_{Pb}), interstitial (X_i and Pb_i) and anti-site atoms (X_{Pb} and Pb_X), arranged according to increasing formation energy, which corresponds to decreasing probability of occurrence. Adpated from [39, 40].*

The nature of defects governs the type of states generated within the bandgap, as shown in Figure 1.6. Numerous studies showed that most defects present in hybrid perovskites generate shallow defect levels localized close to the CB and VB extrema ($E_{Ts} \approx k_B T$ with k_B the Boltzmann constant and T the temperature) [39]. They act as "doping" states rather than recombination states. In $MAPbI_3$, the most common defects are iodine-related such as V_I vacancies, I_i interstitial and anti-sites I_{MA} and I_{Pb} [41]. While vacancies and interstitial ions create shallow states in the bandgap, anti-site ions generate deep trap states and thus promote non-radiative recombinations [42].

Previous works have shown that the defect concentrations are relatively high in hybrid perovskites ($\sim 10^{14}$-10^{17} cm^3) compared to traditional inorganic semiconductors. Since hybrid perovskites exhibit high carrier lifetimes, it was assumed that the material is defects-tolerant [39]. This trait was attributed to the fact that deep defects, such as anti-sites, have a high energy formation and thus a low probability of formation [43].

The formation of defects is an inherent aspect of the thin film deposition and crystallization process. Several studies have shown that the stoichiometry of the precursor solution plays a crucial role in determining the formation energies of defects. Non-stoichiometric regions in the film that are rich or poor in certain ions are more prone to defect formation [38, 43, 44].

In addition to reducing luminescence efficiency and hindering charge carrier transport, these defects also affect the stability of the perovskite materials by promoting ion migration, as discussed in Section 1.3 [45, 46].

1.1.3 Properties of triple-cation double-halide perovskite films

As mentioned in the previous Subsection, composition engineering is usually implemented to tune the bandgap width of hybrid perovskites depending on the targeted application. The fabrication

by solution processing from precursor salts allows to easily vary the composition. By substituting or mixing halides in the X-site, the $MAPbX_3$ perovskites bandgap can range from 1.51 to 3.1 eV [47]. Since constraints on the tolerance factor t must be satisfied to form a photovoltaic perovskite phase, substitution of MA^+ with FA^+ or Cs^+, while having a limited effect on the bandgap ($E_g(FAPbI_3) = 1.52$ and $E_g(CsPbI_3) = 1.73$ eV) is widely used to adjust the tolerance factor [20]. After several prospective studies on perovskite composition, Saliba et al. came out with the so-called triple-cation double-halide perovskite, $Cs_{0.05}FA_{0.78}MA_{0.17}Pb(I_{0.83}Br_{0.17})_3$, referred to as CsMAFA hereafter. The CsMAFA perovskite showed a bandgap of 1.62 eV with an absorption onset at ∼750 nm and was recognized as the best-performing composition in single-junction cells for several years.

Ruf et al. showed experimentally with temperature-dependent measurements that CsMAFA does not show any phase transition in contrast with $MAPbI_3$ between 10 and 300 K (see Figure 1.7(b)).

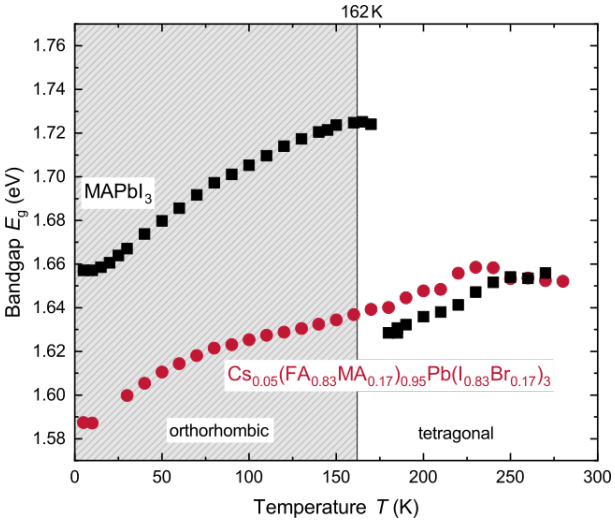

Figure 1.7: *Bandgap energies E_g of $MAPbI_3$ and $Cs_{0.05}FA_{0.78}MA_{0.17}Pb(I_{0.83}Br_{0.17})_3$ (CsMAFA) perovskite thin films, determined from fits of experimental absorption spectra acquired over a temperature range from 5 K to 280 K. $MAPbI_3$ (black squares) exhibits a phase-transition-related jump of around 100 meV in bandgap energy at 162 K. CsMAFA perovskite (red circles) do not show phase-transition-related features. Adapted from [48].*

In this thesis, we focus on this specific composition of hybrid perovskites.

Conclusion of the section

In this Section, the composition of $APbX_3$ hybrid lead halide perovskite materials has been presented. We have shown that the Goldschmidt tolerance factor establish requirements on the composition of perovskite materials for their crystallization in phases photoactives, including cubic and tetragonal symmetries. It was noted that hybrid perovskites can also crystallize in other non-photoactives symmetries, such as hexagonal and orthorhombic. We then discussed the nature of hybrid perovskites as direct bandgap semiconductors and emphasized on the tunability of the bandgap by alloying halides. The strong absorption, long lifetime, and long diffusion length of charge carriers in these materials were also highlighted. We presented different types of defects and noted that shallow defects such as I_i and V_I are prevalent in the hybrid perovskite films studied. Finally, we introduced the composition studied in this work, $Cs_{0.05}FA_{0.78}MA_{0.17}Pb(I_{0.83}Br_{0.17})_3$ (CsMAFA), which exhibits a direct bandgap of 1.62 eV.

1.2 Perovskite solar cells

As discussed in the Introduction, various paradigms of solar cells are currently being studied to improve the performance of photovoltaic systems. PPerovskite solar cells (PSCs) are thin film solar cells whose operating principle is described in this section. A brief description of the deposition processes used for the PSCs fabrication is also provided. Finally, results obtained at the IPVF on the development of CsMAFA-based PSCs are presented.

1.2.1 Basic concepts of thin film solar cells

PSCs include a perovskite absorber film generating free carriers upon absorption of photons energy higher than its bandgap. The generated free carriers, i.e., electron-hole pairs, are naturally separated in the film. Carriers are then transferred to the dedicated charge transport layers (CTLs), i.e., the Electron Transport Layer (ETL) and the Hole Transport Layer (HTL). Finally, the collected carrier diffuses to contact layers, i.e., the anode and the cathode, and contribute to the current in an external circuit. Figure 1.8(a) shows the constituent layers of a PSC (in n-i-p configuration as discussed in the next Subsection)

The ambipolar nature of hybrid perovskites enables charge separation and collection without CTL. However, photovoltaic performances in such configurations are relatively low [49–51]. Optimizing the energy alignment between the absorber and the CTLs allows for selective and efficient carrier collection (see Figure 1.8(b)).

The separation and collection of charge carriers occur through diffusion in the perovskite film and thus are dominated by the diffusion length L_D discussed in the previous Section. The perovskite film is then made thinner than L_D, such as 0.5-0.6 μm, to enable carrier extraction.

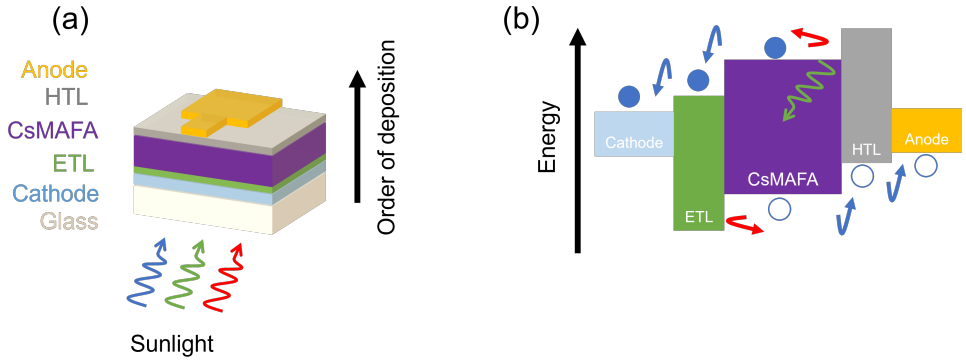

Figure 1.8: *(a) Schematic representation of a typical n-i-p PSC showing all the constituent layers, including the glass substrate, cathode, ETL, perovskite absorber, HTL, and anode, in the order of deposition. (b) The corresponding band alignment and carrier transport are sketched, with blue and red arrows indicating the movement of selected and blocked carriers, respectively.*

A solar cell can be considered as a diode generating current and voltage under illumination. From the general expression of the photo-generated current in a solar cell (see equation 1), three characteristic parameters are identified:

- the current density at short-circuit J_{sc} at which the output voltage is null which increases as non-radiative recombination are reduced.
- the open-circuit voltage V_{oc} at which the output current is null. It characterizes the capacity of transport and extraction of photo-generated charge carriers.

- the Fill Factor FF corresponding to the ratio between the output power P_{MPP} at the maximum power point (MPP) and the product $J_{sc} \times V_{oc}$ such as:

$$FF = \frac{P_{MPP}}{J_{sc} V_{oc}} \tag{1.3}$$

  It is maximal with infinite shunt resistance (R_{sh}) and zero series resistance (R_s) (see Figure 1.9).

These parameters describe the photovoltaic performances of a solar cell. They need to be maximized to enhance the electrical power produced. The power conversion efficiency (PCE) at a given incident illumination power P_{in} is expressed as following:

$$PCE = FF \times \frac{J_{sc} V_{oc}}{P_{in}} \tag{1.4}$$

The solar cell performances are measured through current-voltage (J-V) measurements in "1-sun" standard test conditions, i.e., illumination with the AM1.5 solar spectrum with P_{in} = 1000 W.m^{-2} at 25°C. Figure 1.9 shows an example of a J-V curve measured on a PSC in standard conditions.

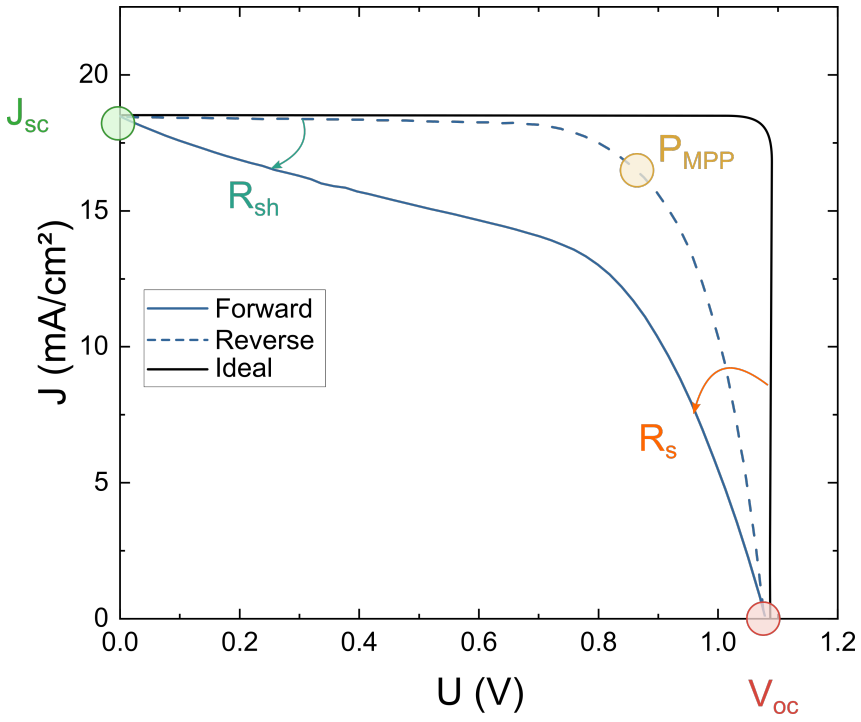

Figure 1.9: *J-V curves of a PSC measured under standard conditions, with a forward (solid line) and reverse (dashed line) scan of the voltage. The current density at short-circuit (J_{sc}), open-circuit voltage (V_{oc}), and maximum power point (MPP) are indicated, along with the impact of shunt (Rsh) and series (Rs) resistances on the fill factor (FF).*

Depending on the direction and the speed of the voltage scan, a difference in J-V characteristics, i.e., an hysteresis, was found in PSCs [52, 53] as shown in Figure 1.9. Such behavior raised the question of the accurate measurement of J-V characteristics of PSCs.

The hysteresis phenomenon has been ascribed to ion migration, which can be slower than voltage scan rates [54], or to the presence of interfacial defects [55]. However, these hypotheses are still under debate in the community that aims at suppressing this phenomenon.

The performances of a solar cell is limited by thermodynamic considerations included in the model introduced by Shockley and Queisser in 1961 [56, 57]. The authors derived a theoretical limit of the PCE as a function of the bandgap, called the Shockley-Queisser (SQ) limit. A maximum value of approximately 33% is reached for a single-junction solar cell with an active layer having a bandgap of approximately 1.4 eV. This limitation results from two major drawbacks of single-junction solar cells: incomplete absorption of the solar spectrum and thermalization losses.

Several strategies have been investigated to overcome this limitation, such as solar concentration [58], hot-carrier management [59], and multi-junction architecture [60]. While some studies have demonstrated the use of perovskite in the two former [34, 61], multi-junction and more specifically tandem (double-junction) architectures have received significant attention from the research community and the industrial actors. Based on the SQ model, a tandem solar cell with optimized bandgaps can reach $\approx 45\%$ PCE. For a perovskite/Si tandem with a combination of 1.70 and 1.12 eV bandgaps, the theoretical SQ limit was estimated to be 44.1% [62], which is promising for future high-efficiency PV systems.

Although having a tunable bandgap is an interesting feature that motivates the development of perovskite-based tandem devices, other characteristics, including precursor prices, process compatibility, and adaptability to other technologies (Si and CIGS), are also significant advantages.

1.2.2 PSC fabrication processes and applications

Architecture

Over the years, the architecture of PSCs has been constantly optimized to improve photovoltaic performance and stability. Initially, PSCs have emerged from the Dye-Sentisized Solar Cells (DSSCs) field. Thus, they were made with a mesoporous TiO_2 scaffold (m-TiO_2) filled with perovskite considered as dyes [13]. The architectures of PSCs has evolved towards a multilayer stack (from bottom to top) such as the one of the thin film PV technologies: glass substrate (for transparency and mechanical integrity); transparent conductive oxide (TCO); bi-layer compact and mesoporous ETL filled and capped by the perovskite absorber; HTL, and conductive electrode (cathode) (see Figure 1.8(a)). This architecture where the ETL is mesoporous and is facing the incoming light is called mesoporous n-i-p. The equivalent architecture without the mesoporous layer is designated as planar n-i-p and benefits from a simplified fabrication procedure. In p-i-n architectures, the ETL and HTL positions are inverted.

Deposition methods

As mentioned in the previous section, hybrid perovskite films benefit from high defect tolerance enabling facile and cheap fabrication methods such as solution processing, or evaporation [63]. Here lies the greatest advantage of PSCs over the other candidates for solar cell applications such as Si, III-V, or chalcogenide materials, which require a more complex and costly manufacturing process [6].

In solution-based procedures, the precursors are usually dissolved in organic solvents and deposited onto a substrate. The liquid layer is then dried and annealed to form a solid polycrystalline perovskite film.

The quality of the film depends on the optimization of the deposition process depends , i.e., the thickness, the morphology, and the homogeneity. In this context, many techniques have been developed to obtain high-quality perovskite films such as solution-based, vacuum-based, and mixed solution and vacuum methods [63, 64].

However, the research efforts are not only focused on improving the deposition of perovskite films. For example, researchers are working to replace the solvents commonly used in the fabrication processes, such as GBL, DMF or NMP, which have a negative impact on the environment and human health [65].

As mentioned in the introduction, scaling up the deposition processes is one of the most important research topics. Currently, the largest reported perovskite solar module (PSM) has been fabricated by Panasonic and exhibits an area of 802 cm^2 for a PCE of 17.9%. Although this is an impressive result, it is still almost 8% (absolute) below the current record for a PSC. PSMs must transition to commercially relevant sizes without such PCE losses to integrate the PV market [7]. To this extent, several large-scale deposition procedures are currently investigated, such as slot-die, blade, inkjet, and spray coating [66, 67].

1.2.3 State-of-the-art PSCs

The rise in efficiency for single-junction PSCs up to 25.7% shows the continuous and rapid progresses that have been made and let expect a bright future for this technology. One of the most realistic application of PSCs lies in their coupling with silicon in tandem devices [68, 69]. In fact, a research team from HZB has reported in December 2022 a record with perovskite/Si tandem solar cells demonstrating a PCE of 32.5%, which confirms their feasibility and motivates their development.

Now that perovskite-based devices reach outstanding efficiencies, improving their stability is crucial for a future introduction in the PV market (see Figure 1.10). If their instability in operating conditions is not solved, application in a tandem solar cell is dubious. In a recently published study on the stability of the perovskite/Si tandem, Duan et al. calculated the Levelized Cost Of Energy (LCOE) with respect to the power loss due to the addition of the perovskite top layer (and the deposition cost). They found that these additional performance losses must not exceed 2% per year to achieve a beneficial LCOE and be competitive with the single silicon solar cell[1] [7]. This study highlights the critical role of perovskite stability in perovskite/Si tandem commercialization.

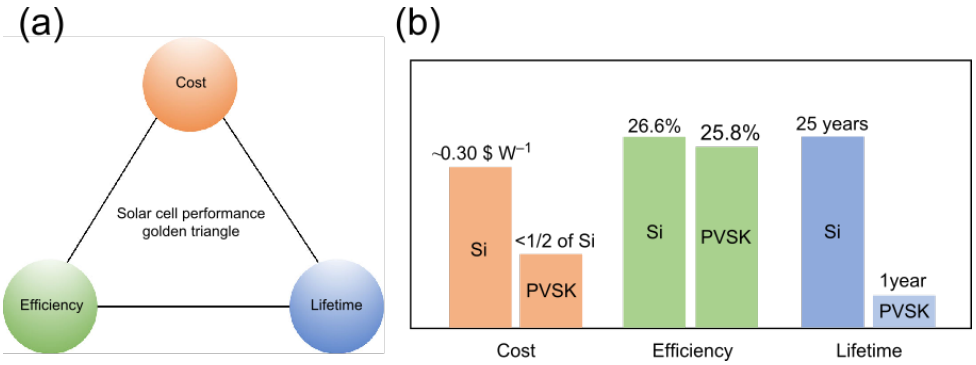

Figure 1.10: *The comparison of perovskite and silicon solar cells. (a) "Golden triangle" of solar cells: cost, efficiency, and lifetime are considered. (b) Corresponding values for silicon and perovskite solar cells. Adapted from [70].*

The growing need for stable PSCs is well represented by the evolution of publications that have reported stabilized PCE in the last decades, shown in Figure 1.11(b). The percentage stayed at 0% during the first ~5 years of research (2009-2014) and increased significantly during the last 4 years.

[1] With the following considerations: mono-Si PCE = 21.8%; 0.67 US$/Si-cell; 25-30 years of lifetime (ΔPCE < 20%); perovskite/Si PCE = 31%; 0.5 US$/Perovskite-cell

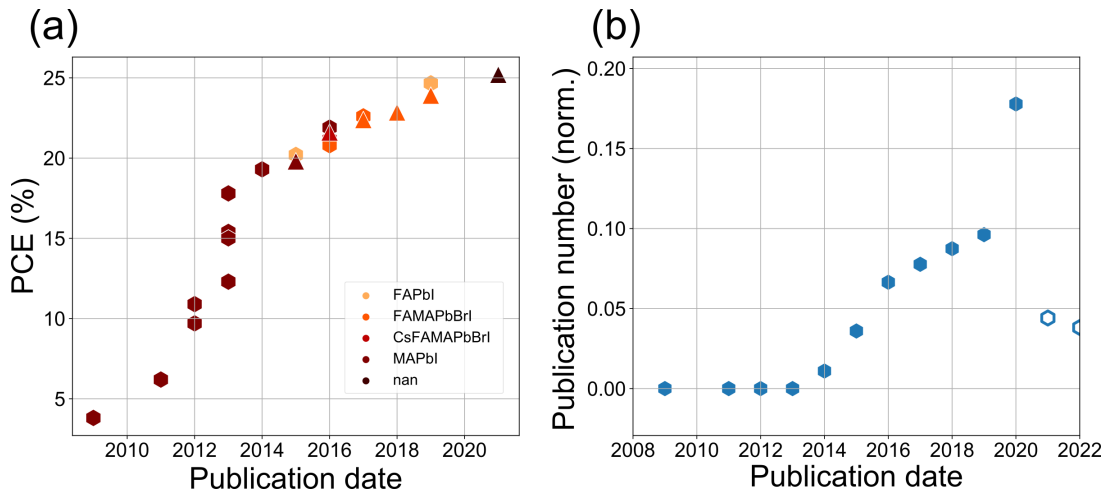

Figure 1.11: *(a) Evolution of record PCE as a function of the publication date. PCE values are in the form of hexagons and triangles, corresponding to non-stabilized and stabilized (during more than 600 seconds) reported PCE, respectively. (b) Number of publications reporting a stabilized PCE normalized by the total number of publications of the year, as a function of date. Data were extracted from the open access perovskite database project [71]. Values for 2021 and 2022 may not be representative of the literature trend.*

Figure 1.11(a) shows the rapid increase in PCE of PSCs with respect to publication dates and perovskite compositions. As mentioned before, the $MAPbI_3$ used to dominate the records of PCE in PSCs before more complex compositions such as MAFA ($MA_xFA_{1-x}Pb(I_yBr_{1-y})_3$) and CsMAFA exhibit higher efficiency. It is worth noting that stabilized values were reported as PCE only after 2015. Nowadays, it is mandatory to report an efficiency record along with its evolution with time ($>$ 600 seconds).

1.2.4 Baseline fabrication process in this thesis

In this thesis, we study CsMAFA-based PSC deposited by solution process and implemented in n-i-p architecture cell. We then give a brief overview of the fabrication procedure employed. First, precursors salts, which include all the constitutive elements of the hybrid perovskite (PbI_2, $PbBr_2$, CsI, MAI, FAI), are dissolved in organic solvents (mix of DMF and DMSO). The mixture is then deposited by spin-coating onto a substrate consisting of glass, FTO, and dedicated ETL, either TiO_2 or SnO_2 in our case. An anti-solvent is dripped to evacuate the ink solvent and to trigger the nucleation of the perovskite film. Finally, the sample is annealed at 100°C for 30 min, and we obtain what we call hereafter a half-cell device.

Another perovskite fabrication route employed at IPVF consists of a two-step solution procedure and is implemented by slot-die coating. A film of PbI_2 is first deposited onto the substrate and subsequently converted into a perovskite film via a second slot-die step with the enduction of organic and inorganic ink on its top. This sequential deposition method enables large device fabrication and fine control on the crystallization [72, 73].

To complete the PSC fabrication, an HTL, either PTAA (poly(triaryl amine)) or Spiro-OMeTAD, is spin-coated on top of the perovskite film. A contact layer, either gold for opaque PSC or ITO for semi-transparent PSC, is finally deposited via thermal evaporation or sputtering, respectively.

Table 1.1: *J-V characteristics of the PSCs analyzed in this thesis. The performances reported correspond to the J-V reverse scan of the champion device measured at 1 sun illumination and stabilized for 600 seconds.*

Absorber	ETL	HTL	J_{sc} ($mA.cm^{-2}$)	V_{oc} (V)	FF (%)	PCE (%)
CsMAFA baseline	m-TiO_2	PTAA	21-22	1.08-1.13	70-75	15.8-18.6
CsMAFA slot [9]	SnO_2	Spiro	21.7	1.108	79.8	19.2

PSCs are promising thin film-based devices for the next generation of photovoltaic systems. They benefit from the outstanding optoelectronic properties of hybrid perovskites and their facile, cheap, and flexible fabrication procedure. Significant efforts were made to adjust the material to foreseen applications such as tandem solar cells and large-scale devices. With the efficiency increasing, an in-depth understanding of the causes of their instability is needed.

1.3 Degradation of perovskite films and solar cells

1.3.1 Thermal instability of perovskite films

Phase transition

A solar cell operates at temperatures typically between 25 and 80°C [74]. Ensuring that hybrid perovskites implemented in PSCs are stable in this temperature range is thus crucial. As mentioned in Section 1.1, at room temperature, hybrid perovskites turn into non-photoactive phases when constraints on the tolerance factor t ($0.71 < t < 1$) are not respected.

The tolerance factor of $MAPbI_3$ is equal to 0.91 at room temperature, and it exists in a black photoactive phase throughout operational temperatures [14, 48]. Conversely, $FAPbI_3$ and $CsPbI_3$ perovskites tend, at room temperature, to revert to yellow δ-phase due to the size of FA^+ and Cs^+ cations, too large and too small, respectively [75]. The films based on these compositions are usually crystallized at elevated temperatures (< 100°C) to form a black phase and then quenched at room temperature. The crystal structure of the film is then cubic but it is metastable and tends to revert to the δ-phase stable at room temperature [76].

This structural issue has motivated researchers to stabilize perovskites in this temperature range by mixing A-site and X-site ions. This approach also enables tuning the material bandgap for targeted applications, as mentioned in Section 1.1. With alloyed-cations, the perovskite benefits from the combination of small and large size cations, tuning the tolerance factor to favorable values to generate a stable photoactive perovskite structure over the operating temperature range [48, 76] (see Figure 1.2).

Additionally, mixed-halide perovskites with Br^- and I^- anions show better thermal stability [76]. Another route to enhance the thermal stability consists in tilting the $[PbX_6]^{-4}$ octahedra as Doherty et al. have recently reported [77]. However, such procedure requires a high control of the crystallization of the film.

Film decomposition

The resistance to thermally activated chemical decomposition is also needed to prevent any losses of components. In theory, the sublimation temperatures of organic and halide species are between 250°C and 400°C as reported for $MAPbX_3$ or $FAPbX_3$ perovskites [78–80]. Thus, no mass

losses are expected during the annealing of the film ($\sim$ 110°C) or under operation. However, lower decomposition temperatures have been reported when perovskite films such as $MAPbI_3$ are annealed in vacuum or dry air [81]. Since the HTL is deposited on the perovskite film (in n-i-p architecture), its potential degradation in vacuum or in dry air limits the choice of deposition methods and of materials. Similar considerations apply to the selection of encapsulation techniques.

Moreover, defective surfaces of hybrid perovskite films have been shown to decompose at relatively low temperatures, such as 85°C for $MAPbI_3$ [82]. It highlights the contribution of defects to the thermal instability of hybrid perovskites.

The MA^+ cation substitution by FA^+ and Cs^+ improves the thermal stability of the film as FA^+ has a lower tendency to release a proton than MA^+ to form gaseous degradation products such as MA, and CsI is less volatile [76].

In the context of surface-mediated degradations, the passivation of the surface defects is promising to enhance thermal stability. In fact, 2D-perovskites, showing already good passivation and encapsulation capabilities [83], have enhanced thermal stability of MA-based perovskites [84]. Covering the perovskite film of a PSC with a 2D-perovskite film is thus a promising route to hinder thermally induced decomposition.

"Carpet like" encapsulation is also a way to limit the leak of gaseous degradation product [85].

Hybrid perovskite films suffer from phase transition in operational temperatures and decomposition at higher temperatures. To avoid these thermal instabilities, the MA^+ organic cations are mixed or replaced by FA^+ and Cs^+ cations. Passivation of surface defects with a 2D-capping layer is also a promising alternative.

1.3.2 Instability of perovskite films under illumination

Ion mobility in halide perovskite films

The ionic nature of hybrid perovskite allows ionic species to migrate throughout the thin film when exposed to light. This phenomenon, first reported by deQuilettes et al. on $MAPbI_3$, is linked to the slow diffusion of ions in the material [86] which is eased by the presence of ionic defects, making migration channels, such as GBs or surfaces, more conductive [87–89]. The photo-induced migration of halides can increase the luminescence intensity perovskite film, as shown in Figure 1.12. This effect depends on the atmosphere and will be discussed later [90].

Halide migration

We mentioned previously that A-site and X-site ions alloying is a privileged route to enhance thermal stability of hybrid perovskite and tune their bandgap. However, Br-rich perovskites become more sensitive to photo-induced ion migrations. In fact, when a mixed-halide perovskite film is exposed to light, the Br^- and I^- anions are moving in different directions. This migration induces the formation of I-rich and Br-rich regions in the film. With further light exposure, these regions can become completely demixed, showing pure I-based and Br-based perovskite phase in distinct areas of the film [91–94].

The phenomenon is experimentally characterized by a red-shift of the luminescence peak with the increase of its intensity as shown in Figure 1.12(a). This shift originates from the difference between the bandgaps of the I-rich and Br-rich perovskite phases. The former exhibits a lower bandgap (see Figure 1.12(b)) and acts as carrier trapping domains. These carriers (holes) are

then recombining radiatively preferentially in the I-rich domains inducing a red-shift of the averaged luminescence.

This phenomenon is called the *Hoke effect* as it was first reported by Hoke et al. in $MAPb(I_xBr_{1-x})_3$ perovskites [28]. The authors also showed that this phenomenon is reversible after removing the light from the sample. It typically occurs in hybrid perovskites with a Br concentration higher than 20% [95], which limits the alloying of halides for bandgap tuning.

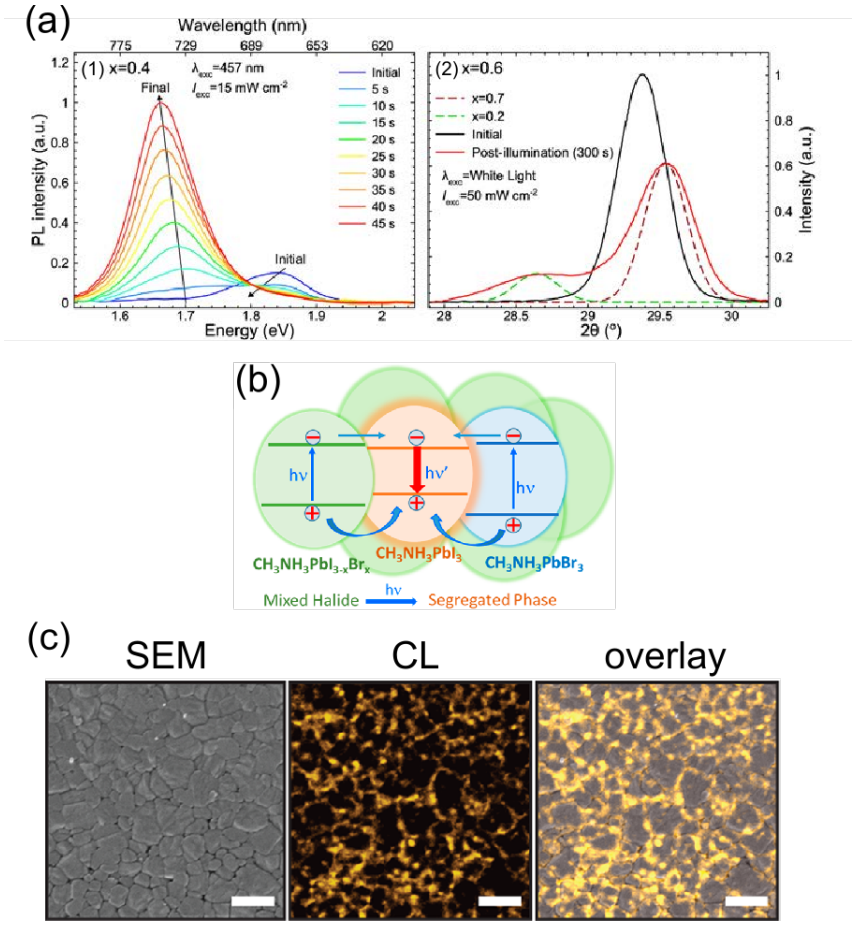

Figure 1.12: *(a) 1: Photoluminescence (PL) spectra of $MAPb(I_{0.6}Br_{0.4})_3$ over 45 seconds of continuous illumination (λ_{exc} = 457 nm, I_{exc} = 15 $mW.cm^{-2}$) at 300 K, measured in 5-second segments. 2: X-ray diffraction (XRD) patterns of a $MAPb(I_{0.4}Br_{0.6})_3$ thin film showing the (200) Bragg reflection before (black solid line) and after (red solid line) 300 seconds of illumination. The dashed green and brown lines are XRD patterns from $MAPb(I_{0.2}Br_{0.8})_3$ and $MAPb(I_{0.7}Br_{0.3})_3$ thin films, respectively, fabricated for comparison purposes. Adapted from [29]. (b) Schematic illustration of the energy levels (CB and VB) of $MAPb(I_xBr_{1-x})_3$ and the segregated phases, $MAPbI_3$ and $MAPbBr_3$. Electron-hole pairs generated in the mixed halide and the Br-rich regions recombine preferentially in the I-rich region. Adapted from [91]. (c) Analysis of a $MAPb(I_xBr_{1-x})_3$ thin film after exposure to light for 5 min at 100 mW/cm^2 with cathodoluminescence (CL). The SEM image shows the polycrystalline morphology of the film with grains and grain boundaries (GBs). The CL map shows highly emissive regions attributed to the I-rich phase. The SEM overlaid with the CL map shows that the I-rich regions are localized at the GBs. The scale bar is 2 μm. Adapted from [96]*

Cation migration

X-site halides are not the only mobile species in hybrid perovskites since A-site cations can also migrate throughout perovskite film. This phenomenon has not been extensively studied in the

literature compared to halide migration. However, it has been reported in several compositions such as $MAPbI_3$ [97], $CsMAFAPbI_3$ [98], CsMAFA (mixed-halide) [99], FAMA (mixed-halide) [100, 101], and CsFAPbI [102] as shown in Figure 1.13. While the halide migration occurs in short-time exposure to light ($\sim$ tens of ms), cation migration is much slower ($\sim$ tens of minutes) and was mostly reported under light coupled with electrical bias.

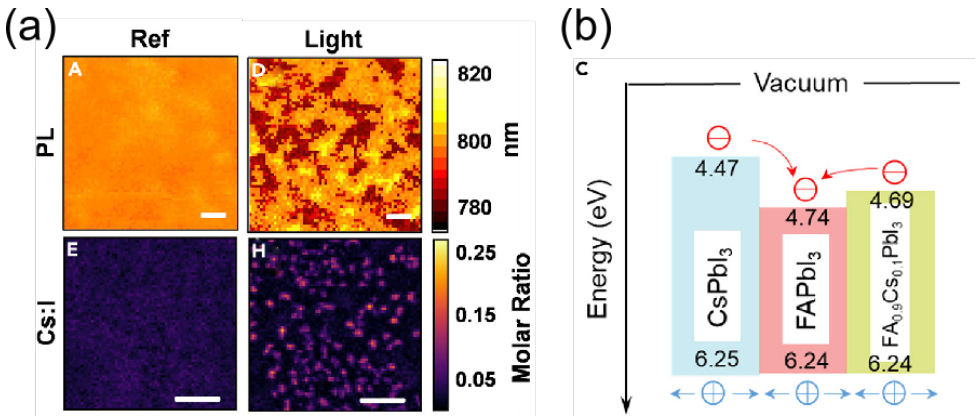

Figure 1.13: *(a) PL and X-ray fluorescence mapping of a $Cs_xFA_{1-x}PbI_3$ perovskite film before (left) and after (right) illumination. The scale bar is 5µm. (c) Band alignment estimated of $CsPbI_3$, $FAPbI_3$, and $FA_{0.9}Cs_{0.1}PbI_3$ perovskites. The photogenerated electrons from the inorganic and the mixed cation perovskite are trapped in the low bandgap $FAPbI_3$ region where they recombine. Adapted from [102].*

Although the literature is still elusive regarding the stress factor that drives the diffusion of cations, we can assume that the formation of photo-induced defects must facilitate cation migration similarly to halide migration [103].

Nowadays, countless experimental results and multiple models show and describe the photo-induced ions segregations in hybrid perovskite [29]. However, an agreement on the mechanisms behind this phenomenon is still lacking in the literature.

Mitigation of the ion migration

Several approaches have been reported so far to avoid photo-induced phase segregation [104]. Most of them are focused on the passivation of defects in the bulk, on the surface, and at the GBs of the film, which would simultaneously hinder the ion migration and enhance optoelectronic properties. The defects can be removed by the addition of molecular additives (Lewis acids) to the precursor solution [105], or the deposition of an extra thin layer on top such as Self-Assembled Monolayers (SAMs) [106], 2D-perovskite layer [83], and polymers (PMMA) [107].

The "natural" passivation of surface defects by illuminating the film in the presence of oxygen or moist air has also been studied [108, 109]. However, as discussed in the following subsection, the same atmospheric molecules (oxygen and water) induce the decomposition of the material.

Increasing the film crystallinity also enhances photo-stability [88, 104] although questions remain on the link between GBs and halide segregation [88, 110]. Interestingly, physical lattice compression through pressurization of the film has shown promising results to hinder photo-induced phase segregation [111].

The illumination induces migration of halides and cations and then phase segregation in hybrid perovskite films. This phenomenon is related to defects in the film and thus can be mitigated through their passivation.

1.3.3 Instability of perovskite films under atmospheric stress factors

Theoretically, PSC and its perovskite absorber layer should never interact with the environment if the encapsulation is efficient. However, it is still crucial to understand degradation mechanisms induced by these extrinsic factors for several reasons. First, the stability of the perovskite layer and the PSC will dictate the degree of packaging required and define acceptable levels of the packaging permeability. Then, even the best encapsulant might occasionally fail, or the cell might be transported in a non-ideal environment during fabrication. Finally, it is a major drawback for industrialization if the whole fabrication must be done in specific atmospheric conditions, such as low oxygen and low relative humidity used in the glove boxes of research laboratories. Hence, developing atmospheric stable perovskite films is crucial for introducing PSCs in the PV market.

Effect of the oxygen

Oxygen molecules alone were shown to have a small effect on hybrid perovskites. However, when coupled with light, their impact on the decomposition of hybrid perovskites becomes dramatic [76, 109, 112]. The mechanism, called photo-oxidation, follows these successive steps: (1) adsorption of oxygen molecules (O_2) on iodide vacancies ($V_I{}^+$) (2) electron trapping in the conduction band (3) formation of superoxide $O_2{}^-$ and (4) acid-base reaction with the A-site cations. The photo-oxidation leads to the formation of gases such as methylamine (MA) or formamidine (FA), and other species such as PbI_2 and water. This mechanism is critical for hybrid perovskite films and can be prevented mainly by reducing the density of iodide vacancies.

Hybrid perovskites based on tin(II) suffer even more from oxygen molecules than lead-based perovskites because tin(II) oxidizes easily into the tin(IV) [16, 17].

Effect of the moisture

The effect of moist air on PSCs has been studied historically on unencapsulated cells exposed to air with relative humidity (RH) higher than 50%, leading to a dramatic degradation of the device performances [113]. It has been shown that water molecules penetrate the perovskite film forming intermediate monohydrate (Reaction 1.5) and dihydrate (Reaction 1.6) phases as illustrated in Figure 1.14(a) for $MAPbI_3$.

$$MAPbI_3 + H_2O \longleftrightarrow MAPbI_3 \cdot H_2O \tag{1.5}$$

$$4[MAPbI_3 \cdot H_2O] \longleftrightarrow MA_4PbI_6 \cdot 2H_2O + 3PbI_2 + 2H_2O \tag{1.6}$$

$$MA_4PbI_6 \cdot 2H_2O \longleftrightarrow MAI \uparrow + 2H_2O + PbI_2 \tag{1.7}$$

The hydration depicted in the reactions above is reversible if all species are retained. Thus, the film recovers its pristine structure after some time in dry air (∼48 hours according to Leguy et al. [118]). If humidity exposure is pursued, the water molecules form strong hydrogen bonds with the A-site organic cations, breaking the octahedron $[PbX_6]^{4-}$ symmetry, and deprotonate the cation (see reaction 1.7). These cations are finally released in a gaseous form such as MA and FA along with hydroiodic or hydrobromic acid (HI and HBr), leaving behind the other elements to form degradation products [76, 119–121]. The moist air is also known to promote $FAPbI_3$ and $CsPbI_3$ conversion into their respective yellow δ-phase [75, 115, 116] (see Figure 1.14(b) and (c)). However, more stable structures are obtained by alloying cations. Finally, high relative humidity levels have been shown to exacerbate degradation mechanisms when coupled with

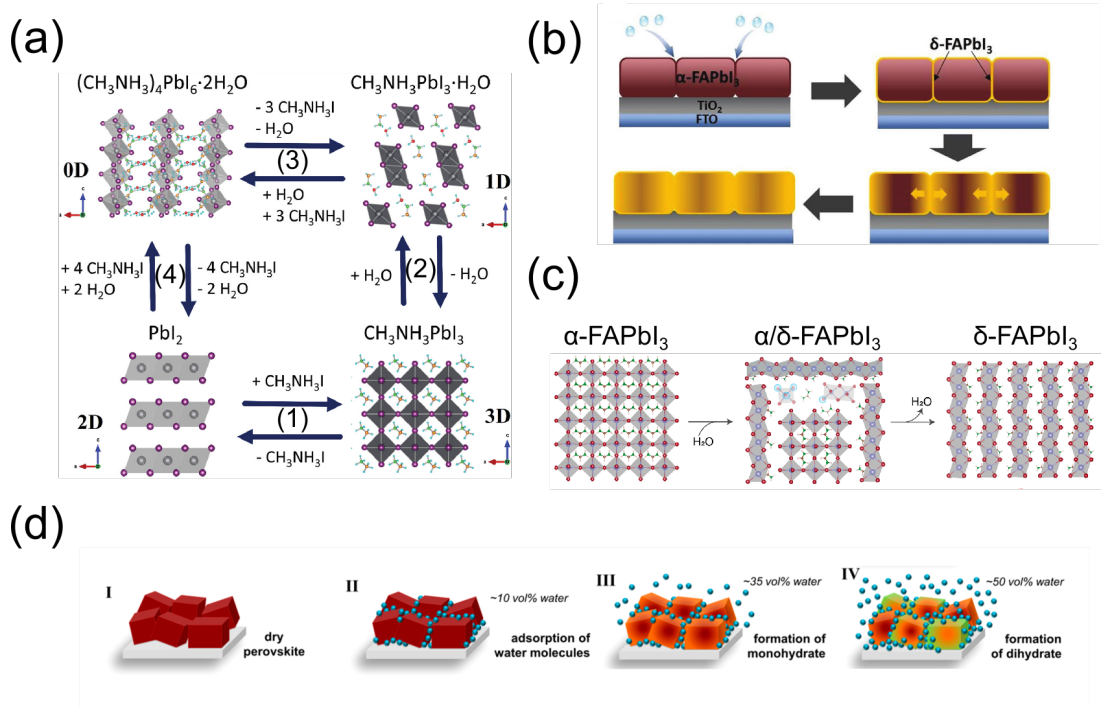

Figure 1.14: *(a) Schematic representation of the reversible reactions between $MAPbI_3$ and H_2O molecules. (1) Formation and decomposition of $MAPbI_3$. (2) Hydration and dehydration between the dry and monohydrated perovskite phases (reaction 1.5). (3) Equilibrium between mono- and dihydrated perovskites (reaction 1.6). (4) Equilibrium between PbI_2, the dihydrate perovskite phase, MAI, and water (reaction 1.7). Figure from [114]. (b) Illustrations of the different stages of the degradation process at the grain level. The water molecules ingress into the film through the GBs and transform α-$FAPbI_3$ into δ-$FAPbI_3$. Figure from [115]. (c) Schematic of the same transformation at the molecular level. The progression of the water molecules in the microstructure of α-$FAPbI_3$ is highlighted in the second scheme. Figure from [116]. Illustration of the influence of RH level on hybrid perovskite polycrystalline film: (I) the film is pristine at low RH level (< 5% RH); (II) at 10% RH, water molecules are adsorbed on the film; (III) at 35% RH, monohydrate phase is formed; (IV) at 55% RH, dihydrate phase is formed. Figure adapted from [117]*

other external stress factors such as heat [79], electrical bias [54], and light [122].

Moisture stability can be improved with several approaches that fall into two families: one focused on the optimization of the absorber and the other focused on the optimization of the PSC stack. The latter is discussed in detail in the next subsection. The optimization of the perovskite is usually done by tuning the lattice parameters to limit the penetration of water molecules.

For example, the alloying of X-site and A-site ions with the addition of Br^- and Cs^+ ions has been shown to significantly improve the moisture stability of hybrid perovskite films [76]. Substitution of halides with thiocyanate (SCN^-) ions also has a beneficial effect on film stability in humid air.

By increasing the film crystallinity, i.e. the grain size, Wang et al. showed a significant improvement of the moisture stability [123]. This may be due to the decrease of the surface area/volume ratio. Reducing the number of GBs, which are doorways for water molecules, is therefore promising.

Large organic cations have also been used in A-sites to transform perovskites into 2D structures on the surfaces and the edges of the film. These phases leverage the hydrophobicity of large cations to repel water molecules.

The degradation mechanisms involved in the decomposition of hybrid perovskites exposed to oxygen and high relative humidity are strongly related to the defect density on the surface and in the bulk, and thus to the quality of the film.

1.3.4 Instability of PSCs due to charge transport layers and electrodes

Photo-stability of charge transport layers

As hybrid perovskite film suffers from instability when exposed to light, heat or humid air, it can be difficult to assess the influence of CTLs. Therefore, studies of the impact of CTLs on PSC stability are also a hot topic nowadays.

Most HTLs such as Spiro-OMeTAD, PTAA, or PEDOT:PSS (Poly(2,3-dihydrothieno-1,4-dioxin)-poly(styrenesulfonate)) are made of organic semiconductors which are known to suffer from changes when exposed to light [124].

On the other hand, it has been reported that the TiO_2 used as ETL has a photocatalytic effect, when exposed to ultraviolet (UV) light, on the perovskite film adjacent, which decomposes via the oxidation I^- ions [125, 126]. This phenomenon motivates the replacement of TiO_2 by other oxide materials such as SnO_2, that can in addition be deposited by low-temperature processes. Filtering or down-converting UV light in the solar spectrum have also been considered to prevent the photocatalytic effect of TiO_2, but they can be complicated to implement.

Impact of atmosphere on CTLs

In principle, the perovskite absorber is protected from the environment first by the encapsulation, then by the contact layers, and finally by the CTLs. However, commonly used HTLs such as Spiro-OMeTAD and PTAA are doped with hygroscopic species, including tBP (tert-Butylpyridine) and Li-TFSI (lithium bis(trifluoromethylsulfonyl)-imide), that allow water molecules to enter the PSC and reach the absorber [127].

Several options have been proposed to prevent water ingress into perovskite. One is to use a protective layer between the CTLs and the perovskite film, such as Al_2O_3, 2D-perovskite, or an organic layer. This layer must protect the perovskite while allowing carrier transfer to the CTLs, which can be challenging [76]. Another alternative is to make the HTL hydrophobic by adding additives such as random copolymer (RCP) [128].

The ingress of oxygen molecules into HTLs is beneficial for PTAA and Spiro-OMeTAD layers, whose p-type conductivity is improved with oxidation. In contrast, when exposed to oxygen and UV light, the photocatalytic effect of oxide transport layers such as TiO_2 is significantly enhanced, which promotes the degradation of the adjacent perovskite layer as mentioned above. To mitigate this effect, researchers have replaced TiO_2 with SnO_2, which is less reactive. The introduction of fullerenes at the interface between the oxide and the perovskite was also investigated and showed promising results [129].

Thermal stability of CTLs

Organic materials such as Spiro-OMeTAD [130, 131], PEDOT:PSS [132], and PTAA [133] are prone to thermal instability. This instability is related to their intrinsic morphological instability

(Spiro recrystallizes at high temperatures) and the additives mentioned previously. These additives are volatile and can evaporate at relatively low temperatures (∼80°C), which has motivated the community to search for more stable dopant-free HTLs or alternative inorganic materials [134].

The degradation of the perovskite layer generates mobile ions that can diffuse towards the HTL. In previous studies, these ions, such as I^-, have been shown to dramatically reduce the conductivity of the HTL [131]. Since the diffusion of mobile ions is enhanced by the temperature increase, the conductivity of the HTL can be significantly affected.

The oxides commonly used in ETLs are thermally stable, with the exception of ZnO, which has been shown to cause degradation of the perovskite absorber [76]. Thermally stable ETLs such as TiO_2 or SnO_2 are therefore generally preferred.

Reactions with electrodes

The electrodes (anode and cathode), hereafter referred to as contact layers, have been shown in several previous works to interact with hybrid perovskite films in operating PSCs.

It has been reported that the aforementioned decomposition products of the perovskite film, such as MAI, HI, and I_2, can move in the PSC and corrode the metal-based contact layer [135]. This reaction can increase the resistance of the contact layer and thus decrease the fill factor FF of the PSC.

Metal atoms have been shown to diffuse from metallic electrodes such as Au, Ag, and Al, into the perovskite layer when exposed to light or heat [136]. These ions can form defect states at the interface or in the bulk of the perovskite film that degrade the V_{oc} and J_{sc} of the PSC [137]. In addition, several studies have reported that the metal from the electrode can reduce the Pb^{2+} cations to Pb^0, inducing the decomposition of the hybrid perovskite film [138].

These issues were addressed by introducing barrier (or buffer) layers between the absorber and the CTLs. Volatile species from the perovskite were then stopped before oxidizing the metal electrodes. The barrier layers also prevent the metal from diffusing into the perovskite layer. The PCBM (fullerene derivative [6,6]-phenyl-C_{61}-butyric acid methyl ester) has already demonstrated efficient barrier effect in several studies [139, 140]. Replacing metal electrodes with carbon-based electrodes or TCOs is also promising, although their conductivity is significantly lower.

In this subsection, we have introduced the degradation mechanisms related to CTLs in PSCs. The oxide layers used as ETLs in n-i-p PSCs can degrade the perovskite film under UV light exposure. This phenomenon is accelerated when the PSC is also exposed to oxygen. The organic HTLs are permeable to water molecules, which can penetrate into the perovskite film and degrade it. In addition, mobile ions from the perovskite film can lead to the breakdown of the HTL conductivity. We have also presented the effects of the electrodes in the PSC. Metal electrodes can react with the perovskite film, which causes its degradation. The perovskite film degradation products can also degrade the metal electrodes. To prevent these phenomena, the architecture of PSCs is generally adapted by adding buffer layers between the CTLs and the perovskite film.

1.3.5 Stability assessment based on ISOS procedures

As the development of PSCs increased, so did the need for standardized procedures to assess device stability. In fact, prior to 2020, the literature contained a wide variety of stability tests, making comparisons difficult. For example, the current "stability record" is held by Grancini et

al. for a PSC with a PCE stabilized for more than 10,000 hours [141]. However, the test was performed with UV-filtered illumination and at ∼45°C, which is not representative of the actual operating conditions of a solar cell.

Azmi et al. reported in April 2022 the fabrication of a PSC that withstands the damp-heat test (from the IEC 61215 standard tests), which places the device in a chamber set at 85°C with 85% RH for 1000 hours [8]. With a 2D-perovskite layer encapsulating the perovskite absorber, the authors were able to stabilize the PSC, which retained >95% of its initial PCE (∼24%) after more than 1000 hours. Such a result "is a step in the right direction for perovskite solar panels" as J. M. Luther and L. T. Schelhas commented [142]. However, comparisons with the work of Grancini et al. are difficult.

In 2020, a consensus statement was published for evaluating and reporting the stability of PSCs with respect to the various stressors mentioned before. The proposed tests are based on the International Summit on Organic Photovoltaic Stability (ISOS) protocols [143]. The publication proposes several tests to assess the stability of PSCs under single and coupled stressors. In Chapter 4, we set the relative humidity to 85% to refer to the ISOS D-1 procedure, which takes into account the effects of humidity on PSCs. In Chapter 5, the stability test on PSCs is performed by the ISOS L-1 procedure, which accounts for stability under bias and light exposure in inert atmospheres.

Conclusion of the section

In this section, the instabilities of hybrid perovskite films were first investigated. It has been shown that the thermal and light-induced degradation is due to the intrinsic instability of the material. It is mainly due to the high defect density of perovskite films, the volatility of their organic compounds, and the instability of their crystalline phase. The effect of oxygen and water molecules in inducing the decomposition of hybrid perovskite materials has also been described. The influence of contact layers and charge transport layers on the stability of PSCs was then presented. This discussion highlighted the need to protect the perovskite film and to use stable materials for these layers. Finally, we briefly presented the current procedures adopted to assess the stability of PSCs, which were the basis of the aging tests performed in this thesis.

1.4 Summary and objectives of the thesis

In this chapter, we first presented the ionic structure that defines perovskite materials and the conditions required to be part of this family. The case of hybrid organic-inorganic halide perovskites was then discussed, followed by their unique optoelectronic properties such as long carrier lifetime and good absorption, and optical bandgap easily tuned. We showed that these properties are advantageous for use as absorber layers in thin film solar cells, which benefit from versatility of the material and can be optimized for multiple applications in the photovoltaic field. These technical observations and the great progress made quickly promise a bright future for the PSCs.

Nonetheless, significant challenges are still to be addressed before the industrialization of this technology. We showed in the following that hybrid perovskite suffers from multiple degradation mechanisms, such as phase transition, separation, and decomposition, which directly affect PSCs performance. Coupled with the CTLs and contact electrodes intrinsic instabilities, the PSCs suffer from instabilities that are detrimental. The triple-cation double-halides perovskite CsMAFA in n-i-p configuration is a promising composition for efficient and stable PSCs. Given the complexity of the composition, multiple degradation mechanisms can occur in the absorber during operation. Comprehending the mechanisms is crucial to designing an efficient and stable PSC. *Therefore, in this thesis, we will perform accelerated aging of CsMAFA perovskite films to understand degradation mechanisms and to improve the stability of future PSCs.*

In this thesis, we work on CsMAFA perovskite film developed at the IPVF and deposited by spin-coating on top of either TiO_2 mesoporous scaffold layer or a thin SnO_2 layer. The degradation mechanisms occurring in CsMAFA perovskite film are investigated through aggressive environmental aging (high relative humidity and oxygen) of the "naked" film (see Chapter 4). Complete PSCs are also tested in operation conditions (light and bias), and the CsMAFA perovskite film state is analyzed after the procedure (see Chapter 5). In both analyses, we thoroughly describe the degradation mechanisms that lead to the observed changes. To this extent, we use a multi-scale correlative approach based on high-resolution analytical techniques included in electron microscopy.

Chapter

2 Electron Microscopy techniques: theory and experimental methods

Chapter content

2.1 Electron-matter interactions 30
2.1.1 Basis of electron-matter interactions 30
2.1.2 Electron-beam induced damages 32
2.2 Scanning Electron Microscope 33
2.2.1 SEM overview 33
2.2.2 Energy dispersive x-ray spectroscopy in SEM 34
2.3 Cathodoluminescence 39
2.3.1 CL set-up overview 39
2.3.2 Resolution 41
2.3.3 Data treatment 43
2.4 Hybrid perovskite degradation under e-beam exposure 44
2.4.1 Impact of the degradation on SEM images 44
2.4.2 Impact of the degradation on CL measurements 46
2.5 Scanning Transmission Electron Microscope 49
2.5.1 Lamella preparation 49
2.5.2 (S)TEM overview 50
2.5.3 Energy dispersive x-ray spectroscopy in STEM 54
2.5.4 Hybrid perovskite degradation in a STEM 57
2.6 Conclusions 60

The first electron microscope prototype was developed by Max Knoll and Ernst Ruska in 1931 and could magnify an image of sample four hundred times. Using electrons as an excitation source and based on the newly developed electromagnetic lenses, it aimed at outreaching the resolution of light-based microscopes. It took only two years to exceed the light diffraction limit and a few more before the first commercial electron microscopes appeared [144].

During this thesis, we are interested in the micro and nano-scale mechanisms governing the instability of hybrid perovskite materials. Among the range of characterization techniques of materials, electron microscopy-based measurements demonstrate the highest spatial resolution and thus suit our purpose.

In the present Chapter, we first describe the fundamental principles of electron-matter interactions (Section 2.1). Then, we give an overview of the three electron microscopes used in this thesis (SEM Merlin Zeiss, CL Chronos Attolight, and (S)TEM Osiris FEI in Sections 2.2, 2.3, and 2.5, respectively), along with specific techniques implemented in each instrument. Challenges due to the perovskite sensitivity to irradiation are addressed in Section 2.4 and Subsection 2.5.4, and suitable experimental conditions are established for the rest of the work.

2.1 Electron-matter interactions

Electron microscopy is a generic term covering all imaging techniques that use electrons as an excitation source. As the wavelength of electrons is much shorter than that of visible photons, electron microscopes (EMs) benefit from a considerably higher resolution than classical light-based microscopes, which are limited by diffraction to about 400 nm. EMs are used to investigate a wide range of small objects, inorganics, or organics. Along with high-resolution images, electron microscopy provides access to information on the composition, structure, and optoelectronic properties of semiconductors. It is thus implemented in multiple analytic techniques described in the Chapter.

This section presents the basis of electron scattering in bulk and thick samples. We depict the essential physical quantities to consider when performing electron microscopy analysis. Finally, we discuss the damages the sample might endure when exposed to electron-beam irradiation.

2.1.1 Basis of electron-matter interactions

In an EM, a flux of electrons, referred to as the electron beam (e-beam), is directed towards the sample with an energy E_b, also called the acceleration voltage in this work. As the electrons penetrate the sample, they may be deflected through interactions with the electrons or the nucleus of the constituent atoms. These interactions lead to electron scattering, which enables the imaging capabilities of electron microscopy.

The electron scattering involves elastic and inelastic processes. In elastic scattering, the impinging electron is deflected from its initial trajectory without losing energy. This deflection happens when the electron experiences Coulomb interaction with the nucleus of an atom in the sample, called the Rutherford scattering. The scattering angle primarily depends on the distance between the electron and the nucleus. When this angle is higher than 90°, the deviated electron is called a "backscattered" electron (BSE). In inelastic scattering, the impinging electron loses some kinetic energy by transferring it to the material. This energy generates in the material secondary electrons (SE), Auger electrons, electron-hole pairs, and phonons. The material may subsequently re-emit X-ray, ultraviolet, or visible photons through mechanisms described in the following Sections.

The interaction volume corresponds to the region in which a significant proportion (∼95%) of the e-beam energy is dissipated through inelastic interactions with the material. The size and shape of the interaction volume are also dictated by the sample geometry, as illustrated schematically in Figure 2.1 for thin (a) and bulk samples (b).

In thin samples analyzed in Transmission Electron Microscopes (TEMs), incident electrons interact with the specimen and can pass through it if their energy is sufficient, typically greater than 30 keV, and the sample is thin enough, in the order of 100 nm.

In bulk samples analyzed in Scanning Electron Microscopes (SEMs), all the incident electrons interact with the material within a "pear" shaped interaction volume. This peculiar shape is due to a relatively small elastic scattering cross-section, which corresponds to the probability of deflection of an electron, resulting in limited lateral scattering. As the electrons lose energy, they start to scatter sideways, forming this pear shape. The penetration depth R_e represents the maximum depth at which incident electrons are stopped within the material. It can be approximated using the following formula [146]:

$$R_e = (k/\rho)E_b^{\alpha}, \tag{2.1}$$

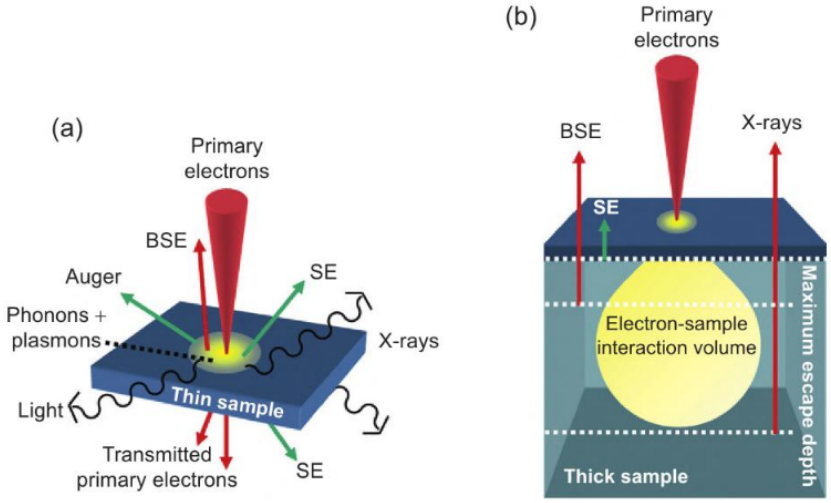

Figure 2.1: *Schematic representation of the interaction volume between impinging primary electrons and a thin (a) and a bulk (b) sample. The radiations produced by the interaction are indicated: Secondary Electrons (SE), Backscattered Electrons (BSE), X-rays, light, and transmitted electrons. Reprinted from [145].*

where ρ is the material density, E_b is the energy of the e-beam, and k and α depend on E_b and the atomic number of the material. The approach of Everhart and Hoff is the one mostly used to determine the volume of electrons scattered within a material [147]:

$$R_e = (0.0398/\rho)E_b^{1.75}, \tag{2.2}$$

with E_b given in keV and ρ in g/cm^3. With higher energies, electrons generate radiations deeper within the sample. It is worth noting that the interaction volume gets more hemispherical in high atomic number (Z) materials.

The interaction volume can also be estimated by the CASINO software, which implements a numerical method based on Monte Carlo simulations [148]. A CASINO simulation was performed using electrons with an $E_b = 3$ keV directed in a probe size of 10 nm onto a 500 nm thick layer of CsMAFA perovskite with a density 4.16 g.cm^{-3} as reported in previous studies for this material [149]. The simulation results, presented in Figures 2.2(a) and (b), show the obtained trajectories of the electrons within the sample and show the contour plot of the energy dissipated within the sample, respectively. It was found that approximately 95% of the energy of the e-beam is dissipated within 60 nm laterally and 100 nm in depth. The latter value is considered as the R_e.

The spatial resolution of electron microscopy techniques is limited by engineering challenges related to the instrument (its environment, its electronic components, and its electron optics), as well as physical limitations related to the electron-matter interactions (the interaction volume and the escape depth of the emitted radiation). In this Chapter, we will provide specific details for each technique used, highlighting the spatial resolution limitations associated with these physical limitations.

The electron dose is the number of incident electrons per area unit in the irradiated region during the exposition time. It corresponds to a particle fluence which is expressed by the following equation:

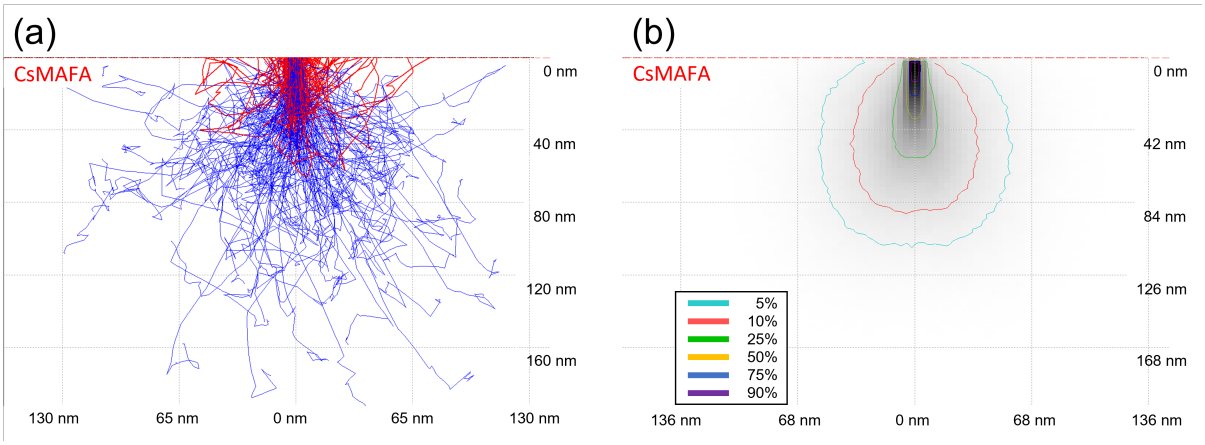

Figure 2.2: *Results of the CASINO simulation for a 3 keV acceleration voltage and a 10 nm probe size in a CsMAFA sample. (a) Blue lines describe the trajectories of primary electrons within the material. Red lines describe the trajectories of BSEs. (b) Contours of the dissipated energy of the e-beam within the sample summed over the normal direction of the graphic plane. Each line marks a volume where a certain portion of the e-beam (in %) is dissipated.*

$$D_e = \frac{I_p \times \tau}{q \times S}. \tag{2.3}$$

I_p is the e-beam current, q is the charge of an electron ($\approx 1.602 \times 10^{-19}$ C), τ is the duration of exposure of the sample to the e-beam, and S is the surface area exposed to the e-beam. The value of the surface area may vary across different reports, as in some cases, the size of the e-beam projected onto the sample (probe size) is taken into account, while in other cases, the distance between two consecutive positions of the beam (pixel width) is considered [150]. In this study, the distance between two consecutive positions of the e-beam is used to define the surface area. The dose is expressed in units of $e^-/Å^2$. As discussed in the following Section, the dose is a parameter of significant importance when it comes to electron microscopy on sensitive materials such as perovskites [151].

2.1.2 Electron-beam induced damages

During inelastic scattering, impinging electrons lose energy which might cause irreversible changes to the sample. These changes are referred to as e-beam-induced "damages" (see Figure 2.3) and follow the subsequent mechanisms:

- **Knock-on**: it occurs when the e-beam is scattered at high angles. It transfers energy to the nucleus and induces the displacement of the atom out of the crystal lattice, creating a point defect. This damage usually happens at high E_b (> 100 keV) in TEM. This process is also referred to as electron sputtering.
  How to minimize it? By lowering the acceleration voltage of the e-beam.

- **Heating**: it occurs when the e-beam transfers its kinetic energy to phonons, resulting in local heating of the sample. Heat-sensitive materials with low thermal conductivity might suffer from amorphization, melting, or sublimation.
  How to minimize it? By cooling down the sample (with a cryogenic stage) or reducing the acceleration voltage or the dose (see equation 2.8).

- **Radiolysis**: this phenomenon breaks interatomic bonds and creates vacancies and free radicals. It is especially harmful to sensitive materials like polymers and minerals whose

chemistry and structure can be easily altered. It is related to the amount of energy dissipated and, thus, to the dose.
How to minimize it? By using lower doses.

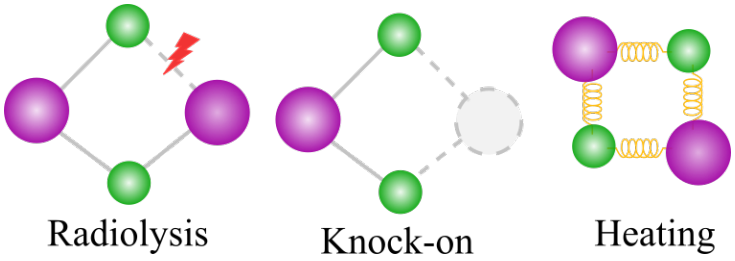

Figure 2.3: *Schematic representation of the degradation mechanisms induced by electron beam irradiation: knock-on damage, radiolysis, and heating. Adapted from [152].*

Previous works on perovskite thin films evidenced after e-beam exposure the formation of vacancies, amorphization of the crystal structure, and losses in volatile species such as MAI [152]. The radiolysis was found to be the prevalent damage mechanism in most of these studies.

It is worth noting that damages identification is challenging; their emergence can lead to the misidentification of damaged perovskite as pristine perovskite, resulting in misinterpretations of the results obtained through electron microscopy-based techniques [153–156]. It is then crucial to find a trade-off in EM parameters to prevent as much deterioration of the perovskite as possible while getting sufficient information for analysis.

In the following Sections, we describe each electron microscopy technique used in the thesis more specifically. The optimization of EM experimental parameters for perovskite material investigation will also be discussed.

2.2 Scanning Electron Microscope

In this Section, we first briefly describe the SEM and the high-resolution imaging techniques (SE and BSE) used during this thesis. We then present the principle of EDS measurement used to analyze the distribution and the evolution of the composition.

2.2.1 SEM overview

Figure 2.4(a) displays a schematic representation of the SEM Merlin Compact VP from Zeiss and its components.

The SEM is equipped with a Schottky Field Emission Gun (FEG) electron source, from which electrons are generated. This technology provides good properties in terms of brightness and stability and allows to operate on an energy range spanning from 0.02 to 30 keV. The high-energy electrons are then focused by a series of electromagnetic lenses and apertures (condensor, magnetic lens, and electrostatic lens), forming an e-beam. In imaging mode, the e-beam is deflected by scan coils, and scanned across the sample.

Electron imaging

Primary electrons interact with atoms of the sample and generate various radiations, as described in the previous Section. In imaging mode, two types of electrons emitted from the sample are used:

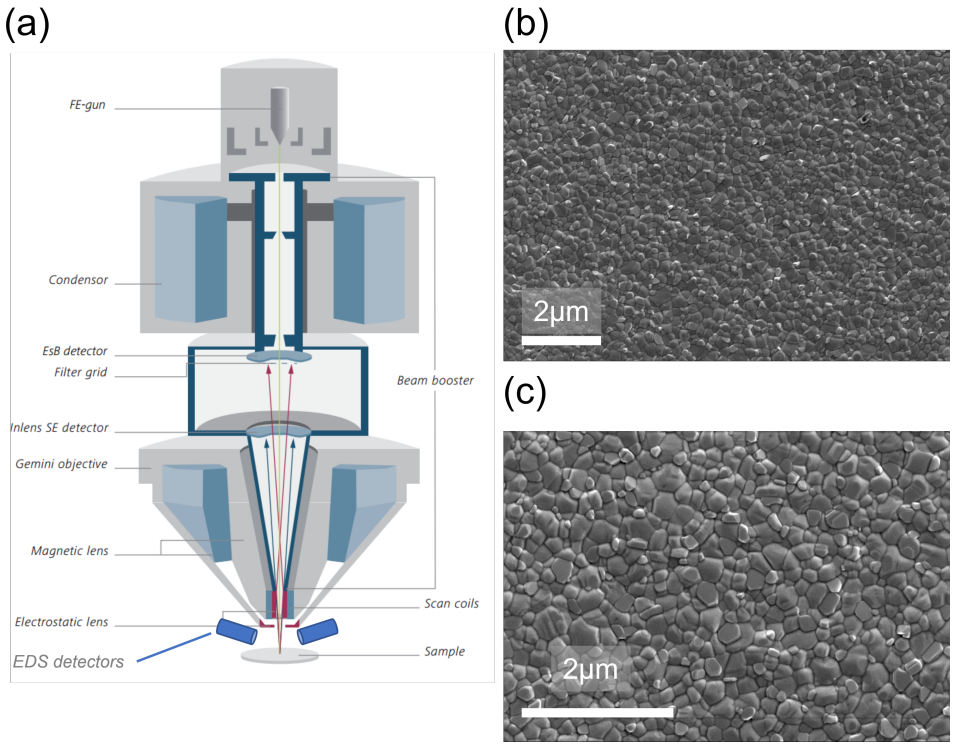

Figure 2.4: *(a) Schematic of the basic components of the SEM Merlin. Adapted from [145].(b,c) SEM images of a CsMAFA perovskite thin film acquired with the SEM Merlin.*

- Secondary electrons (SE) generated via inelastic scattering of impinging electrons. They exhibit low kinetic energy (usually < 50 eV) and thus are easily absorbed by the material. Only SEs generated close to the surface can escape and be detected, which justifies why SE detectors are used to image the topography and the surface of samples. The spatial resolution of SE imaging is limited by the escape probability of the SEs and is estimated at few nanometers in insulating samples [157].

- Backscattered electrons (BSE) are primary electrons that are deviated by the nucleus of the atoms. Their energy is higher than SEs, and they are more deflected by heavy nucleus, making them useful for qualitative Z-contrast, i.e., chemical contrast, imaging. The spatial resolution of BSE imaging is limited by the escape volume of the BSEs from the sample [158]. As the CASINO simulation showed in Figure 2.1(a), this volume is of about 1/3 of the penetration depth (∼33 nm) at 3 keV in a CsMAFA perovskite film.

One specificity of this SEM is that the SE and BSE detectors are positioned in the emission column of the tool. It enables high-resolution imaging and simultaneous acquisition. This type of detector is referred to as in-lens detector [158].

2.2.2 Energy dispersive x-ray spectroscopy in SEM

As mentioned previously, the inelastic scattering of an e-beam in a sample can generate X-ray photons (X-rays) which are employed in Energy Dispersive Spectroscopy (EDS). In this Subsection, we first describe the processes that generate characteristic X-rays. We then discuss the limitations of EDS measurements performed in a SEM. Finally, we present the method for obtaining quantitative concentrations from EDS spectra.

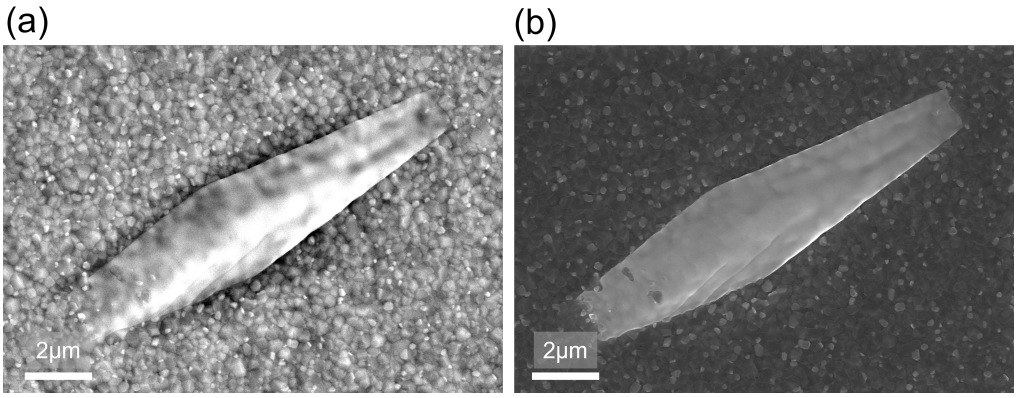

Figure 2.5: *(a) SEM images acquired on a needle-shaped heterogeneitiy in a film of CsMAFA at 5 keV, 2 nA with (a) SE and (b) BSE detectors. The needle and some PbI_2 clusters appear brighter than the surrounding CsMAFA film in the BSE image, due to their higher density or atomic number.*

General principles of EDS

When a high-energy enters a sample, it can interact inelastically with the core electrons of the constituting atoms. If enough energy is transferred to an inner-shell (e.g. K-shell) electron, the latter is ejected above the Fermi level. The atom is then left in an excited state, i.e., ionized, which is relaxed by the downward transition of an electron from a higher energy lever filling the gap in the inner-shell (see Figure 2.6(a)). This transition produces the emission of either an X-ray photon or an Auger electron. In both cases, the energy of the emission is equal to the difference between the upper and lower energy levels (i.e., ionization energy) and is characteristic of each specific element.

During the acquisition, the e-beam is scanned over the sample, and X-rays are collected at each e-beam position to form an EDS map. The map is divided into square-shaped pixels with a width equal to the distance between two consecutive e-beam positions. The EDS map is a hyperspectral cube of data with two spatial dimensions (in μm) and one spectral dimension (in keV).

Figures 2.6(b) and (c) show typical results obtained with EDS measurements: (b) the EDS spectrum averaged over the whole map with X-ray peaks identified as characteristic X-ray lines including $Br_{L\alpha}$, $Cs_{L\alpha}$, Pb_{M}, $I_{L\alpha}$, and $Sn_{L\alpha}$; (c) the SE image of the sample region analyzed and the corresponding elemental maps in which a characteristic X-ray line is integrated on each pixel and plotted with a false color ($Br_{L\alpha}$ in red, Pb_{M} in blue, $I_{L\alpha}$ in green, and $Sn_{L\alpha}$ in orange).

The characteristic X-ray photons, also referred to as "lines", have specific energies. Depending on which K, L, or M shell transition is involved, they are grouped in "families". Within a given family, not all electron transitions are equally probable. In the S(T)EM, we only use the most intense lines, α and β, depending on the spectrometer resolution.

To eject an electron from the inner-shell of an atom, the energy transferred must be higher than the critical ionization energy (E_C) of the atom, which increases with Z. As transitions from higher energy levels become available with increasing Z, the energy of X-rays lines also increases.

In addition, the fluorescence yield, which corresponds to the number of X-ray photons emitted per number of excitations, is significantly lower than 1 in low-Z atoms ([158]). Hence, EDS is not suitable for the study of light elements.

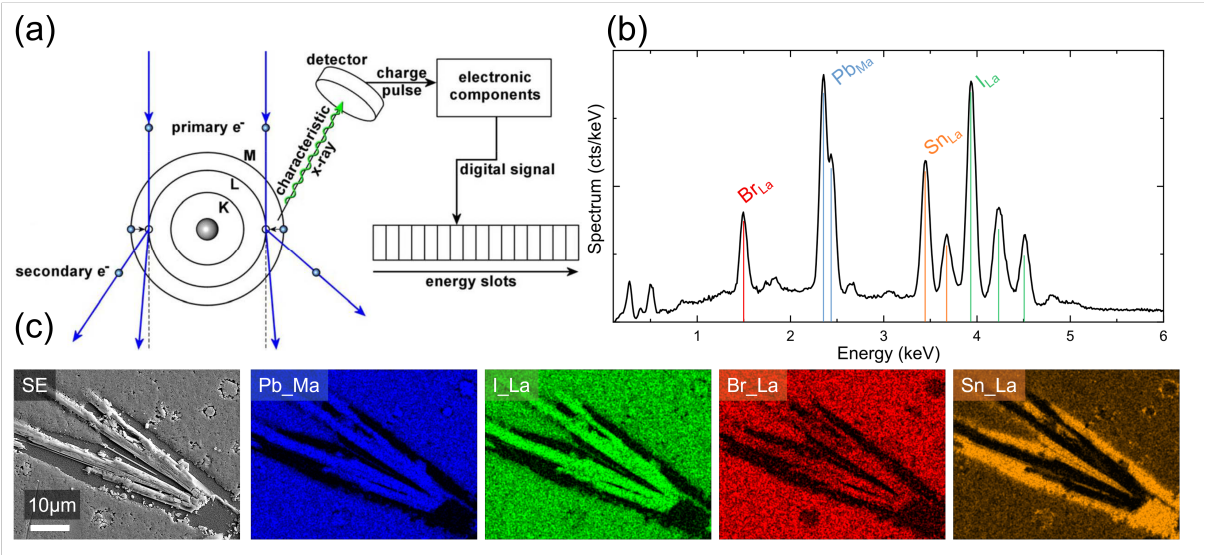

Figure 2.6: *(a) Schematic of the EDS measurement principle. The characteristic X-rays are emitted from the sample, collected by a detector, and assigned to the corresponding energy in the spectrum by electronic components. Reprinted from [159]. Typical results obtained with SEM-EDS measurement. (a) SEM-EDS spectrum with $Br_{L\alpha}$, $I_{L\alpha}$, $Pb_{M\alpha}$ and $Sn_{L\alpha}$ X-ray lines indicated. (c) SE image and corresponding elemental maps obtained with SEM-EDS.*

SEM-EDS limits

EDS exhibits multiple advantages for chemical analysis of single-element samples. However, it can be challenging to study samples composed of multiple distinct elements, such as perovskite materials [160], due to several phenomena affecting the X-ray lines emitted. We present here three sources of X-ray line variations.

- **The atomic number** Z plays a role in the X-rays emission as it dictates the stopping power (i.e., the rate at which an electron losses energy), the fraction of backscattered electrons, and the ionization energy E_C. Notably, the stopping power is inversely proportional to the atomic mass.
- **The absorption** of X-rays generated deep within the sample might occur. It depends mainly on the energy of the X-ray and the mass absorption coefficient, which is related to the nature and environment of the atom. The environment, i.e. the surrounding elements, differs significantly between a sample containing a single element and another containing a mixture of elements.
- **The fluorescence** is a phenomenon in which a high-energy X-ray is absorbed by an atom and re-emitted as a lower energy X-ray. The probability of fluorescence is higher when the energy of the primary X-ray is just above the ionization energy of the atom. The volume of the sample affected by this phenomenon can be substantial, as schematically presented in Figure 2.7.

The spatial resolution of EDS mapping is first limited by the interaction volume with the sample. According to Equation 2.2, this volume is micron-sized for the typical EDS mapping acceleration voltage, i.e. 5 to 15 keV. However, since X-ray migration can be high in the sample, the fluorescence increases the size of the X-ray emitting region by about an order of magnitude according to Goldstein et al.[160]. It thus reduces the spatial resolution of the measurement as

shown in Figure 2.7(b).

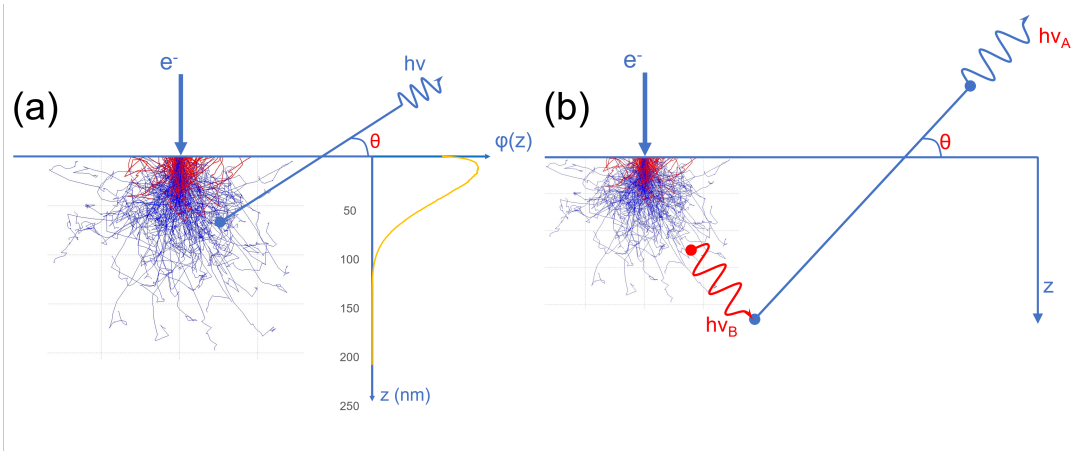

Figure 2.7: *(a) Same result of a CASINO simulation as in Figure 2.2 (CsMAFA perovskite film, $E_b = 3$ keV, probe size ≈ 10 nm). Figure presents the X-ray generation and collection by the detector positioned at an angle ("take-off" angle) θ. The distribution of the $Br_{L\alpha}$ X-ray line (1.48 eV) in-depth calculated with CASINO is plotted alongside. (b) Schematic of the fluorescence phenomenon and its impact on SEM-EDS spatial resolution. An X-ray line from A atom excites an atom B re-emitting an X-ray line, which is collected by the detector. Inspired by [161]*

Materials composed of elements with a high discrepancy in their atomic number, like hybrid perovskites, are more subject to absorption and fluorescence [160], reducing spatial resolution and making the interpretation of results challenging.

Depending on the EDS detector position, a sample with non-flat topography may obstruct the X-ray collection and induce "shadowing" in EDS maps. The Merlin is equipped with two oppositely positioned EDS detectors (see Figure 2.4), which multiply by two the collected signal and hinders this "shadowing".

It is worth noting that EDS spectral resolution is rather poor and is estimated at ~130 eV as defined by convention by the full width at half maximum (FWHM) of the $Mn_{K\alpha}$ peak.

PhiroZ standard-based quantification

A quantitative estimation of the perovskite thin films composition can be challenging from SEM-EDS measurements. The "PhiroZ" method from the commercial software *Esprit 2* (from Bruker) is used to quantify relatively light elements in samples and is thus relevant in our case.

The PhiroZ quantification method is historically an analytic procedure using theoretical models to determine the matrix correction ZAF, which links the X-ray line intensity of the element A, I_A, to its concentration, C_A, as shown in Equation 2.4

$$I_A = C_A[Z][A][F]. \tag{2.4}$$

However, the uncertainty on each theoretically calculated terms is so high that it is usually preferred to determine these terms experimentally with samples whose composition is known [158, 160]. These standards are measured in the same microscopic conditions as future measurements (acceleration voltage, beam current, detector position), and the obtained EDS spectra are stored in a library of standards.

Quantification procedure

X-ray lines are fewer at high energies allowing better deconvolution of neighboring elements. Acquisitions are then performed at 15 keV for the calibration of the standards library and subsequent EDS measurements. The optimal working distance (position of the sample in the specimen chamber) for the X-rays detection is 10 mm. We use the 60 μm-wide aperture in "high current" mode, setting the beam current at 2 nA.

The procedure of quantification is illustrated on an EDS spectrum in Figure 2.8 and goes as follows:

- Selection of the region-of-interest (ROI) in the SE image, in which the EDS spectrum is averaged.
- Elements and X-ray lines selection. As EDS is not relevant for light elements, the focus is made on $Pb_{M\alpha}$ (2.34 keV), $I_{L\alpha}$ (3.9 keV), $Br_{L\alpha}$ (1.4 keV), and $Cs_{L\alpha}$ (4.2 keV). We also consider $Sn_{L\alpha}$ (3.4 keV) due to the FTO layer underneath perovskite film. The $Sn_{L\alpha}$ line is deconvoluted, but the composition is fixed at 0%. The same is done for $Ti_{K\alpha}$ (4.5 keV) when TiO_2 is used as an ETL.
- Background subtraction. The background intensity is averaged over spectral ranges windows positioned on both sides of the peak (as shown in Figure 2.8). The background is estimated by the interpolation under the peak of the value obtained in the windows.
- The X-ray peaks considered are fitted with a Gaussian function, integrated, and the background is subtracted.
- Quantification. The standard-based "PhiroZ" procedure is used to determine the composition. The ratio between the background-subtracted peak integrated intensity from the sample and the standard gives an estimated concentration. Results are normalized by the total composition and are given in % atomic.

Due to the close positioning of the $Cs_{L\alpha}$ lines to the $I_{L\alpha}$ lines, it is challenging to accurately estimate the Cs content in materials such as CsMAFA that contain both elements, particularly when the Cs concentration is low. To determine whether Cs should be taken into account for quantification, we determined that if the $Cs_{L\beta}$ lines are present in the EDS spectrum, Cs is quantified. For the particular case of pristine CsMAFA film, we set the Cs composition to approximately 5% of Pb.

According to Williams and Carter [162], since X-ray emission is a random process, its occurrence is considered as following a Gaussian distribution. The uncertainty on the element composition is estimated at three times the standard deviation σ on the X-ray lines which are used to determine the composition.

Conclusion of the section

We described the SEM Merlin used in this study. The specific electronic column combined with in-lens detectors enables high-resolution electron imaging. Two EDS detectors are used to acquire EDS maps. Quantification of the different elements is performed via the built-in method PhiroZ and with a standard-based library for Pb, I, and Br. The composition is given with an error evaluated of $3\times\sigma$.

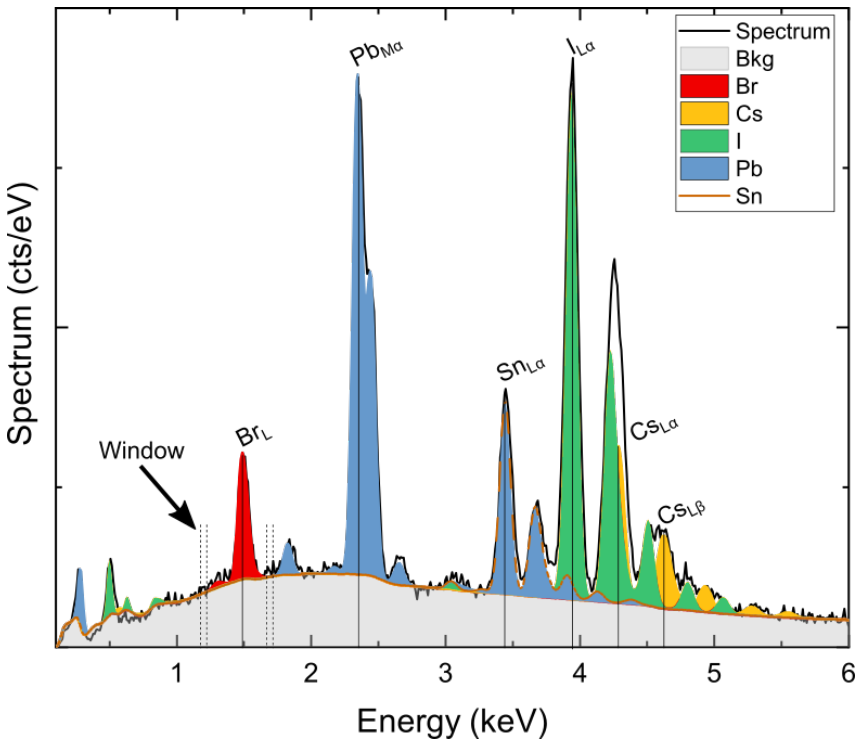

Figure 2.8: *EDS spectrum with the background subtracted manually in gray. The X-ray lines $Cs_{L\alpha}$, Br_L, $I_{L\alpha}$, and $Pb_{M\alpha}$ positioned 4.2, 1.4, 3.9, and 2.34 keV respectively, are fitted with a Gaussian function and deconvoluted from the original EDS spectrum. The background intensity is estimated in windows positioned on both sides of each line considered, here represented around only Br_L. The background is subtracted to the X-ray line intensity which is then used for quantification.*

2.3 Cathodoluminescence

As mentioned in Section 2.1, the inelastic scattering of incident electrons in a semiconductor can generate electron-hole pairs within the sample. These charge carriers can then recombine radiatively (see Chapter 1), emitting photons with an energy close to the semi-conductor bandgap. This emission is referred to as *Cathodoluminescence* (CL). The mechanism of emission is similar to other luminescence-based techniques, such as Photoluminescence (see Chapter 3), and Electroluminescence, and thus provides similar information on the optoelectronic properties of samples, with the added advantage of the high spatial resolution offered by the SEM.

In this Section, we first present the equipment used in this thesis and describe the acquisition procedure of a CL map. We then discuss the spectral and spatial resolution of the CL measurements on CsMAFA perovskite films. Finally, we give information on the treatment performed on the data.

2.3.1 CL set-up overview

The equipment used for all CL experiments is a Chronos from Attolight. A schematic presentation of the instrument is given in Figure 2.9.

The electron source of the CL is similar to the Merlin SEM presented in the previous Section. It possesses a Schottky FEG source coupled with electromagnetic lenses (included in the Gun lens on the schematic) that focus the electrons to form a e-beam. The latter is filtered by an aperture giving control over its size and its current. The objective lens focuses then the beam onto the sample in the vacuum chamber. SE detectors collect SEs emitted from the sample.

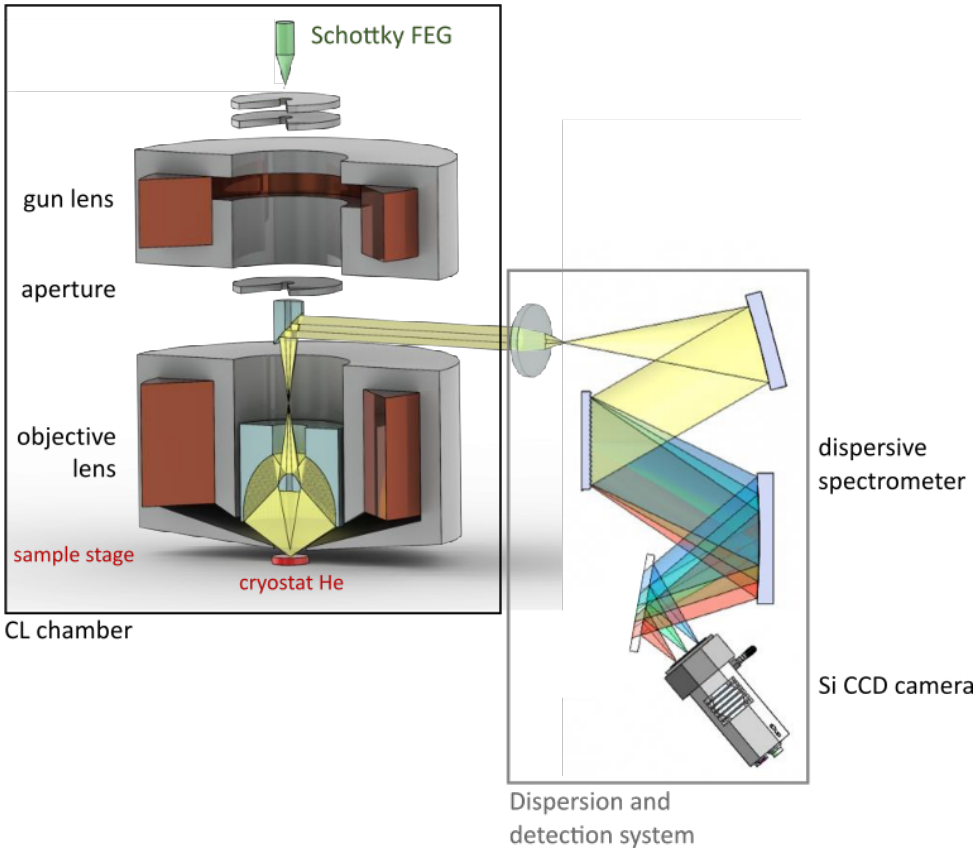

Figure 2.9: *Schematic of the Attolight Chronos set-up. The CL chamber is represented with the Schottky FEG source, the aperture, the electromagnetic lenses and the collection optics. The sample is represented in red and is positioned on a cryogenic stage (with helium (He)) not represented. The dispersion and detection system are displayed with a schematic of the dispersive spectrometer and the CCD camera. Adapted from [163].*

In contrast with the Merlin SEM, a light collection system is positioned on top of the sample holder. This system is composed of a Cassegrain mirror integrated into the column that directs the collected light on the optical path leading to the spectrometer. The latter disperses the photons collected with a reflective diffraction grating onto the CCD camera, recording the spectral response.

In hyperspectral imaging mode, the e-beam is scanned over the sample. The resulting SEs are collected along with the emitted luminescence. We obtain an SE image of the topography and, with the CCD camera, an hyperspectral CL map, which is a data cube composed of both spatial (in nm) and spectral information (in nm).

It is worth noting that most CL instruments use a parabolic mirror installed in standard SEMs to collect the luminescence, as reported in previous studies [164–166]. Conversely, the instrument used in this study employs an embedded optical collection system that allows for more efficient and spatially uniform light collection, expanding the filed-of-view (FOV) of acquisition areas up to 200 μm. This collection system does not require optical alignment, and samples only need to be placed in the focal plane. As a result, this system enables quantitative comparison between samples analyzed under the same conditions.

Thanks to the remarkable mechanical stability of the stage (less than 250 nm/h [167]), long signal integration and, thus, CL acquisitions are possible with a limited drift of the sample. The cryogenic stage can reduce the temperature of the sample holder down to 5 K. It should be noted that the actual temperature of the sample is superior than the holder temperature, and

depend on the nature of the substrate and the mounting procedure.

Low-temperature measurements can be advantageous in enhancing the luminescence intensity of the sample [168], as well as reducing the e-beam damages due to localized heating. The latter will be discussed in Subsection 2.4.2.

Finally, the CL can be operated in pulse mode to acquire time-resolved datasets. In this mode, the electron gun is actuated by a pulsed laser, thus generating a pulsed e-beam focused on the sample. The diffracted luminescence is then oriented toward a Streak-Camera synchronized with the laser. However, this function has not been used in this thesis.

Acquisition procedure

The sample is fixed to a small holder made of copper using silver paint, and mounted on a piezo-controlled stage that allows for movement in both in-plane and out-of-plane directions. The main SEM parts of the set-up are controlled through a software. We set the accelerating voltage, the Gun Lens that defines the e-beam current, the objective lens that defines the height of the e-beam focus point, the deflectors that align the e-beam, and the stigmators lenses that correct the astigmatism of the e-beam. The aperture positioned at the exit of the gun reduces the e-beam size and thus limits the impinging current.

After optimizing the e-beam roughly, we obtain the first SE image of the sample. Then, we have to position the sample in the focal plane of the light collection system (which is fixed) to harvest most of the luminescence emission. At this stage, the integration time of the CCD required to collect enough signal is determined, along with the spectral range of the spectrometer.

The usual acquisition parameters are given for each experiment of this thesis in Table 2.5.

2.3.2 Resolution

Spectral resolution

The CL spectral resolution depends on the grating of the spectrometer used. In this thesis, we use only the grating "150/500" with 150 grooves/mm and blazed at 500 nm (meaning that the maximum response is reached at λ=500 nm). The dispersion power is of 0.53 nm/pixel. We estimate that four pixels are needed to form an emission peak in our experimental conditions leading to a spectral resolution of about 2 nm.

Spatial resolution

The spatial resolution of CL maps is first limited by the interaction volume of impinging electrons within the sample. The interaction volume was estimated with CASINO for a 10 nm e-beam probe size with various acceleration voltage in a CsMAFA perovskite film. The energy dissipated in depth is presented in Figure 2.10.

The sample was modeled as previously in Figure 2.2. Figure 2.10 shows that the maximum depth of the energy dissipated increases significantly with the acceleration voltage, reducing the spatial resolution.

The spatial resolution of CL is also limited by the diffusion of e-beam-generated carriers. The carriers that diffuse and recombine outside of the probed area may still contribute to the collected signal due to the wide FOV of collection. The diffusion length in perovskite thin films

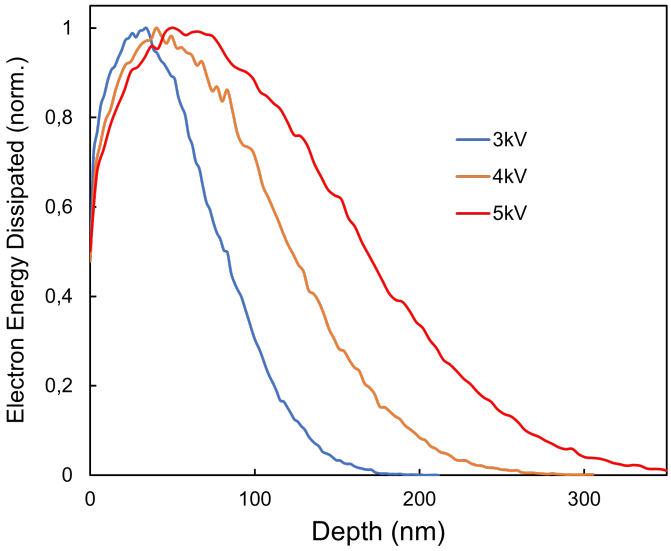

Figure 2.10: *CASINO simulation for the distribution in depth of the dissipated energy in a CsMAFA perovskite film. The e-beam size was set at 10 nm, and the acceleration voltage was set at 3, 4, and 5 keV (plotted in blue, yellow, and red, respectively). The dissipated energy was normalized by the maximum.*

can be relatively large ($L_d \approx 1$ μm) thus affecting the CL map resolution [169, 170]. However, it is observed that the spatial resolution of the CL is much greater than 1 μm as smaller features are discernible in CL maps (see next Chapters). Since the diffusion length may also be influenced by the injection level of excess carriers (the excitation regime mentioned in Chapter 1), it is further discussed in the following paragraph.

Injection level

The injection level, which corresponds to the density of injected carriers, affects their transport properties and their recombination in perovskite thin films [86]. The number of carriers generated in a perovskite film under e-beam exposure has been determined in several works already [168, 171, 172]. To evaluate this number in the CsMAFA perovskite studied in this thesis, we follow the approach of Guthrey et al. using an empirical model that considers e-beam parameters and the composition of the perovskite [168]. The electron-hole pairs generation rate G is expressed as follows:

$$G = (1 - \eta) \times \frac{I_b}{e} \frac{E_b}{E_i}, \tag{2.5}$$

where I_b and E_b are the e-beam current and energy, respectively. E_i is the energy required to generate an electron-hole pair by ionization estimated by the relationship $E_i = 2.1E_g + 1.3$ [146] where E_g is the bandgap. η is the backscattering coefficient corresponding to the fraction of backscattered electrons. It depends on the composition of the material as presented in equation 2.6, but it can also be estimated from CASINO simulations.

$$\eta = E_b^m \times c, \tag{2.6}$$

with $m = 0.1382 - \frac{0.9211}{Z^{0.5}}$ and $c = 0.1904 - 0.2235\ln Z + 0.1292(\ln Z)^2 - 0.01491(\ln Z)^3$. For a multi-element material such as CsMAFA perovskite, a weighted sum of the backscatter coefficients η_i is used.

In addition, the carrier generation rate is usually expressed as a function of the interaction volume, i.e., in (pairs)$cm^{-3}.s^{-1}$. The interaction volume is supposed to be spherical as shown by the results of the CASINO simulation in Figure 2.2(a) (aspect ratio ≈ 1). The sphere radius, which is the half of the dissipation depth of the e-beam energy, $R_e/2$, is estimated by the CASINO simulation. The obtained volumic carrier generation rate G_V is expressed as:

$$G_V = G \times \left[\frac{4}{3}\pi\left(\frac{R_e}{2}\right)^3\right]^{-1}. \tag{2.7}$$

We estimated these values for CL acquisitions in "standard" conditions described in Table 2.1 alongside the results of the calculations.

Table 2.1: *On the left: table summarizing the acquisition parameters for a typical CL measurement. On the right: table summarizing estimated parameters of the volumic generation rate equation 2.7*

Parameters	Value
E_b	3 keV
I_b	0.7 nA
Aperture	50 μm
Integration time	10 ms
Pixel width	100 nm
Dose	70 $e^-/Å^2$

Parameters	Value
η	0.21
$R_e/2$	50 nm
E_i	4.681 eV
G_V	**4.5 $\times 10^{24}$ $cm^{-3}.s^{-1}$**

We considered $R_e/2 \approx 50$ nm from the CASINO simulation, $\eta \approx 0.21$ from Equation 2.6, E_g =1.63 eV from UV-vis absorption measurements (see Chapter 1). We found $G_V = 4.5 \times 10^{24}$ $cm^{-3}.s^{-1}$ which is some orders of magnitude higher than low injection conditions in PL ($\sim 10^{21}$ $cm^{-3}.s^{-1}$) close to 1 sun illumination [34, 35].

According to Caprioglio et al. [171], these generated charges might recombine at a high rate, leaving little time for their transport by diffusion. It would mean that the diffusion of the generated charges could be neglected in this range of injection level. The CL maps have then a spatial resolution limited by the interaction volume, i.e., ~100 nm. The resolution of the CL maps presented in this thesis, which is higher than the diffusion length in hybrid perovskite films, is consistent with our hypothesis.

2.3.3 Data treatment

Several corrections procedures are required in post-treatment of the CL maps obtained. The processing is made through HyperSpy and LumiSpy, python-based libraries optimized for hyperspectral data analysis [173, 174]. The corrections done on CL maps consist in the following:

- The CCD detector and the spectrometer using the grating "150/500" have diffraction efficiencies that depend on the wavelength. Their theoretical spectral responses have been extracted from the products datasheet and are divided to the CL spectrum at each pixel. It is worth noting that the spectral response of the system grating/CCD drops dramatically under 300 nm and above 1100 nm (due to CCD limits), making irrelevant any measurements outside of this spectra range.
- The background of the spectrum is systematically measured in the same recording conditions regarding the grating/CCD system (i.e., integration time, readout frequency). Due

to a "bowing" effect at the ends of the spectral range some low signal zones might become negatives after background subtraction. Usually, we average spectrum over a few tens of nm on low or high wavelength spectral ranges to determine the noise level, which is then subtracted.

- The edges of the CL maps demonstrate a higher signal than the rest. Maps are thus cropped by removing 3 pixels on each side.

Conclusion of the section

We described the CL Chronos set-up used in this thesis. The unique light collection system embedded in the specimen chamber enables wide FOV acquisitions and quantitative comparison of samples. In our experimental conditions, the spectral resolution of CL measurement is evaluated at ∼4 nm. Limitations on the spatial resolution in perovskite material were also discussed and evaluated to ∼100 nm.

2.4 Hybrid perovskite degradation under e-beam exposure

2.4.1 Impact of the degradation on SEM images

As we mentioned in Subsection 2.1.2, incident electrons can induce damages to samples analyzed. Hybrid perovskites are sensitive materials, and it has already been demonstrated that they degrade when exposed to highly energetic e-beam [152, 175, 176]. To avoid this phenomenon as much as possible, we need to identify which degradation mechanism is predominant.

Figure 2.11 shows an SEM image (SE) of a typical CsMAFA perovskite film where ten successive CL maps have been performed with $E_b = 5$ keV and $I_b = 0.68$ nA, inducing a total dose of $D_e = 58$ e$^-$/Å^2.

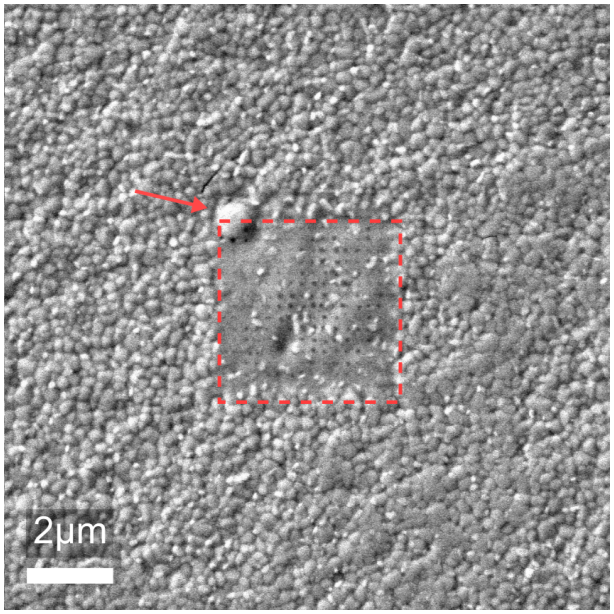

Figure 2.11: *SEM image of a CsMAFA film where ten CL maps were performed in the area delimited by the red dashed square.*

We observe a significant change between the acquisition area where grains look melted, and the surrounding pristine film. White little particles looking like remaining native PbI_2 clusters

are randomly spread in the acquisition area. Tiny black dots, that are periodically arranged in lines and columns and equally distant are also observed. Their arrangement suggests that they are impacts induced by the e-beam during the scan. Finally, a red arrow indicates a protuberance in the top left corner of the acquisition area, suggesting a more advanced film degradation in this region. We presume that it is due to beam blanking at the corner in the time laps between imaging and hyperspectral mode in the CL interface.

The acceleration voltage in an SEM usually ranges from 1 to 30 keV. At this energy level, knock-on damages should not be the most detrimental degradation process [177]. This phenomenon mostly occurs at higher energies, especially those implemented in TEM applications. In the specific case of hybrid perovskite, if some studies have confirmed that knock-on damage is not the dominant mechanism [178], few authors showed that e-beam in SEM can induce formation of defects by knock-on, which are significantly harmful to halide perovskies [175, 179]. These observations will be further discussed in Section 2.5.4.

Given perovskite sensitivity to temperature (see Chapter 1), we also need to assess the elevation of temperature induced by e-beam irradiation. According to previous works, the e-beam localized heating is linked to the its current, energy, and interaction volume size. The elevation temperature due to the e-beam can be calculated using the following equation [180]:

$$\Delta T = \frac{1.5 I_b E_b}{\pi k R}, \tag{2.8}$$

with I_b the beam current, E_b the acceleration voltage, k the thermal conductivity of the material and R the electron penetration range. In this measurement (E_b = 5 keV, I_b = 0.68 nA) performed on a 500 nm-thick CsMAFA film (k =0.26 $W.m^{-1}.K^{-1}$ according to [181], and R =0.17 μm calculated by CASINO) we estimate $\Delta T \approx 37$ K. Such heating might induce small changes in CsMAFA film (local stress or ion migration), but would not lead to a complete decomposition [76, 80].

As mentioned in Section 2.1.2, radiolysis has been shown to dominate the degradation of hybrid perovskites in SEM and TEM. In this degradation process, inelastic scattering of impinging electrons lead to the breakage of chemical bonds in the material. The crystallinity of the perovskite, which is highly related to the order of ions, is also affected. As a consequence, volatile molecules such as MAI or FAI might escape from the material giving rise to an overall mass loss [182]. Milosavljevic et al. proposed in 2016 [183] the following chemical reaction to describe the mechanism of degradation of $MAPbI_3$ under low-energy e-beam exposure.

$$CH_3NH_3PbI_3 + e^- \longrightarrow CH_2 + NH_3 \uparrow + HI \uparrow + PbI_2. \tag{2.9}$$

Here, the incident electrons break the bonds between the $[PbI_6]^{4-}$ octahedron and the MA^+ cation, which then volatilizes as methylamine [MA (CH_3NH_2)]. The same degradation mechanism has been reported by Yadavalli et al. on several perovskite compositions studied with an SEM [176]. They show that the volatilization of organic molecules induces the formation of cracks in the thin film after a few minutes of exposure. They illustrate their observation with a schematic shown in Figure 2.12.

The combination of localized heating and radiolysis is likely responsible for the morphological changes observed in Figure 2.11.

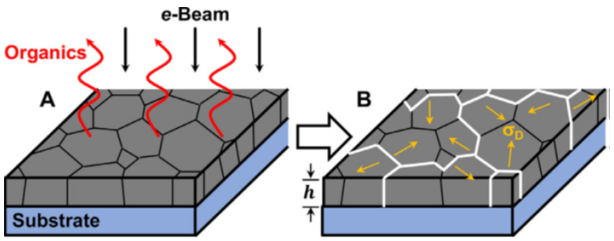

Figure 2.12: *Schematic representation of the mechanisms responsible for the generation of grain-boundary fractures in hybrid thin films upon exposure to an e-beam. Reprinted from [176].*

2.4.2 Impact of the degradation on CL measurements

The work of Xiao et al. showed that e-beam damages are characterized by a decrease in luminescence together with the emergence of new contribution peaks [179].

In general, CL and SEM-EDS require high electron beam currents, typically around 1 nA, to obtain sufficient signal for hyperspectral mapping [168]. Therefore, it is important to investigate the evolution of the CL signal as a function of the dose exposure in order to determine optimal acquisition parameters for the analysis of hybrid perovskites.

For all samples studied, a measurement of the perovskite emission peak intensity as a function of the impinging electron dose is performed before in-depth investigations and CL mapping. Figure 2.13 shows an example.

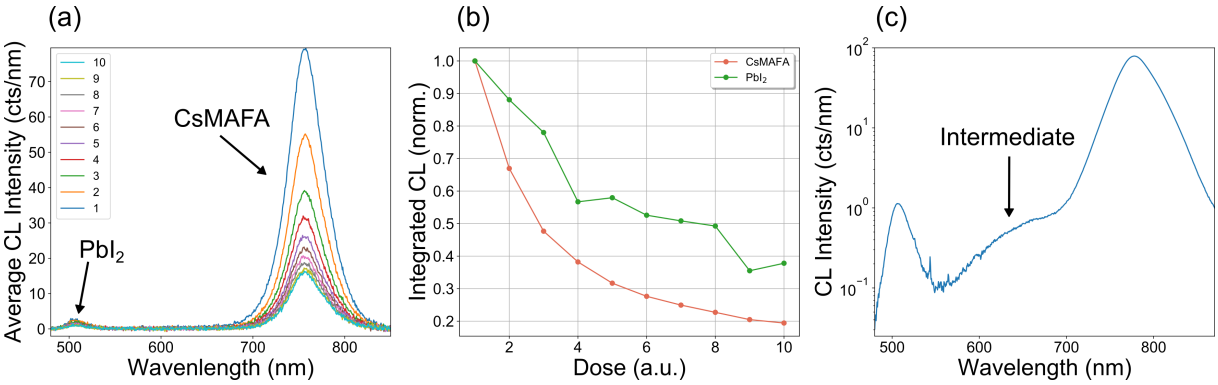

Figure 2.13: *(a) CL spectra acquired successively on the same area of a CsMAFA perovskite film. Each acquisition is equivalent to a dose of 5.5 $e^{-}/Å^2$. The signal is integrated over the spectral range 775 ±75 nm, and the obtained values are normalized by the first one and plotted as a function of dose exposure (from 1 to 10) in (b). The same integration procedure is done on the PbI_2 contribution (500 ±10 nm) and plotted in green. (c) CL spectrum acquired with a longer integration time of 20 ms on a CsMAFA film and plotted in a semi-logarithmic scale. The emergence of a broad ("intermediate") emission peak at 660 nm is striking.*

The CL signal is spatially averaged and plotted for all the ten successive expositions in Figure 2.13(a). The emission peak at 760 nm is attributed to band-to-band recombination from CsMAFA perovskite, while the peak at 500 nm to PbI_2 emission. We calculate the intensity of the emission peaks integrated over 700-850 and 490-510 nm spectral ranges on each CL spectrum. We plot in Figure 2.13(b) the obtained values as a function of electron dose (1 exposure = 5.5 $e^{-}/Å^2$).

After the first exposition, the intensity of the perovskite peak decreases significantly (∼30%). According to Xiao et al., such perovskite peak variation is due to knock-on damage and Frenkel-type defects formation. These defects appear when an atom is ionized and move to an interstitial

site which might create non-radiative recombination sites and thus decrease the CL peak intensity [179]. The peak position stays relatively constant while the FWHM increases slightly (+4%). The broadening of the CL peak (the FWHM increase) can be attributed to distortions in the crystal structure due to atom displacement.

The presence of a PbI_2 emission peak in the pristine perovskite is likely due to the excess of PbI_2 included in the precursor solution. In comparison to CsMAFA perovskite, the intensity of the PbI_2 peak is low (approximately 1%) and decreases as the electron dose increases (see Figure 2.13(b)), indicating that it is also subject to beam damage. This observation suggests that CsMAFA perovskite does not decompose into PbI_2 during irradiation, in contrast to the radiolysis mechanism described in reaction 2.9.

This finding is consistent with previous studies on CL characterization of hybrid perovskites, which also reported the appearance of a new emission peak near 600 nm [179, 184, 185]. The authors ascribed this peak to an intermediate phase which is the result of e-beam-induced perovskite degradation. In our case, the absence of new CL peaks implies either that the phase is not emitting or that the acquisition parameters (current or integration time) are insufficient to unveil it. We thus performed an acquisition with a higher integration time (20 ms) on a pristine area of the thin film.

Figure 2.13(c) shows the CL spectrum of the sample, averaged over the acquired map, in semi-logarithmic scale. In addition to the emission peaks of CsMAFA perovskite and PbI_2, a new broad peak at 660 nm is now visible, corresponding to the intermediate phase mentioned before. Specifically, Xiao et al. attributed this peak to the formation of an intermediate phase due to the heating effect of the e-beam. Using measurements at low temperatures (∼80 K), the authors showed that the intermediate phase was hindered, providing evidence for the heating hypothesis [179].

Notably, Ferrer-Orri et al. have extensively studied the e-beam degradation of CsMAFA perovskite using the same CL set-up as the one used in this thesis. They obtained results that corroborates our observations [184].

We will strive to reduce this phenomenon by performing measurements at lower doses and low temperatures.

Impact of the acceleration voltage

In this Subsection, we investigate the effect of the acceleration voltage on the CsMAFA perovskite CL emission. We performed successive exposures on the same area using acceleration voltages of 2, 3, and 5 keV. The results are shown in Figure 2.14(a).

CsMAFA emission peak intensity decreases similarly for all the e-beam energies tested. However, it declines faster for 2 keV and 5 keV than for 3 keV. This is expected for 5keV, as the local heating is promoted by higher acceleration voltage (see equation 2.8). The faster emission drop with 2 keV is not intuitive, but it can be explained by the fact that decreasing the e-beam energy promotes inelastic scattering, which enhances the radiolysis effect in the sample. In addition to a slower drop of the perovskite emission, 3 keV beam energy resulted in a higher signal-to-noise ratio (SNR) in the CL map and higher resolution in SE imaging. Therefore, we chose to use 3 keV for the CL map acquisitions of this thesis.

These observations are in good agreement with the study from Ferrer-Orri et al. who showed that acceleration voltages lower than 5 keV have a negligible effect on the perovskite.

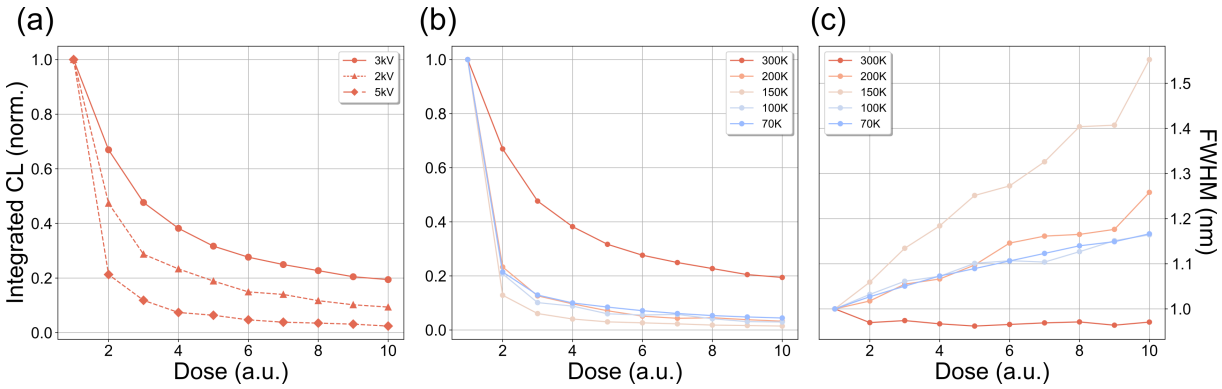

Figure 2.14: *(a) Plot of the CsMAFA peak integrated intensity evolution as a function of the electron dose and for acceleration voltages: 2, 3, and 5 keV. We followed the same procedure as presented in Figure 2.13. Each acquisition is equivalent to a dose of 5.5* $e^-/Å^2$*. (b) The same work was performed with multiple acquisition temperatures: 300, 200, 150, 100, and 70 K. (c) The evolution of CsMAFA perovskite peak FWHM with dose.*

Impact of cryogenic temperatures

We performed the same procedure as described before at low temperatures (cryogenic CL) to elude the sample degradation through localized heating. Figure 2.14(b) shows the evolution of the CsMAFA perovskite peak with cumulative dose at 300, 200, 150, 100, and 70 K.

The integrated intensity of CsMAFA emission decreases faster at lower temperatures, suggesting that e-beam damage is more severe at low temperatures. Previous studies on Cryogenic Electron Microscopy (Cryo-EM) characterizations of hybrid perovskites have produced conflicting results, with some showing less damage at cryogenic temperatures and others indicating the opposite [152], which is consistent with our findings. Several authors observed that the e-beam-induced crystal-to-amorphous transition is facilitated at cryogenic temperatures, which can immobilize the defects induced by the e-beam. Defects tend to accumulate and create clusters in the sample, which becomes amorphous in these areas. Chen et al. and Rothmann et al. showed that it takes less electron dose (about 1/3) to induce crystal-to-amorphous transition at -180°C than at room temperature (RT) [186, 187].

As a result, using low temperatures is not solving the perovskite degradation issues even if it decreases heating effects.

It is noteworthy to mention that cesium-based halide perovskites ($CsPbX_3$) are known to suffer less from e-beam damages than hybrid perovskites [175, 179, 188]. We see in Chapter 3 how they withstand higher doses without showing any decomposition artifacts.

Conclusion of the section

In this section, we presented the effect of e-beam on CsMAFA perovskite film. We have shown that the most detrimental degradation mechanism in SEM is radiolysis. However, localized heat and knock-on damages could still combine to degrade the films, especially in EDS measurements. The e-beam induces a loss of the CL signal and the appearance of artifacts in the spectrum, which can be attributed to radiolysis and heating, respectively. We analyzed the effect of acceleration voltage and temperature on the degradation and showed that CL map acquisitions performed at 300 K and 3 keV induce relatively less damage. This section focuses on beam damage in the context of SEM, but most of the principles apply to (S)TEM as well. Similarities and differences will be discussed in the next section.

2.5 Scanning Transmission Electron Microscope

We mentioned in Section 2.1 that e-beam scattering is not the same in bulk and thin samples. If the sample is thin enough - we say it is electron-transparent - then highly accelerated electrons will pass through it. This phenomenon implemented in Transmission Electron Microscopes (TEMs) greatly enhances the spatial resolution of electron imaging (down to 0.5 Å in high-resolution TEM [189]), allowing direct observation of the atomic structure of samples. Besides, radiations generated in bulk samples are also produced in thin ones enabling high-resolution spectroscopic and analytic analysis such as CL, EDS, and Electron Energy-loss Spectroscopy (EELS).

In the past decade, TEM-based techniques contributed significantly to understand the fundamental origins of perovskite material properties and instability [152, 155, 190]. In this thesis, we use techniques related to Scanning Transmission Electron Microscopy, a specific mode of TEMs. This section provides a description of the thin sample preparation through Focus-Ion-Beam (FIB) milling, an overview of the STEM instrument and the techniques used in this thesis, and a discussion about the e-beam-induced damages in STEM.

2.5.1 Lamella preparation

The samples analyzed in this thesis with STEM-based techniques consist of slices of the multi-layered PSCs called "lamellae". They are electron-transparent and are prepared using an FEI Helios DualBeam FIB miller. This instrument comprises an electronic column mounted in a vertical position in the specimen chamber, enabling electron imaging. In addition, an ionic column positioned at an angle of 52° with respect to the electronic column provides a focused Ga^+ ion beam used to mill the sample. The Ga^+ ions can etch the material thanks to their large atomic mass [191]. This dual-beam system allows visualization and localized etching simultaneously. It also has a gas injection system (GIS) for local deposition of platinum (Pt) and a micromanipulator for moving small samples inside the chamber. These features are essential during the *in-situ* lift-out procedure employed for lamella preparation.

The *in-situ* lift-out method used in this thesis is adapted from the standard procedure provided by the FIB constructor (FEI). It involves several steps during which a thick slice is patterned on the sample (Figure 2.15(a)(1-3)), is welded to the micromanipulator with Pt and cut out from the bulk sample (Figure 2.15(a)(4)), and then is extracted, moved, and welded to one finger of a molybdenum TEM grid (Figure 2.15(a)(5-6)). The thick slice surface is finally thinned down to several hundreds of nm to reach electron transparency (Figure 2.15(a)(7-8)). This last operation is crucial and consists in successive irradiation steps on the Pt side (top of the lamella) where the ion beam is slightly tilted. Besides, the energy and current are decreased to remove irradiated material from the sides of the lamella and reveal the pristine region of the cross-section (Figure 2.15(a)(9)).

FIB milling can introduce various artifacts to the sample, including contamination by redeposition (protective Pt, glass), Ga^+ ion implantation, or material amorphization due to heating. While Ga^+ ion implantation is generally not a concern in PSC lamellae and contaminations can be eliminated through the cleaning steps of the procedure, amorphization of the perovskite material is frequently observed in PSC lamellae [187, 192]. Therefore, the FIB milling process should be optimized to avoid damage. To that end, we slightly reduced the ion beam energy (30 to 16 keV) and current ($\sim$1/2) compared to the standard FEI procedure.

Traditionally, microscopists aim at preparing the thinnest lamella possible to enhance electron imaging spatial resolution. To this extent, they constantly improve FIB milling procedures

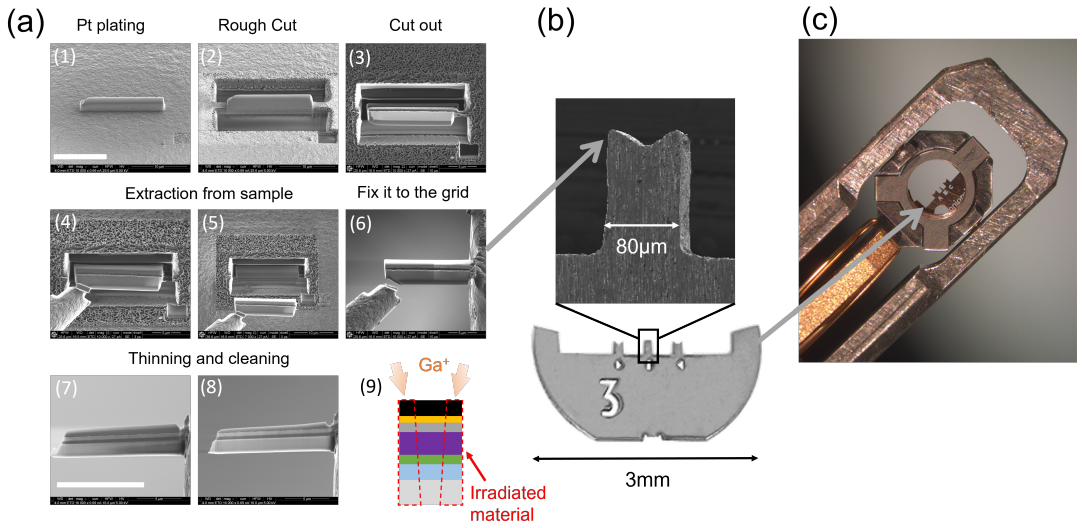

Figure 2.15: *(a) SEM images acquired during the procedure to cut an electron-transparent, cross-sectional PSC lamella with a FIB. (b) Photograph of the TEM grid on which the lamella is fixed. (c) Photograph of the holder double-tilt used for the EDS analysis.*

[193]. On the other hand, STEM-EDS measurements require relatively thick lamellae, as discussed in section 2.5.3. The sensitivity of hybrid perovskite materials also restrains from reducing the thickness too much. Jeangros et al. found that 200 nm is the optimal thickness to avoid perovskite decomposition into PbI_2 during FIB milling while providing electron transparency and good SNR in STEM-EDS [194]. We then chose this value for our experiments.

Once the lamella is attached to the TEM grid (made of copper (Cu) and molybdenum (Mo)), it is taken out of the FIB miller, thus out of the vacuum, and is **manually** positioned on the FEI double-tilt TEM holder shown in Figure 2.15(c). The whole set is then introduced inside the TEM for analysis. The operation requires additional precautions while being fast since it is conducted in the air. We strive to reduce the time of transfer to less than 10 minutes.

It is worth noting that nowadays, other ion sources have been used for FIB millings, such as Xe, Ar, or Ne. They were shown to induce fewer artifacts or faster milling in some cases. Such systems might be suited to e-beam sensitive sample preparation for TEM analysis as PSCs, but they were not implemented in this thesis.

FIB milling is used to prepare lamellae from PSC. We aim at a lamella thickness of 200 nm for EDS measurements. The Ga^+ ions energy and current are reduced during the lamella thinning to reduce implantation and amorphization due to localized heating. After fabrication, lamellae are transferred directly to the STEM, spending less than 10 minutes in the air.

2.5.2 (S)TEM overview

We used in this thesis a TEM in STEM mode to investigate PSCs and degradation products. We give in the present subsection an overview of the set-up followed by a brief description of the working principle of the STEM mode. Then, we discuss the electron imaging techniques used and their resolution.

Set-up

Figure 2.16 shows a schematic diagram of a TEM. The FEI Tecnai Osiris, hereafter referred to as "Osiris", consists of an "X-FEG" electron source (Schottky FEG) that provides high brightness and high stability of the beam current over time. The generated e-beam is shaped by the interplay of three electromagnetic lenses called condenser lenses C1, C2 and C3. The C1 lens magnifies or demagnifies the gun crossover (i.e., the beam focus point) depending on the desired illumination size. The C2 lens focuses the resulting e-beam onto the focal point of the C3 lens to produce a parallel e-beam that illuminates the sample. The C2 lens is associated with an aperture of various sizes to allow control of the e-beam size and current.

In contrast with SEMs, TEM images are formed underneath the sample. The latter is crossed by the e-beam from which the objective lens constructs either an electron image or a diffraction pattern (DP). In both cases, the signal is passed to the projector lenses to be magnified and then projected onto a CCD detector, replacing the fluorescent screen from the "old" TEM.

It is worth noting that all these lenses bear aberrations reducing the spatial resolution of TEM imaging. These deviations are known as spherical aberrations (due to the lens edges), chromatic aberrations (due to the beam energy heterogeneity), and astigmatism. They are corrected in this TEM by the astigmatism and aberration lenses and the coma.

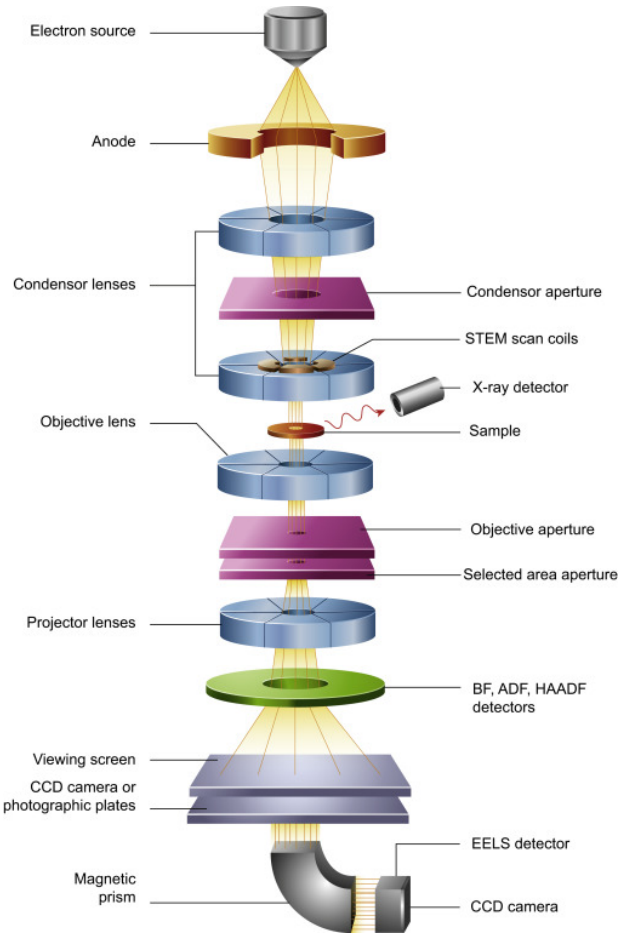

Figure 2.16: *(a) Schematic of the basic components of a TEM microscope. Reprinted from [145].*

The TEM is operated at 200 keV for all the experiments. We control the beam current by tuning the Gun Lens, the C2 aperture, and the Spot Size. The beam current is measured by

a detector positioned beneath the CCD camera. It measures the e-beam current after passing through the sample and thus might be underestimated.

The TEM imaging system comprises additional features such as beam deflectors, scanning coils, and drift correctors. The TEM imaging procedure and principles are not covered here but are thoroughly described in dedicated textbooks [158, 162].

The system is also equipped with analytical detectors for chemical analysis of samples through EDS and EELS measurements. These techniques are particularly interesting for investigation of hybrid perovskites, but they are performed in STEM mode.

In this thesis, we performed Selected Area Electron Diffraction (SAED) on three occasions from which we obtained diffraction patterns of the region analyzed. The acquisition and analysis of diffraction patterns will be briefly described before presenting the results in Chapter 4. Further details on the techniques can also be found in dedicated textbooks [158, 162].

STEM mode

The STEM combines the advantages of a TEM with the scanning capability of SEM. The C3 lens focuses then the e-beam and forms an electron probe on the sample plane (see Figure 2.17(a)). Scanning coils scan the beam across the sample, generating signals are detected, resulting in images and hyperspectral cubes where each pixel corresponds to the beam position.

As in SEM imaging, the spatial resolution is limited by the interaction volume in the sample and the probe size. Kosasih et al. estimated the effective beam diameter d_{eff} to be ~9 nm on a CsMAFA PSC lamella with the same microscope as the one used in this thesis [195]. The spatial resolution suffers from the same aberrations as in TEM imaging.

STEM is also useful for electron beam-sensitive samples. Scanning the beam allows precise control of the irradiated region of the sample, so it is a form of low-dose microscopy.

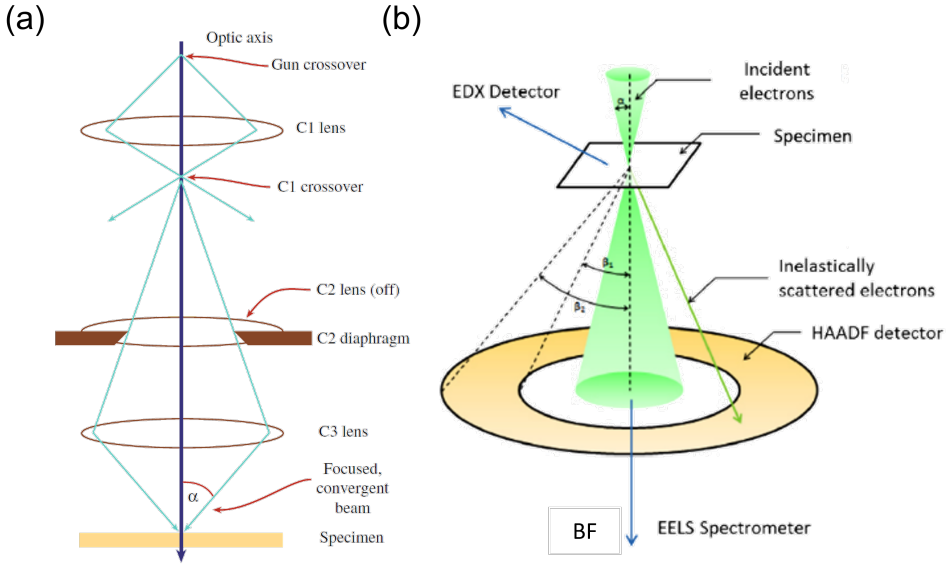

Figure 2.17: *(a) Schematic diagram of a TEM operating in STEM mode. Reprinted from [162]. (b) Schematic view of the interaction of the incident electrons with the specimen. Transmitted electrons are captured by a BF detector, inelastically scattered electrons are captured by a HAADF detector, and an EDS detector captures emitted X-rays. Adapted from website https://www.jeol.co.jp.*

Imaging in STEM mode

Although electron optics no longer operate under the same parallel illumination conditions, the imaging contrasts of the TEM mode can be produced in the STEM mode. In STEM imaging, transmitted electrons are collected by a bright field (BF) detector, while scattered electrons are collected by annular dark field (ADF) and high angle dark field (HAADF) detectors (see Figure 2.17(b)). The BF detector is circular, while the DF are annular, but they are all centered on the optical axis, allowing simultaneous imaging, unlike equivalent TEM imaging. Figure 2.18 shows an example of a STEM-BF and HAADF image obtained on a lamella damaged during FIB milling preparation.

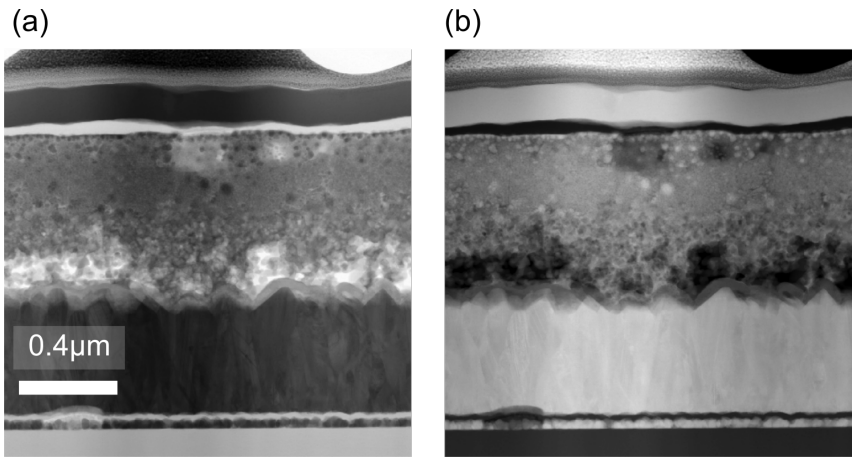

Figure 2.18: *Cross section STEM BF (a) and HAADF (b) images acquired at 200 keV, I = 500 pA, dwell time = 10 µs on a PSC lamella (glass/FTO/c-TiO_2/m-TiO_2/CsMAFA/PTAA/Au).*

In BF imaging, the contrast is equivalent to a TEM BF image combining diffraction and mass-thickness contrast. In the final image, the vacuum appears bright, while dense, thick, or crystalline features appear dark. BF imaging allows simultaneous and direct visualization of light and heavy atoms in contrast to DF imaging.

The HAADF detector in our system harvests electrons deflected by the sample as shown in Figure 2.17(b). The heavier the atom, the higher the scattering intensity and the brighter the atom appears in the image. The scattered electron plane waves are collected simultaneously and averaged by the system, making HAADF imaging incoherent. As a result, the contrast is not sensitive to the crystallographic orientation of the sample.

The image contrast is then only related to the elastic scattering of electrons in the sample. The probability of such events is proportional to the Z of the atom and the film thickness t (Rutherford scattering). According to Hartel et al., it can be expressed as [196]:

$$I = tZ_{eff}^{1.8}. \tag{2.10}$$

We see that HAADF images are easy to understand and interpret and thus are widely used to analyze multi-layer samples such as PSCs. HAADF is better suited to identify heavy compounds of the PSC (Pb, Au, Ti, Sn) than light elements (O, N, C, B, and Li).

In this subsection, we presented the lamella preparation procedure by FIB milling. Then we briefly described the TEM FEI Tecnai Osiris and how it is operated. The focus was made on the STEM mode and its imaging procedures: BF and HAADF imaging. Their working principles and benefits were also specified.

2.5.3 Energy dispersive x-ray spectroscopy in STEM

The EDS performed in an (S)TEM and an SEM is based on the same fundamental principles, including characteristic X-ray emission, collection, dispersion, and analysis. However, STEM-EDS provides several benefits discussed in this subsection.

The first comment we can make is on the nature of the sample. The STEM allows the analysis of multi-layer devices like PSCs in lateral view (cross-section) with high resolution. The study of PSC cross-sections with SEM-EDS implies a specific and not straightforward sample preparation along with poor spatial resolution due to the interaction volume making interpretation uncertain. Results obtained in this configuration seem unreliable and stay qualitative in general [197].

As mentioned in the previous subsection, the Osiris is equipped with an electron source with a small convergence angle enabling high spatial resolution in analytic microscopy measurements such as EDS measurements. The detector installed in the Osiris is a Super-X EDS detector system (from Bruker) composed of four detectors increasing the collection angle significantly, and thus the SNR of EDS signal [198]. In addition, the set-up enables to perform acquisition on the samples positioned horizontally, which reduce shadowing effects.

The spatial resolution of STEM-EDS is limited by the probe size, e-beam interaction volume, X-ray absorption, and fluorescence in the sample. We used the CASINO software to simulate the trajectory of electrons in a 200 nm thick CsMAFA perovskite lamella. Figure 2.19(a) shows the results obtained with electrons accelerated at 200 keV and focused into an e-beam of radius 9 nm (as calculated by Kosasih et al. [195]).

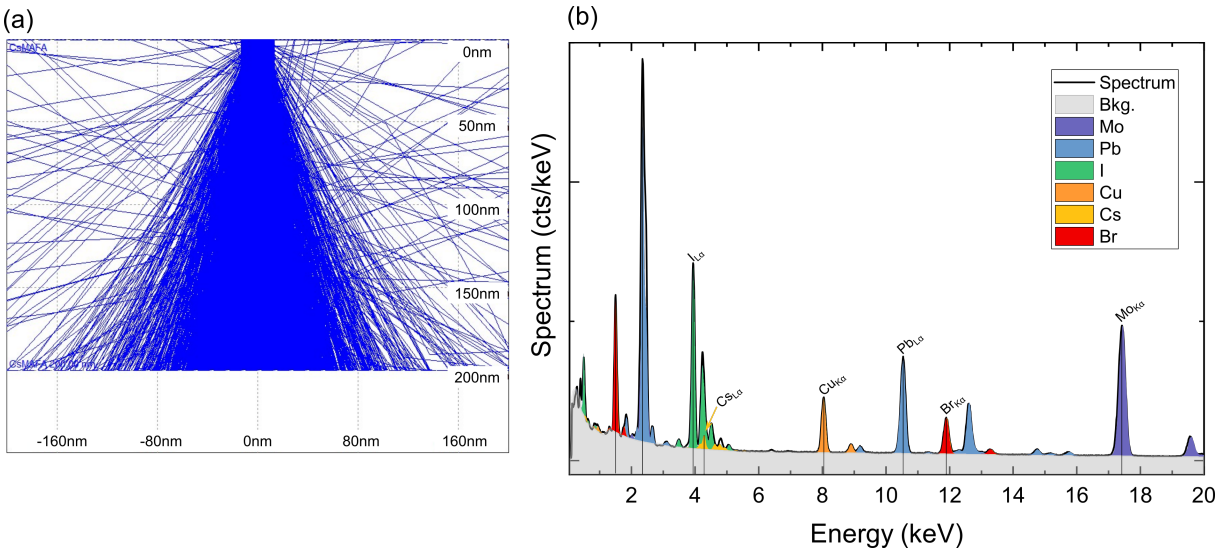

Figure 2.19: *(a) Simulated electron beam trajectories using CASINO at 200 keV for a 200 nm-thick CsMAFA perovskite lamella. (b) Typical STEM-EDS spectrum averaged over pixels included in a CsMAFA film.*

Most electron trajectories are contained within an interaction volume of ∼90 nm radius. Based on the "thin foil criterion", most STEM-EDS studies assume that the sample is thin enough to neglect absorption and fluorescence within the sample [162]. In fact, X-ray absorption is inversely proportional to its thickness and is therefore significantly reduced in a lamella. The same is true for fluorescence, which also depends on the elements present in the sample. However, given the thickness of PSC lamellae and the complex composition of CsMAFA perovskites (light and heavy atoms), absorption and fluorescence can still cause artifacts in the obtained X-ray spectrum. These phenomena have little effect on the qualitative interpretation of the STEM-EDS maps, but can be critical for quantitative estimations, as discussed in the next subsection.

In addition, the spectral range studied differs between SEM and STEM-EDS measurements. In the latter, the signal is usually collected up to 20 keV, which is well below the primary energy (200 keV) but still higher than in SEM (see the spectrum in Figure 2.19(b)). It gives access to other X-ray lines, especially for high Z elements in CsMAFA perovskite such as $Pb_{L\alpha}$ (at 10.5 eV) and $Br_{K\alpha}$ (at 11.9 eV).

Semi-quantification with the Cliff-Lorimer method

The quantification of STEM-EDS spectra follows the same procedure as in SEM-EDS (see section 2.2) except for the method used. The generally implemented Cliff-Lorimer ratio method considers two elements, A and B, whose concentrations (C_A and C_B) are assumed to be proportional to their corresponding background-corrected EDS integrated peak intensities (I_A and I_B). The proportionality coefficient k_{AB}, referred to as the Cliff-Lorimer factor or "k-factor", allows the following expression to be written:

$$\frac{C_A}{C_B} = k_{AB}\frac{I_A}{I_B}. \tag{2.11}$$

We can calculate the two elements concentrations by considering a binary system, i.e., $C_A + C_B = 1$. This method has been extended to more complex compositions with multiple elements. Given that the k-factor is relative to a pair of specific X-ray lines, it has to be defined relative to one arbitrary element. By convention, the Si is used, and multiple component quantification is performed via the relation $k_{AB} = k_{A/Si} \times k_{Si/B}$.

To obtain the equation 2.11, Cliff and Lorimer derived the equation 2.4 for a binary system and considered the "thin foil criterion", thus neglecting absorption and fluorescence (A and F). The k-factor depends on the material (ionization cross section and fluorescence yield), the instrument used (detector efficiency), and the acquisition conditions such as e-beam energy and current (probability of transition), and can be calculated theoretically. They can also be determined experimentally from samples of known composition. However, care must be taken to ensure that the k-factor calibration is performed under the same experimental conditions as the subsequent analysis.

K-factor calibration

We now give details on the calibration of the k-factors in the context of the CsMAFA perovskite study, which is required for the following reasons.

First, the PSC lamella thickness used in this thesis, i.e., 200 nm, might allow absorption of low-energy X-rays coming from light atoms [199].

The combination of light and heavy atoms in CsMAFA perovskite might also introduce artifacts in EDS spectra that can be related to fluorescence. According to Williams and Carter, the uncertainties induced by the fluorescence are negligible compared to parasitic absorptions [162]. However, an accurate comparison in the context of hybrid perovskite analysis is lacking in the literature. By determining experimentally k-factors specifically for CsMAFA compounds, we take into account these uncertainties in the calibration and avoid the calculation of an absorption correction factor.

Finally, hybrid perovskite is a fragile material suffering from various e-beam damages during STEM-EDS measurements. In the next section, we will see that e-beam damages can be reduced but not completely avoided in STEM. The e-beam-induced degradations in the standards and the samples investigated should be the same as long as the acquisition parameters are identical. The experimentally calculated k-factors then account for possible changes that might occur during acquisition.

Two distinct k-factor calibrations were conducted: one using perovskite precursor powders of PbI_2 and $PbBr_2$, and the other using a standard CsMAFA perovskite-based PSC lamella. In the first calibration, we leveraged the precise knowledge of the powders composition. However, the scattering environment was slightly different as compated to future measurements on CsMAFA perovskites due to the absence of MA, FA, and Cs.

The second calibration on the PSC lamella more accurately reproduces the environment of measurements, but the lack of knowledge of the exact CsMAFA film composition may still introduce uncertainties in the determination of the k-factors. The calibrated k-factors for $Br_{K\alpha}$, $I_{L\alpha}$, and $Pb_{L\alpha}$ are presented in Table 2.4 for both cases.

Table 2.2: *K-factors from Esprit 2 library, calculated from precursor powders PbI_2 and $PbBr_2$ and from a standard PSC.*

Lines	Esprit 2	Calib precursors	Calib CsMAFA
$I_{L\alpha}$ (3.9 keV)	3.715	3.943	5.678
$Br_{K\alpha}$ (11.9 keV)	3.390	3.973	2.718
$Cs_{L\alpha}$ (4.2 keV)	3.846	N.A.	3.583
$Pb_{L\alpha}$ (10.5 keV)	5.643	5.643	5.643

Parasitic X-ray lines from the TEM grid (Mo and Cu) are present in the EDS spectrum (see Figure 2.19). We address these lines by deconvoluting the peaks and setting their composition at 0%.

The determination of the Cs content is handled similarly to SEM-EDS: if the $Cs_{L\beta}$ line is prominent in the EDS spectrum, Cs is taken into account for the composition estimation. In cases where the Cs signal is too low but the Cs is actually present in the composition, such as in pristine CsMAFA perovskite, the Cs content is fixed at a value that gives Cs/Pb ≈ 0.05 ($\sim$1.4) and is displayed in red in the summary tables.

The error on the quantification of elements is considered to be three times the standard deviation σ of the X-ray lines used for the estimation. This value is related to the X-ray line counts, which are significantly lower in STEM-EDS than in SEM-EDS, resulting in a higher uncertainty in STEM quantification compared to SEM as sample investigated is thinner.

These k-factors were then used to estimate the composition of a pristine CsMAFA layer. Results are presented as ratios in Table 2.4 for each set of k-factors. The Cs content was fixed

due to the low intensity of $Cs_{L\beta}$ as shown in the Appendix (see Figure 24).

Table 2.3: *Comparison quantification with k-factors from Esprit 2, k-factors calibrated on precursors salts PbI_2 and $PbBr_2$, and on a CsMAFA-based pristine PSC.*

Lines	Esprit 2	Calib precursors	Calib CsMAFA
I/Pb	2.15±0.74	2.28±0.78	3.15±1.05
Br/Pb	0.45±0.13	0.52±0.13	0.36±0.09
Cs/Pb	0.06	0.06	0.07

The estimated concentrations are relatively consistent, although the k-factors from *Esprit 2* tend to underestimate the concentrations of iodine (I) and bromine (Br) while k-factors obtained from the calibration on CsMAFA-based lamella tend to overestimate the I concentration. The calibration based on the precursor salts will be utilized in this study.

In this subsection, we introduced the STEM-EDS chemical analysis technique. Similar to SEM-EDS, STEM-EDS allows high-resolution chemical analysis of a FIB-prepared PSC cross section. We showed with a CASINO simulation that the spatial resolution is significantly improved compared to SEM-EDS. The Cliff-Lorimer quantification method and its calibration on two types of standards were then presented.

2.5.4 Hybrid perovskite degradation in a STEM

The discussion on e-beam-induced damage during SEM-based measurements on hybrid perovskite films in Section 2.3 applies to STEM-based techniques as well. However, these techniques require e-beam energies that are an order of magnitude higher than in an SEM and therefore affect the degradation mechanisms.

In principle, knock-on damages should emerge as the dominant degradation mechanism with acceleration voltage increasing. However, radiolysis has been shown experimentally to be the most damaging mechanism during (S)TEM measurements of sensitive materials [151] such as hybrid perovskites [152, 182, 186, 187, 200, 201]. In particular, the studies by Rothmann et al. revealed the extreme sensitivity of MAPI to e-beam irradiation [187, 201]. The authors showed that a dose higher than 100 $e^-/Å^2$ can be critical for the material, which then suffers from radiolysis. Such a low threshold suggests that *e-beam damages in hybrid perovskite are relatively unavoidable during TEM acquisitions.*

The radiolysis induces the breakage of chemical and ionic bonds, enabling atomic displacement in the sample. According to experimental results reported by Chen et al. at 300 keV, the mobile atoms/ions form an intermediate phase with ordered vacancies ($MAPbX_{2.5}$) which then loses volatile organic molecules and decomposes into final PbX_2 phases [182]. This decomposition pathway corroborates with results reported by Rothmann et al. on TEM acquisitions at 200 kV [187]. The formation of this intermediate phase is a step in the general decomposition mechanism described in the reaction 2.9. As a result, we should be critical regarding the elements quantification results that we obtained via STEM-EDS on iodine (I) content.

Recently, several works debated the dominant mechanism in e-beam-induced damages during STEM measurements on hybrid perovskites [202]. In an experimental study focused on the atomic-scale imaging of $FAPbI_3$ samples, Rothmann et al. showed losses in FA^+ ions, ascribed

to the radiolysis, and in I^- ions, ascribed to knock-on damages [203]. The overall degradation would be then a combination of the two phenomena.

This claim was supported by Cai et al., who reported a first-principle analysis of the e-beam interaction with MAPI perovskite. According to the authors, the knock-on damage emerges from ∼3 keV and amplifies as the energy increases. They showed that under 200 keV, knock-on damage concerns only the lightest elements, such as H, C, and N, which are moved in the sample or extricated from it. Heavier elements such as I and Pb were not shown to move due to the e-beam induced knock-on damage below 250 keV (1 MeV for Pb). However, the material might still suffer from defects formation, loss of crystallinity, loss of mass, and enhancement of phase instability.

These works highlight the importance of knock-on damage in (S)TEM-based measurements, even though radiolysis stays the main degradation process. In this thesis, we operate the Osiris at 200 keV, which might induce some knock-on of light compounds of CsMAFA perovskite. Therefore, the determination of the composition of these light elements may not be relevant in these experimental conditions, and thus will not be performed.

As in an SEM, STEM e-beam induces localized heating of the sample due to inelastic interaction between primary and atomic electrons. The temperature increase relies on several parameters, from the e-beam (energy, probe size, and current), the sample (thermal conductivity), and the supporting TEM grid (thermal conductivity). Due to the small probe diameter and the relatively low current, the sample heating in STEM is usually limited [180]. In his thesis, Felix Kosasih has estimated for similar experimental conditions (Osiris STEM operated at 200 keV; CsMAFA perovskite sample) an increase in temperature of 0.19 K [204], which is relatively small and thus will be neglected in our work.

Given these observations, it is essential to limit e-beam damages as much as possible to rigorously investigate degradation mechanisms of CsMAFA perovskite. It took a certain time before the community became concerned about these damages and the possible artifacts that they generate in EM-based measurements (specifically for electron diffraction) [152]. In this context, the studies from Rothmann et al. and Chen et al. paved the way for better EM measurements and relevant information on hybrid perovskites.

Kosasih et al. published, in 2020, a remarkable work in which they evaluated the impact of the electron dose on STEM-EDS results [195]. This study is of interest to us because they analyze the same perovskite composition with the same instrument. First, they showed how $Pb_{L\alpha}$, $I_{L\alpha}$, and $Br_{K\alpha}$ lines detection is tightly related to the electron dose. They estimated a detection threshold dose of ∼2900 $e^-/Å^2$ below which detection of $Br_{K\alpha}$ composition measurement is uncertain.

They then propose a criterion based on HAADF imaging to ensure that e-beam damage induced by EDS mapping remains low, thus confirming the relevance of the results. This work provides insight into the optimal acquisition parameters to obtain the most relevant results on CsMAFA perovskite lamellae, and we use it to guide our own measurements.

Z-contrast criterion for STEM-EDS mapping

As we mentioned in Section 2.5, the contrast in a HAADF image results from variations in mass and thickness. The approach of Kosasih et al. consisted in acquiring an HAADF image before and after the EDS mapping on a specific region. Then, they established an empirical relation between variations of Z_{eff} and the number of I^- ions lost during the EDS mapping. This operation enabled to link variations in the HAADF intensity in the perovskite film and the damages induced by the EDS mapping.

They established that a decrease of 3% of the HAADF intensity (HAADF ratio before/after ≈ 0.97) indicates a loss of less than 10% of I^- ions. Based on these findings, we consider for the rest of this work that HAADF ratio should not decrease below 0.97.

We applied the same procedure on a PSC lamella where an EDS mapping has been performed with a high dose ($\approx 2 \times 10^4 e^-/Å^2$). HAADF images were acquired before and after the EDS mapping, with a relatively low dose ($\approx 200 e^-/Å^2$) to avoid the e-beam damages due to the imaging.

The obtained images are displayed in Figure 2.20 and the ratio between their intensity spatially averaged on the perovskite layer was estimated at 0.98, suggesting that the perovskite layer did not undergo significant degradation during the EDS mapping.

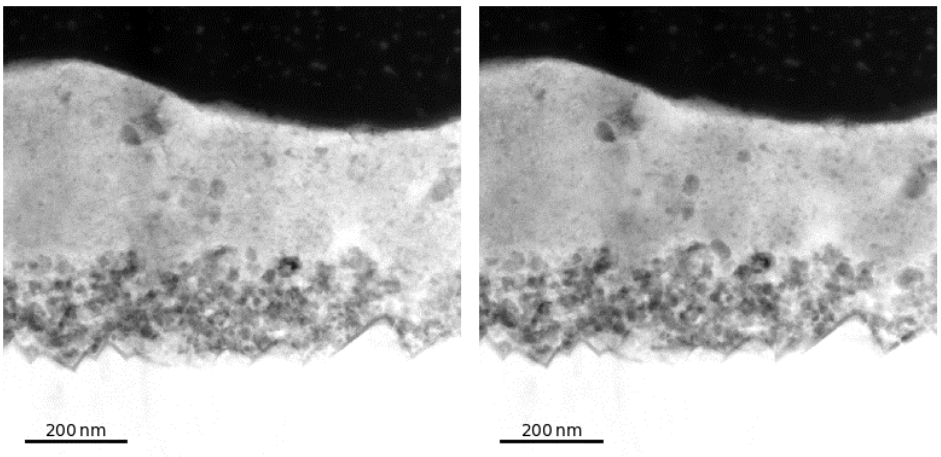

Figure 2.20: *HAADF before (left) and after (right) an EDS mapping performed at E_b = 200 keV, I_b = 0.34 nA, pixel size = 1 nm, and dwell time = 800 µs (Dose $\approx 2 \times 10^4 e^-/Å^2$).*

To go further, we aimed at determining the impact of the EDS mapping on the composition in I and Br measured. We performed two consecutive EDS measurements on the same area of a PSC lamella (with TiO_2 used for the ETL). The acquisition parameters were changed compared to that of HAADF images in Figure 2.20 (E_b = 200 keV, I_b = 0.43 nA, pixel size = 1.3 nm, dwell time = 400 µs) leading to a dose exposure for one acquisition of approximately $6 \times 10^3 e^-/Å^2$ (see Table 2.5). The estimated composition of the perovskite layer are summarized in Table 2.4. We do not observe significant variations in I and Br content between the first and the second acquisition, suggesting that e-beam damages were limited.

Table 2.4: *Results of element quantification of two successive STEM-EDS measurements.*

Element	Measure n°1	Measure n° 2
$I_{L\alpha}$	60.2±14.9	60.4±14.9
$Br_{K\alpha}$	10.1±2.2	9.9±2.2
$Cs_{L\alpha}$	0.5±1.0	0.7±1.0
$Pb_{L\alpha}$	27.2±12.4	27.1±12.3

2.6 Conclusions

In this Chapter, the electron microscopy techniques that were implemented during this thesis were described thoroughly.

- In Section 2.1, the mechanisms of electron-beam interactions with samples used in electron microscopy were discussed. The parameters that govern this interaction, including the interaction volume, the depth of e-beam penetration in the sample, and the electron dose, were defined and their effects on the sample were described. Furthermore, the e-beam induced damages that may occur during imaging and analysis were also discussed and highlighted.

- In Section 2.2, the characteristics of the SEM Merlin, which was utilized during this thesis, were briefly outlined along with a discussion of the SE and BSE imaging modes offered by the instrument. A comprehensive explanation of the principle behind EDS measurements was provided. EDS will be employed as the primary method for investigating the chemical composition of perovskite samples throughout this thesis. In this context, the limitations of the spatial resolution of SEM-EDS and the Phiro-Z method for estimating the composition of samples were also discussed.

- In Section 2.3, the principle of Cathodoluminescence (CL) was discussed, and a brief description of the CL Chronos instrument used in this thesis was provided. The utility of the CL technique in analyzing the optoelectronic properties of semiconductors was highlighted, and the spectral and spatial resolution of the instrument was evaluated at 2 nm and less than 100 nm, respectively.

- In Section 2.4 the e-beam-induced degradation of hybrid perovskite materials was studied using SEM imaging and CL mapping. The analysis revealed that the degradation was primarily due to radiolysis, indicating that reducing the electron dose can mitigate this degradation. Further experiments were conducted with different acceleration voltages and low temperatures to investigate the effect of these parameters on degradation. Results showed that an acceleration voltage of 3 keV was the most appropriate for the investigation of CsMAFA perovskites. Additionally, temperatures below 300 K were found to enhance the degradation of perovskite.

- In the last Section 2.5, the fabrication of lamella with the FIB miller was described. The STEM Osiris, which was used to analyze these samples, was briefly introduced along with the working principle of its HAADF imaging mode and EDS mapping capabilities. HAADF imaging offers high resolution observations (in the tens of nanometers range) of the sample morphology. The STEM-EDS allows for more localized composition estimations than SEM-EDS. Additionally, the degradation of hybrid perovskite in STEM was discussed, and a criterion based on the comparison of HAADF images acquired before and after each EDS mapping was established to assess the degradation.

The following table summarized the acquisition parameters used to perform the different electron microscopy experiments during this thesis.

Table 2.5: *Acquisition parameters used to perform CL, STEM and SEM EDS.*

Sample	Acquisition	E_b (keV)	I_b (nA)	Pixel (μm)	FOV (μm)	dwell time (ms)	*Dose* ($e^-.Å^{-2}$)	Figures
CsMAFA	SEM-EDS	15	2	0.007	8.8	0.11	285	2.6
$CsPbBr_3$	SEM-EDS	15	2	0.15	172	0.15	0.9	3.4
$CsPb_2Br_5$	SEM-EDS	15	2	0.7	880	0.16	0.5	3.13
Needle	SEM-EDS	15	2	0.037	44	0.24	22	4.8
Disc	SEM-EDS	15	2	0.015	18	0.16	88	4.7
Hexagon	SEM-EDS	15	2	0.004	5.3	0.032	250	4.6
Flower	SEM-EDS	15	2	0.073	88	0.24	5.6	4.15
Needle	SEM-EDS	15	2	0.03	18	0.64	89	4.18
Inclusion	SEM-EDS	15	2	0.007	12	0.064	163	5.13
CsMAFA	STEM-EDS	200	0.43	0.003	1.3	0.4	6×10^3	2.4
Needle	STEM-EDS	200	0.5	0.001	0.9	0.1	3×10^3	4.9
Inclusion	STEM-EDS	200	0.43	0.006	4.4	0.34	2.5×10^2	5.14,5.15
CsMAFA	CL RT/LT	3	0.6	0.1	13	5	21	4.7, 4.6
CsMAFA	CL (stab)	3	0.6	0.25	4	8	5.5	2.13
$CsPbBr_3$	CL	3	0.6	0.1	13	10	41	3.6
$CsPb_2Br_5$	CL	6	0.25	0.06	8	20	79	3.15
Hexagon	CL RT	3	0.6	0.1	13	23	95	4.6
Disc	CL RT	3	0.6	0.2	26	22	23	4.7
Flower	CL RT/LT	3	0.6	0.2	23	20	30	4.15
Needle	CL RT/LT	3	0.6	0.2	23	20	30	4.11,4.13
Inclusion	CL RT/LT	3	0.6	0.1	13	10	41	5.9 5.12

Chapter

3 Analysis of cesium, lead, and bromide-based perovskite

Chapter content

3.1 Ternary phases of the Cs-Pb-Br material system 64
3.2 Analysis of the $CsPbBr_3$ perovskite phase 65
3.2.1 Optical properties 65
3.2.2 Analysis of a $CsPbBr_3$ film 66
3.3 Analysis of the $CsPb_2Br_5$ phase 71
3.3.1 Optical properties 71
3.3.2 Analysis of $CsPb_2Br_5$ micro-crystals 73
3.4 Conclusions 78

In Chapter 1, cesium, lead, and halide-based inorganic perovskites, $CsPbX_3$, were described as alternative light absorbers in PSCs due to their overall better stability than their hybrid organic-inorganic counterparts [75, 205]. These phases demonstrate remarkable optoelectronic properties, and are good candidates for manufacturing devices such as LEDs, transducers for CO_2 conversion or lasers [206].

It has also been reported that multi-cation mixed-halide perovskites, such as CsFAMA or CsFA, transform into pure cesium halide phases, such as $CsPbX_3$ and $CsPb_2X_5$, after degradation upon exposure to humidity (see Chapter 1). The purpose of this study is to advance both the identification and the knowledge of this material.

The bromine-based cesium-lead perovskite is more widely studied than its iodine or chlorine-based relatives, notably because its bandgap is larger, leading to more numerous applications. Because of these properties, we analyzed $CsPbBr_3$ films and $CsPb_2Br_5$ micro-crystals to ascertain their properties and to support the degradation mechanisms of hybrid perovskite analysis.

In this Chapter, we detail the essential information gathered from the literature on these phases and then present and discuss our experimental results obtained through PL, CL, and EDS measurements.

3.1 Ternary phases of the Cs-Pb-Br material system

Within the inorganic perovskite family, cesium, lead, and bromide-perovskites are remarkable because they exhibit three phases stable at room temperature: classic three-dimension $CsPbBr_3$ (3D), two-dimension $CsPb_2Br_5$ (2D) and zero-dimension Cs_4PbBr_6 (0D[1]). These phases can coexist in any form that perovskite takes: thin films, single crystals, cubes, and plates [172, 207–212].

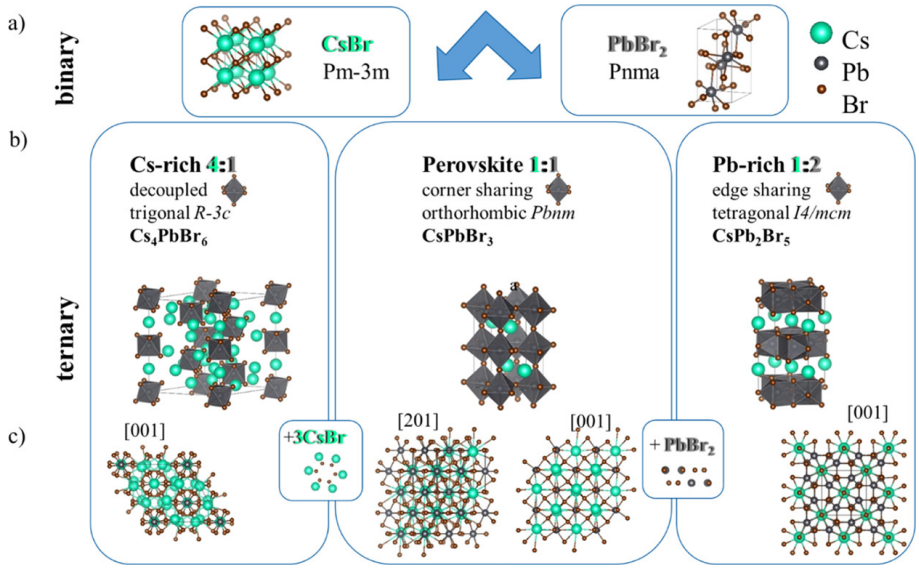

Figure 3.1: *Binary ($CsBr$ and $PbBr_2$) and ternary ($CsPbBr_3$, $CsPb_2Br_5$, and Cs_4PbBr_6) compounds of the Cs-Pb-Br system at room temperature. Reprinted from [172].*

Figure 3.1 shows the atomic structure of binary ($CsBr$ and $PbBr_2$ in (a)) and ternary ($CsPbBr_3$, $CsPb_2Br_5$ and $CsPb_4Br_6$ in (b)) compounds in the Cs-Pb-Br system. The figure includes the space group and the connectivity of the $[PbBr_6]^{4-}$ octahedron for each phase. It is also indicated that the addition of $3\times CsBr$ to Cs_4PbBr_6 forms $CsPbBr_3$, and the addition of $PbBr_2$ to $CsPbBr_3$ forms $CsPb_2Br_5$.

In contrast to the $CsPbI_3$ perovskite discussed in Chapter 1, the $CsPbBr_3$ perovskite is photoactive at room temperature (300 K), [213, 214]. This composition still undergoes two phase transitions when cooled from high temperatures: α cubic ($Pm3m$) to β tetragonal ($P4/mbm$) at 130°C and to γ orthorhombic ($Pbnm$) at 88°C [172, 206]. However, the three phases of $CsPbBr_3$ exhibit similar properties, indicating that this material can be used over a wide temperature range, from 200 to 500 K.

The $CsPb_2Br_5$ phase is sometimes referred to as the $PbBr_2$-rich phase or 2D cesium-based inorganic perovskite, easily fabricated by adding an excess of $PbBr_2$ in a $CsPbBr_3$ fabrication process [210, 211, 215]. This phase crystallizes in a tetragonal symmetry within the $I4/mcm$ space group. The structure is a sandwich with alternating Cs^+ and $PbBr_8$ layers. Consequently, this 2D material exhibits high stability and is used as a protective material for $CsPbBr_3$-based devices [172, 216, 217]. Some reports even showed that the coexistence of $CsPbBr_3$ and $CsPb_2Br_5$ enhances perovskite luminescence [218–221], which might be related to the defect passivation of the $CsPbBr_3$ surface. However, this hypothesis is still under discussion in the literature [197].

[1]Isolated $[PbBr_6]^{4-}$ octahedra not connected by their corners

While $CsPbBr_3$ perovskite can be transformed into $CsPb_2Br_5$ by the addition of $PbBr_2$, the phase transition can also be induced by environmental stresses such as water molecules. Notably, Liu et al. draw a hypothetical evolution of the crystal structure depicted in Figure 3.2 [222]. According to the authors, the transformation process is initiated by water molecules infiltrating the crystal structure and extracting CsBr molecules. A similar phase transformation has been observed and reported in other experimental works [223]. This information could be valuable for analyzing the evolution of hybrid perovskite degradation products at high humidity (see Chapter 4).

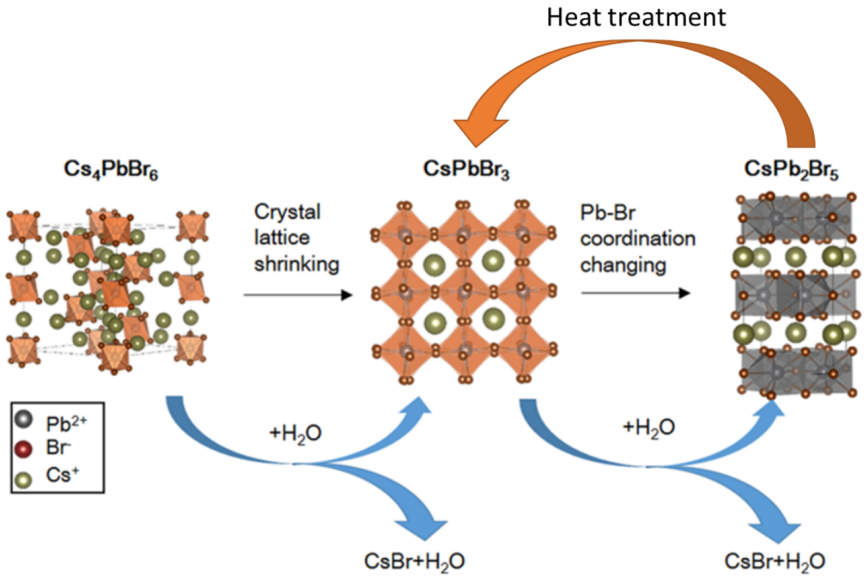

Figure 3.2: *Schematic of the potential phase transformation induced by water molecules on phases from the Cs-Pb-Br material system. The ingress of water molecules in the Cs_4PbBr_6 allows extraction of the CsBr component out of the crystal, which turns into $CsPbBr_3$. A similar process occurs in $CsPbBr_3$, which turns into $CsPb_2Br_5$. Reprinted from [222].*

To the best of our knowledge, the Cs_4PbBr_6 phase has not been observed in hybrid perovskite degradation products, so we have not analyzed this phase in this work. In the following sections, we will then present our analysis of the two compositions of interest, $CsPbBr_3$ and $CsPb_2Br_5$.

3.2 Analysis of the $CsPbBr_3$ perovskite phase

3.2.1 Optical properties

Although it has been shown that the optoelectronic properties of $CsPbBr_3$ do not vary significantly with its crystal structure, the discrepancy in the bandgap values reported in the literature has motivated their theoretical estimation. The calculations were performed using a DFT-based method by Dr. P. Baranek, a researcher at the IPVF. Details of the calculation procedure can be found in the appendix (see Section 5.4). Table 3.1 summarizes the calculated and experimentally determined bandgap values from the literature and our calculations for each of the symmetries mentioned.

The bandgaps are slightly different depending on the crystal structure, as is the emission

Table 3.1: *Bandgap values for each symmetry of the $CsPbBr_3$ calculated with a DFT-based procedure at room-temperature. For comparison, bandgap values from the literature determined by calculations and experimentally are given.*

System	Space group	Literature		Our work
		Calc.	Exp.	
Cubic	$Pm\bar{3}m$	2.15[a] 1.78[b]	2.3[c], 2.25[d]	2.57
Tetragonal	$I4/mcm$[b] $P4/mbm$	1.82[b]	2.37[e]	2.39
Orthorhombic	$Pnma$	2.43[a] 2.01[b] 2.89[b]	2.36[f], 2.37[e]	2.2

References: [224][a], [225][b], [226][c], [227][d],[213][e] , [207][f].

wavelength. Therefore, from an experimental point of view, one can distinguish the $CsPbBr_3$ phase transition with structural characterization such as X-ray diffraction spectroscopy (see details on this technique in the appendix 5.4) and luminescence techniques, e.g. PL or CL. Many reports on the emission peak of $CsPbBr_3$ perovskite can be found in the literature [207, 226, 227]. Figure 3.3(a) shows an example of PL and absorption measurements performed on $CsPbBr_3$ nanocrystals. The PL emission peak is located at 525 nm (∼2.36 eV), close to the theoretical bandgap of the tetragonal phase.

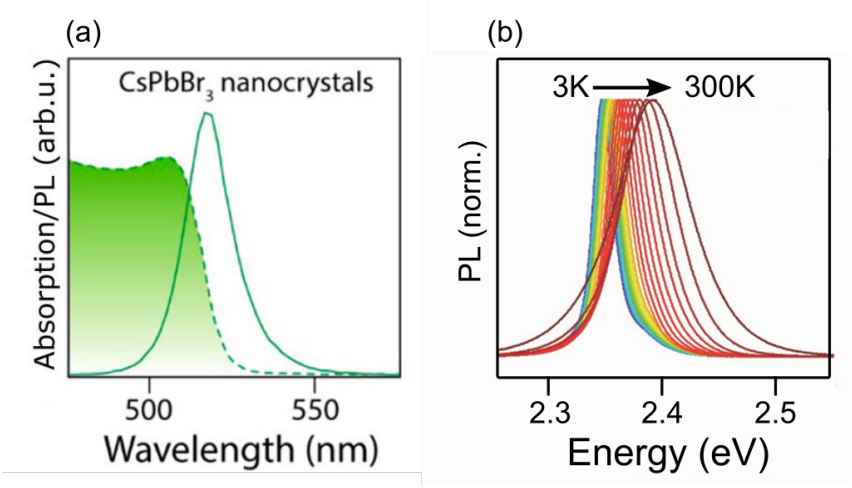

Figure 3.3: *(a) Absorption and PL spectrum of $CsPbBr_3$ nanocrystals at room temperature (∼300K). Reprinted from [172]. (b) PL spectra evolution while temperature decreases. Reprinted from [228].*

Figure 3.3(b) shows the evolution of $CsPbBr_3$ nanocrystal PL emission with temperatures spanning from 3 K to 300 K reported by Diroll et al. [228]. The emission peak blue-shifts monotonously as the temperature increases. This blue shift corroborates previous reports on the evolution of perovskite bandgap with temperature [213, 229], even though it is contrary to common semiconductor behaviors [230].

3.2.2 Analysis of a $CsPbBr_3$ film

The synthesis of the $CsPbBr_3$ perovskite sample was conducted using a melting method by Dr. D. Cerrati, a researcher at IPVF. CsBr and $PbBr_2$ were ground and mixed in equimolar proportions using a mortar and pestle. Approximately 20 g of the obtained powder was loaded into a quartz ampule, placed in a furnace, and heated at ∼630°C, above the melting point CsBr. The melt was maintained at this temperature for several hours, and a piece of FTO glass was briefly

immersed and subsequently removed to form a thin layer on its top. The obtained sample was then cooled down to room temperature for approximately 15 hours.

EDS investigation

SEM-EDS measurements were performed on the sample to assess its homogeneity. Figure 3.4 shows the SEM image of the region analyzed and the corresponding cesium (Cs) and lead (Pb) elemental maps, colorized in yellow and blue, respectively.

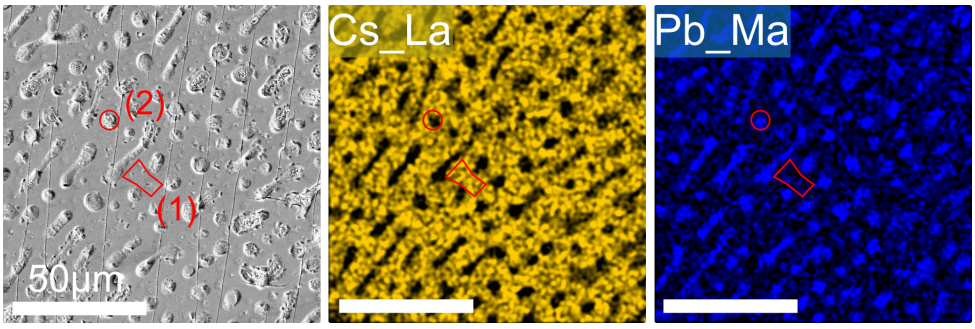

Figure 3.4: *SEM image and corresponding Cs and Pb elemental maps determined by SEM-EDS. Two regions are indicated in the SEM image and correspond to areas where the composition was estimated by quantification. Corresponding results are summarized in Table 3.2.*

The specimen displays a heterogeneous morphology, characterized by the presence of inclusions measuring approximately ten microns in size. Examination of the elemental maps reveals variations in the Cs and Pb contents between the inclusions and the surrounding matrix. Qualitatively, the inclusions appear to possess a greater concentration of Pb and a smaller concentration of Cs than the matrix. The composition of the matrix and the inclusions were quantified using the PhiroZ method, as described in Subsection 2.2.2. The quantification results are presented in Table 3.2.

Table 3.2: *Summary of the estimated composition in zone (1) and (2) displayed in the SEM image Figure 3.4.*

Feature	Br/Pb	Cs/Pb
Matrix	2.76±0.46	1.15±0.29
Inclusion	1.61±0.31	0.19±0.18

The composition of the matrix is consistent with that of $CsPbBr_3$ perovskite, as expected. However, the composition of the inclusions does not align with any known compound within the Cs-Pb-Br material system. Nevertheless, it is hypothesized that the inclusions are composed of $PbBr_2$ due to their high Pb and low Cs concentrations. To confirm this hypothesis, further measurements at higher magnification would be necessary; however, these were not performed due to limitations in time. We confirmed that our specimen mainly consists of $CsPbBr_3$ matrix, and we can now dive into its optical properties.

Analysis with Photoluminescence imaging

To investigate the optical properties of the $CsPbBr_3$ sample, we used the set-up of Hyperspectral Photoluminescence (PL) imaging available at IPVF, which principle is briefly described in the

appendix 5.4.

The measurements were performed by Dr. M. Kim, a researcher at IPVF, on the same sample investigated with SEM-EDS. The PL emission was spatially averaged in the area delimited by a square in Figure 3.5(b) and plotted in Figure 3.5(a).

A single peak at 2.34 eV composes the spectrum close to what was reported so far for $CsPbBr_3$ as mentioned previously (see Table 3.1), confirming that the sample is mainly composed of $CsPbBr_3$.

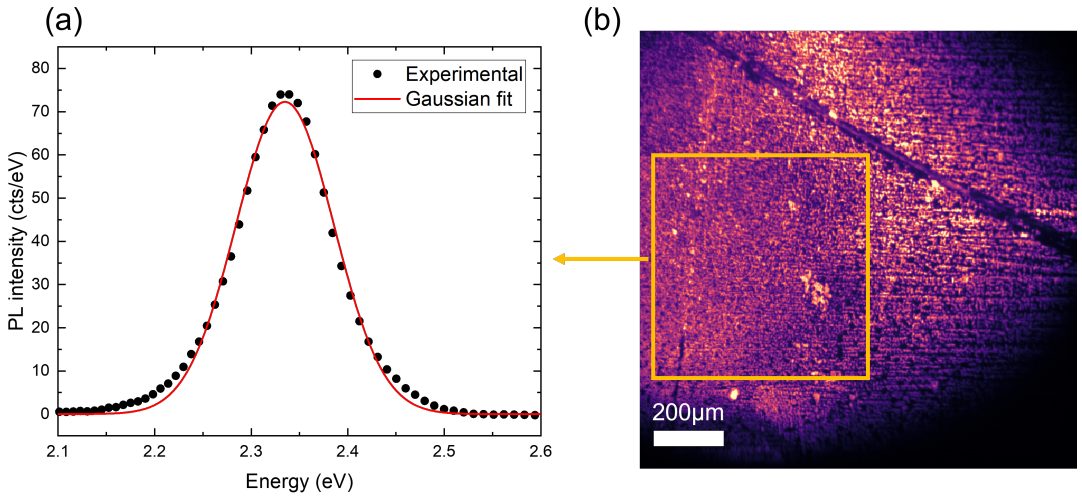

Figure 3.5: *(a) PL spectrum obtained on a $CsPbBr_3$ specimen. The experimental data are fitted with a Gaussian function which gives the position and the FWHM of the emission peak: ∼2.33 eV and ∼0.12 eV, respectively.(b) Panchromatic PL map of the sample shows luminescence inhomogeneities. The PL spectrum in (a) is averaged over the zone delimited in the yellow square.*

Figure 3.5(b) presents the panchromatic PL map of the specimen, in which the PL signal in each pixel is integrated over the entire spectral range. The image shows that the specimen exhibits inhomogeneities, which could correspond to the variations in composition revealed by SEM-EDS (the aforementioned inclusions). Therefore, we employed CL to investigate the specimen further.

Analysis with Cathodoluminescence

Figure 3.6(a) shows the SEM image of the region investigated with CL. The CL spectrum was averaged over this area and plotted in (b). Two emission peaks are visible: one is located at 2.38 eV and the other at 2.3 eV. The spectrum was fitted with two Gaussian functions to confirm the position of each peak. The same fit was performed on each pixel, and the intensity map of each contribution was plotted in (c) and (d) (in green and red for the peak at 2.38 and 2.3 eV, respectively).

The CL maps show that both peaks originate from the matrix, suggesting that they are emitted by the $CsPbBr_3$ phase. The high-energy peak is most likely related to a bandgap transition, while the low-energy peak might be related to a shallow defect level, considering the width of its peak and the slightly lower emission energy. A similar CL emission has been reported by Cohen et al. in a recently published study in which $CsPbBr_3$ nanocrystals were investigated using PL, CL, and TRCL [231]. The authors attributed the high-energy peak to band-to-band

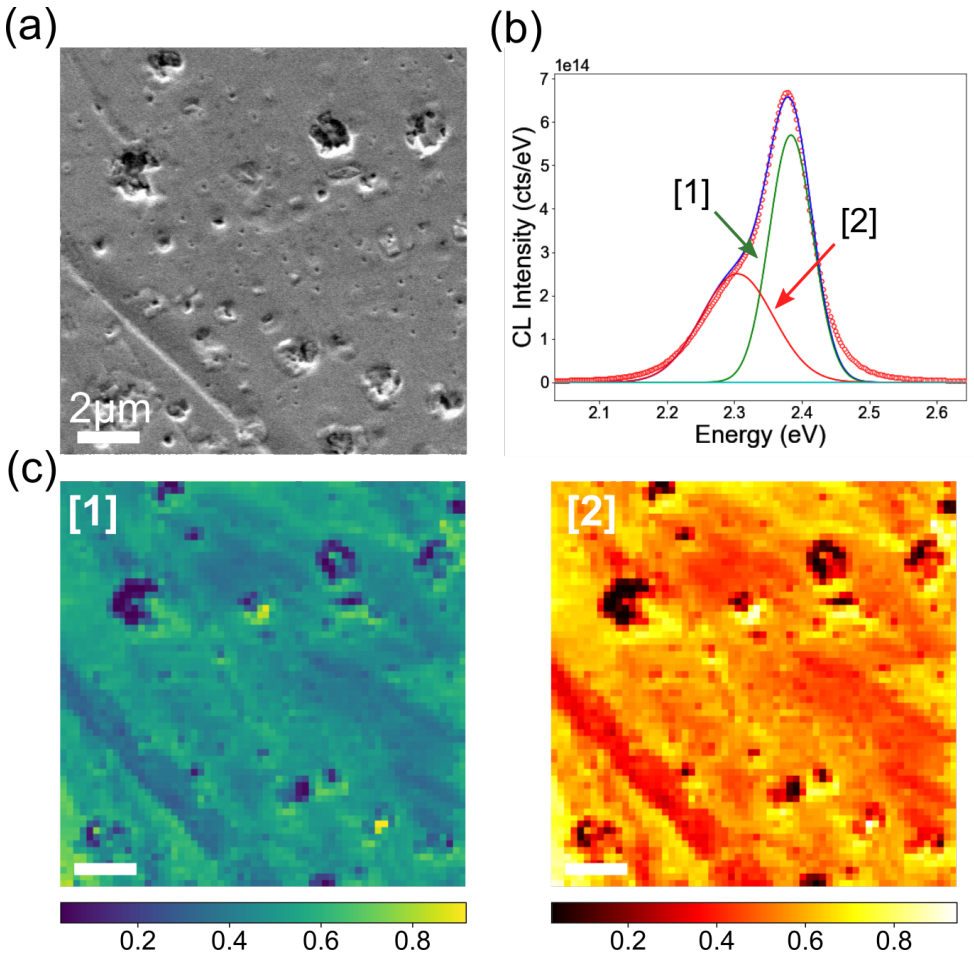

Figure 3.6: *(a) SEM image (b) Averaged CL spectrum (red dots) fitted with two Gaussian laws centered at ∼2.38 ([1] in green) and at ∼2.3 eV ([2] in red). The cumulative curve (sum of the two functions) is in blue and matches well with experimental data. (c) Corresponding intensity maps of the two contributions [1] and [2] obtained via a similar fit on each pixel.*

recombination and the low-energy peak to defect-mediated recombination, which is consistent with our observations.

It is noteworthy that the inclusions exhibit minimal luminescence within the studied energy range (from 1.43 to 3.75 eV). Based on the results obtained from SEM-EDS, it would be expected for a $PbBr_2$ precipitate to exhibit an emission peak near its bandgap energy which is about 2.57 eV [232]. These findings are not conclusive in determining the chemical nature of these inclusions. Further experimentation with varying precursor concentrations may provide insight into the nature and growth of these inclusions. However, our study focuses primarily on the properties of the $CsPbBr_3$ phase of the sample.

As mentioned in Chapter 2, conducting CL measurements at low temperatures can improve the SNR of the CL maps. It also allows picturing the behavior of the specimen emission when the temperature decreases and can reveal structural changes that may occur in these temperature ranges.

To the best of our knowledge, CL measurements at low temperatures have only recently been conducted on cesium-based halide perovskites, such as $CsPbBr_3$, by a single research team [231]. These considerations motivated to conduct CL measurements between 70 K and 300 K.

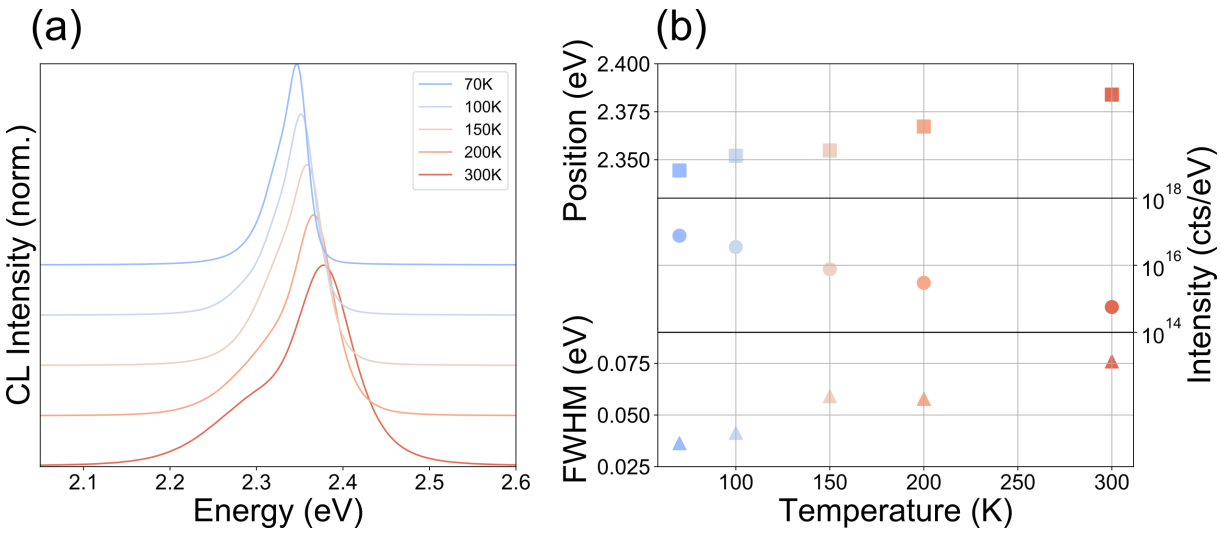

Figure 3.7: *(a) Spatially averaged normalized CL spectra for various temperatures. (b) Evolution of the position, the intensity, and the FWHM of the main CL peak (positioned at 2.38 eV at 300 K) with the temperature.*

Figure 3.7(a) shows the spatially averaged normalized CL spectra obtained for various temperatures between 70 and 300 K. The position and the intensity of the main CL peak (at 2.38 eV at 300 K) is plotted as a function of the temperature in Figure 3.7(b).

We observe that the main CL peak red-shifts monotonously from 2.34 eV to 2.38 eV when the temperature is decreased. The range of the red-shift of approximately 40 meV is consistent with what has been reported previously in temperature-dependent PL studies on $CsPbBr_3$ [228, 233]. In addition, the monotonous evolution of the CL peak position suggests that the $CsPbBr_3$ phase did not undergo phase transition at low temperature.

We also note that the low-energy peak disappeared at low temperatures. This observation suggests that the defect-mediated transition could be thermally activated.

The FWHM of the CL peak decreases from 75 meV to 36 meV with decreasing temperature. This trend has been observed in PL studies and is attributed to the reduction of lattice vibrations at low temperatures [80, 234]. The interaction of the generated excitons with phonons is hindered at low temperatures, resulting in a narrow emission peak.

Finally, the intensity of the main CL peak increases significantly with decreasing temperature, suggesting, primarily, that radiative recombinations are facilitated at low temperatures.

Based on previous studies on temperature-dependent PL measurements of hybrid perovskites [235–238], we suppose that the mechanism responsible for the quenching of the CL peak intensity can be attributed to a thermally activated, non-radiative process with an activation energy E_a. Such phenomenon can be described by an Arrhenius law, as written in Equation 3.1:

$$\frac{I_0}{I_{CL}(T)} = 1 + B \exp\left(-\frac{E_a}{k_B T}\right), \tag{3.1}$$

where I_{CL} and I_0 are the integrated CL peak intensity at the temperature T and 70 K respectively, k_B is the Boltzmann constant, and B is a constant.

To confirm that our results verify this hypothesis, the inverse of the integrated CL peak intensity was calculated, plotted as a function of the temperature, and fitted with the Arrhenius law as shown in Figure 3.8.

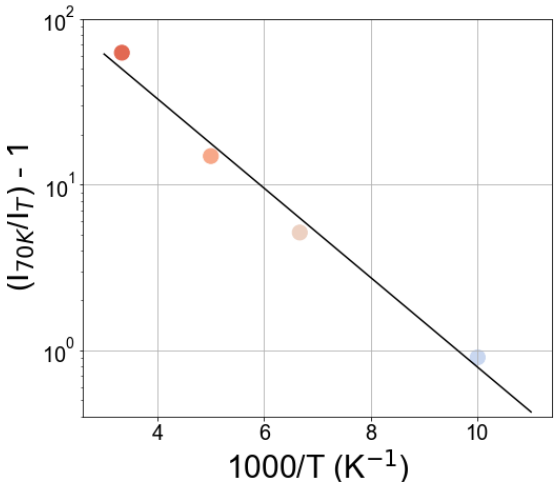

Figure 3.8: *The main CL peak positioned at 2.38 eV at 300 K was integrated at each temperatures. The data were normalized by the value at 70 K, and the inverse was calculated and plotted. The Arrhenius function written in 3.1 was used to fit the data.*

The function provides a good fit to the data, indicating that the quenching of the CL peak with temperature is likely the result of a thermally activated process. Through this fit, we estimate the activation energy of this process to be 54 meV.

This value has been linked in previous reports to the exciton binding energy, as increasing thermal energy promotes the dissociation of excitons and consequent non-radiative transitions in perovskites. Studies using temperature-dependent PL measurements for $CsPbBr_3$ have estimated a value of approximately 50 meV [239–241] for $CsPbBr_3$. However, thermal quenching of the PL or CL peak is not necessarily the result of exciton dissociation [36]. Other mechanisms such as exciton hopping from the $CsPbBr_3$ matrix to defects near the matrix-inclusion interface can also cause thermal quenching of the emission. As such, the exciton binding energy may not be accurately determined from temperature-dependent PL or CL measurements.

This activation energy is a characteristic feature of the $CsPbBr_3$ sample analyzed. A similar approach is used to analyze the degradation products of hybrid perovskite films in Chapters 4.

3.3 Analysis of the $CsPb_2Br_5$ phase

3.3.1 Optical properties

Theoretical calculations reported previously in the literature show that tetragonal $CsPb_2Br_5$ has a large indirect bandgap around 3 eV [215, 242]. Although it has been verified by multiple theoretical studies, many experimental results demonstrate a much lower energy emission [215, 243].

Indeed, in 2016, Wang et al. [244] had reported a green luminescence coming from $CsPb_2Br_5$ nanoplatelets. This result was then later observed in many other specimens [210, 211, 245]. In most of these studies, they identified two onsets in the absorption spectrum measured by UV vis spectroscopy: one at 400 nm (∼3.1 eV) consistent with the theoretical bandgap of $CsPb_2Br_5$, and one at 530 nm (∼2.3 eV), corresponding to the notorious green emission as shown in Figure 3.9.

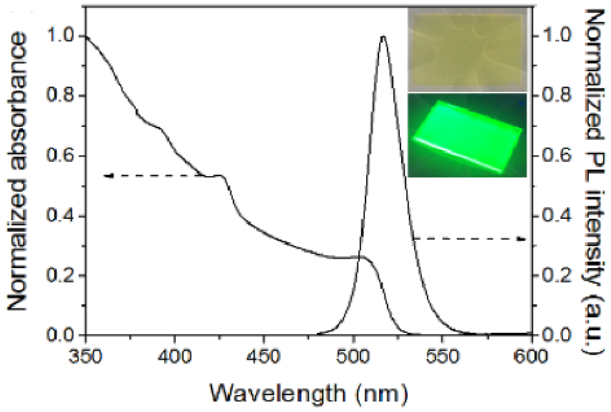

Figure 3.9: *Absorption (left) and PL (right) spectra normalized of centrifugal-coated $CsPb_2Br_5$ films on fused silica. The insets are photograph of the sample without (top) and with (bottom) UV irradiation (image of the sample in inset). Reprinted from [243].*

The origin of this emission peak, strangely close to the emission peak of $CsPbBr_3$, is still under debate. Some explanations found in the literature are developed herein.

Presence of $CsPbBr_3$ residues

Similarity in PL and absorption spectra between $CsPb_2Br_5$ and $CsPbBr_3$ suggests that after fabrication some $CsPbBr_3$ residues remain.

For instance, Li et al. observed that during the transformation of $CsPbBr_3$ nanocubes into $CsPb_2Br_5$ nanosheets, the green luminescence decreased [211]. The authors supposed then that the green emission was coming from the $CsPbBr_3$ phase. This hypothesis has been further supported by other (experimental) works, such as the one from Caicedo-Davila et al. (coupling CL, XRD, and PL measurements) [246] and from Wang et al. [247].

In a recent study, Shen et al. compared simulations with experimental results on the evolution of the bandgap for $CsPb_2Br_5$ and $CsPbBr_3$ phases [248]. Simulations revealed that lattice expansion does not affect the bandgap of $CsPb_2Br_5$, while the bandgap of $CsPbBr_3$ blue-shifts as illustrated in Figure 3.10(a). On the other hand, they observed that the PL peak of micro-spheres (supposedly) composed of $CsPb_2Br_5$ was blue-shifting ($\sim$80 meV) as the temperature increased (see in Figure 3.10(b)). The authors have, thus, interpreted this blue-shift as a mark of the presence of $CsPbBr_3$ in the micro-spheres.

Defect-related transition

In a study focusing on $CsPbBr_3$ thin films coated with $CsPb_2Br_5$ [197], Caicedo-Davila et al. performed PL and CL measurements on the samples and observed the green emission peak at 2.3 eV with both techniques. However, CL measurements also revealed a unique broad peak at 1.8 eV. This peak was attributed to recombination via deep defect transitions due to its width and lower energy, which is significantly lower than the $CsPbBr_3$ and $CsPb_2Br_5$ bandgaps (see Figure 3.11).

Zhou et al. also investigated the hypothesis of defects-mediated transitions being responsible for the green emission through first-principles calculations in [242]. They demonstrated that the green emission could originate from various types of defects in the material, such as bromine vacancies or cesium interstitials.

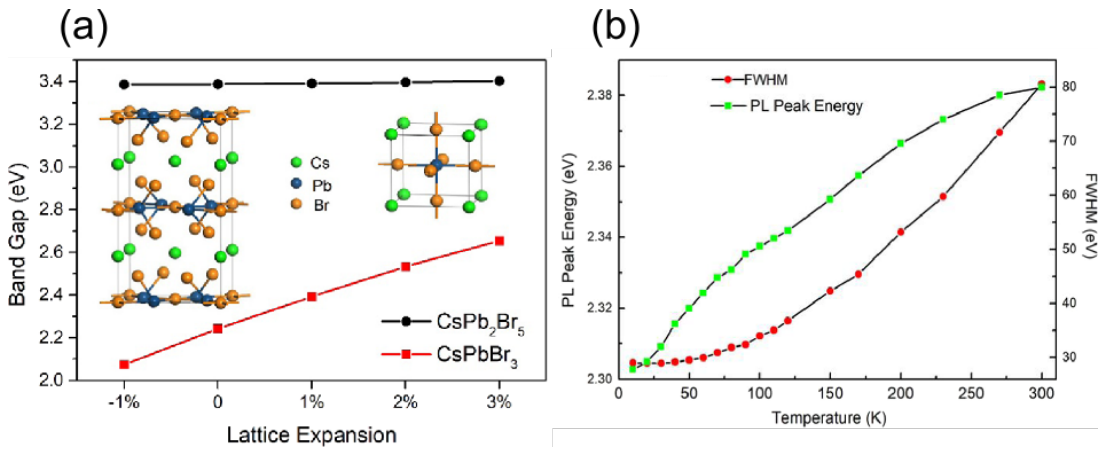

Figure 3.10: *(a) Calculated evolution of the band gap for tetragonal $CsPb_2Br_5$ and cubic $CsPbBr_3$ as a function of the lattice expansion, from -1 to 3%. The insets show the unit cell of tetragonal $CsPb_2Br_5$ and cubic $CsPbBr_3$. (b) Evolution of the PL peak position and FWHM of (supposedly) $CsPb_2Br_5$ micro-spheres from 10 to 300 K. Reprinted from [248]*

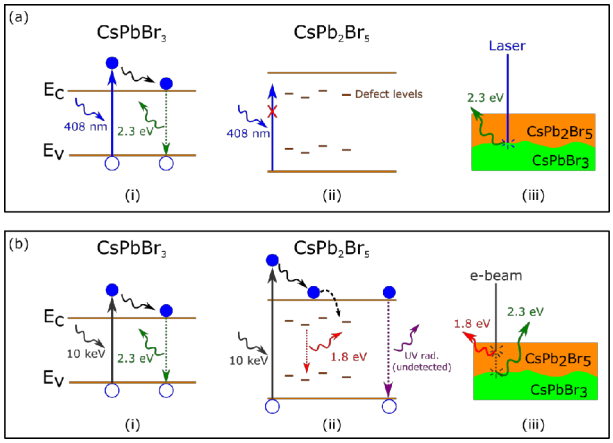

Figure 3.11: *Schematic diagrams showing the differences between (a) PL and (b) CL emission from the $CsPbBr_3$ part of the film (i), and from the $CsPb_2Br_5$ part of the film (ii). The PL signal originates from radiative recombination at the $CsPb_2Br_5/CsPbBr_3$ interface, where the $CsPbBr_3$ effectively absorbs the light, as schematically drawn in (a-iii). The CL signal of the surface originates from defect-assisted, and band-to-band radiative recombination at the surface $CsPb_2Br_5$ and at the $CsPb_2Br_5/CsPbBr_3$ interface respectively, as schematically shown in (b-iii) Reprinted from [197].*

3.3.2 Analysis of $CsPb_2Br_5$ micro-crystals

Specimen preparation

The $CsPb_2Br_5$ micro-crystals studied in this Section were fabricated by Dr. A. Kazemi in the framework of a collaboration between the IPVF and the LRCS[2]. The description of the preparation is inspired by the *Experimental* Section of a work published by this research group [249].

The micro-crystals were synthesized by crystallization reaction of $PbBr_2$ and CsBr, which were dissolved in an HBr solution. The mixture was heated at 118°C and stirred overnight. The solution was cooled down at room temperature, and the micro-crystals were collected by vacuum filtration, washed with diethyl ether, and dried under vacuum at 60°C. The crystal structure of the micro-crystals was analyzed by X-ray diffraction (XRD) spectroscopy (see Chapter 4 for details on this technique), which confirmed that they are composed of $CsPb_2Br_5$ tetragonal

[2]Laboratoire de Réactivité et Chimie des Solides - Université d'Amiens, Amiens, France

phase.

For CL and EDS analysis, a PEDOT:PSS film was deposited on an n-doped silicon (Si) wafer on which the powder was spread. This procedure ensures the electrical contact between the micro-crystals and the sample holder, thus preventing any charge effect during electron microscopy measurements. Besides, it is more suitable for low temperatures measurements than usual carbon tape. Figure 3.12 presents an SEM image of a mm-sized crystal and a schematic cross-section view of the sample.

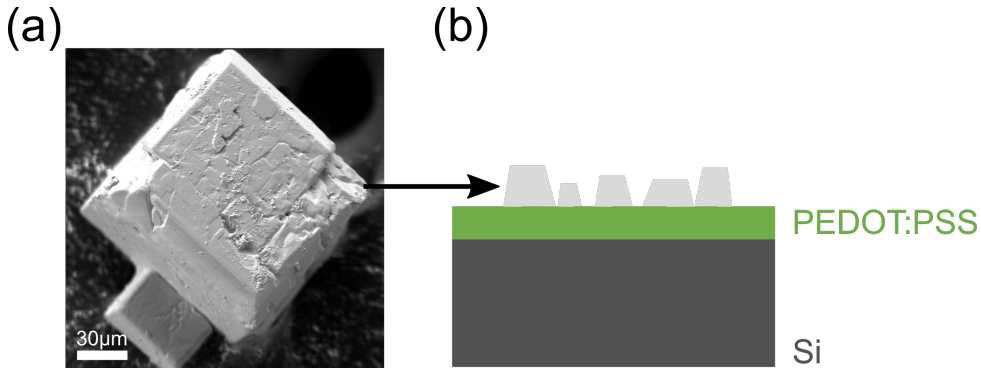

Figure 3.12: *SEM image of a millimeter-size crystal of $CsPb_2Br_5$. Schematic view of the specimen for low-temperature electron microscopy measurements.*

EDS investigation

The morphology and composition of the micro-crystals were analyzed by SEM-EDS. Figure 3.13 shows an SEM image of the micro-crystal analyzed with its corresponding bromine (Br), cesium (Cs), and lead (Pb) elemental maps. The acquisition parameters are summarized in Table 2.5.

The composition was estimated in the micro-crystal by quantification of the EDS map, and the results are summarized in Table 3.3.

Table 3.3: *Summary of the estimated composition in zone 1 and 2 displayed in the SEM image Figure 3.4.*

Feature	Br/Pb	Cs/Pb
Crystal	2.4±0.3	0.7±0.1

The results are close to what was expected from $CsPb_2Br_5$ (2.5 and 0.5 for Br/Pb and Cs/Pb, respectively), while the element distribution does not exhibit any substantial variations. We conclude that $CsPb_2Br_5$ microcrystals are homogeneous.

Analysis with Photoluminescence

The optical properties of several micro-crystals were analyzed with the PL imaging set-up previously described. The PL spectrum was averaged over one specific crystal and plotted in Figure 3.14.

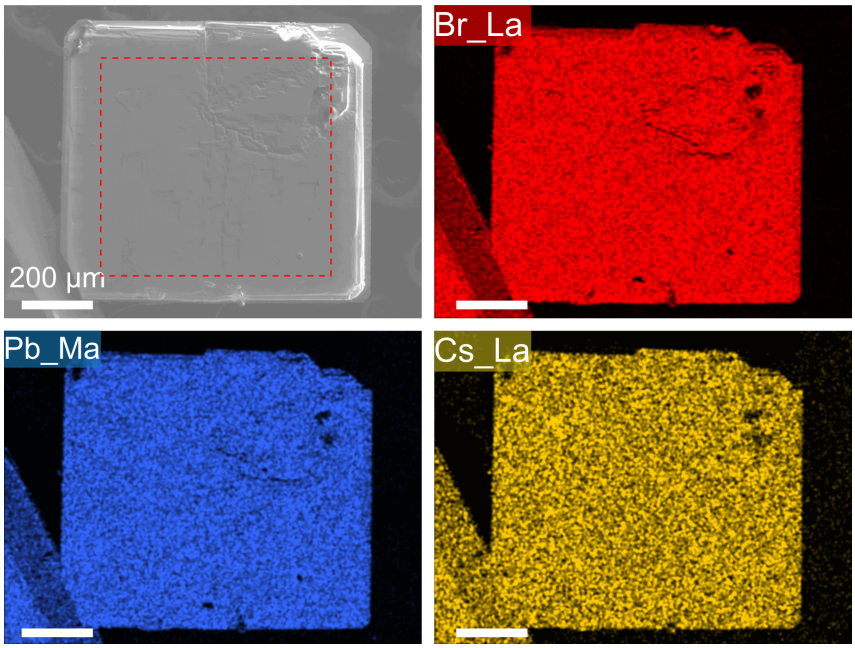

Figure 3.13: *SEM image and corresponding Cs and Pb elemental maps determined by SEM-EDS. The region indicated in the SEM image corresponds to the area where the composition was estimated by quantification. Corresponding results are summarized in Table 3.3.*

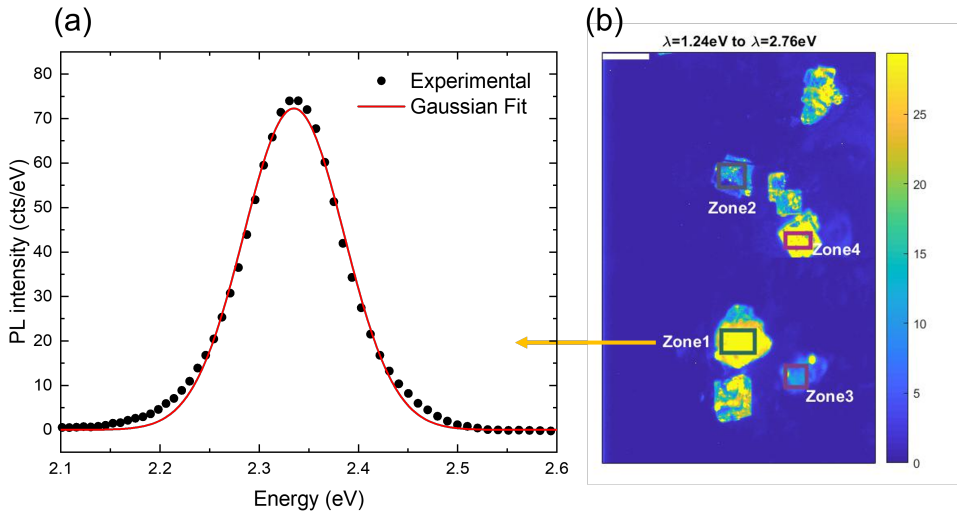

Figure 3.14: *(a) PL result obtained on a $CsPb_2Br_5$ microcrystal. The experimental data normalized are fitted with a Gaussian law which gives the position and the FWHM of the emission peak: ∼2.33 eV and ∼0.10 eV.(b) Panchromatic PL map of the luminescent microcrystals. The PL spectrum in (a) is averaged over the micro-crystal indicated in (b).*

The PL emission peak was observed at 2.33 eV in the micro-crystal, which is consistent with the findings of multiple studies [197, 210, 211, 243, 244, 248]. As previously mentioned, this emission peak may originate from $CsPbBr_3$ domains remaining after the formation of $CsPb_2Br_5$. However, no domains of $CsPbBr_3$ composition were detected by EDS measurements.

Given the limited spatial resolution of PL imaging, we performed CL measurements to to get more local insights on the optoelectronic properties of the crystal.

Analysis with Cathodoluminescence

CL measurements were conducted on the crystal presented in the SEM image of Figure 3.15(a). The CL signal was averaged in the area indicated by the square in the SEM image and plotted in Figure 3.15(b). Two broad emission peaks are observed, one at 1.72 eV and the other at 1.33 eV.

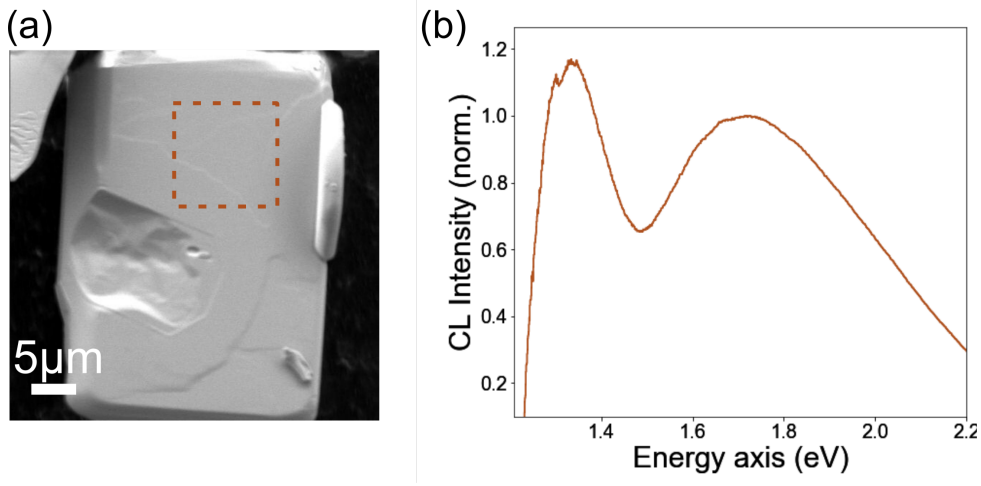

Figure 3.15: *(a) SEM image of the micro-crystal analyzed with CL. The square indicates where the CL signal was averaged to plot the CL spectrum in (b).*

As mentioned previously, a similar high energy peak to the one at 1.72 eV has been observed at 1.8 eV by Caicedo-Davila et al. on $CsPb_2Br_5$ films analyzed with CL [197]. The authors attributed this peak to recombination via deep defects in the bandgap (see Figure 3.11). This interpretation was further supported by DFT calculations reported by Yin et al. [250].

Conversely, the low energy peak at 1.33 eV has no correspondence in the literature, and its origin remains to be determined.

The optoelectronic properties of the $CsPb_2Br_5$ were further analyzed with CL performed at low temperatures between 100 K and 300 K. The measurements at 100 K and 150 K were performed on different days. Therefore, the intensity of the CL spectra obtained at these temperatures will not be considered for the reasoning.

Figure 3.16(a) shows averaged CL spectra measured at different temperatures, which have been normalized by the intensity of the high energy peak positioned at 1.72 eV at 300 K. As the temperature decreases, the intensity of the low energy peak increases while its position remains unchanged. This trend suggests that the recombination process associated with this peak is facilitated at low temperatures. The fixed position of the peak, regardless of the temperature, suggests that the recombination process does not come from band-to-band transition, as we would have expected a shift with the temperature [246, 251]. This observation supports the hypothesis of deep defect-mediated recombination. However, further investigations are required to confirm the nature and origin of this low energy peak.

The evolution of the high-energy peak intensity and position are presented in Figure 3.16(b). It can be observed that the peak intensity increases by a factor of three as the temperature decreases from 300 K to 175 K. Furthermore, the peak position shifts to higher energy as the temperature increases and reaches a plateau between 225 K and 300 K.

Although the trend of the high-energy peak of $CsPb_2Br_5$ is similar to that of $CsPbBr_3$ pre-

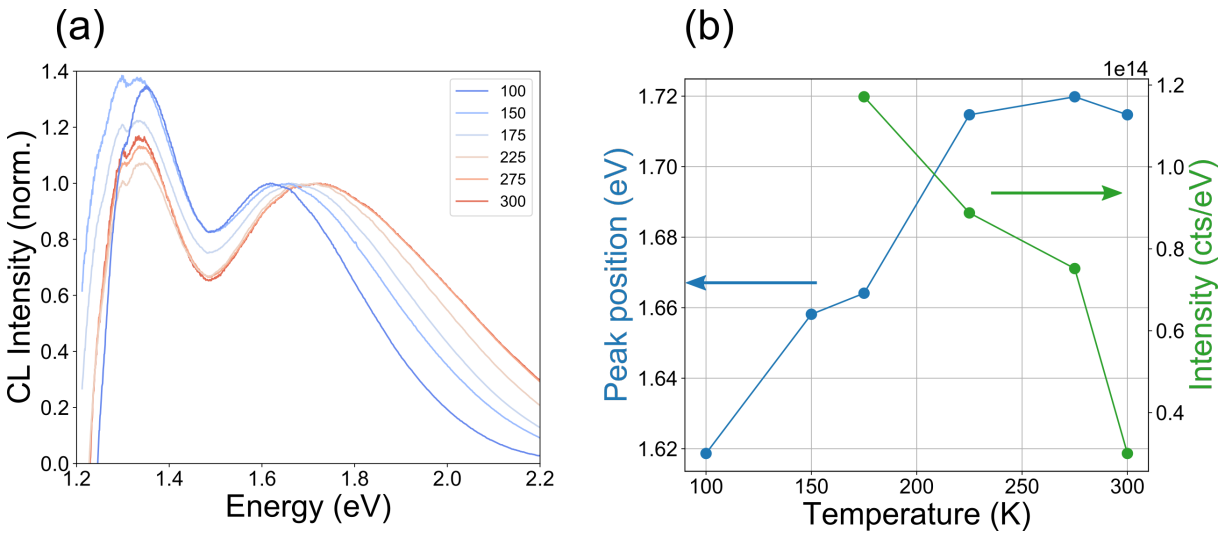

Figure 3.16: *(a) Spatially averaged normalized CL spectra measured at different temperatures on a $CsPb_2Br_5$ micro-crystal. (b) Evolution of the intensity and the position of the high energy peak with temperature.*

viously observed, the ranges of variations are significantly different. In the $CsPbBr_3$ phase, the peak is red-shifted by 40 meV and its intensity is multiplied by ∼130 (see previous section), while the high energy peak of $CsPb_2Br_5$ exhibits a red-shift of 100 meV and an intensity multiplied by 3. These observations suggest that the emission measured in the $CsPb_2Br_5$ micro-crystals does not originate from traces of $CsPbBr_3$.

These results indicate that two different recombination processes coexist in this $CsPb_2Br_5$ micro-crystal.

3.4 Conclusions

In this chapter, we examined two ternary phases from the Cs-Pb-Br material system: $CsPbBr_3$ and $CsPb_2Br_5$. For both phases, we reviewed literature on their crystalline structure, optoelectronic properties, and temperature-dependent phase transitions.

- In Section 3.2, we compared bandgap values of $CsPbBr_3$ reported in literature with the values we calculated for the three different crystal structures,i.e., cubic, tetragonal, and orthorhombic. The variations in bandgap values between different crystalline phases underscore the importance of analyzing the optoelectronic properties to determine the phase symmetry.

  We subsequently presented the analysis performed on $CsPbBr_3$ samples fabricated using a melting procedure. We verified through SEM-EDS that the samples were effectively composed of $CsPbBr_3$. The samples were analyzed using PL imaging measurements and exhibited emission consistent with the bandgap of the tetragonal phase calculated previously. PL imaging revealed inhomogeneities in the sample, which prompted further investigation using CL measurements. The latter revealed two distinct emission peaks in the $CsPbBr_3$ phase: a high-energy peak at 2.38 eV attributed to band-to-band recombination and a low-energy peak at 2.3 eV corresponding to shallow defect-mediated recombination. The high-energy peak was further investigated using CL measurements at low temperatures. The results indicate that the CL peak is likely the result of a band-to-band transition quenched by a thermal effect at room temperature. We determined the activation energy of this effect to be 54 meV and questioned its association with the exciton binding energy made in several studies. The current findings provide insight into the $CsPbBr_3$ phase that can help in its identification in other samples, as discussed in Chapter4.

- In Section 3.3, we discussed the ongoing debate surrounding the bandgap of the two-dimensional material $CsPb_2Br_5$. While theoretical calculations predict an indirect bandgap of 3 eV, experimental results, such as PL measurements, indicate a green emission around 2.3 eV. The literature presents two main hypotheses to explain this discrepancy: (1) the green luminescence originates from residual $CsPbBr_3$, and (2) the green luminescence is the result of deep defect-mediated recombination processes.

  Using a similar approach as in the previous section, we analyzed $CsPb_2Br_5$ micro-crystals fabricated through a crystallization reaction. SEM-EDS confirmed the composition and chemical homogeneity of the micro-crystal. PL imaging showed a green luminescence with a peak at 2.33 eV, while CL measurements revealed the presence of two emission peaks: one at a low energy of 1.4 eV and another at 1.8 eV. The former has not been reported in previous literature and displays behavior at low temperatures consistent with deep defect-mediated recombination, as its position remains unchanged with decreasing temperature. In contrast, the high-energy peak exhibits characteristics consistent with a band-to-band transition. However, the range of this peak variation differs significantly from that of $CsPbBr_3$, which definitely excludes the hypothesis of residual $CsPbBr_3$ in the $CsPb_2Br_5$ microcrystals. The current findings offer new insights into the optoelectronic properties of $CsPb_2Br_5$. While contributing to the ongoing debate about the green luminescence of this phase, we have identified CL emission peaks that can be used as markers for phase identification in future studies.

Chapter

4 Analysis of CsMAFA perovskite degradation products

Chapter content

4.1 Aging process of the CsMAFA-based half-cell device 80
4.1.1 Analysis of the morphology 80
4.1.2 Analysis of the structure 82
4.1.3 Analysis of the opto-electronic properties 83
4.2 Formation of PbI_2 84
4.2.1 Hexagon-like degradation product 84
4.2.2 Disc-like degradation product 85
4.3 Formation of cesium-based inorganic perovskite 87
4.3.1 Chemical analysis of the needles with SEM and STEM-EDS 88
4.3.2 Structural analysis of the needles with Selected Area Diffraction 89
4.3.3 Optical analysis of the needles 91
4.3.4 Analysis of the "flower" 96
4.4 Discussion and proposed degradation mechanisms 97
4.5 Aging with other stress factors 100
4.5.1 Humidity and light 100
4.5.2 Humidity and nitrogen 101
4.6 Conclusions 102

As we mentioned in Chapter 1, there are still several open questions regarding the identification of the different degradation products of perovskite formed in humid environments. Here, we use electron microscopy to observe humidity-induced chemical and optical changes of $Cs_{0.05}(MA_{0.15}FA_{0.85})_{0.95}Pb(I_{0.83}Br_{0.17})_3$ (CsMAFA) thin films, revealing the formation of new phases which are often undetected in macroscopic analysis. The formation of such compounds drastically affects the optoelectronic properties of perovskite thin films, potentially leading to a reduction of the device lifespan. We investigate perovskite thin films exposed to humid air (under 85% RH) for 30 minutes to 6 hours and perform successive characterizations at different scales, including X-ray Diffraction Spectroscopy (XRD), spectrally-resolved Photoluminescence (PL) imaging, Energy Dispersive Spectroscopy (EDS), Cathodoluminescence (CL) and Selected Area Electron Diffraction (SAED). These experimental results are then compared with first-principle calculations using Density Functional Theory (DFT) of crystalline structures and their bandgap. This way, we determine the structural, optical, chemical, and morphological properties of multi-cation perovskite degradation products. We highlight the emergence of three inorganic decomposition phases: PbI_2, $CsPb(I_{0.9}Br_{0.1})_3$ and $CsPb_2(I_{0.74}Br_{0.26})_5$. Finally, based on ion migration, we propose mechanisms governing the degradation of CsMAFA under moisture.

4.1 Aging process of the CsMAFA-based half-cell device

Experimental approach

The structure under investigation includes the following layers: glass/FTO/SnO_2/perovskite, as shown in Figure 4.1(a). The stack, called hereafter half-cell, is exposed to humid air, with 85% of relative humidity (RH) for different durations: 30 minutes, one hour, two, four, and six hours. The set-up used is schematically presented in Figure 4.1(b).

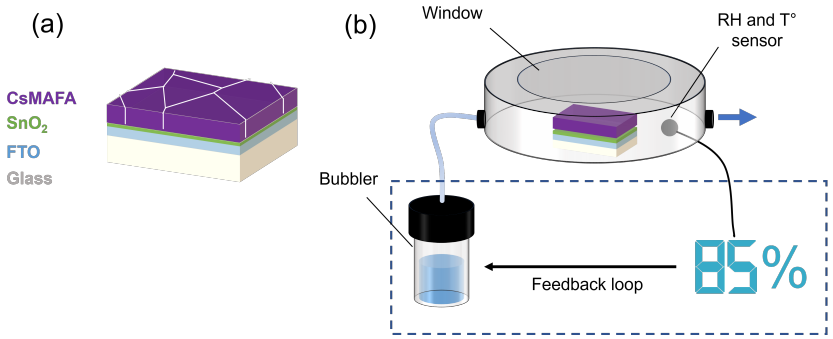

Figure 4.1: *(a) Sketch of the CsMAFA-based half solar cell with the following layers: glass/FTO/SnO_2/CsMAFA perovskite. (b) Sketch of the climatic chamber used to perform the aging of the half-cell.*

The set-up consists of a chamber with two openings, a transparent cover, a tube through which the humid air is introduced into the chamber from a bubbler, and a temperature and humidity sensor that regulates the action of the bubbler.

The transparent lid serves as an optical window enabling *in-situ* characterizations, which means that during the aging process, the sample can be characterized with optical-based techniques such as optical microscopy or PL.

In this study, the lid was covered with a black aluminum foil to keep the sample in the dark. The relative humidity was set at 85% and the temperature at 25°C. The inlet of the chamber was connected to the bubbler, which provided humid air, while the outlet was open throughout the aging process. Since the ambient humidity in the laboratory was significantly lower ($\approx$ 40% RH) than the targeted 85% RH, the bubbler had to continuously provide a flow of humid air into the chamber. After aging, the aged samples were removed from the chamber and stored in the dark and under vacuum until characterization.

4.1.1 Analysis of the morphology

The morphology of the aged samples was first inspected with a confocal microscope. The latter enables high-resolution three-dimensional imaging, down to several microns, but we use it here as an automatic high-resolution optical microscope.

In the optical image Figure 4.2(b), we note the emergence of several degradation products with unique geometries. As aging time increases, their density increases together with the formation of voids in the perovskite film, as shown in Figures 4.2(c) and (d).

The morphology of these emerging phases is further investigated by SEM imaging displayed in Figure 4.3. In the pristine thin film, we can easily identify the grain boundaries of the perovskite as well as the presence of PbI_2 clusters due to the excess of PbI_2 in the precursor solution

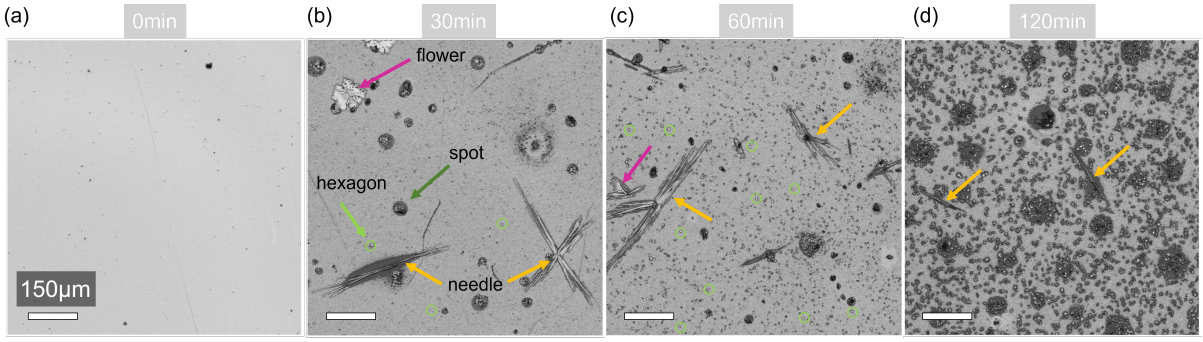

Figure 4.2: *Images of the pristine and the aged specimens were obtained with a confocal microscope. After only 30 minutes at 85% RH, degradation features appear in the film - same observations in the sample after 60 minutes. The sample aged 120 minutes shows more voids regions, hence less residual perovskite film between degradation features.*

as mentioned in Chapter 1. The average grain size is around 320 nm, in line with values reported for state-of-the-art PSCs [252]. However, moist air aging induced the formation of new compounds with four different morphologies: hexagon (2), disc-like (3), needle-like (4,5), and flower-like (6) structures.

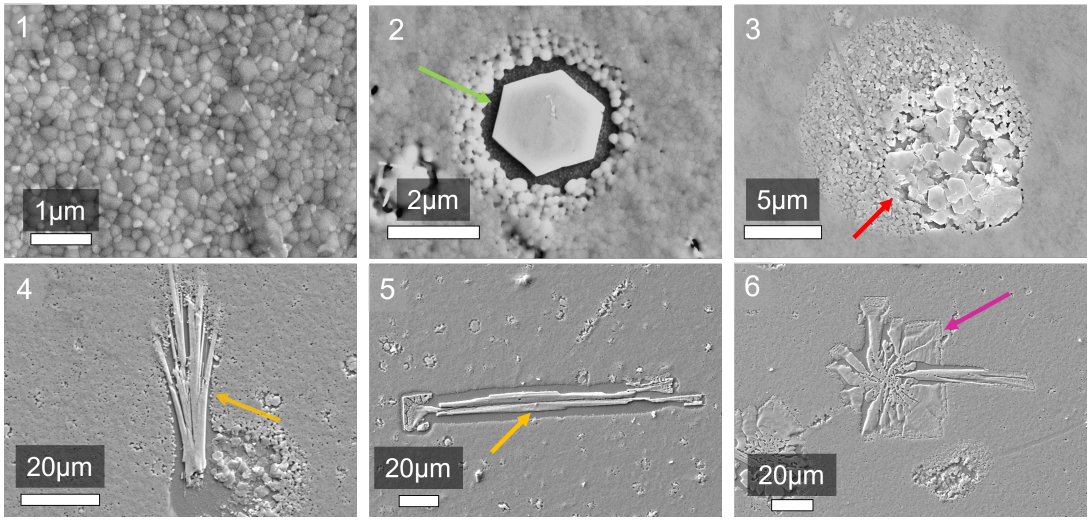

Figure 4.3: *SEM images (SE) corresponding to pristine sample (1) and features appearing in aged samples such as: hexagon (2), disc (3), needles (4) and (5), and flower (6).*

The decomposition of a perovskite film under humid air and the appearance of such features are consistent with previous reports [121, 122]. Needle-like structures were evidenced by Marchezi et al. in double-cation perovskites exposed to moisture and were related to hydrated perovskite intermediates [121]. Similar observations were made in the investigation of the degradation mechanisms of $MAPbI_3$ [113, 253] and $FAPbI_3$ [254] exposed to high relative humidity. Nishida et al. also report the emergence of needle-like heterogeneities in $Cs_{0.05}(MA_{0.17}FA_{0.83})_{0.95}Pb(I_{0.83}Br_{0.17})_3$ perovskite films exposed to water-vapor [255]. However, localized investigations of these degradation products composition and structure are lacking in these studies, preventing an accurate identification of their specific nature.

4.1.2 Analysis of the structure

We used XRD to identify the crystalline nature of the new phases that appear in aged samples. Figure 4.4 presents the diffraction patterns obtained on a fresh sample (not aged) and a sample aged under high humidity during 1 hour.

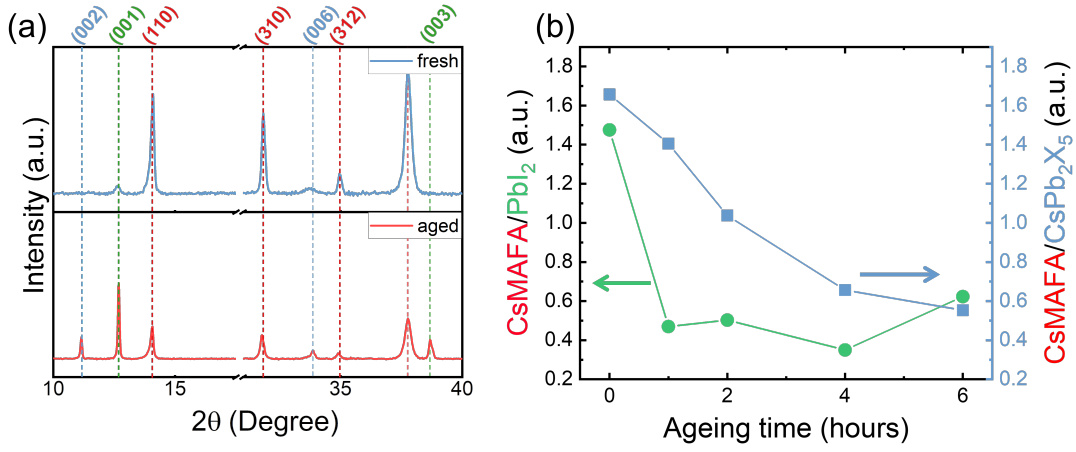

Figure 4.4: *(a) Diffractograms obtained via XRD measurements performed before and after 1 hour of aging under 85% RH, in blue and red, respectively. XRD peaks of CsMAFA, PbI_2, $CsPb_2X_5$ are indexed in red, green, and blue, respectively, according to the study by Kazemi et al.[249] (b) Variation of the area ratio of the (110) CsMAFA peak over the (001) PbI_2 and (002) $CsPb_2X_5$ peaks, with aging time.*

We observe diffraction peaks at $2\theta = 14.09°$, 31.8°, 34.9°, and 37.8° corresponding to the (110), (310), (312), and (204) crystallographic planes of the CsMAFA tetragonal structure, respectively, confirming the initial state of the film. Additional Bragg peaks are present in the pristine thin film at $2\theta = 12.6°$ and 38.7° and correspond to (001) and (003) planes of the hexagonal PbI_2. These peaks are usually observed when an excess of PbI_2 is introduced into the precursor solution [256].

In the XRD patterns of the aged samples, the PbI_2 contribution becomes more prominent. Besides, additional peaks appear at 11.2° and 32.9° that can be assigned to the (002) and (006) planes of inorganic $CsPb_2X_5$ tetragonal structure (where X stands for a halide) [210, 257], suggesting the emergence of a full inorganic compound in the aged perovskite film.

Figure 4.4(b) displays the evolution with time of the area ratio of the CsMAFA main peak ($2\theta = 14.09°$) over the most intense diffraction peaks of PbI_2 ($2\theta = 12.6°$) and $CsPb_2X_5$ ($2\theta = 11.2°$) when the samples are exposed to humid air (85% RH) during up to 6 hours. The emergence of PbI_2 seems to coincide with the decrease in CsMAFA peak intensity, suggesting that perovskite decomposes into PbI_2 when exposed to humid air, as reported in previous studies [76, 119, 258]. In parallel, the CsMAFA/$CsPb_2X_5$ ratio also decreases, indicating a transformation of CsMAFA into $CsPb_2X_5$. This assumption is supported by several works that have reported a similar water-induced phase transition in mixed-cation perovskite films [120, 249]. After 4 hours of aging, the ratio CsMAFA/PbI_2 increases due to a decrease in PbI_2 content known to decompose into lead salts in humid air [259].

4.1.3 Analysis of the opto-electronic properties

The formation of new phases in the perovskite layer significantly affect the optoelectronic properties of the absorber and, therefore, the device performance. To investigate this aspect, we performed PL imaging measurements as presented in Chapter 3 [260]. We acquired maps for samples exposed to humidity for one, two, and four hours, monitoring the local evolution of the PL spectra.

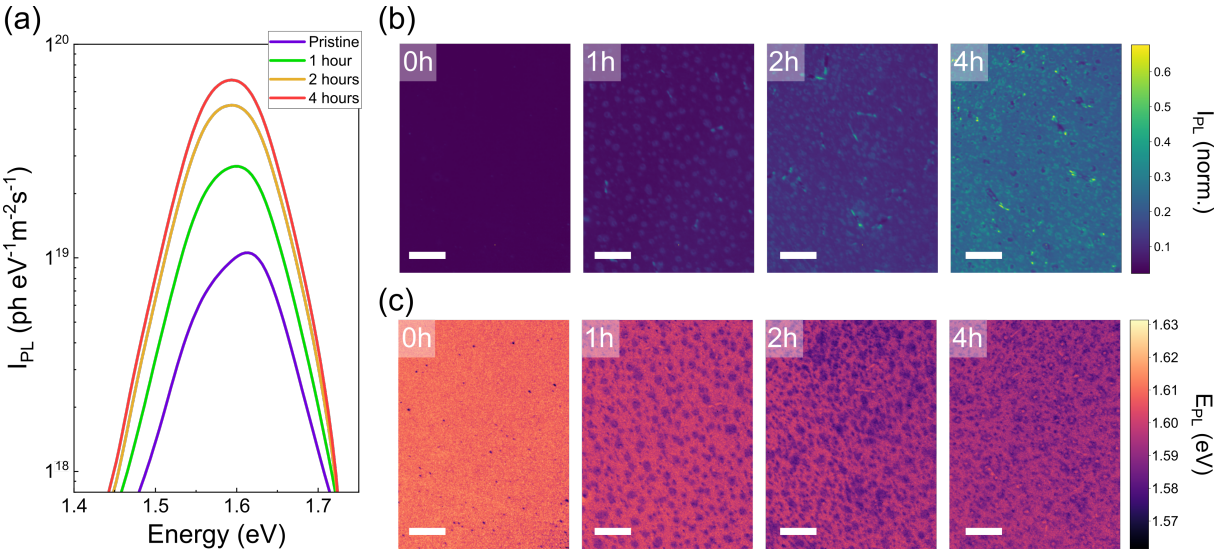

Figure 4.5: *(a) Spatially averaged (over an area of 700 × 950 µm) PL spectra acquired on specimens exposed for 0, 1, 2, and 4 hours to 85% RH. (b) Corresponding panchromatic PL images of the perovskite films. (c) Maps of the PL peak maximum position. The scalebar of 150 µm applies to all images.*

Figure 4.5(a) shows spatially averaged PL spectra for the four aging durations. Initially, the spectrum exhibits a maximum PL peak position at 1.61 eV, that progressively red-shifts until reaching a value of 1.59 eV after 4 hours. Moreover, the PL peak intensity significantly rises for increasing exposure times. Such moisture-induced evolution of the PL spectra of halide perovskite thin films was already observed in the literature [217, 261], and the increase of PL peak intensity was found to be proportional to the RH% [119].

As mentioned in Chapter 1, photo-induced halide segregation can lead to a red-shift in the emission of mixed halide perovskites. Our observations are consistent with this phenomenon and may be due to both photo-induced segregation and the effect of moist air on the material. The local distribution of the optical properties was then examined.

Figure 4.5(b) shows panchromatic PL maps for each specimen with the same intensity scale. We observe the apparition of highly luminescent features on the specimen aged for 1 hour and an overall increase in PL signal intensity.

Corresponding PL peak maximum position maps are displayed in Figure 4.5(c). While the pristine sample (0h) shows a homogeneous distribution of the PL peak position at about 1.61 eV, the samples exposed to humid air show a shift of the PL peak at 1.59 eV and a second phase emitting below 1.58 eV.

Spatially resolved investigation of the perovskite thin films thus reveals variations of their optoelectronic properties after aging. The increase of the PL peak intensity may suggest a reduction of non-radiative losses, which could be related to the passivation of the surface defects of the perovskite layer [262] by humid air and to the formation of highly emitting iodine–rich (I-rich) domains. However, some of the degradation products observed by optical microscopy and detected by XRD measurements are not resolved by photoluminescence imaging. This probably

arises from their poor contribution to the overall active layer emission and their size, of the order of micrometers, which is too small to be observable with the optical set-up used for the photoluminescence analysis. Although there is an increase in PL intensity there is an increase in inhomogeneities in the thin films. These early signs of degradation expand for longer exposure times, resulting in more heterogeneous luminescence of the absorber.

Conclusion of the section

CsMAFA-based half-cells were aged in the dark under air with 85% relative humidity. Analysis of the aged samples showed that the crystallographic contribution of CsMAFA decreased, while PbI_2 and a new phase made of $CsPb_2X_5$, increased. PL imaging revealed the emergence of small highly-luminescent red-shifted impurities in the film, and optical microscopy unveiled the emergence of peculiarly shaped degradation products over time. To gain further insight into the humidity-induced degradation products, we have performed a systematic, nanoscale analysis by coupling several electron microscopy techniques detailed in the following Sections.

4.2 Formation of PbI_2

In this section, the degradation products related to PbI_2 are thoroughly analyzed.

4.2.1 Hexagon-like degradation product

Figure 4.6(a), (b), and (c) show the SEM image and the elemental maps obtained via an SEM-EDS measurement on an hexagonal feature. Bromine (Br) and iodine (I) contents appear in red and green, respectively, allowing for a qualitative examination of the element distribution in this specific region. The hexagon exhibits higher I and lower Br contents than the surrounding film. Concentrations in Cs, Br, I, and Pb are estimated by element quantification (see Chapter 2 for details on the method used) in the hexagon and the surrounding film. The results are normalized by the concentration of Pb and are displayed in Table 4.1.

Table 4.1: *Results of the quantification of the composition in I, Br and Pb obtained via SEM-EDS measurements on the hexagon and the surrounding film displayed in Figure 4.6(a).*

Feature	I/Pb	Br/Pb	Composition
Film	2.6±0.3	0.5±0.1	CsMAFA
Hexagon	2.2±0.2	0.1±0.05	PbI_2

In the hexagonal feature, the I/Pb ratio is close to 2, indicating the formation of pure PbI_2. The presence of a small Br concentration (Br/Pb $\approx$ 0.1) may come from perovskite residues beneath the hexagon.

This feature exhibits the typical hexagonal morphology of PbI_2 crystals, suggesting a highly anisotropic growth along the (001) axis. Such anisotropic growth is consistent with the steep increases of the PbI_2 contribution in XRD pattern shown in Figure 4.4.

Hexagonal degradation products have been further characterized by CL as shown in Figure 4.6(e,f). Their emission spectrum is compared to the pristine CsMAFA perovskite and exhibits two visible peaks; the first at 1.65 eV is related to CsMAFA, and the other at 2.41 eV is attributed to the PbI_2 phase. This is confirmed by the CL maps plotted in Figure 4.6(e),

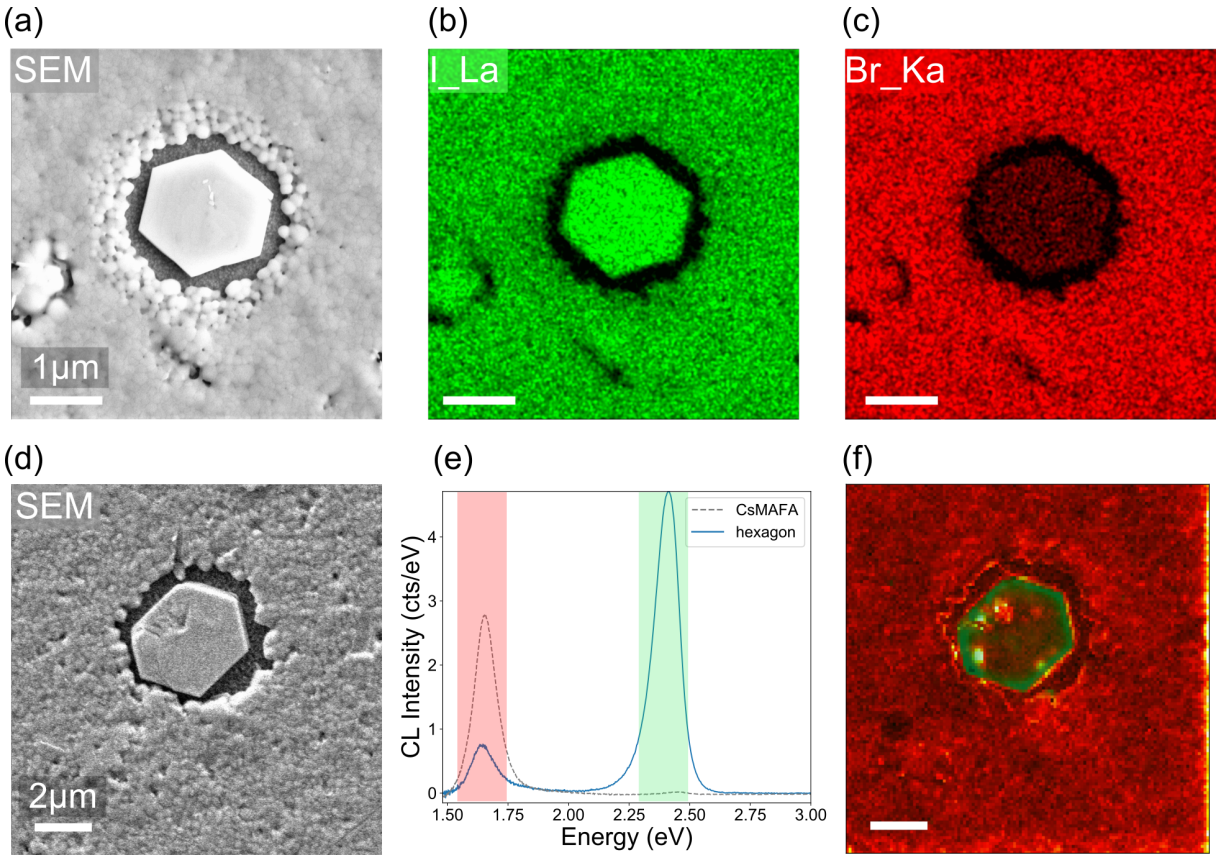

Figure 4.6: *Hexagonal feature. (a) SEM image of the hexagon analyzed with EDS. (b) and (c) Corresponding EDS elemental maps showing the distribution of iodine and bromine in green and red, respectively. (d) SEM image of the hexagon analyzed with CL. (e) Averaged CL spectra integrated over the hexagon in blue and over a pristine CsMAFA perovskite film in gray (dash line). (f) CL map with false colors showing the luminescence integrated over two different spectral regions: red [1.6 eV, 1.7 eV], and green [2.25 eV, 2.5 eV] corresponding to the emission of the CsMAFA perovskite and the PbI_2 phase, respectively. For each pixel, the integrated intensity of each band is normalized by the maximum.*

where the CsMAFA and PbI_2 peaks are highlighted in red and green, respectively. A weak but noticeable response around 1.65 eV in the hexagon can be associated with remnants from the parent perovskite film located beneath the hexagon.

4.2.2 Disc-like degradation product

A similar analysis was performed on degradation products exhibiting a disc shape, as shown in Figure 4.2(b) and displayed at higher magnification in Figure 4.3(3). Figure 4.7(a) shows the SEM image of the feature analyzed with corresponding elemental maps of I and Br (in green and red respectively) distribution obtained by SEM-EDS.

The SEM image reveals three distinct regions: (1) micro-crystals indicated by a green arrow; (2) the film, near the micro-crystals, with large grains indicated by a red arrow; and (3) the surrounding bulk perovskite film. The composition in these three regions was estimated and is summarized in Table 4.2.

The elemental maps show that the micro-crystals have a higher I content and lower Br content compared to the surrounding regions. The estimated composition of these micro-crystals suggests that they are composed of PbI_2, similar to the hexagonal degradation products studied

previously.

The area surrounding these PbI_2 crystals, which has larger grain size than the rest of the film, does not show any chemical variations in either elemental maps or the estimated composition.

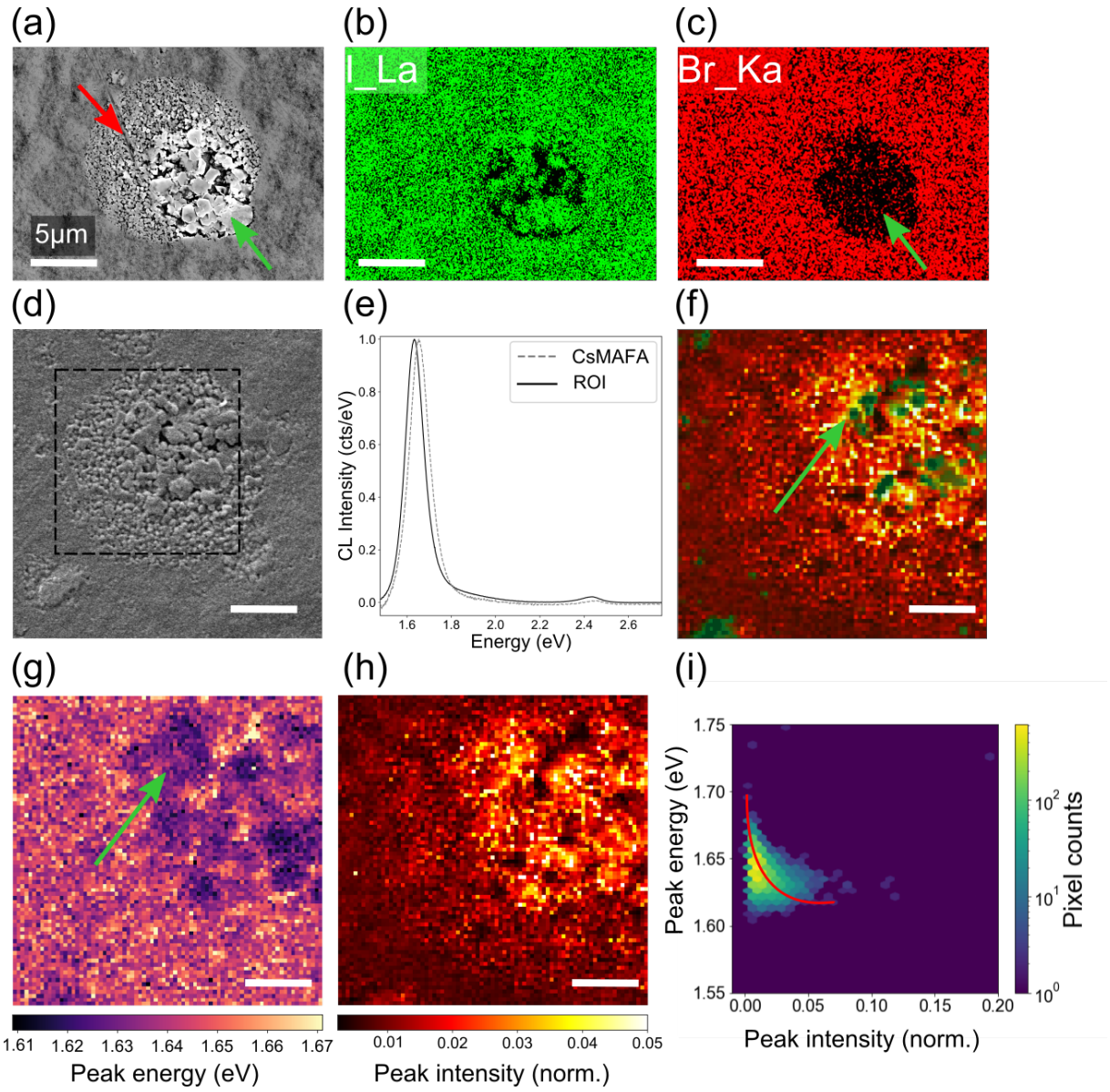

Figure 4.7: *(a) SEM image of the disc-like degradation product analyzed with EDS. (b) and (c) Corresponding EDS elemental maps showing the distribution of iodine and bromine in green and red, respectively. (d) SEM image of the disc-like degradation product analyzed with CL. (e) CL spectra averaged over the region delimited by a black square on the SEM image, and in a pristine CsMAFA perovskite film, in black and gray (dash line), respectively. (f) CL map with false colors showing the luminescence integrated over two different spectral regions: red [1.6e V, 1.7 eV], and green [2.25 eV, 2.5 eV] corresponding to the emission of the CsMAFA perovskite and the PbI_2 phase, respectively. For each pixel, the integrated intensity of each band is normalized by maximum. (g) CL peak energy (g) and intensity normalized map. (i) 2D histogram of the CL peak position as a function of its intensity normalized. The red line is a guide the eye.*

As mentioned in Chapter 1, other studies have shown that hybrid perovskite crystallinity can be enhanced by humidity exposure. The emergence of the large-grain area in our samples

Table 4.2: *Results of the quantification of the composition in Cs, I, Br and Pb obtained via SEM-EDS measurements three different regions displayed in Figure 25(a). EDS signal was too weak to quantify Cs content as shown in Figure 25.*

Feature	I/Pb	Br/Pb	Composition
(1)	2.24±0.22	0.10±0.04	PbI_2
(2)	2.69±0.30	0.55±0.11	CsMAFA
(3)	2.67±0.29	0.51±0.11	CsMAFA

may therefore be attributed to this phenomenon.

Figure 4.7(d) shows the SEM image of a similar degradation product analyzed using CL. The spatially averaged CL spectrum in the region delimited by the black square is plotted in black in Figure 4.7(e). It exhibits a perovskite emission peak at 1.63 eV, slightly red-shifted (∼20 meV) as compared to the reference spectrum shown in gray. A small contribution of the PbI_2 phase is also observed at 2.41 eV. A CL map with CsMAFA and PbI_2 peaks highlighted in red and green, respectively, is plotted in Figure 4.7(f). This map shows the presence of PbI_2 micro-crystals, indicated by a green arrow, and reveals that the perovskite peak in the vicinity of these PbI_2 micro-crystals has a higher CL intensity than the rest of the film.

The position and intensity of the perovskite peak were then determined in the map and plotted in Figure 4.7(g) and (h). A local red-shift in the peak position is observed in the vicinity of the micro-crystals (indicated by a green arrow). The map Figure 4.7(h) suggests a correlation between this variation in peak position and the increase in peak intensity. This relationship is further supported by the 2D histogram displayed in Figure 4.7(i) (in which the peak position for all pixels in the map is on the ordinate, and the normalized intensity is on the abscissa). The trend line in red shows that the peak intensity evolves with the peak position for many pixel counts. This behavior can be attributed to the halide migration in a CsMAFA perovskite film, which generates I-rich domains and causes similar variations in peak emission.

These observations suggest that exposure to moist air may induce halide segregation in the CsMAFA perovskite film followed by its decomposition into PbI_2 micro-crystals. Indeed, given the spatial proximity of the segregated phase of CsMAFA perovskite and the PbI_2 micro-crystals (see Figure 4.7(f) and (g)), we can hypothesize that halide segregation precedes the complete decomposition into PbI_2 crystals.

Conclusion of the section

The chemical analysis of the hexagonal degradation products showed that they are composed of pure PbI_2, further confirmed by CL measurements. Their growth is highly anisotropic, corroborating the XRD results discussed in the previous Section. The degradation products in the shape of discs were shown to be composed of PbI_2 but also of I-rich perovskite. These observations are consistent with results obtained by PL and suggest that moist air exposure induces halide segregation before degrading perovskite.

4.3 Formation of cesium-based inorganic perovskite

Different needle-like structures can be found in the aged samples that do not differentiate by their morphology but present very distinct structural and optoelectronic attributes. We showed

in Figure 4.3(4) and (5) an example for each type of needle on which SEM-EDS, STEM-EDS, SAED, and CL were performed.

4.3.1 Chemical analysis of the needles with SEM and STEM-EDS

Cs, I, and Br distribution maps obtained by SEM-EDS for each needle category are displayed in Figure 4.8. Notably, the Cs and I contents are higher in needles than in the surrounding perovskite film. The quantification of the elements from SEM-EDS evidences that the two needles have a distinct composition. In the first needle (see Figure 4.8(c)), the ratio Cs/Pb is close to one suggesting the formation of a fully inorganic perovskite, i.e., $CsPbX_3$. In the second needle (see Figure 4.8(f)), on the other hand, the ratio Cs/Pb is close to 0.5, which could correspond to the lead-rich pure inorganic perovskite $CsPb_2X_5$.

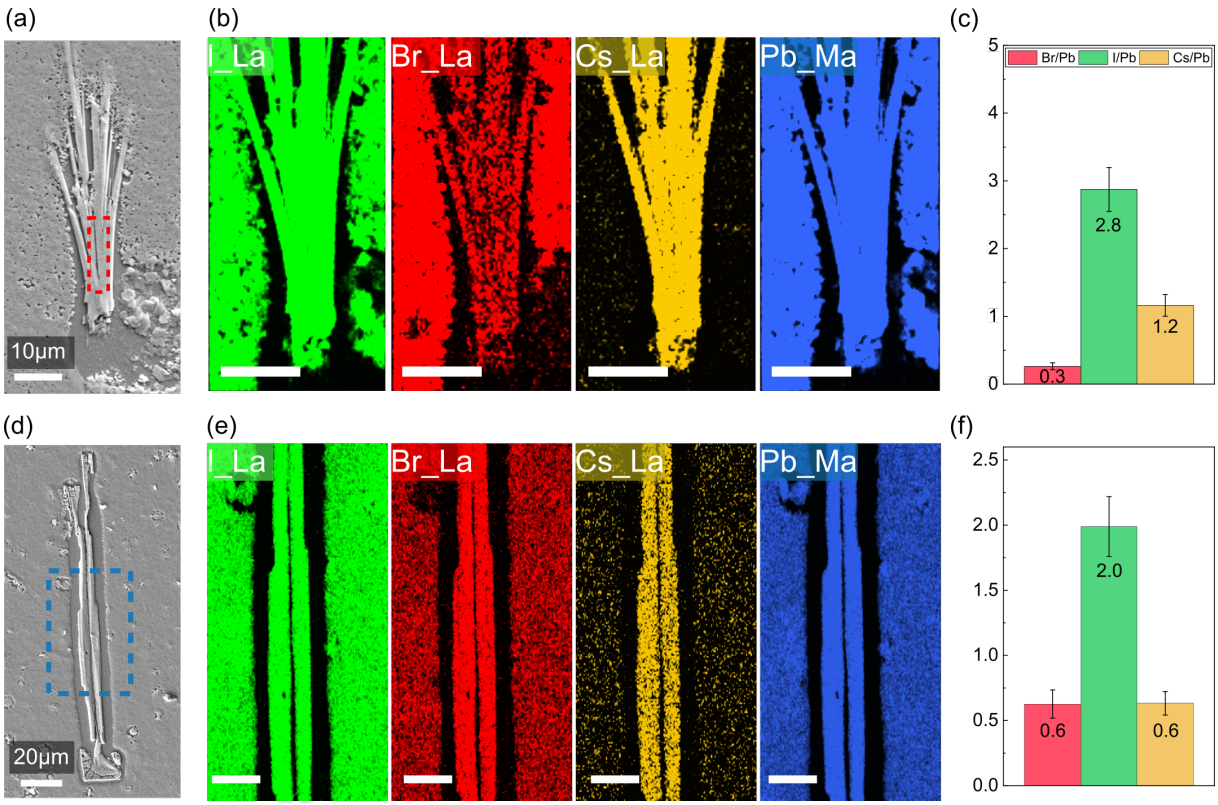

Figure 4.8: *(a,d) SEM images of the two needles studied. (b,e) Corresponding SEM-EDS elemental maps (I, Br, Cs and Pb). (c,f) Corresponding ratios of Br/Pb, I/Pb, and Cs/Pb determined by quantification of SEM-EDS spectrum presented in a bar plot. Composition of needle (a) and (d) is equal to: $CsPb(I_{0.9}Br_{0.1})_3$ and $CsPb_2(I_{0.7}Br_{0.3})_5$, respectively.*

The halogen concentration also varies between the two specimens. In the second needle, the ratio I/Pb around 3 is systematically lower than in the first needle (close to 2), while the ratio Br/Pb is slightly higher (0.7 versus 0.3). We then propose the following composition for these cesium-based perovskite phases: $CsPb(I_{0.9}Br_{0.1})_3$ and $CsPb_2(I_{0.7}Br_{0.3})_5$.

Given the limits of SEM-EDS for analyzing complex systems mixing elements with high and low atomic number (see Chapter 2), the relevance of these compositions might be challenged. Therefore, FIB lamellae were prepared from the same type[1] of needles and analyzed by

[1]SEM-EDS had been performed before the lamellae fabrication to ensure that degradation products were equivalent (see Figure 26).

STEM-EDS, as shown Figure 4.9. Results from quantification are displayed in the bar plots in Figure 4.9(c) and (d). Although there are larger uncertainties due to the small volume probed (and thus fewer X-ray counts collected [162]), the results are confirming the SEM-EDS quantification and further support the assumed composition of the needles.

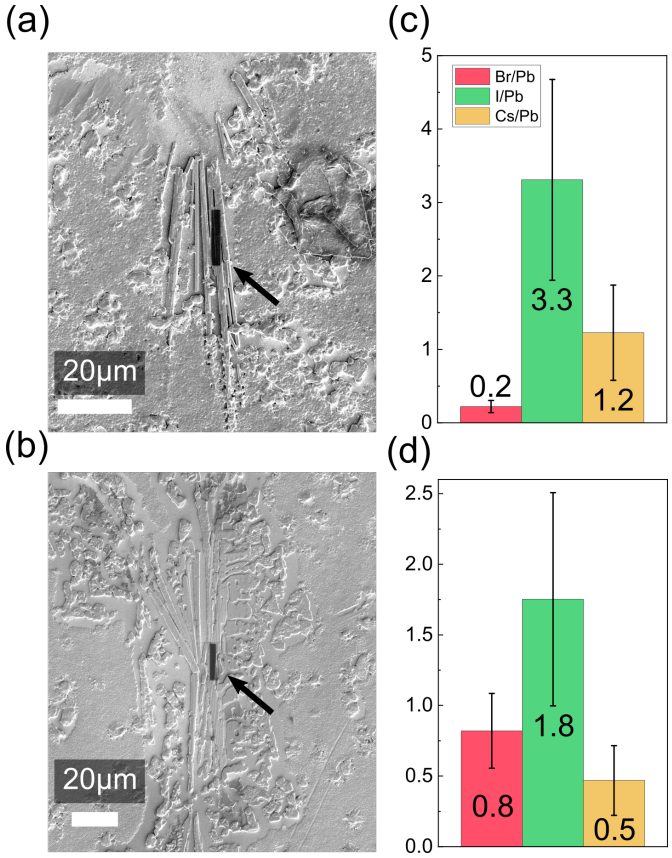

Figure 4.9: *(a,b) SEM images of the regions from which a FIB lamella has been extracted. (c,d) Corresponding ratios of Br/Pb, I/Pb, and Cs/Pb determined by quantification of STEM-EDS measurements, presented in a bar plot. The composition of the needles (a) and (b) is equal to: $CsPb(I_{0.9}Br_{0.1})_3$ and $CsPb_2(I_{0.7}Br_{0.3})_5$, respectively.*

4.3.2 Structural analysis of the needles with Selected Area Diffraction

According to the literature, $CsPbI_3$ and $CsPbBr_3$ crystallize in various possible configurations depending on the temperature. The iodine-based compound is cubic (α) at high temperatures (above 310°C) and turns into tetragonal (β), ordered (γ) and disordered (δ) orthorhombic phases successively when temperature decreases [75]. Its bromine-based counterpart evolves from cubic (above 130°C) to tetragonal (β) and then to orthorhombic (γ) phase [206].

The occurrence of this specific phase in the degraded film may be too low to be detected by XRD measurements, which is why we did not observe diffraction peaks at $2\theta = 10°$ or 15° as expected for such orthorhombic or cubic structures [263].

To determine the crystallographic nature of the $CsPb(I_{0.9}Br_{0.1})_3$ and the $CsPb_2(I_{0.7}Br_{0.3})_5$ needles, we performed Selected Area Electron Diffraction (SAED) (described in the appendix 5.4) in a TEM on the same specimens prepared by FIB milling. The resulting diffraction patterns are displayed in Figure 4.10(a) and (c).

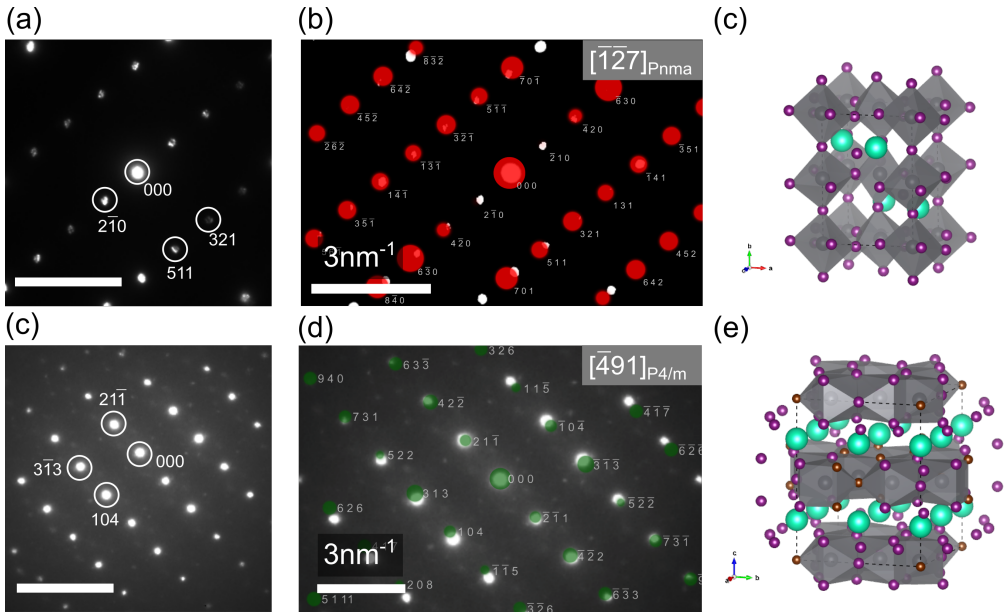

Figure 4.10: *(a,d) Electron diffraction patterns obtained via SAED measurements performed on the same lamellae displayed in Figure 4.9(a) and (b). (b,e) Simulated electron diffraction patterns overlayed on experimental diffraction patterns. (c,f) "Balls and sticks" sketches of the simulated structures. The indexation shows that needle $CsPb(I_{0.9}Br_{0.1})_3$ diffraction pattern is oriented along the* $[1\bar{2}\bar{7}]$ *zone axis and needle $CsPb_2(I_{0.7}Br_{0.3})_5$ along the* $[\bar{4}91]$ *zone axis.*

The presence of spots instead of rings suggests that the samples are composed of a single monocrystal. These spots correspond to reflections of the impinging electrons with the lattice planes.

To properly identify the crystallographic nature of the $CsPb(I_{0.9}Br_{0.1})_3$ specimen, the corresponding structures (cubic, orthorhombic ordered and disordered, triclinic, and tetragonal) were simulated by Dr. P. Baranek using a similar DFT-based method as mentioned in Chapter 3 for $CsPbBr_3$ phases. Table 6 summarizes the space group and the lattice parameters considered for each simulated structures. For each structure, the bandgap is also calculated and indicated in Table 4.3.

These structures were then used to simulate electron diffraction patterns in multiple crystalline orientations to fit the experimental data. Figure 4.10(b) shows the simulation results obtained with *Pnma* structure (orthorhombic disordered) overlayed with the experimental diffraction pattern. The orientation of the simulated structures and the deviation between simulation and experiment expressed as the "sum-of-square error" (Σs^2 in mm^2) are displayed in Table 4.3. The best fit (with the lowest Σs^2 value) is obtained with the cubic structure ($Pm\bar{3}m$), but the diffraction patterns of the ordered and disordered orthorhombic structures are also matching well the experimental pattern. SAED is a technique that can produce similar diffraction patterns for distinct crystalline structures and orientations [162]. Hence, the accurate discrimination between the presumed symmetries of $CsPb(I_{0.9}Br_{0.1})_3$ would require complementary structural measurements or additional calibration of the SAED measurement.

A similar protocol is carried out for the $CsPb_2(I_{0.7}Br_{0.3})_5$. The tetragonal structure of $CsPb_2(I_{0.7}Br_{0.3})_5$ ($P4/m$), $CsPb_2I_5$ ($I4/mmc$), and $CsPb_2Br_5$ ($I4/mmc$) phases have been simulated by DFT and their bandgap was estimated, as shown in Table 4.3. The simulation of electron diffraction patterns from the $CsPb_2(I_{0.7}Br_{0.3})_5$ phase is compared to the experimental diffraction pattern in Figure 4.10(e). The tetragonal $CsPb_2(I_{0.7}Br_{0.3})_5$ matches well the experi-

mental data with less than 0.51 mm^2 Σs^2 error . The needle tetragonality is further supported by the emergence of a similar phase in the XRD diffraction patterns shown in Figure 4.4. We can therefore ascribe the appearance of the tetragonal phase in aged CsMAFA perovskite to the formation of such needles. Microscopic investigation of the aged films strengthens results obtained via macroscopic measurements.

Table 4.3: *Table summarizing the space group and the calculated bandgaps at 300 K considered for each structure simulated. The fitting error with experimental data is indicated in mm^2*

Compounds	Space group	Bandgaps	Σs^2 error (mm^2)
$CsPbI_3$	$Pm\bar{3}m$	1.61	8.9
$CsPb(I_{0.9}Br_{0.1})_3$	$Pm\bar{3}m$	2.06	0.3
	$P4mm$	2.15	1.55
	$P\bar{1}$	2.26	1.38
	$Pnma$ ord.	2.18	0.89
	$Pnma$ disord.	3.49	0.77
$CsPbBr_3$	$Pm\bar{3}m$	2.20	97.03
$CsPb_2I_5$	$I4/mcm$	2.83	1.21
$CsPb_2(I_{0.7}Br_{0.3})_5$	$P4/m$	2.99	0.371
	$P11m$	2.99	0.265
$CsPb_2Br_5$	$I4/mcm$	3.98	1.30

4.3.3 Optical analysis of the needles

To investigate their optoelectronic properties, we performed CL measurements on the same $CsPb(I_{0.9}Br_{0.1})_3$ and $CsPb_2(I_{0.7}Br_{0.3})_5$ needles as those described in Figure 4.8. Results are presented in the following Subsection.

Focus on the $CsPbX_3$ needle

Figure 4.11(a) and (b) presents an SEM image of the needle analyzed and the corresponding spatially averaged CL signal (in the red-square) where four optical transitions are present: a peak at 1.65 eV assigned to the remaining perovskite phase, one at 2.41 eV corresponding to PbI_2 emission, and finally, two peaks at 2.71 and 2.25 eV. We use four Gaussian functions to decompose the spectrum.

To localize the source of these emissions we integrate the luminescence on the following spectral ranges: 2.71±0.09 eV, 2.23±0.06 eV, 2.41±0.05 eV, and 1.6±0.01 eV. The integrated luminescence are normalized on each pixel by the maximum value of the map and the obtained filtered CL maps are plotted in Figure 4.11(c). The needle is emitting luminescence in the two first filtered CL maps, suggesting that the two peaks at 2.71 and 2.25 eV in the spectrum may be attributed to the $CsPb(I_{0.9}Br_{0.1})_3$ phase. However, the first filtered map shows that the FTO layer beneath the needle also emits in this spectral range (blue arrow). The CL peak at 2.71 eV may thus originate from both the needle and the FTO. The CL signal was averaged on 100 pixels in this region (25 x 4) as shown in Figure 33. The CL spectrum shows the CL peak at 2.71 eV, which confirms previous hypothesis.

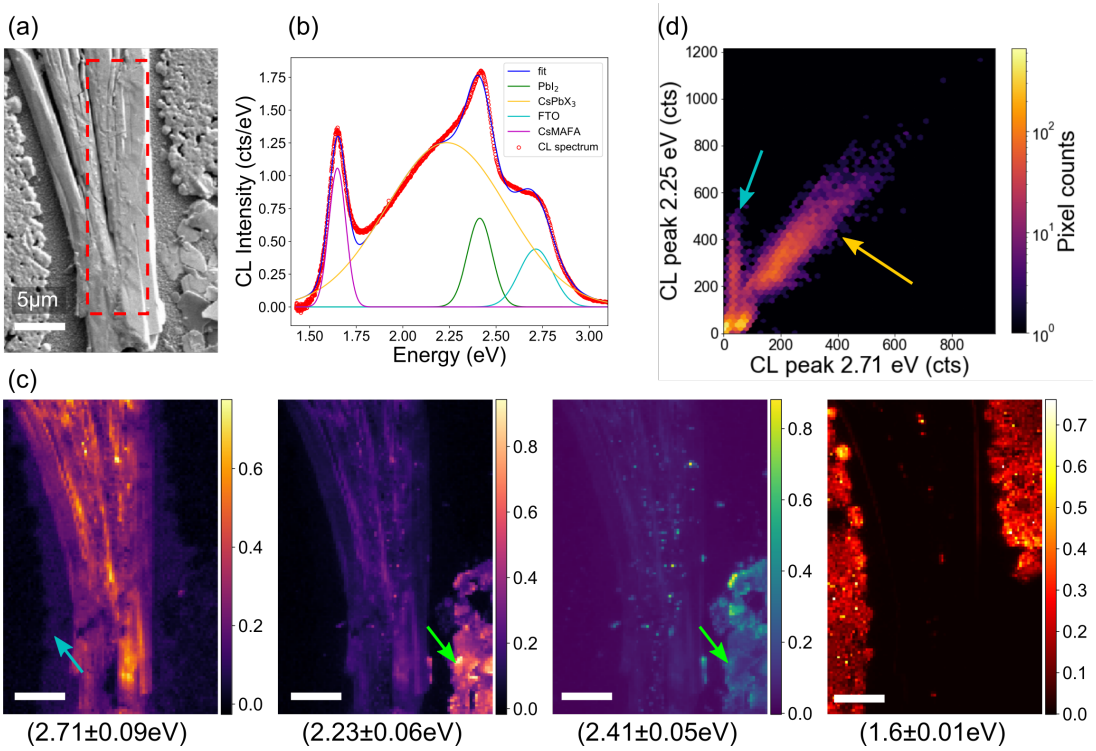

Figure 4.11: *(a) SEM image of the $CsPb(I_{0.9}Br_{0.1})_3$ needle analyzed. (b) Spatially averaged CL spectra in the needle presented in (a). The CL spectrum is fitted with four Gaussian functions corresponding to contributions at 1.65 (in purple), 2.25 (in yellow), 2.41 (in green), and 2.71 eV (in blue), respectively. (b) CL maps with false colors showing the luminescence integrated over four different spectral regions: [2.62 eV, 2.8eV], [2.17 eV, 2.29 eV], [2.36 eV, 2.46 eV], and [1.59 eV, 1.61 eV]. The three latter corresponds to the emission of $CsPb(I_{0.9}Br_{0.1})_3$, the PbI_2 phase, and the CsMAFA perovskite respectively. For each pixel, the integrated intensity of each band is normalized by the maximum. (d) 2D histogram of the intensity of 2.25 and 2.71 eV peaks.*

The integrated luminescence maps on these two spectral ranges were then compared in a 2D histogram as shown in Figure 4.11(d). The results suggest that the CL peaks at 2.71 and 2.25 eV are correlated in many pixels of the CL map as indicated by the yellow arrow, which corresponds to the $CsPb(I_{0.9}Br_{0.1})_3$ phase. Pixels indicated by the blue arrow only emit at 2.71 eV and correspond to the FTO.

The PbI_2 hexagons present in the bottom-right corner of the map (indicated by green arrows) are emitting in the second filtered CL map due to the broadness of their CL peak localized at 2.41 eV. Small clusters are emitting in the needle in the third filtered CL map.

Table 4.3 lists calculated values of the bandgap of $CsPb(I_{0.9}Br_{0.1})_3$ perovskite according to the different crystallographic structures that can be formed. The cubic $CsPbI_3$ and $CsPbBr_3$ are also added for comparison purposes. Given the high injection condition in CL acquisitions, previous studies have considered that CL peak position corresponds to the bandgap of the material analyzed [171]. We therefore venture to compare the position of the CL peak with the calculated bandgaps. We consider the CL peak at 2.25 eV for the comparison. The triclinic ($P\bar{1}$) symmetry of $CsPb(I_{0.9}Br_{0.1})_3$ with a bandgap of 2.26 eV is the closest to the CL peak followed by the tetragonal ($P4mm$) and the ordered orthorhombic ($Pnma$) symmetries with a bandgap of 2.15 and 2.18 eV, respectively. Conversely, the indexing of electron diffraction patterns showed a better match with the ordered orthorhombic symmetry than with triclinic and tetragonal. We thus propose that the $CsPb(I_{0.9}Br_{0.1})_3$ phase crystallized in the orthorhombic ordered crystal

system ($Pnma$).

We then performed cryogenic CL measurements to analyze the evolution of optoelectronics properties as the temperature of the sample decreases. Figure 4.12 shows the spatially averaged CL spectra normalized for various temperatures ranging from 300 K down to 30 K.

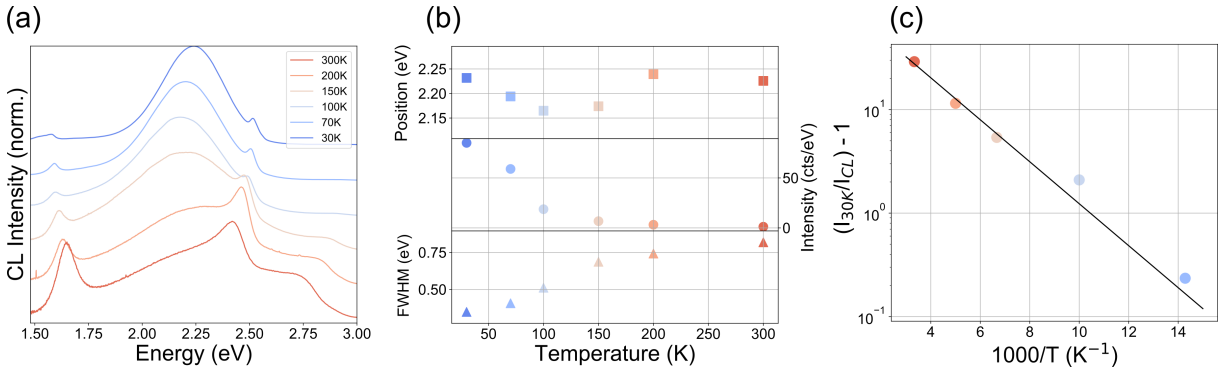

Figure 4.12: *(a) Spatially averaged CL spectra in the $CsPb(I_{0.9}Br_{0.1})_3$ needle presented in Figure 4.11(a) at 300, 200, 150, 100, 70, and 30 K. (b) The position, the intensity, and the FWHM of the emission peak position from $CsPb(I_{0.9}Br_{0.1})_3$ (2.25 eV at 300 K) as a function of temperature. (c) $(I_{30K}I_T) - 1$ as a function of 1000/T, with I_T the integrated CL peak intensity at T.*

The evolution of the position, the intensity, and the linewidth (FWHM) of the CL peak at 2.25 eV are plotted as a function of temperature in Figure 4.12(b).

As the temperature decreases, the CL peak intensity increases, suggesting that the associated radiative recombination process is facilitated at lower temperatures. This evolution may be attributed to the suppression of non-radiative recombination processes that quenched the emission at ambient temperature, as mentioned in Chapter 3.

Then, the FWHM of the CL peak decreases with decreasing temperature, which may be due to the reduced interactions between the generated carriers and phonons [228].

Finally, the position of the CL peak exhibits a non-monotonic evolution between 2.15 and 2.25 eV. This evolution of the emission may result from the interplay of the contributions from thermal lattice shrinkage, which induces a shrinkage of the bandgap, and phase transitions, that occur with decreasing temperature [235].

Similarly to our analysis of the emission of the $CsPbBr_3$ sample in Chapter 3, we aim to estimate the activation energy of the non-radiative recombination process that quenches the CL peak of the needle at ambient temperature. The inverse of the integrated CL peak was then plotted as a function of temperature and fitted with an Arrhenius law (see Figure 4.12(c)).

There is a good agreement between the data and the fit, suggesting that the evolution of the CL peak is dictated by a thermally activated process. Its activation energy was estimated at 40 meV, which is comparable to the value of 60 meV reported by Yi et al. on $CsPbI_3$ nanocrystals [240]. However, as mentioned in Chapter 3, the correspondence between the activation energy determined by temperature-dependent luminescence measurements and the exciton binding energy is dubious [36]. It is even more questionable for the $CsPb(I_{0.9}Br_{0.1})_3$ needle, which may have undergone a phase transition at low temperatures.

These findings provide more direct evidence that strengthen our hypothesis on the composition of the needle as it exhibits similar temperature dependence to that of $CsPbX_3$ phases reported in previous studies [228, 234, 239, 240].

Focus on the $CsPb_2(I_{0.7}Br_{0.3})_5$ needle

Figures 4.13(a) and (b) show the SEM image of the $CsPb_2(I_{0.7}Br_{0.3})_5$ needle and the corresponding spatially averaged CL spectrum in the blue-dashed square. Three CL peaks are present: a broadband peak around 1.70 eV, a narrow green emission peak at 2.45 eV, and a low-intensity peak around 2.71 eV. The CL spectrum is fitted with three Gaussian functions and a relatively large offset representing the background signal. The latter is significant due to the overall low intensity of the CL spectrum.

Figure 4.13(b) presents CL maps filtered on the following spectral ranges: 1.6±0.01 eV, 2.41±0.05 eV, and 2.71±0.09 eV.

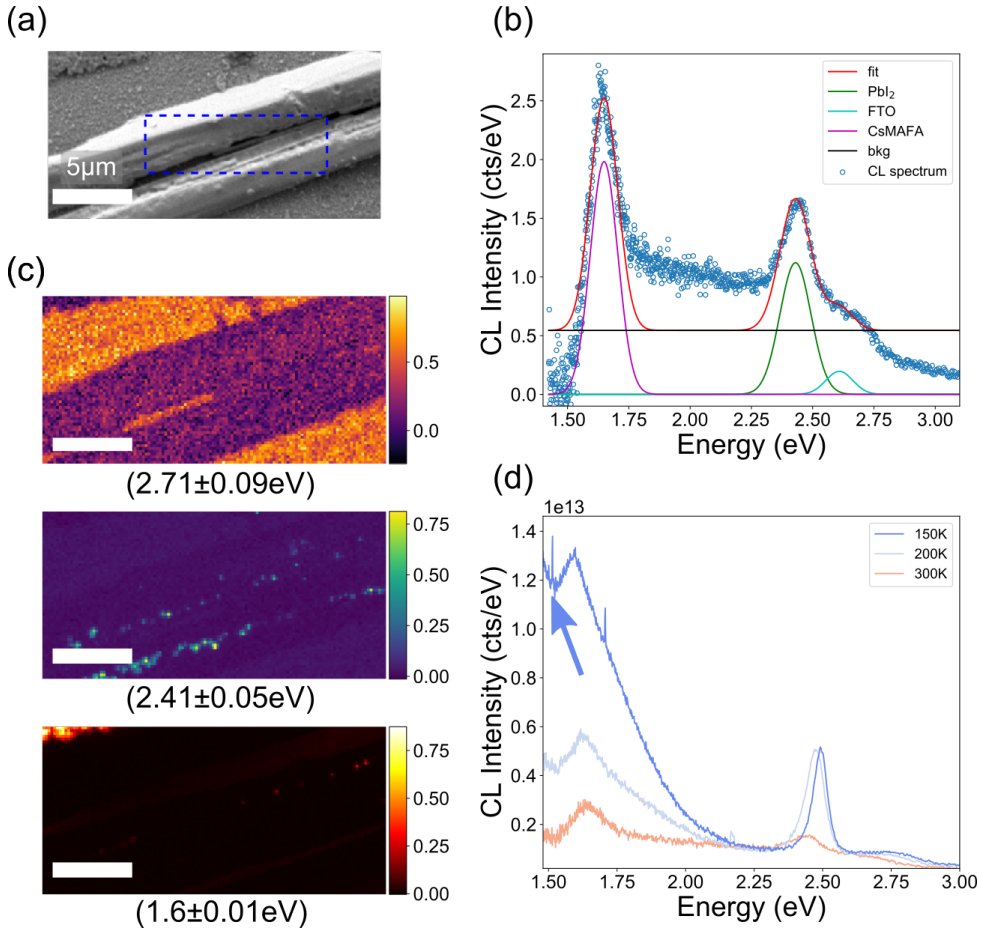

Figure 4.13: *(a) SEM image of the analyzed $CsPb_2(I_{0.7}Br_{0.3})_5$ needle. (b) CL maps with false colors showing the luminescence integrated over three different spectral regions: [2.62 eV, 2.8 eV], [2.36 eV, 2.46 eV], and [1.59 eV, 1.61 eV] corresponding to the emission of the FTO, the PbI_2, and the CsMAFA perovskite, respectively. For each pixel, the integrated intensity of each band is normalized by the maximum. (c) Spatially averaged CL spectra in the needle presented in (a). CL spectrum is fitted with three Gaussian functions corresponding to CsMAFA (in purple), FTO (in light blue), and PbI_2 (in green) contributions at 1.68, 2.41, and 2.71 eV, respectively. (d) CL spectra acquired at 300, 200, and 150 K.*

Regardless of the filtered CL map, the needle does not emit, suggesting that none of the CL peaks mentioned can be related to the degradation product itself. The CL peaks at 1.70 and 2.45 eV are mainly due to small particles, which can be attributed to residual CsMAFA perovskite (that did not fully decompose during aging) and PbI_2 clusters, respectively (see Figure 4.13(c)). As previously observed, the CL peak positioned at 2.71 eV originates from the FTO below the needle.

These observations show that the two needles considered exhibit very distinct optoelectronic

properties further supporting the assumption of distinct phases.

The correlation between XRD, EDS, and SAED results leads us to speculate the formation of $CsPb_2(I_{0.7}Br_{0.3})_5$. However, we could not find any specific optical emission originating from this phase, and it is worth noting that the luminescence of $CsPb_2Br_5$ is still under debate in the literature (see Chapter 3) [248].

The optical properties of this specimen have been further investigated with cryo-CL measurements. The spatially averaged CL spectra at 300, 200 and 150 K are displayed in Figure 4.13(d). The intensity of PbI_2 and CsMAFA perovskite CL peak (at 2.45 and 1.71 eV) increases as the temperature decreases as expected. Notably, the CL signal below 1.5 eV (indicated by a blue arrow) increases as well suggesting the presence of an emission peak at lower energy.

Motivated by this observation, we performed new CL acquisitions between 1.2 eV and 1.8 eV. The measurements were conducted on another needle-like structure showing the same CL signal at room temperature (see SEM image in Figure 4.14(a)). The CL spectra at 200, 150, 100, 70, and 35 K are displayed in Figure 4.14(b). Three CL peaks are present and their intensities increase as temperature decreases. They are positioned at 1.6, 1.55, and 1.3 eV. The former two might be related to the remaining CsMAFA perovskite, while the latter, which is rather broad even at low temperature, must originate from the needle. If we assume that this broad peak originates from band-to-band recombination, its energy suggests that the needle bandgap is close to 1.30 eV. This observation contradicts with the bandgap calculated for the tetragonal $CsPb_2(I_{0.7}Br_{0.3})_5$ phase at 2.99 eV.

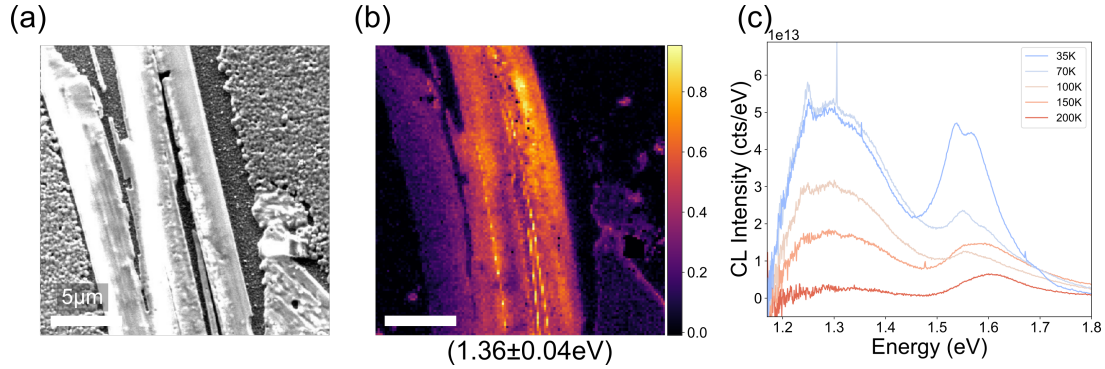

Figure 4.14: *(a) SEM image of the analyzed $CsPb_2(I_{0.7}Br_{0.3})_5$ needle. (b) CL map with false colors showing the luminescence integrated over the spectral region [1.32 eV, 1.4 eV] (normalized by the maximum integrated intensity in the map). (c) Spatially averaged CL spectra in the $CsPb_2(I_{0.7}Br_{0.3})_5$ needle presented in (a) at 200, 150, 100, 70, and 35 K.*

The results of our calculations, displayed in Table 4.3, indicate that $CsPb_2Br_5$ exhibits an indirect bandgap of up to 3.98 eV. However, several experimental studies have reported absorption and emission spectra (obtained by UV-vis and PL spectroscopy) with an optical transition at 2.35 eV [259, 261], which conflicts with this theoretical bandgap. The same discrepancy is observed for the $CsPb_2I_5$ phase, for which we estimated the bandgap at 2.83 eV, while PL peaks were observed at 1.8 eV in the literature [244].

Theoretical and experimental bandgaps found in the literature are thus quite distinct, which is consistent with our observations. However, we expected the $CsPb_2(I_{0.7}Br_{0.3})_5$ perovskite to have a CL emission peak at a higher energy than that reported for $CsPb_2I_5$. Further experimental analysis would be required to fully understand this discrepancy.

The origin of this CL peak remains unclear but these results still provide material for the study of the luminescence of these cesium-based materials, which are currently widely investigated [243, 264].

4.3.4 Analysis of the "flower"

The degradation product referred to as the "flower," shown in Figures 4.2 and 4.3(6), was then analyzed. Figures 4.15(a) and (b) display an SEM image of the degradation product along with Cs, I, and Br elemental maps obtained through SEM-EDS. I and Br maps are superimposed in the last image.

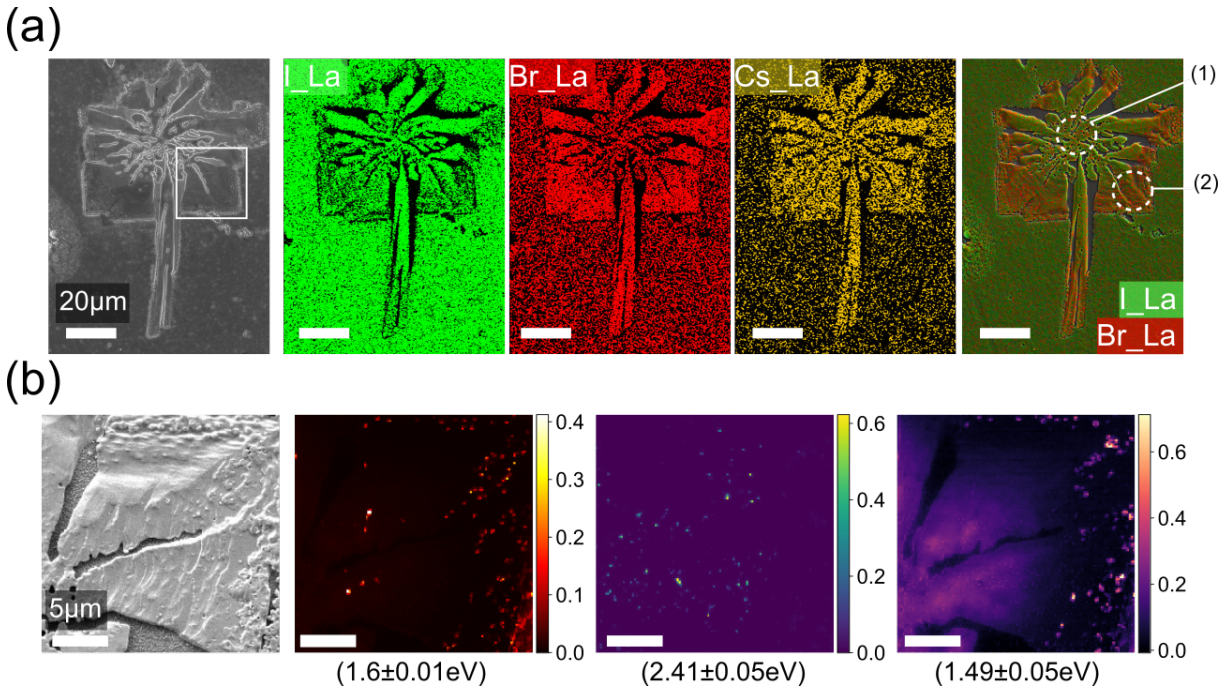

Figure 4.15: *Flower feature : (a) SEM image of the flower analyzed and corresponding I, Br, and Cs elemental maps obtained by SEM-EDS. (b) SEM image of the region of the flower analyzed with CL and corresponding CL maps with false colors showing the luminescence integrated over three the spectral regions: [1.59 eV, 1.61 eV], [2.17 eV, 2.29 eV], and [1.44 eV, 1.54 eV].*

The Cs elemental map suggests that the flower has a higher Cs content compared to the surrounding perovskite film, similar to the observation made for the needles. In addition, the I/Br map indicates that the center of the flower has a higher I content than the edges, which are enriched in Br.

The composition was estimated in two distinct regions indicated in the I/Br elemental map by circles. The results, summarized in Table 4.4, suggest that the flower is composed of $CsPb_2(I_xBr_{1-x})_5$, similar to the second needle studied, with an I/Br ratio that varies depending on the region probed.

CL was then performed in the area indicated in Figure 4.15(a). The SEM image of the area analyzed and filtered CL maps are presented in (c) and (d), respectively. The perovskite emission, shown in the first map, is localized in the edges of the degradation product in the form of small clusters. PbI_2, shown in the second map, is also localized in small clusters but is

present throughout the flower. The third filter map shows that the center of the flower exhibits higher emission compared to the edges. This observation suggests that the I-rich regions are more prone to emit than the Br-rich regions.

The CL spectrum averaged over the degradation product has the same shape as that of the $CsPb_2(I_{0.7}Br_{0.3})_5$ needle (see Figure 30). These degradation products demonstrate the same optoelectronic response at room temperature and low temperatures. Given the feature size and its peculiar shape, the flower might be the following stage of the second needle-like degradation product. A direct observation of the needle "blooming" into a "flower" might be required to confirm this hypothesis.

Table 4.4: *Results of the quantification of the composition in Cs, I, Br and Pb obtained via SEM-EDS measurements on two regions of the flower displayed in Figure 4.15(a).*

Feature	I/Pb	Br/Pb	Cs/Pb	Composition
(1)	2.11±0.24	0.60±0.11	0.57±0.10	$CsPb_2(I_{0.8}Br_{0.2})_5$
(2)	1.87±0.23	0.81±0.14	0.58±0.11	$CsPb_2(I_{0.7}Br_{0.3})_5$

4.4 Discussion and proposed degradation mechanisms

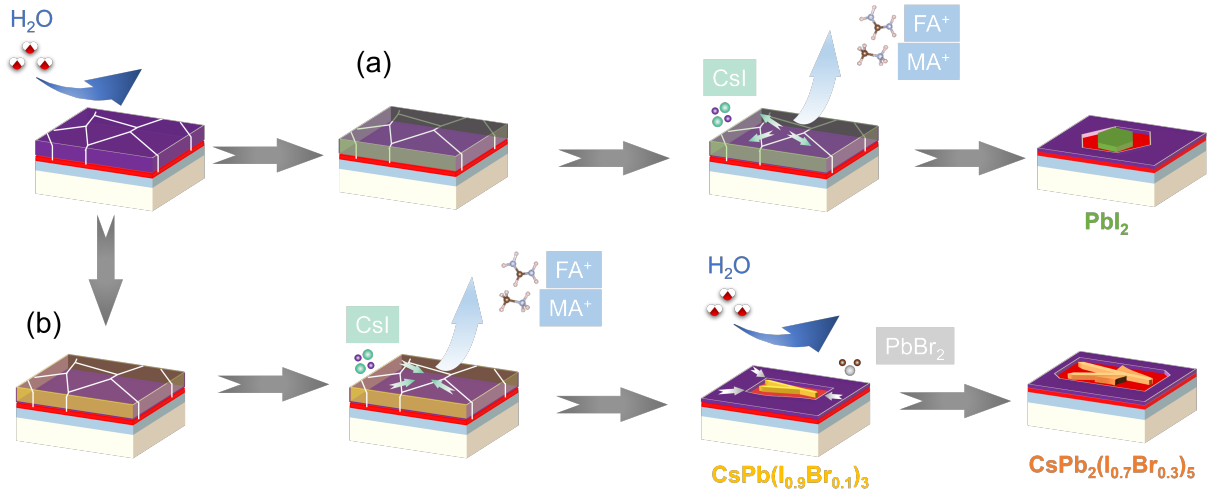

Figure 4.16: *Decomposition mechanisms proposed for the CsMAFA perovskite film under high relative humidity. Water molecules increase the mobility of ions, leading to the demixing of the CsMAFA film. Two distinct degradation mechanisms are proposed starting with this demixed film. (a) Organic cations and halides volatilize in the form of MAI → MA↑ + HI↑ (or FAI → FA↑ + HI↑). Cs+ cations migrate towards the surrounding film leaving behind PbI_2, forming hexagonal degradation products. (b) The same volatile species are extracted from the material leaving the remaining elements form $CsPb(I_{0.9}Br_{0.1})_3$ needles. Upon further moist air exposure, the latter grows into larger $CsPb_2(I_{0.7}Br_{0.3})_5$ needles by reacting with decomposition products, i.e., PbI_2 and $PbBr_2$, from surrounding material.*

Our observations show that a CsMAFA film irreversibly transforms into various degradation products with distinct geometries and compositions upon exposure to high relative humidity levels. Based on our results, we propose degradation pathways of the CsMAFA perovskite film under moist air starting with a phase segregation. With increased humidity level, the ionic species become more mobile [217]. Halides migrate, which leads to the formation of I-rich and Br-rich regions in the film. The appearance of these regions is consistent with the red-shift

observed in PL emission in Section 4.1.3. A-site cations can also migrate, but at a much slower time scale, and their migration leads to the formation of Cs-rich, FA-rich, and MA-rich regions. Cation migration has been verified in mixed-cation perovskite films exposed to voltage bias, illumination, or heat [98, 102, 265]. Although no study explicitly reports that moisture favors cation migration, it increases the concentration of defects which promotes ion migration [265]. The unbalanced local concentration in halides and cations leads to a complete demixing into purely inorganic and organic perovskites such as $CsPbX_3$ and $FA_{1-y}MA_yPbX_3$, respectively [266].

Prolonged humidity exposure enables organic A-site cations (FA^+ and MA^+) to volatilize following a redox reaction. According to Long et al., FA^+ cations have a stronger bond with Br^- ions than with I^- ions due to the larger electronegativity of Br^- ions [267]. They also showed that FA^+ cations volatilize preferentially with Br^- ions at temperatures above 250°C. In addition, Tan et al. have reported that CsMAFA perovskite films sequentially release MA+ and FA+ during annealing at 150°C in air with 60% RH [268]. We can then assume that our CsMAFA perovskite decomposition in humid air follows the same sequential pathway where MA+ volatilize with I^-, followed by FA^+ with Br^-, and finally the remaining FA^+ with I^-, leaving Pb^{2+} and I^- to form hexagonal PbI_2 crystals. This process is summarized in the reaction 4.1 and schematically represented in Figure 4.16(a).

$$\begin{aligned} Cs_{0.05}(MA_{0.15}FA_{0.85})_{0.95}Pb(I_{0.84}Br_{0.16})_3(s) \xrightarrow{H_2O} PbI_2(s) + 0.1425 \times MAI(g) \\ +0.3775 \times FAI(g) + 0.43 \times FABr(g) + 0.05 \times CsBr(s) \end{aligned} \quad (4.1)$$

The formation pathway of $CsPb(I_{0.9}Br_{0.1})_3$ needle is initiated in Cs-rich regions of demixed CsMAFA perovskite, and is illustrated in Figure 4.16(b). As described previously, it starts with the organic cations volatilizing with halides from the film exposed to humid air. However, depending on the composition of the segregated region in I and Cs, the number of reaction byproducts such as PbI_2 varies. Although in this study the exact quantities of byproducts could not be determined, we can still propose the reaction 4.2 as a hypothetic degradation pathway based on pristine CsMAFA perovskite.

$$\begin{aligned} 20 \times Cs_{0.05}(MA_{0.15}FA_{0.85})_{0.95}Pb(I_{0.84}Br_{0.16})_3(s) \xrightarrow{H_2O} CsPb(I_{0.9}Br_{0.1})_3(s) + 19 \times PbI_2(s) \\ +2.85 \times MAI(g) + 6.85 \times FAI(g) + 9.3 \times FABr(g) \end{aligned} \quad (4.2)$$

Notably, PbI_2 formation displayed in reaction 4.1 could provide Cs^+ cations as reagents of the reaction 4.2, allowing the two to act together. Such concomitant reactions require a high diffusion coefficient of Cs+ cations to allow their migration through the film. This coefficient is related to the activation energy barriers, which in turn depends on the material and its environmental conditions. Water molecules and oxygen are known to decrease such activation barriers through defect fabrication [109, 217] and therefore Cs^+ cations could migrate sufficiently far in the film. A real-time observation of the formation of PbI_2 hexagons and the successive appearance of $CsPb(I_{0.9}Br_{0.1})_3$ needles could ultimately confirm our hypothesis.

Regarding $CsPb_2(I_{0.7}Br_{0.3})_5$, it has been shown in several publications [211, 212, 217, 222, 269] that $CsPbBr_3$ turns into $CsPb_2Br_5$ when exposed to moisture. According to Turedi et al. [269], this reaction occurs first through a complete decomposition of $CsPbBr_3$ into $PbBr_2$, Cs^+, and Br^-. The enrichment in $PbBr_2$ coupled with water molecules then gathers all the conditions to finally crystallize residual $CsPbBr_3$ in tetragonal $CsPb_2Br_5$. Conversely, Liu et

al. claimed that $CsPbBr_3$ transformation happens by losing CsBr through the action of water molecules [222]. Given these two mechanisms, we highly suspect that $CsPb(I_{0.9}Br_{0.1})_3$ needles transform into $CsPb_2(I_{0.7}Br_{0.3})_5$ needles during aging, as illustrated in Figure 4.16(b). Their morphological similarity and the scarcity of $CsPb(I_{0.9}Br_{0.1})_3$ needles in aged film of more than 1 hour support this hypothesis.

Drawing from the reasoning of Liu et al., we propose the hypothetical chemical reaction 4.3 where $CsPb(I_{0.9}Br_{0.1})_3$ loses Cs and I content, accompanied by PbI_2 formation. However, if we compare the size of the needles, we can see that $CsPb(I_{0.9}Br_{0.1})_3$ needles are smaller and thinner than $CsPb_2(I_{0.7}Br_{0.3})_5$ needles (see Figures 4.3). As the density of these compounds are relatively close ($\rho(CsPb(I_{0.9}Br_{0.1})_3)/\ \rho(CsPb_2(I_{0.7}Br_{0.3})_5) \approx 0.9$), it is unlikely that losing material is the route followed during formation of the $CsPb_2(I_{0.7}Br_{0.3})_5$ needles.

$$5 \times CsPb(I_{0.9}Br_{0.1})_3(s) \xrightarrow{H_2O} CsPb_2(I_{0.7}Br_{0.3})_5(s) + 3 \times PbI_2(s) + 4 \times CsI(s) \tag{4.3}$$

The chemical reaction 4.4 presents the pathway proposed by Turedi et al. where the $CsPb_2(I_{0.7}Br_{0.3})_5$ needle forms by adding $PbBr_2$, and PbI_2 to a $CsPb(I_{0.9}Br_{0.1})_3$ needle. We assume that these are coming from the decomposition of pristine CsMAFA described in reaction 4.5.

$$CsPb(I_{0.9}Br_{0.1})_3(s) + 0.4 \times PbI_2(s) + 0.6 \times PbBr_2(s) \xrightarrow{H_2O} CsPb_2(I_{0.7}Br_{0.3})_5(s) \tag{4.4}$$

$$\begin{aligned} 2.5 * Cs_{0.05}(MA_{0.15}FA_{0.85})_{0.95}Pb(I_{0.84}Br_{0.16})_3(s) \xrightarrow{H_2O}\ & 0.4 \times PbI_2(s) + 0.6 \times PbBr_2(s) \\ & + 1.5 \times PbI_2(s) + 0.125 \times CsI(s) + 0.33625 \times MAI(g) + 2.01875 \times FAI(g) \end{aligned} \tag{4.5}$$

This mechanism is the most plausible, considering the size of needles. The edges of the $CsPb(I_{0.9}Br_{0.1})_3$ needle in Figure 4.3(4) are positioned under the surrounding film which support the hypothesis that needles grow by consuming decomposition products of the surrounding film.

The emergence of different degradation products may lie in the compositional heterogeneity in the pristine thin film. In their recent contribution, Nishida et al. ascribed local preferential degradations to cation inhomogeneities in the perovskite film [255]. Therefore, further measurements sensitive to these heterogeneities on the pristine film should be implemented in future studies.

The decrease of PbI_2 reflections in XRD diffractograms (see Figure 4.4(b)) coincides with the appearance of voids instead of PbI_2 hexagons after a few hours of aging (see Figure 4.2(d)), suggesting that PbI_2 is further decomposed. PbI_2 is known to decompose into metallic lead Pb^0 and I_2 with light [270] or lead salts such as PbO, $Pb(OH)_2$, or $PbCO_3$ in humid air [121]. Metallic Pb^0 is considered as a catalyst of hybrid perovskite decomposition. Therefore, degradation of hexagons might promote the overall decomposition of the thin film.

In addition, we observe that native PbI_2 clusters are absent in the surrounding of degradation products (see Figure 4.3), indicating that they disappeared during the aging process. While describing the degradation product formation, the role of native PbI_2 clusters as reagents of the reaction was not considered. Lately, several published studies showed that clusters could dramatically affect perovskite integrity and, thus, solar cell stability [270–272]. Through decomposition, native PbI_2 clusters might be promoting the CsMAFA perovskite phase degradation.

Consequently, further studies should also account for the effect of PbI_2 clusters on the parent perovskite film exposed to air with high relative humidity.

4.5 Aging with other stress factors

The stability of CsMAFA perovskite has been investigated under different stress factors than moist air. The same approach as before was used, which consists in analyzing CsMAFA-based half cells after the aging procedure. The results are presented in this Section.

4.5.1 Humidity and light

The experimental setup described in Section 4.1 was used to expose CsMAFA-based half-cells to air with a controlled relative humidity of 55% and a 1-sun illumination (1000 mW/cm² AM 1.5G spectrum), which was provided by a sun simulator. The temperature during the exposure was not controlled, but was measured at 40°C under the sun simulator

The morphology of the perovskite film was observed using a confocal microscope after 30 and 60 minutes of exposure. Comparisons were also made with samples aged in the same atmosphere (air with 55% RH) in the dark at room temperature. Images of the samples are shown in Figure 4.17.

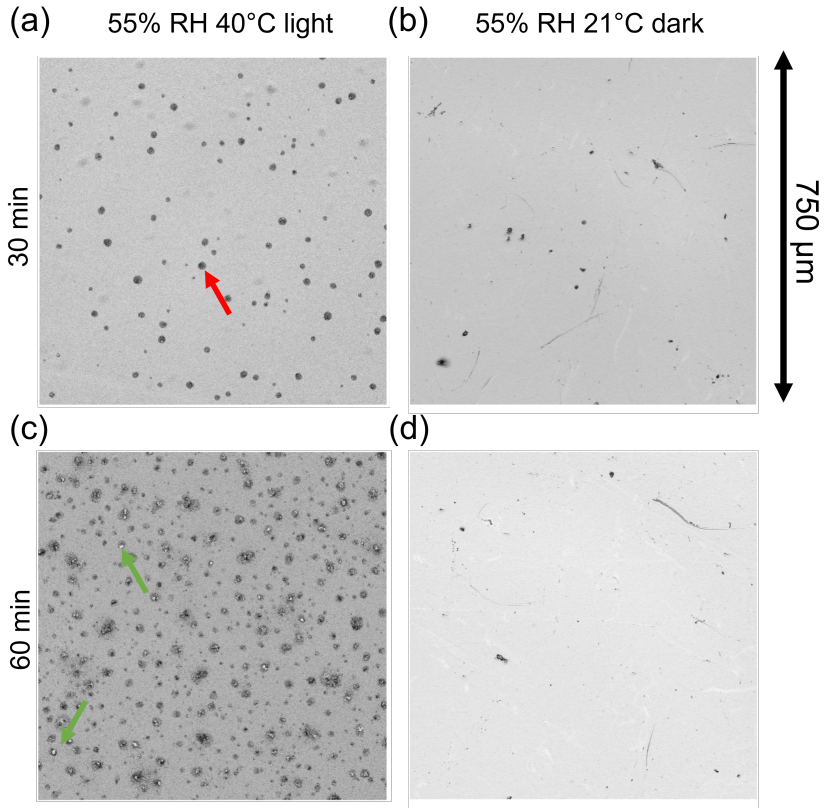

Figure 4.17: *(a,c) Images of a CsMAFA perovskite film after 30 and 60 minutes under AM 1.5G illumination, oxygen, and 55% RH. (b,d) Images of a CsMAFA perovskite film after 30 and 60 minutes in dark, oxygen, and 55% RH.*

Figure 4.17(a) and (c) show small heterogeneities, indicating that the perovskite film has been damaged. After 60 minutes, the sample exhibits degradation products that may correspond to

the hexagon and disc-like degradation products analyzed previously, indicated by green and red arrows, respectively.

In contrast, the sample in the dark at room temperature does not show any sign of degradation. The air with 55% relative humidity may not have been enough to damage the perovskite film in 60 minutes. This observation suggests that light, temperature, or both may have contributed to accelerate degradation of the perovskite film in the other sample.

As previously discussed in Chapter 1, temperatures lower than 50°C are unlikely to cause degradation in perovskite materials. It is possible that the combination of light and other stress factors played a role in the observed degradation in this case. Further comparative studies are necessary to fully understand the role of these factors on perovskite degradation.

4.5.2 Humidity and nitrogen

A separate study was conducted to examine the effects of oxygen on the morphology of CsMAFA perovskite. The samples were aged in a high humidity (85%) atmosphere using N_2 as humidity carrier gas, which allowed for the removal of oxygen as a stress factor.

The aging was performed at room-temperature and in the dark for 15 hours. The film morphology was then inspected with SEM and the obtained images are displayed in Figure 4.18. Figures 28 show SEM images of a CsMAFA film from the same batch, aged in air at 85% RH, where we observe the specific needles previously studied.

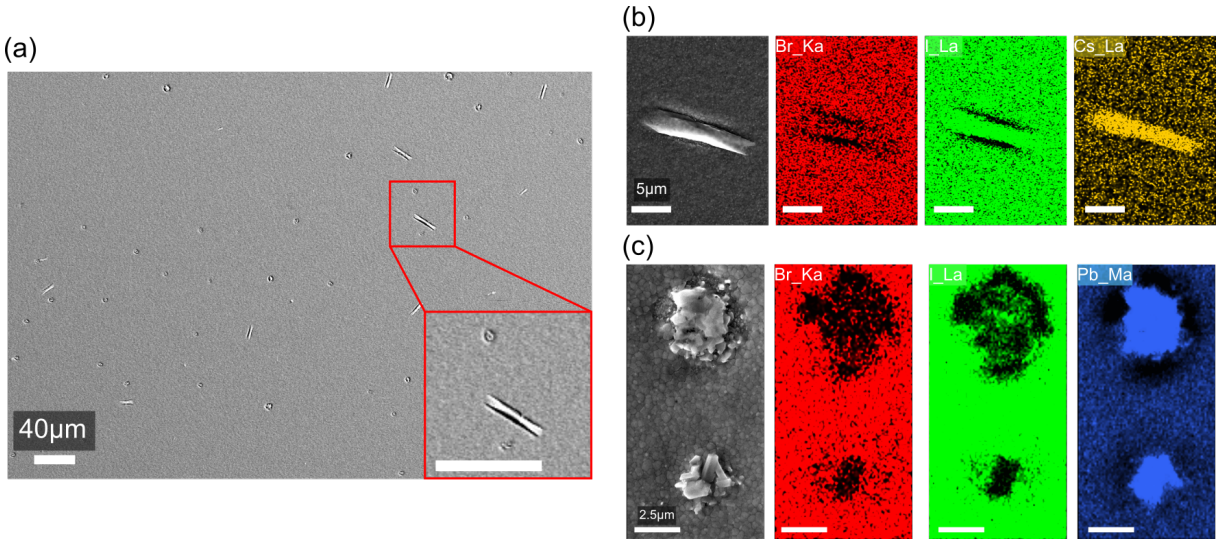

Figure 4.18: *(a) SEM image of a CsMAFA perovskite film after 14 hours of aging in dark, under an atmosphere of N_2 and 85% RH. (b,c) SEM images of the degradation products observed in the film after the aging process and corresponding elemental maps obtained by SEM-EDS.*

The SEM image of the perovskite film after aging in N_2 atmosphere reveals heterogeneities with a size of approximately 15 μm that are distant on the surface of the film. This suggests that the film has not been significantly damaged by the aging process, in contrast to the results obtained in the presence of oxygen and high relative humidity.

Further investigation of the observed heterogeneities, which are suspected to be perovskite degradation products, was conducted using SEM-EDS at higher magnification. Figures 4.18(b)

and (c) show SEM images and corresponding elemental maps of a needle-like and a round structure.

The needle-like structure exhibits the same element distribution as the $CsPb(I_{0.9}Br_{0.1})_3$ needles studied previously, with higher levels of Cs and I compared to the surrounding film. This is further confirmed by the estimated composition of this region, as summarized in Table 4.5. The size of the degradation product suggests that it is in the early stages of formation and would have grown if the aging process had been continued.

The second degradation product analyzed with SEM-EDS exhibits a higher concentration of Pb and a lower concentration of I and Br as compared to the surrounding film. The estimated composition of this region is presented in Table 4.5. We do not clearly identify the specific degradation product. Despite the presence of Br and I, we can suppose that the structure is composed of pure metallic Pb.

Table 4.5: *Results of the quantification of the composition in Cs, I, Br and Pb obtained via SEM-EDS measurements on the two degradation products in Figure 4.18(b).*

Feature	I/Pb	Br/Pb	Cs/Pb	Composition
Needle	2.81±0.33	0.38±0.08	1.17±0.18	$CsPb(I_{0.9}Br_{0.1})_3$
Feature	I	Br	Pb	Composition
Disc	24.5±3.8	2.1±1.2	73.3±3.5	Pb^0

Overall, the CsMAFA perovskite exhibits better stability under high relative humidity in an N_2 atmosphere as compared to an air atmosphere. While the presence of degradation products suggests that the film is still undergoing changes in its chemical composition, these changes occur at a slower rate than in air. This may be related to the reactivity of oxygen with perovskite compounds, as discussed in Chapter 1.

Conclusion of the section

In this Section, we presented the aging of CsMAFA-based half-cells under other environmental stresses than in previous Sections. The preliminary analysis of the sample aged under light and air with 55% RH suggests that light has accelerated the degradation of the film. The study of a sample aged under N_2 atmosphere with 85% RH revealed the detrimental effect of the oxygen contained in the air for the perovskite material. These preliminary results are insightful to understand the combined effect of different stress factors.

4.6 Conclusions

In this chapter, we investigated the degradation of CsMAFA perovskite half-cells exposed to humid air at 85% RH. Our study revealed that the CsMAFA perovskite film forms various geometrical degradation products, including hexagonal, disc-like, needle-like, and flower-like features. They were systematically analyzed by correlation of CL and SEM-EDS, and STEM-EDS and SAED for the needle-like features. Through these techniques, we identified the chemical nature and crystal structure of these degradation products as hexagonal PbI_2, orthorhombic (ordered) $CsPb(I_{0.9}Br_{0.1})_3$, and tetragonal $CsPb_2(I_{0.7}Br_{0.3})_5$.

Based on our results, we have identified several degradation mechanisms that occur when CsMAFA perovskite films are exposed to high relative humidity. We have proposed different pathways to describe these mechanisms. First, the perovskite film undergoes phase segregation leading to the formation of I-rich and Cs-rich regions. While the I-rich regions decompose preferentially into PbI_2 crystals by extraction of volatile species in gaseous form (see reaction 4.1), the Cs-rich regions form $CsPb(I_{0.9}Br_{0.1})_3$ needles (see reaction 4.2). We then postulated that these needles are subsequently transformed into $CsPb_2(I_{0.7}Br_{0.3})_5$ needles and flowers by the addition of PbI_2 and $PbBr_2$ coming from the surrounding decomposed CsMAFA perovskite (see reactions 4.4). These conclusions were supported by the macroscopic measurements performed on aged perovskite films, such as XRD and PL imaging.

These degradation mechanisms can have a significant impact on the performance of CsMAFA-based PSCs and are primarily caused by halide segregation and the release of volatile species. By employing compositional engineering strategies or incorporating protective layers, as discussed in Chapter 1, we could mitigate these instabilities and, in turn, improve the reliability of PSCs.

In section 4.5, we presented measurements on CsMAFA perovskite films aged under combined stressors including 1-sun illumination, heat (50°C), humidity, and air. Illumination was shown to exacerbate the degradation caused by humid air. We also performed aging of CsMAFA perovskite films in high relative humidity and N_2 atmosphere. The small size of the degradation products and the lower kinetics of degradation highlighted the critical role of oxygen in the degradation of CsMAFA-based samples observed in the first study.

In future studies, we will follow the same approach to gain more knowledge about the effects of different stressors on hybrid perovskite films, which will ultimately help to improve the stability and reliability of PSCs.

Chapter

5 Analysis of the degradation products in PSC aged under operation conditions

Chapter content

5.1 Optimization of the PSC fabrication 106
5.1.1 Addition of $Pb(SCN)_2$ and optimization of its concentration 106
5.1.2 Heating of precursor solution before deposition 107
5.2 Material characterizations 109
5.2.1 Macroscopic analysis of the aged PSC 109
5.2.2 STEM analysis of three different PSCs 110
5.2.3 Contact layers peeling off and perovskite film morphology 111
5.2.4 Cathodoluminescence measurements of the aged perovskite film 113
5.2.5 Chemical analysis of the aged perovskite film with EDS 118
5.2.6 Crystalline structure of the inclusion analyzed by SAED 122
5.3 Discussions about the formation of inclusions 124
5.3.1 Inclusions formation 124
5.3.2 Impact of changes in the perovskite film on the PSC performance 127
5.4 Conclusions 128

The stability of CsMAFA-based PSCs under continuous light and operating conditions is investigated in this chapter. First, we tuned the composition to enhance PSC long-term stability by adding thiocyanate (SCN^-) ions in the precursor solution of CsMAFA film. The optimal concentration of the additive was found to significantly improve the performance and stability of the devices.

The long-term stability enhancement was pushed further by adding a step in the fabrication process of heating the precursor solution before the perovskite film deposition. The optimized cells were then aged under continuous light and in operation conditions (maximum power point) in an inert atmosphere (N_2) for more than 1000 hours while their photovoltaic properties, including P_{MPP}, J_{MPP}, and V_{MPP} were recorded. The performances of the PSCs showed remarkable stability, notably with a T_{80} higher than 1000 hours. Their evolution was analyzed, and the losses were related to a slight decrease in current density.

After 1000 hours of aging, the structural and optical properties of the perovskite film were investigated with XRD and EQE. The presence of heterogeneities in the perovskite film was revealed with electron microscopy imaging. Their chemical, optical and structural nature was thoroughly studied to draw hypothetical formation mechanisms. These mechanisms involved reported degradation processes like phase segregation, organic cations volatilizing, and PbI_2 photolysis. Finally, we related these phenomena with the evolution of PSC performances.

5.1 Optimization of the PSC fabrication

5.1.1 Addition of $Pb(SCN)_2$ and optimization of its concentration

Thiocyanate ions (SCN^-) were initially used to increase the grain size of polycrystalline $MAPbI_3$ perovskite films. These films demonstrated a lower density of grain boundaries (GBs) but also better stability against moist air [273]. The reduction of GBs density also enhanced the minority carrier lifetime of the perovskite film, leading to an improvement in the PCSs performance.

The SCN^- ions are usually introduced by adding salts like $Pb(SCN)_2$ in the perovskite precursor solution. Several studies have shown that only a small amount of these salts is required to enhance the crystallinity of the perovskite film. According to Mahapatra et al., SCN^- ions promote the release of methylamine (MA) and thiocyanic acid (HSCN) gases during the annealing of the perovskite film [274]. This phenomenon would be responsible for crystallinity enhancement.

In a preliminary comparative study (not shown here), two additives were investigated: $Pb(SCN)_2$ and KSCN. Results showed a higher potential for $Pb(SCN)_2$ compared to KSCN regarding degradation rate reduction under light soaking. This study also showed an optimal $Pb(SCN)_2$ concentration between 0 and 5% to enhance PSC long-term stability. We thus used $Pb(SCN)_2$ to fabricate the solar cells presented in this chapter. The concentration of $Pb(SCN)_2$ is given in % mol with respect to PbI_2 concentration in the precursor solution.

Figure 5.1(a) shows SEM images obtained on CsMAFA films with the addition of 0%, 1%, 2%, and 3% $Pb(SCN)_2$ into the precursor solution. In each film, the grain size was measured and plotted as a function of $Pb(SCN)_2$ concentration in Figure 5.1(b). As expected, the grain size significantly increased with concentration, suggesting that adding $Pb(SCN)_2$ enhanced the crystallinity. The $Pb(SCN)_2$ addition must also enhances PSCs performances and stability to environmental stress.

The impact of $Pb(SCN)_2$ on PSCs stability was then investigated. To identify the optimal concentration, PSCs with 0.5, 1, 3, and 5% of $Pb(SCN)_2$ were fabricated and aged for 380 hours in a climatic chamber from Cicci Research. The tests were performed by continuously illuminating the samples with LED simulating AM1.5G spectrum (containing UV light) at 1 sun (i.e., 100 mW/cm^2). The samples were either biased for J-V curve acquisition [forward (FW) and reverse (RV)] or driven at maximum power point (MPP). For the MPP tracking, a tracker with a perturb and observe algorithm that adjusts the maximum power voltage every 30 s was used. It is worth noting that the tracking of the MPP tends to follow the evolution of the FW scan. J-V curves were measured with a scan speed of 20 $mV.s^{-1}$ and a voltage step of 20 mV every 15 min. The temperature and the relative humidity inside the chamber during illumination were set at 23°C and lower than 42%, respectively. The atmosphere was filled with N_2 to hinder the effect of O_2 on PSC performances. This experimental set-up corresponds to the ISOS-L1 protocol defined in the consensus statement for PSCs reliability testing [143].

Figure 5.1(a) shows the evolution of absolute P_{MPP}, in mW/cm^2, for 0.1, 5, 10, 200, 300, and 380 hours as a function of the concentration of PbSCN. The P_{MPP} at 0.1 hour is considered the initial power. Thus, the most efficient devices before the aging were PSC +0% and PSC +1% with 15 mW/cm^2. They were followed closely by the 0.5% exhibiting 14.5 mW/cm^2. The PSC +3% and +5% are substantially lower, exhibiting 11 and 10 mW/cm^2, respectively. The first 10 hours of aging were detrimental for all the conditions tested. The power of the PSC +0% and PSC +1% decreased down to 11.5 mW/cm^2 (Δ ~23%), the PSC +3% and the PSC +5% decreased down to 8.5 mW/cm^2 (Δ ~15%), and the PSC +0.5% decreased down to 12 mW/cm^2

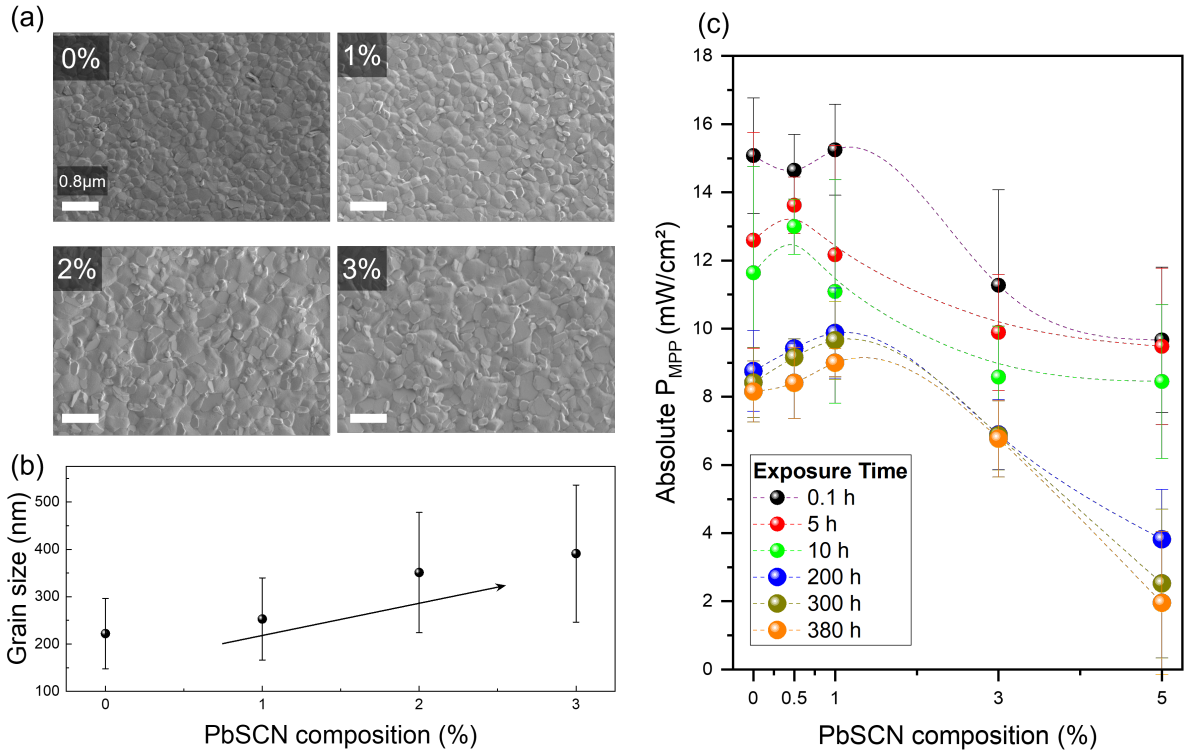

Figure 5.1: *(a) SEM images of perovskite film with +0, +1%, +2%, and +3% of PbSCN added. (b) Evolution of the grain size of the film as a function of the PbSCN composition. (c) Evolution of the absolute P_{MPP} (mW/cm^2) for different aging time, 0.1, 5, 10, 200, 300 and 380 hours, as a function of PbSCN composition +0, +0.5, +1, +3 and +5%.*

(Δ ~13%). After 200 hours, the power loss stabilized for all the conditions tested. At 380 hours of aging, the PSC +1% exhibited the highest P_{MPP} of 9.8 mW/cm^2 (Δ ~40%). This device demonstrated the highest initial efficiency and stability. +1% of $Pb(SCN)_2$ was then considered as the optimal concentration for enhancing PSC long-term stability as it has already been reported in the literature [275].

The addition of $Pb(SCN)_2$ in the precursor solution enhanced the crystallinity of the film. An optimal concentration of 1% is found, leading to a slight increase in PSC efficiency and remarkable enhancement of its stability in operation under continuous light in an N_2 atmosphere and ambient temperature.

5.1.2 Heating of precursor solution before deposition

The preparation of the precursor solution can be optimized to enhance the performance and stability of PSCs. As reported before [276], the solution can be heated at 70°C for 1 hour before the deposition to assist dissolution of the precursors. We compared the performances obtained after heating the solution ("heated" PSC) and without heating ("not-heated" PSC). Both devices contained 1% of $Pb(SCN)_2$ added to their solution.

The stability of these devices was investigated for more than 1000 hours in the same aging conditions as before (ISOS-L1). During the aging, the MPP characteristics (V_{MPP}, J_{MPP}, FF_{MPP}, P_{MPP}) were tracked. The set-up was shut down after 400 hours of working due to

technical issues and started again. Therefore, it produced a blank in plotted data, not related to variations in the performances of the devices.

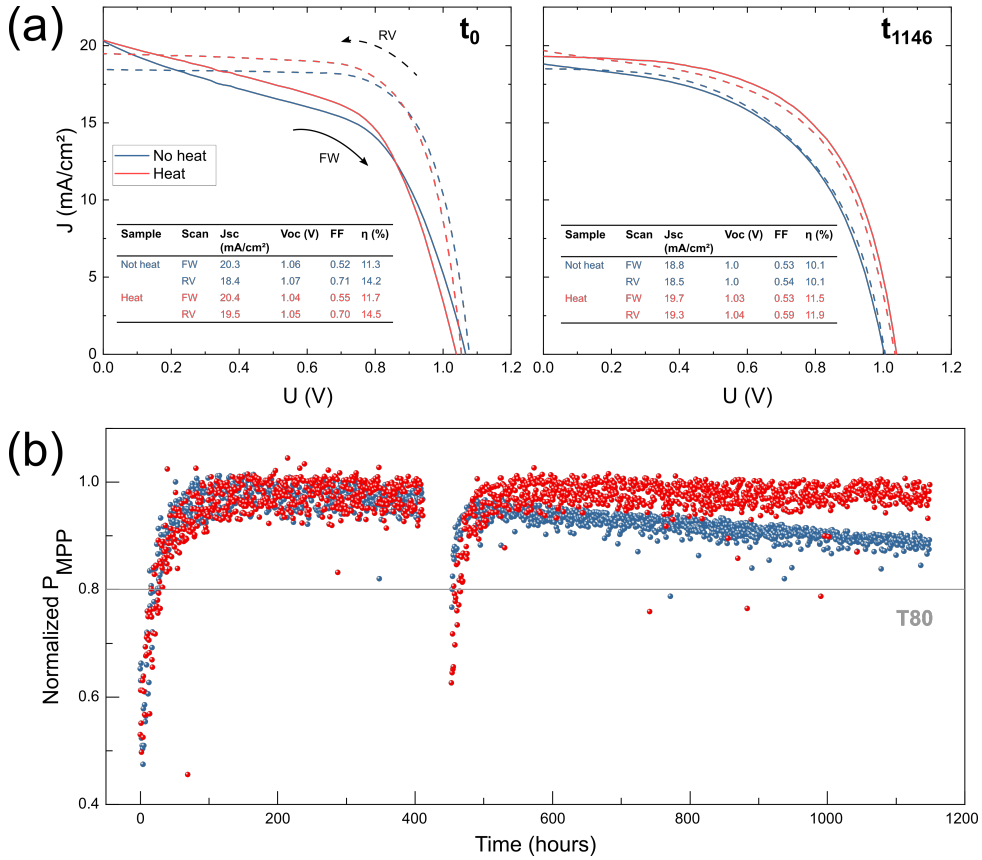

Figure 5.2: *(a) J-V curves at t_0 and t_{1146} of PSCs. The precursor solution is heated at 70°C before deposition for one hour in one cell (in red) and not the other (in blue). For both solar cells, a voltage scan is performed in FW (solid line) and RV (dashed line) direction. A table sums up the photovoltaic performances of the two PSCs. (b) Evolution of the normalized P_{MPP} for the two devices (same color code as in (a)) driven at MPP during 1100 hours of continuous light exposure.*

J-V curves before (t_0) and after (t_{1146}) aging are displayed in Figure 5.2(a) along with extracted photovoltaic performances. At t_0, a significant hysteresis is observed in both PSCs with $FF_{RV} > FF_{FW}$. The heated PSC shows a slightly better J_{sc} than the not-heated PSC, but their PCE is similar. At t_{1146}, the hysteresis becomes negligible with the decrease of the FF in the RV scan J-V curve. The PSC not-heated shows a lower PCE (- 1.5% absolute) than its heated counterpart.

Figure 5.2(b) presents the normalized P_{MPP} of both devices recorded during the aging process. Both devices' P_{MPP} remain above 80% of their maximum value. This stability may have been caused by the $(SCN)^-$ ions, as suggested by the previous study on $Pb(SCN)_2$ (see Figure 5.1(c)). However, there are still differences between heated and not-heated devices as the normalized P_{MPP} from the latter decreases more rapidly. The current (J_{MPP}) and voltage (V_{MPP}) during aging are plotted in Figure 5.3.

V_{MPP} is relatively constant in both solar cells while J_{MPP} decreases by 9% and 13% for heated and not-heated PSC, respectively. The decrease in P_{MPP} showed in Figure 5.2 is therefore driven by variations in J_{MPP}. The latter depends on the J_{sc} and the FF of the PSC. The decrease of the J_{MPP} is consistent with the decrease of J_{sc} and the FF_{RV} shown in Figure 5.2(a).

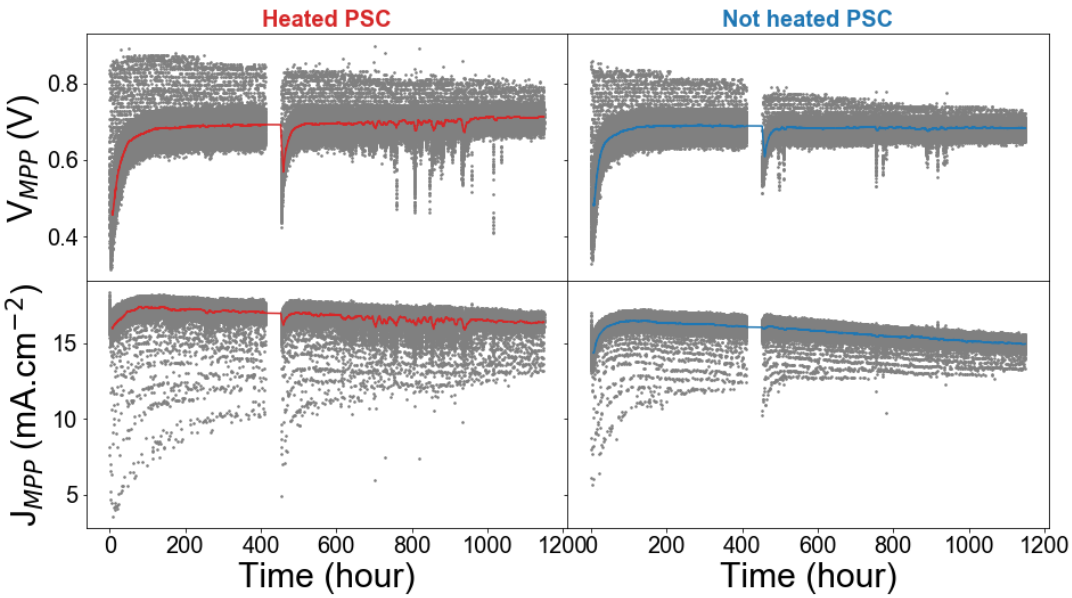

Figure 5.3: *V_{MPP} and J_{MPP} from the heated (left) and the not heated (right) PSC as a function of aging time (in hours). Values recorded every 20 seconds are displayed in gray. The moving average of these values is displayed in colored continuous line to help the reader.*

In this subsection, we evaluated the impact of heating the precursor solution before fabrication of the PSC on the performance and the stability. J-V characterizations performed after fabrication showed that heating the solution enhanced slightly the current initially and during aging in operation conditions. In the following Section, the perovskite layer of these PSCs is analyzed.

5.2 Material characterizations

The variations observed in J_{MPP} and P_{MPP} likely originated from changes in the absorber of the PSCs. In this section, we will examine the degradation of the perovskite layer by studying its morphology, optical properties, and crystal structure at macro and nano scales.

5.2.1 Macroscopic analysis of the aged PSC

The degradation is analyzed by coupling electrical measurements with different characterization techniques. XRD and External Quantum Efficiency (EQE) give macroscopic insights into the film structural state, quality, and optical properties. Figure 5.4(a) displays X-ray diffractograms obtained on a CsMAFA film of reference and the PSC aged.

The X-ray diffractogram from the aged PSC shows a reflection peak at 14.1° that can be indexed as (110) planes from the tetragonal CsMAFA structure and another at 11.6° indexed as (001) planes from the hexagonal PbI_2. These two reflections are also present in the film of reference. However, the ratio between peak areas of PbI_2 and CsMAFA is higher in the aged PSC than in the reference ($0.65 > 0.19$). It suggests that the perovskite film has been partially decomposed into PbI_2 during aging.

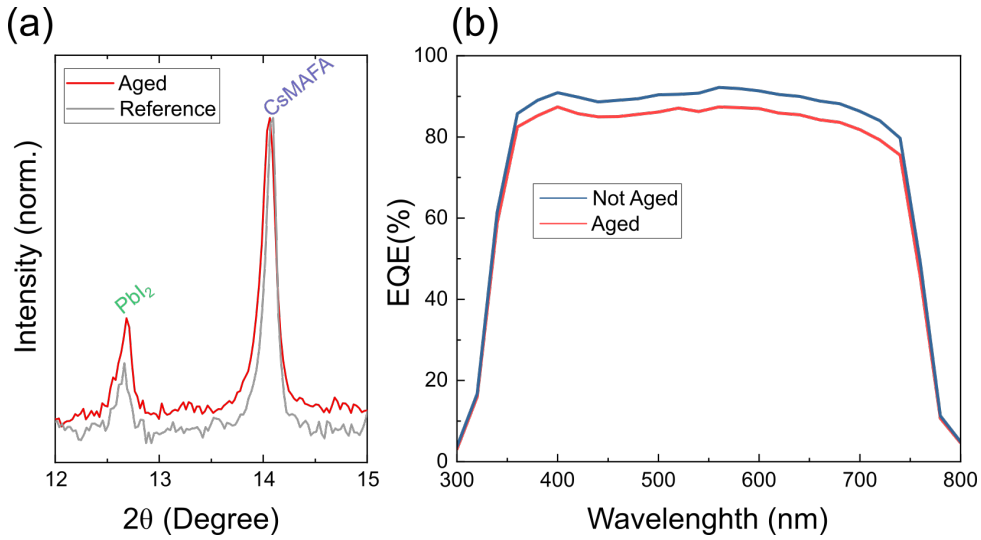

Figure 5.4: *(a) XRD diffractograms acquired on PSC aged, and on a CsMAFA film of reference. The diffraction peak at 14.1° is indexed as the tetragonal CsMAFA structure (110) plane (in purple). The peak at 12.6° is indexed as the hexagonal PbI_2 (001) plane (in green). (b) EQE on PSC aged, and on its "twin" fabricated at the same time but kept in vacuum in the meantime ∼50 days (Not aged).*

Figure 5.4(b) shows the EQE measurements acquired on the aged and the "not-aged" PSC fabricated with the same conditions and at the same moment, but kept under vacuum in the dark for the duration of the aging process. The aged PSC exhibited losses in quantum efficiency over the whole wavelength range analyzed. These losses were manifested by a 5% reduction in the J_{sc} calculated from the EQE (from 18.4 to 17.6 mA/cm^2).

Due to the observed variations, a more localized analysis of the active layers of the PSCs was deemed necessary. In the following Subsections, electron microscopy techniques will be employed to investigate the morphology, composition, and optoelectronic properties of the active layers of the aforementioned PSCs.

5.2.2 STEM analysis of three different PSCs

Cross-sectional lamellae were prepared from the not-aged heated PSC (on which EQE was performed) (1), the not-heated PSC (2), and the heated PSC (3) (both aged). STEM-HAADF measurements were conducted on these specimens, and the resulting images are shown in Figure 5.5.

Due to the numerous heterogeneities in the three lamellae, EDS measurements were conducted at higher magnifications in areas delimited by colored squares. The corresponding HAADF images are presented in (b). The concentrations of I, Br, Pb, and Cs were determined using the Cliff-Lorimer method in zones indicated in the HAADF images (b) and compared to pristine CsMAFA, as shown in Table 5.1.

The not-aged heated PSC lamella (1) shows small clusters, highlighted by green arrows, with high contrast at the interface between the perovskite and PTAA layers. These clusters are present along the entire length of the lamella and have sizes in the order of 200 nm. The ratio I/Pb in the cluster is of 2.4 ± 0.8, suggesting that they are made of PbI_2. These clusters must have originated from the excess of PbI_2 in the precursor solution.

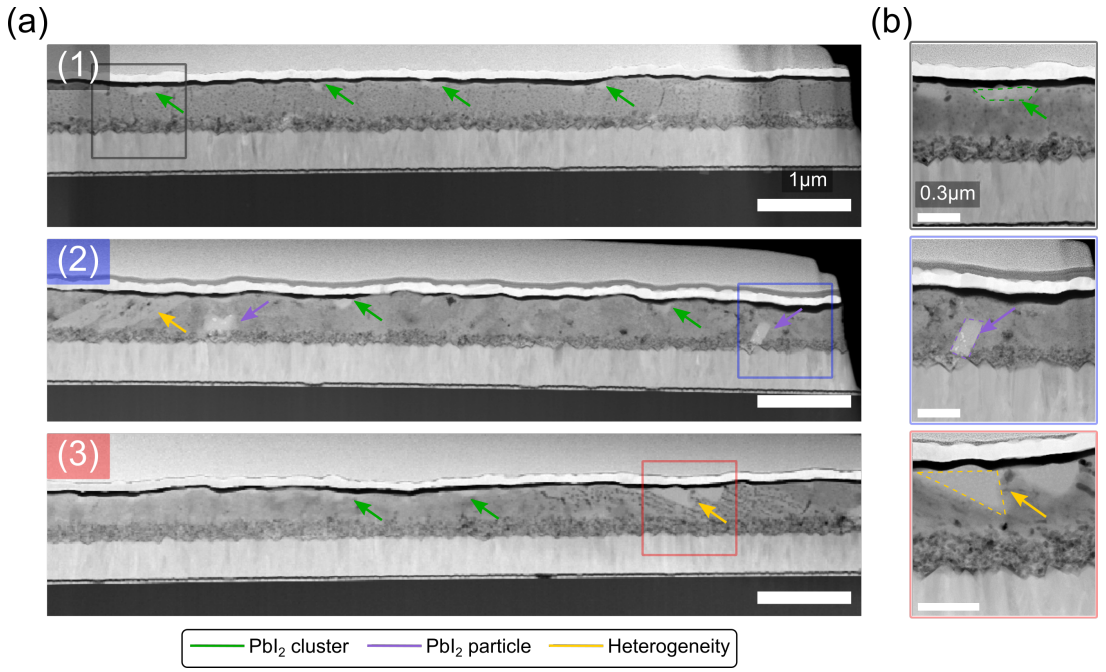

Figure 5.5: *(a) STEM-HAADF images of lamellae extracted from three different PSCs such as: (1) PSC heated and not-aged (2) PSC not-heated and aged (3) PSC heated and aged. The fabrication of lamellae has been performed after the aging procedure in the active area of the PSCs. Some features are highlighted with arrows of different colors: in green native PbI_2 clusters; in purple PbI_2 particles at the interface with m-TiO_2; in yellow aggregates positioned at the interface with PTAA. Zoomed HAADF images for each specimen are shown in (b).*

In the other lamellae, wider high-contrast regions are observed. The ones marked by purple arrows in lamella (2) are positioned at the perovskite/m-TiO_2 interface and are composed of PbI_2, as shown by EDS measurements (see Table 5.1). The presence of these particles in aged PSCs suggests that they formed through a reaction between the perovskite and m-TiO_2 layers, a phenomenon previously reported in TiO_2-based PSCs.

The third type of heterogeneity, marked by yellow arrows in Figure 5.5, is observed in lamellae (2) and (3) from aged PSCs. These heterogeneities are about 1 μm in size and are positioned near the PTAA layer. In lamella (2), the heterogeneity occupies the full depth of the film, while in (3), it is thinner. The heterogeneity exhibits a higher concentration of Br, at the expense of I, and surprisingly has a much higher Cs content than pristine CsMAFA (see Table 5.1).

The following study is focused on the perovskite layer from the aged and heated PSC (3).

5.2.3 Contact layers peeling off and perovskite film morphology

As mentioned in Chapter 2, CL measurement of the absorber cannot be performed when contact layers cover it. Therefore, the procedure reported in three recently published studies [102, 131, 277] was followed to remove the contact layers by delamination with Kapton tape. The authors did not report any damage during the process, and most of the photovoltaic performances were retained after the PSCs refabrication [102, 131]. This procedure is thus expected to preserve the perovskite film.

After removing the heated PSC contact layers, the perovskite film morphology was analyzed using SEM imaging. The device stack before and after delamination is presented schematically

Table 5.1: *Quantification of the element content from EDS analysis performed in regions delimited by a dashed line of the lamella displayed in Figure 5.5(b).*

Regions	(1)	(2)	(3)	CsMAFA
$I_{L\alpha}$	66.1± 14.4	65.1± 14.4	47.9±16.1	53.9±14.4
$Br_{K\alpha}$	2.2± 2.0	2.8± 0.8	19.4±4.1	16.1±1.2
$Cs_{L\alpha}$	0	0	6.1±3.7	1.4
$Pb_{L\alpha}$	29.5± 13.3	30.0± 13.3	24.8±12.3	27±12.1
Regions	(1)	(2)	(3)	CsMAFA
I/Pb	2.42± 0.79	2.34± 0.76	2.14± 0.85	2.17±0.75
Br/Pb	0.09± 0.05	0.10± 0.03	0.85± 0.29	0.63±0.16
Cs/Pb	0	0	0.28± 0.14	0.05

in Figure 5.6(a). The two zones indicated with arrows on the peeled device correspond to the positions where SEM images presented in Figure 5.6(b) were recorded. Figure (1) corresponds to a region where PTAA and gold were not peeled, and (2) to the uncovered perovskite film.

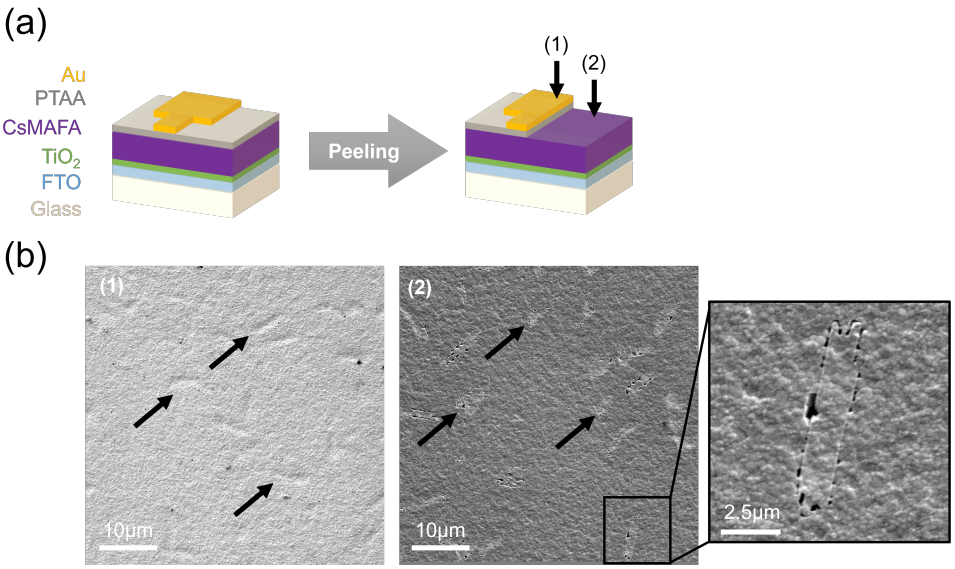

Figure 5.6: *(a) Schematic of the PSC architecture. The gold contact is shaped as in reality, where the active area of the solar cell is defined by the square (0.16 cm^2 sized). The same device with part of PTAA and gold layers removed is drawn schematically on the right. (b) SEM images recorded in the regions indicated in the previous schematic, corresponding respectively to: (1) gold layer in the active area of the PSC; (2) uncovered perovskite in the active area of the PSC.*

The SEM image (1) shows contrast variations corresponding to heterogeneities of about 10 μm, highlighted by black arrows. In SE imaging mode, these contrast variations are due to changes in the specimen topography. The same heterogeneities are observed in the peeled area of the PSC presented in image (2). Thus, we assume that the heterogeneities observed in images (1) and (2) are similar. As of now, we will call these heterogeneities **inclusions**.

Figure 5.7(a) displays SEM images recorded outside the active area on the perovskite surface, previously covered by the PTAA layer. The film exhibits small grains and pits distributed all over the region. However, we do not notice any features showing the same shape as previously

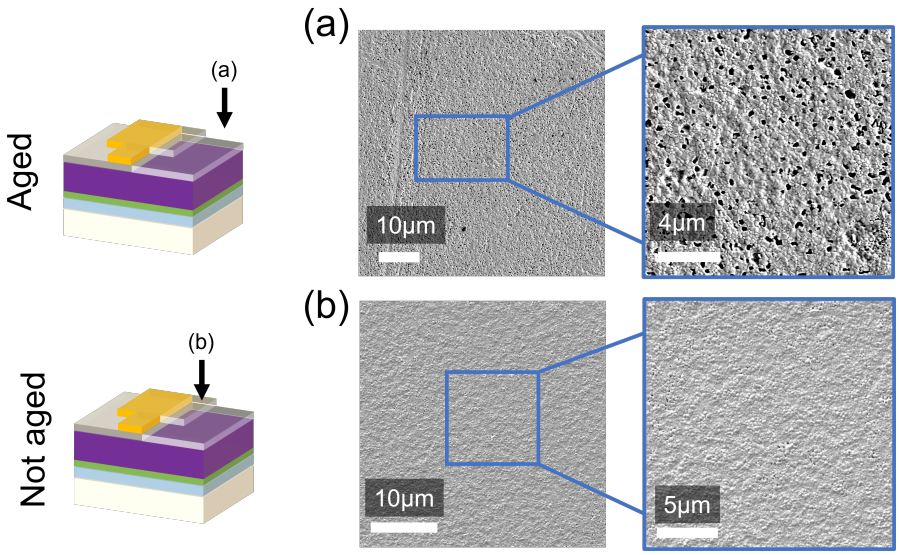

Figure 5.7: *SEM images of the revealed perovskite layer a) outside of the active area of the sample aged, b) and inside the active area of the not-aged sample.*

discussed. Figure 5.7(b) presents an SEM image of the not-aged PSC. The perovskite film in the cell active area does not exhibit features like inclusions or pits.

These observations suggest that the inclusions appeared in the perovskite film during the aging and are not related to the peeling step. Before drawing any conclusions on their origins and effect on PSC performances, we still need to identify their nature.

5.2.4 Cathodoluminescence measurements of the aged perovskite film

A CL map was acquired on the perovskite film of the aged PSC. Figure 5.8 presents an SEM image of the film (a) compared to the CL normalized panchromatic map of the same region (b). The inclusions observed in the SEM image perfectly correspond to low-intensity signal regions that appear black on the CL panchromatic map.

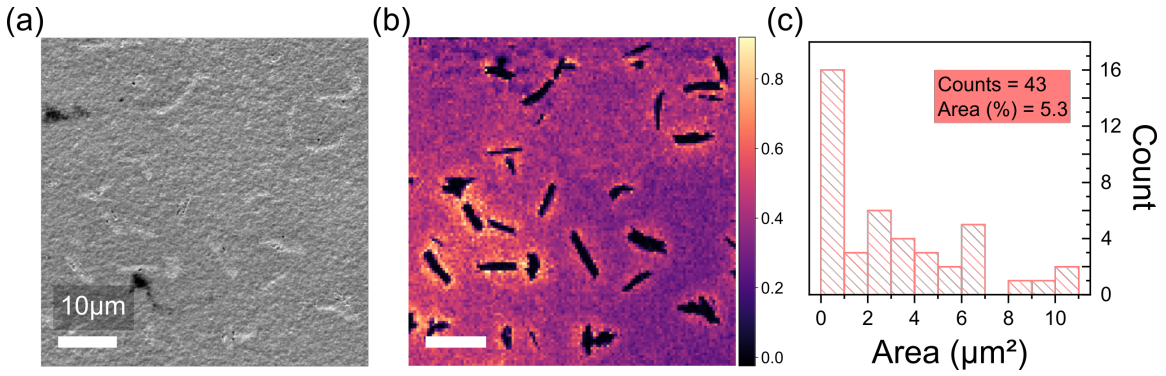

Figure 5.8: *(a) SEM image and (b) corresponding panchromatic CL intensity map normalized. (c) Histogram of the inclusion number with respect to their size.*

The density of inclusions was determined from the CL map, and their size distribution was plotted in the histogram (c). The inclusions occupy approximately 5% of the total area considered. Due to their significantly low luminescence, their presence must be detrimental to the

photovoltaic performances. The MPP tracking showed that the heated aged PSC lost 9% of its maximum current after the 1000 hours of operation. Therefore, these losses might be at least partly attributed to the formation of inclusions in the active area.

To identify the nature of these inclusions, we performed a CL acquisition focusing on one specific inclusion, the results of which are presented in Figure 5.9. The SEM image of the region analyzed and the corresponding normalized panchromatic CL map are displayed in (a) and (b), respectively. The CL spectrum was averaged over the entire map (plotted in blue) and in an inclusion (the probed zone is indicated in (b) by a green circle and plotted in green in (c)). These spectra were plotted alongside a reference spectrum (in dashed-gray line) obtained on a fresh sample with the same experimental conditions (summarized in Table 2.5).

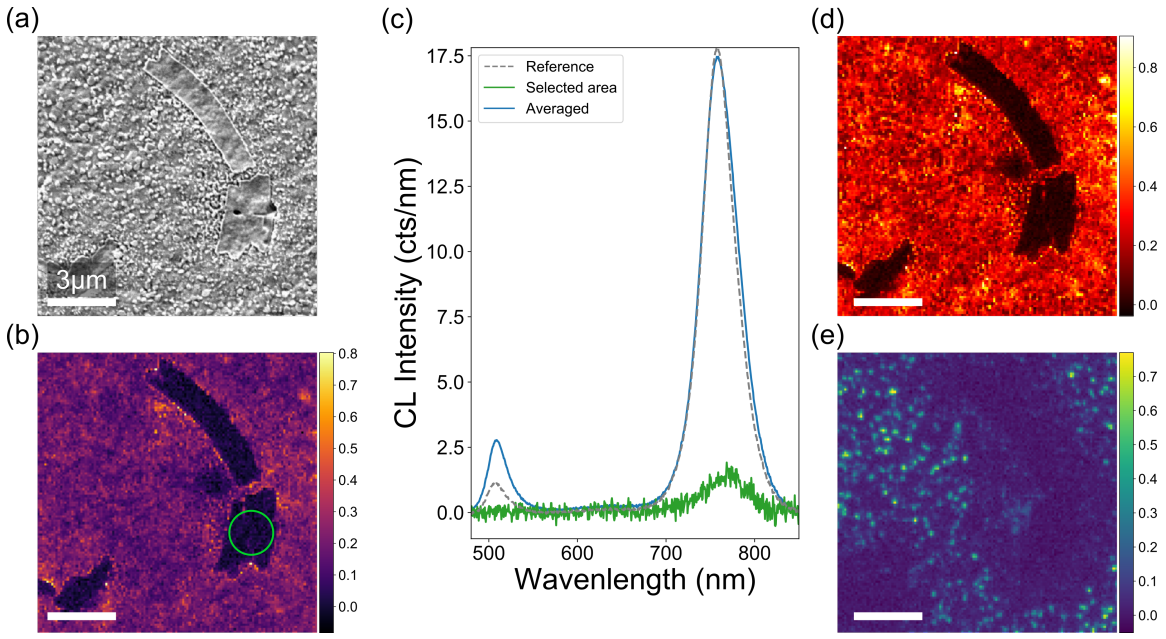

Figure 5.9: *(a) SEM image of the uncovered perovskite layer. (b) normalized panchromatic CL intensity map. (c) CL spectrum averaged over the whole map (in blue), and over the area delimited by the green circle shown in (b) (in green) and on a half-cell non-aged perovskite device taken as a reference (in gray dashed line).(d,e) CL maps with false colors showing the luminescence integrated over two different spectral regions: red (d) [745 nm, 765 nm], and green (e) [490 nm, 510 nm] corresponding to the emission of the CsMAFA perovskite and the PbI_2 phase, respectively. For each pixel, the integrated intensity of each band is normalized by the maximum of the filtered map.*

The blue CL spectrum exhibits the two usual emission peaks at 757 nm and 500 nm, corresponding to the CsMAFA and PbI_2 contributions, respectively. The CsMAFA emission peak from the aged samples matched remarkably in position and intensity with the one from the reference film. As a first approximation, this match indicated that the emitting perovskite was not damaged during the aging of the PSC under continuous illumination.

In contrast, the green CL spectrum averaged in the inclusion shows a significantly weaker signal (nearly one order of magnitude) with a small emission peak at 768 nm. This peak is slightly red-shifted (∼10 nm) as compared to the emission of pristine perovskite, indicating that the inclusion is likely composed of red-shifted perovskite. Given the low intensity of the emission peak, it may also come from parasitic recombinations in the surrounding film (see CL spatial resolution in Chapter 2).

The spatial distribution emission peak was then examined over the area analyzed. False colors were attributed to the two spectral bands 755±10 (red-yellow) and 500±10 nm (blue-green). The obtained normalized filtered maps are displayed in Figure 5.9(d) and (e), showing the distribution of perovskite and PbI_2 phase, respectively. The perovskite peak in map (d) is relatively homogeneous, except in the low-luminescent inclusions. Map (e) reveals the presence of PbI_2 clusters as usually observed in perovskite films. In contrast with pristine film where clusters are homogeneously spread, here we observe no clusters at less than ∼3 μm from the inclusions. This peculiar arrangement must originate from the changes occurring in the film during PSC operation.

Analysis of the distribution of PbI_2 clusters

A more specific analysis of the PbI_2 clusters was carried out to determine if the remaining clusters are natives (i.e., if they existed before the aging) or if they formed during the aging. For this purpose, we considered the areas delimited by a white square in the filtered maps Figure 5.10 (a). In aged PSC, the region analyzed was chosen because its location is far from the inclusions.

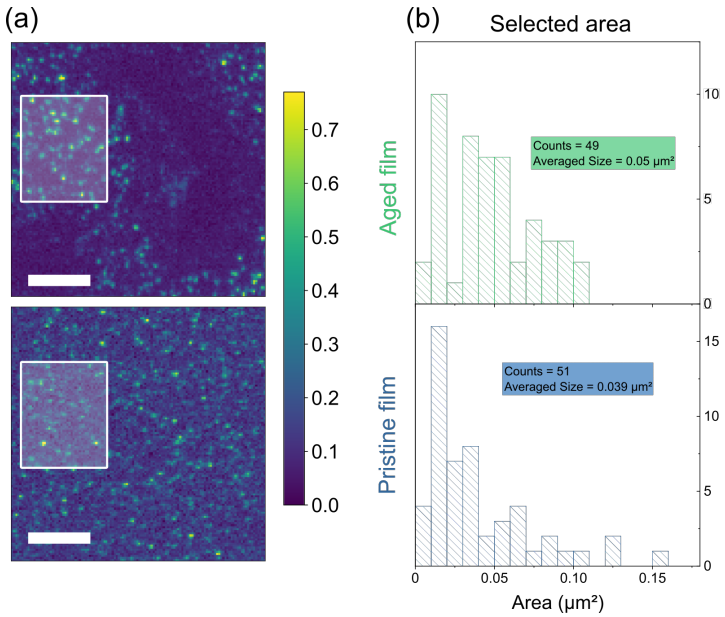

Figure 5.10: *(a) CL maps filtered on 500±10 nm revealing PbI_2 clusters.(b) Corresponding cluster histograms as a function of their size in μm^2 in the selected areas shown in (a). The same analysis performed on the whole map is displayed in Figure 29*

The number and size of clusters in these regions were determined and plotted in histograms in Figure 5.10(b). Detailed results are also summarized in Table 5.2.

Table 5.2: *Summary of the analysis performed on the maps of PbI_2 for the specimen in Figure 5.10 and for a reference sample.*

Sample	Number (counts)	Averaged size (μm^2)	Total Area (%)
Reference	51	0.039	8.49
PSC	49	0.05	10.41

In the areas considered, the number of clusters is relatively close in the two samples. The cluster size is slightly bigger in the aged PSC than in the reference. However, this difference

might come from the uncertainties of the method.

The similar number of clusters in the two specimens suggests that the PbI_2 clusters are native to the region analyzed in the aged specimen. Thus, clusters initially located in the vicinity of inclusions may have been incorporated in the film or contributed to the formation of the inclusions. This subject will be discussed further in Section 5.3. In the following, the near-inclusion perovskite film is analyzed more specifically.

Perovskite CL peak analysis in the vicinity of the inclusion

The perovskite emission peak located at 757 nm has been fitted by a Gaussian model for each pixel of the hyperspectral CL map. The obtained peak intensity, position, and FWHM maps are presented in Figure 5.11(a), (b), and (c), respectively, together with the averaged CL spectrum fitted in (d).

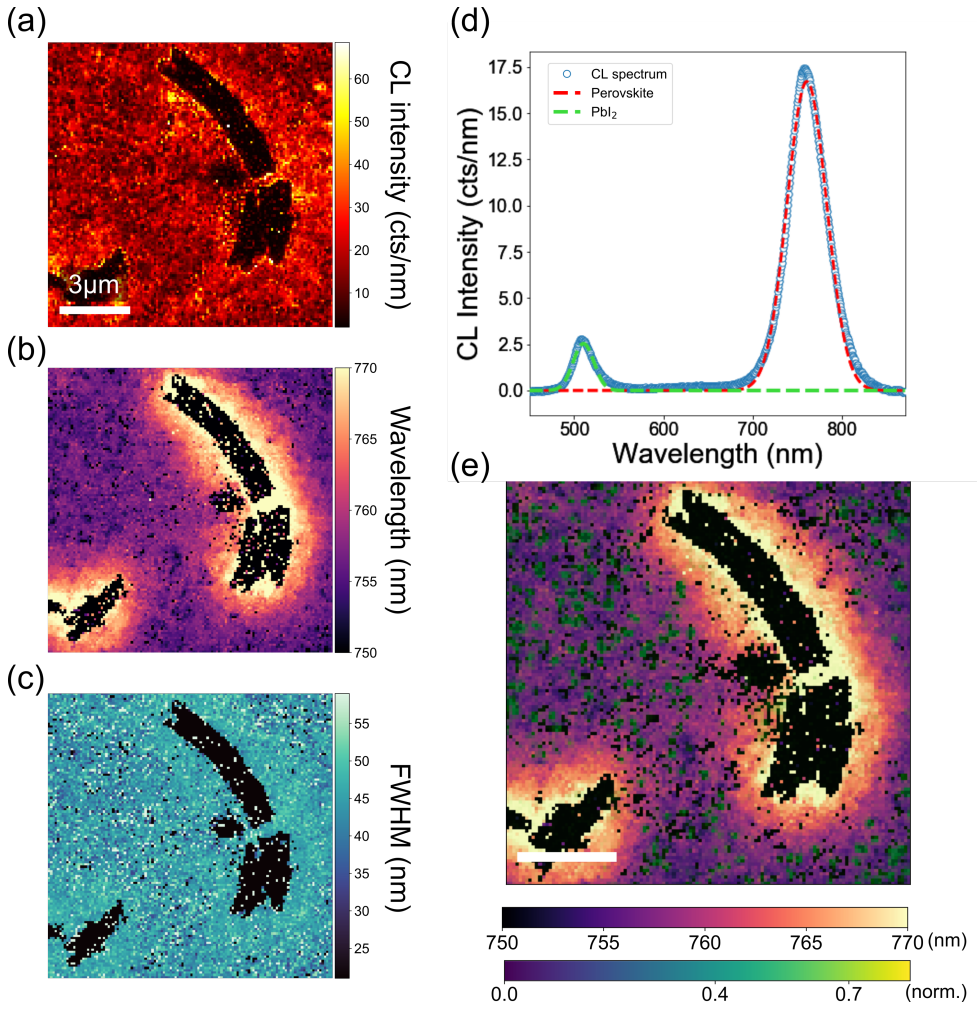

Figure 5.11: *The perovskite emission peak is fitted with a Gaussian function for each pixel. (a) CL peak intensity map; (b) CL peak wavelength map; (c) CL peak FWHM map. (d) Averaged CL spectrum (blue circles) fitted with a two-Gaussian function corresponding to perovskite (in dashed-red line) and PbI_2 (in dashed-green line) emission. (e) Perovskite peak wavelength map overlayed with the CL map filtered on 500±10 nm revealing the presence of PbI_2 clusters.*

The intensity map is similar to the filtered map shown in Figure 5.10 exhibiting a relatively

homogeneous distribution of the CL peak intensity except in the inclusion. Conversely, a red-shift of the emission peak is observed in the zone surrounding the inclusion in the wavelength map. This shift is close to $\Delta\lambda$=20 nm (ΔE=50 meV) and may be induced by halides or cations migration.

In the literature, the investigation of $Cs_{0.17}FA_{0.83}Pb(I_xBr_{1-x})_3$ perovskites showed that an increase in iodine (I) content of x=0.1 gives rise to a PL emission red-shift of 20 nm [278].

As mentioned in Chapter 1, the concentration of the cations has a lower impact on the bandgap of perovskites than halides. In the literature, the analysis of the PL peak evolution as a function of cesium (Cs) content in $Cs_xFA_{1-x}Pb(I_{0.83}Br_{0.17})_3$ perovskite film showed that the Cs content would have to decrease to 0 to cause a 20 nm red-shift [94].

These studies where a single element varies are insightful for understanding the CL peak position variation. However, halides and cations might both have migrated during the aging of the specimen, combining their effect on the obtained bandgap.

Figure 5.11(e) shows the peak wavelength map (same as (b)) overlayed with the CL map filtered over 500±10 nm (same as Figure 5.8(e)). This image reveals that PbI_2 clusters disappeared in the red-shifted area close to the inclusion, suggesting that these phenomena are related. The photolysis of native PbI_2 clusters into Pb^0 and I^- has been widely reported in the literature [256, 271, 272] and happens through oxidation of I^- into I_2 and Pb^{2+} reduction into Pb^0.

One potential explanation for these observations is that PbI_2 clusters decomposed, releasing I^- ions into the film beneath, resulting in a red-shift of its emission. Another possibility is that I^- ions migrated from the region where the inclusion is located. In this scenario, the I^- ions migration (and losses) is part of the inclusion formation. Therefore, determining the inclusion composition is crucial for understanding the decomposition mechanisms.

Low-temperature Cathodoluminescence

Figure 5.12(a) shows CL perovskite peak wavelength maps acquired at 300, 200, 100, and 70 K with the same acquisition parameters. We consider in each map three regions over which the CL signal is averaged for comparison: bulk perovskite marked by a yellow triangle; red-shifted near-inclusion perovskite marked by a blue square; inclusion marked by a green circle. Corresponding normalized spectra are plotted in (b), (c), and (d).

First, the emission from the bulk perovskite red-shifts by ΔE ≈32 meV while the temperature decreases from 300 to 70 K. This trend is close to the evolution of pristine CsMAFA perovskite emission with decreasing temperature shown in Chapter 2 (ΔE ≈36 meV). The near-inclusion film also red-shifts with a similar amplitude ΔE ≈30 meV. The CL peak is red-shifted at all temperatures compared to the bulk perovskite. Finally, the inclusion exhibits a higher peak intensity emission at low temperatures. The peak position follows the same trend as the two other regions with a red-shift of ΔE ≈37 meV. However, there is no new contribution at low-temperature in this wavelength range, as we might have expected from a cesium-based inorganic perovskite (see Chapter 3).

Strikingly, the evolution of the CL peaks is rather monotonous regardless of the region analyzed, suggesting that none of these regions underwent a phase transition at low temperatures.

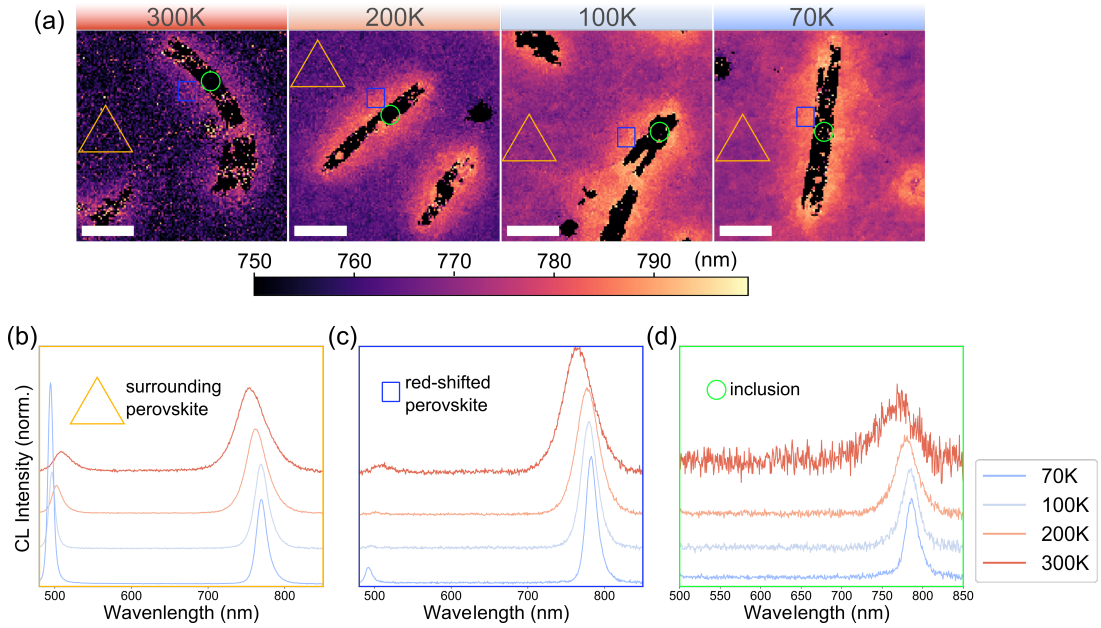

Figure 5.12: *(a) Maps of the perovskite peak wavelength measured at 300, 200, 100, and 70 K. On each map, three regions are indicated over which we average the CL signal: the triangles correspond to the surrounding perovskite, the circles to the inclusions, and the squares to the red-shifted perovskite (close to inclusions). The spectra are plotted in (b), (c), and (d) with respect to temperature of the measurement.*

After continuous operation over 1000 hours, inclusions are formed in the perovskite film. In subsection 5.2.4, we showed that these inclusions are not emitting and occupy about 5% of the active area of the PSC and, therefore, might be related to losses in photogenerated current. Further CL analysis showed that the photo-decomposition of the native PbI_2 clusters might be involved in the inclusion formation and iodine enrichment in the near-inclusion area. CL measurements at low temperatures did not reveal any phase transition. These results impel to determine the chemical nature of the inclusions to establish the mechanism of their appearance during the stability test.

5.2.5 Chemical analysis of the aged perovskite film with EDS

In the following subsection, we present a chemical investigation of the inclusions and their environment, performed subsequently by SEM-EDS and STEM-EDS.

Chemical analysis with SEM-EDS

Figure 5.13 shows the result for SEM-EDS acquired on the perovskite film after aging under illumination. SEM image (a) combines SE and BSE images in such a way that contrast reveals topography and chemical variations. The film composition is measured in all the area (see elemental maps in (b)) and along the white dashed line indicated on the SEM image (see linescan in (c)) [1].

An inclusion and PbI_2 clusters are clearly visible in the SEM image with higher contrast than the surrounding film. The near-inclusion region, which lacks PbI_2 clusters, is also well-defined

[1] 15kV / I=2nA / dose = 1.6×10^2 $e^-Å^2$

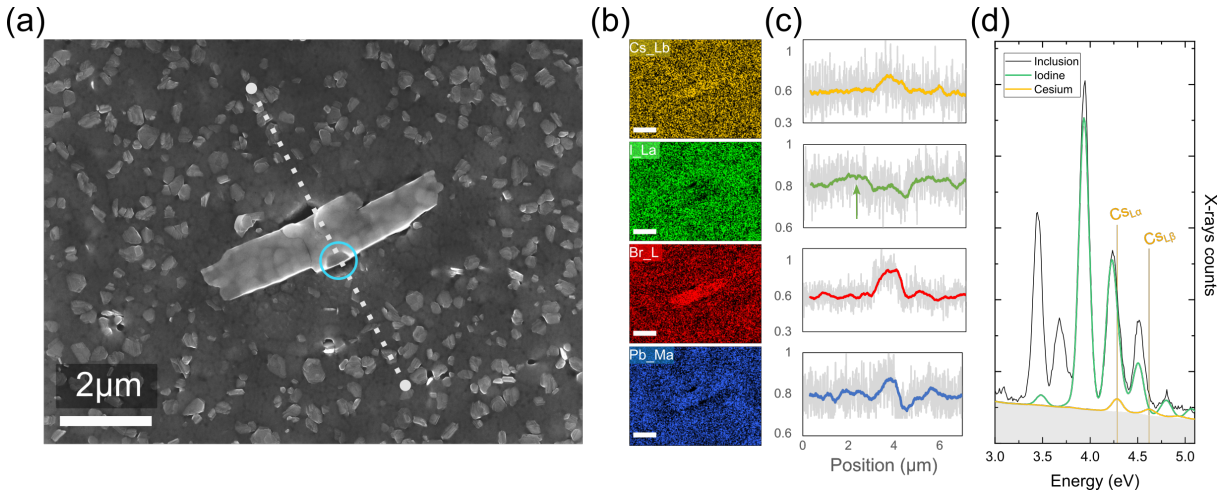

Figure 5.13: *(a) SEM (SE+BSE) image of the inclusion showing the path used to obtain the EDS linescan in (c) and the corresponding elemental maps showing the distribution of Cs, I, Br, and Pb in (b). Linescan plots display raw data in grey and moving average trendline, smoothing out data fluctuations, in color. (d) EDS spectrum averaged in the inclusion (in grey) with deconvoluted contribution of $I_{L\alpha}$ and $Cs_{L\alpha}$ in green and yellow respectively. The $Cs_{L\alpha}$, $Cs_{L\beta}$ lines and the background subtracted are indicated.*

and corresponds to the red-shifted region shown in Figure 5.11(e).

The elemental maps show an increase in Br and Cs content in the inclusion, as confirmed by the linescan plots. The linescan plot of I content exhibits a slight increase followed by a drop at 2 μm indicated by a green arrow. It suggests that I^- ions have migrated from the inclusion towards the near-inclusion area. The lead (Pb) content shows a slight increase in the inclusion and the corresponding linescan plot exhibits an abrupt decline at the edge of the inclusion due to the hole highlighted in Figure 5.13(a) by a blue circle.

Table 5.3: *Quantification of the element content from EDS analysis performed in regions displayed in Figure 5.13.*

Region	Inclusion	Bulk perovskite
$I_{L\alpha}$	54.8±4.2	61.8±3.9
$Br_{K\alpha}$	16.7±3.4	13.1±2.8
$Cs_{L\alpha}$	3.9±1.8	1.4
$Pb_{L\alpha}$	24.3±3.4	24.8±3.5

Ratio	Inclusion	Bulk perovskite
I/Pb	2.27±0.25	2.50±0.25
Br/Pb	0.70±0.12	0.53±0.09
Cs/Pb	0.16±0.05	0.06

The composition in the inclusion was quantified and compared to the surrounding bulk perovskite as it is summarized in Table 5.3. The composition of the surrounding bulk perovskite is in good agreement with results obtained on pristine CsMAFA, while the inclusion shows significantly higher Br and Cs content. Interestingly, its Cs/Pb ratio reaches 0.16, which may be questionable given the weak $Cs_{L\beta}$ line in the EDS spectrum shown in Figure 5.13(d). The Cs content may have been overestimated due to the overlap of $I_{L\alpha}$ and $Cs_{L\alpha}$ lines, as discussed in Chapter 2. At this stage, it can only be concluded qualitatively that the inclusion exhibits higher Br and Cs content than the surrounding bulk material.

Thus, the chemical analysis of the inclusion has been continued using STEM-EDS, which is more accurate spatially.

Chemical analysis with STEM-EDS

A lamella was prepared on the device in a location where PTAA and gold remained. Figure 5.14 shows the results obtained on this lamella with (STEM)HAADF imaging (a), EDS mapping (b), and EDS linescan (c).

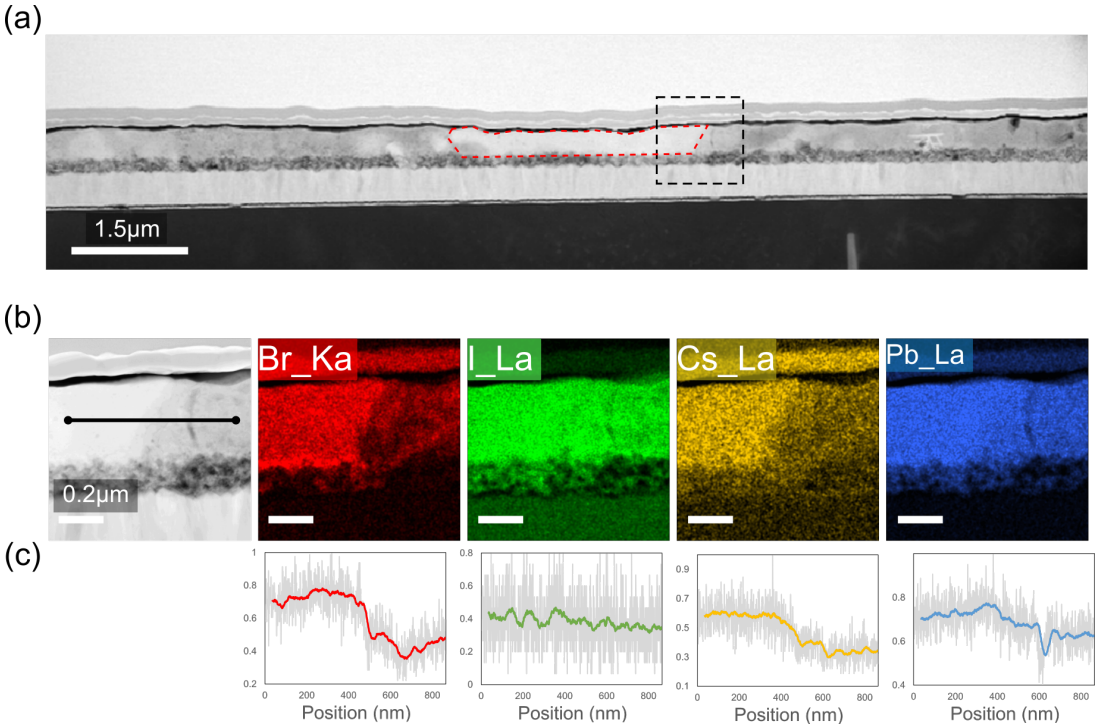

Figure 5.14: *(a) STEM-HAADF image of the lamella studied. The constitutive layers of the PSC are specified along with the position of the following EDS map (dashed square).(b) HAADF image showing the path used to obtain the EDS linescan in (c), and the corresponding elemental maps showing the distribution of $Br_{K\alpha}$, $I_{L\alpha}$, $Cs_{L\alpha}$, and $Pb_{L\alpha}$ X-rays in (b).*

The inclusion (delimited by the red dashed line) exhibits a higher contrast than the surrounding perovskite in the HAADF image presented in Figure 5.14(a). Such variation of contrast in HAADF images could be related to a local increase in density, as discussed in Chapter 2.

The image also highlights that the inclusion occupies the full depth of the active layer and is in contact with the m-TiO_2. Its thickness is smaller than the rest of the specimen; hence we confirm that the topography variations in Figure 5.6(b) are indeed caused by the formation of the inclusion.

STEM-EDS measurement was performed in the region delimited by the dashed-black square in Figure 5.14(a). The obtained qualitative EDS maps and profiles (see Figures 5.14(b) and (c)) show higher concentrations of Br, Cs, and Pb in the inclusion than in the surrounding film. These findings are well aligned with the qualitative SEM-EDS maps presented previously, except for I content which appears constant on the whole map.

The analysis of the inclusion and its vicinity was carried further with EDS measurements on three regions of the lamella regions displayed in the HAADF images of Figure 5.14(b). The first (1) is 3 μm distant from the inclusion, the second (2) is 1.5 μm, and the third (3) is inside the inclusion.

I and Br maps from each zone are displayed in (c) and (d), respectively. The halide distribution is laterally and vertically homogeneous in the perovskite film of the zone (1).

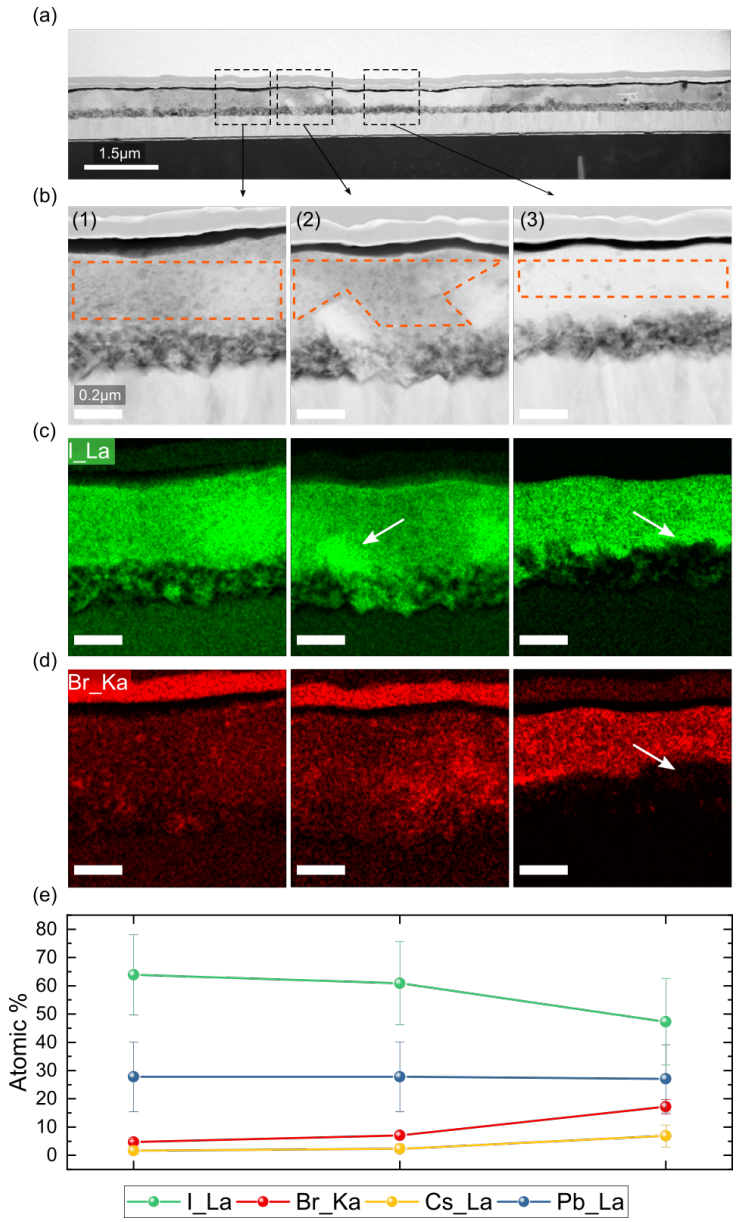

Figure 5.15: *(a) STEM-HAADF image of the lamella studied showing the areas analyzed with EDS. Corresponding HAADF, $I_{L\alpha}$ and $Br_{K\alpha}$ element maps are presented in (b), (c), and (d), respectively. The compositions of the areas delimited in (b) are quantified, plotted in (e) and summarized in Table 5.4.*

A region with an increased concentration of I is visible in the zone (2), indicated by a white arrow. This region is likely a PbI_2 particle formed by the photo-oxidation of the perovskite due to m-TiO_2, as mentioned in Chapter 1.

Zone (3) exhibits strong I enrichment and Br depletion in the region indicated by white arrows. Given its position, that may also be a PbI_2 particle formed at the interface between perovskite and m-TiO_2 layers. Interestingly, the m-TiO_2 is empty beneath the inclusion. The formation of the inclusion could be related to this lack of material.

The EDS spectrum is averaged over pixels in the areas delimited by a dashed line in the HAADF images of Figure 5.15(b) (circumventing the PbI_2 particle in (2)). The concentrations of I, Br, Cs, and Pb are then determined with the Cliff-Lorimer method. Table 5.4 and Figure 5.15(e) present the concentrations obtained compared to results from pristine CsMAFA.

Table 5.4: *Quantification of the element content from EDS analysis performed in three regions of the lamella displayed in Figure 5.15.*

Regions	(1)	(2)	(3)	CsMAFA
$I_{L\alpha}$	63.9±14.2	60.9±14.6	47.3±15.3	53.9±14.4
$Br_{K\alpha}$	4.7±0.9	7.0±1.3	17.2±2.6	16.1±1.2
$Cs_{L\alpha}$	1.7±1.1	2.3±1.5	6.8±3.9	1.4
$Pb_{L\alpha}$	27.8±12.3	27.8±12.3	27.1±12.1	27±12.1
Regions	(1)	(2)	(3)	CsMAFA
I/Pb	2.48±0.80	2.36±0.79	1.90±0.71	2.17±0.75
Br/Pb	0.18±0.06	0.27±0.08	0.68±0.20	0.63±0.16
Cs/Pb	0.07±0.03	0.09±0.05	0.28±0.13	0.05

The zones (1) and (2) are located within a distance of less than 2 μm from the inclusion. Therefore, it can be inferred that regions (1) and (2) fall within the red-shifted area surrounding the inclusion (see Figure 5.13). The concentration of I in these zones is significantly higher than that in pristine CsMAFA, as shown in Table 5.4. This result is consistent with the observations made using SEM-EDS and explains the red-shift in the CL peak.

The inclusion in (3) exhibits higher Cs and Br concentrations than pristine CsMAFA. Besides, it is likely that the inclusion still follows the ABX_3 configuration. Therefore, the Cs/Pb ratio of 0.28 suggests that the A-site is occupied not only by Cs^+ but also by organic cations such as FA^+ and MA^+. As mentioned in Chapter 1, MA^+ cations are more likely to escape from the perovskite framework due to its smaller ionic radius [279]. It can then be assumed that FA^+ cations fill the remaining A-sites of the inclusion composition, resulting in the following: $Cs_{0.28}FA_{0.72}Pb(I_{0.74}Br_{0.26})_3$.

According to previous studies, perovskite films with a similar composition and structure exhibit a bandgap of approximately 1.73 eV [29, 94, 280]. It would result in a PL/CL emission peak at around 715 nm, significantly different from the CL peak measured at 768 nm in the inclusion.

Goldschmidt tolerance factor t was calculated for this composition based on Equation 1.1. The resulting value is 0.95, indicating that it is likely to form a stable photoactive perovskite phase (cubic or tetragonal), as it has been previously reported in the literature [20].

In this subsection, we used SEM and STEM-EDS to analyze the composition of an inclusion and its surrounding. We confirm with the BSE image that the near-inclusion area does not exhibit any PbI_2 clusters. This region demonstrates an enrichment in I content consistent with the red-shift of the emission peak. We have hypothesized the inclusion composition using EDS in STEM. From these hypothetical compositions and the Goldschmidt tolerance factor, we predict that the inclusion crystallizes in perovskite cubic or tetragonal symmetry.

5.2.6 Crystalline structure of the inclusion analyzed by SAED

Apart from the prediction made with the tolerance factor, information on the crystal structure of the inclusions is lacking. Indeed, the XRD did not provide evidence of any new phase emerging after the aging of the PSC. The number of inclusions in the area probed by XRD (~ 1 cm^2) might not be sufficient to appear in the diffractogram. Localized structural measurements, i.e.,

SAED, were then performed on the inclusion inside the prepared lamella (delimited red zone in Figure 5.14).

SAED was performed on the sample oriented in two distinct directions. Figure 5.16(a) presents the two electron diffraction patterns obtained, oriented along these two different zone axis[2]. These patterns show regular arrays of bright spots, indicating that the inclusion is a single crystal.

EDS measurements and tolerance factor calculation have suggested that the inclusion crystallized in a cubic or tetragonal phase. To identify the crystal structure, the electron diffraction patterns were indexed by fitting them with simulated diffraction patterns of known structures, as shown in Figure 5.16. The simulated diffraction patterns were generated using cubic ($P1$) and tetragonal ($P4/mbm$) structures of $FAPbI_3$ from the work of Doherty et al. on CsMAFA perovskite [77]. The sum-of-square error (Σs^2) made during the fit on the intereticular distances is summarized in Table 5.5 and expressed in mm^2.

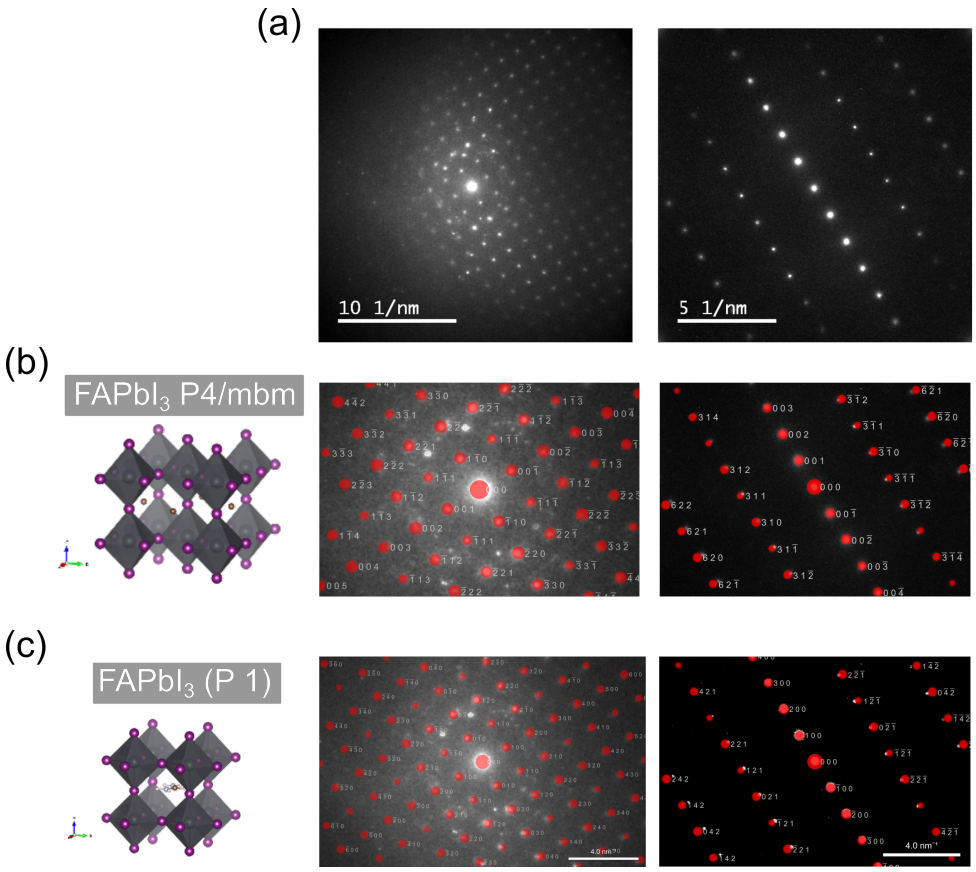

Figure 5.16: *(a) Electron diffraction patterns acquired on the inclusion oriented in two distinct zone axis. (b) Atomic representation of the $FAPbI_3$ tetragonal structure used to simulate electron diffraction patterns, represented on the left in red, and superimposed on experimental electron diffraction patterns. (c) Representation of the $FAPbI_3$ cubic structure and the corresponding simulated electron diffraction patterns. The differences between simulated and experimental diffraction patterns Σs^2 are given in Table 5.5.*

The first diffraction pattern shows more diffraction spots with smaller distances between them than the second diffraction pattern. The former corresponds to a zone axis with a lower

[2]high-symmetry orientation in a crystal structure

Table 5.5: *Summary of the zone axis [uvw] used for indexing the electron diffraction pattern and the corresponding root-mean-square error made on the fit with simulated diffractogram of presumed crystal structures taken from literature [149, 281].*

Composition	Structure (Space group)	[uvw] Σs^2 (mm^2)	[uvw] Σs^2 (mm^2)
$FAPbI_3$	Cubic ($P1$)	[001] 0.159	[0-12] 4.167
$FAPbI_3$	Tetragonal ($P4/mbm$)	[110] 0.005	[1-30] 2.470

index and thus holds more information on the crystal structure [162].

Both phases match the first diffraction pattern perfectly, although the error is lower with the tetragonal phase (0.005 mm^2) than with the orthorhombic. For both phases, the error is more significant for the second diffraction pattern. But the tetragonal phase shows the lowest error between the two.

The two phases are close symmetries that electron diffraction might not be able to distinguish firmly [162]. Therefore, we cannot conclude in which symmetry the inclusion crystallized. However, we confirm that its crystalline structure shows a highly symmetrical orientation consistent with the tolerance factor predictions.

Electron diffraction confirms the single-crystal nature of the inclusion. From the indexation of a diffractogram, we conclude that the inclusion is not composed of the perovskite δ-phase. However, it remains challenging to distinguish which in which crystallographic symmetry inclusions crystallize.

Conclusion of the section

After aging, the macroscopic analysis of the PSC showed a slight loss in QE, although no degradation phase was evidenced in the XRD diffractogram. Microscopic investigation of the CsMAFA film showed the presence of impurities in the active area. They exhibit low luminescence and are surrounded by red-shifted perovskite and no PbI_2 clusters. By studying their chemical composition with STEM-EDS, we draw their hypothetical composition richer in Br and Cs than native perovskite. We showed with localized diffraction that they are composed of mono-crystal highly symmetrical. The following section will discuss their appearance during the PSC aging.

5.3 Discussions about the formation of inclusions

In the previous section, we analyzed the CsMAFA film after aging in solar cell configuration. The results opened some questions on the mechanisms of the inclusions formation and their impact on solar cell performances. In the following section, we attempt to rationalize the mechanism of inclusion appearance by considering the interplay of several factors.

5.3.1 Inclusions formation

The role of ion migration

Figure 5.17(a) illustrates the first proposed mechanism driven by ion migration. As previously discussed in Chapter 1, I^- ions are known to migrate throughout perovskite films exposed to

light. This leads to the complete demixing of the CsMAFA film, resulting in the formation of I-rich and Br-rich regions. The I-rich region corresponds to the red-shifted region near the inclusion, which showed iodine enrichment. The Br-rich region might correspond to a first "state" of the inclusion that also showed bromine enrichment.

This study has also shown that the inclusion contains a significant amount of Cs. Given that A-site cations are known to migrate in hybrid perovskite films under certain conditions, we propose that after halide migration, Cs^+ cations migrate towards the Br-rich region (see (3) in Figure 5.17). This would result in a depletion of Cs surrounding the inclusion, which is also consistent with the observed red-shift in this region.

The Cs and Br-rich region that is obtained is eventually recrystallized into a single crystal. This phenomenon within the perovskite layer has not been widely reported in the literature. It is worth noting that Lu et al. observed the formation of needle-like structures in PSCs under operation and exposed to humid air [282]. However, the reasons behind the transformation of the polycrystalline film into a single crystal are still unclear.

As mentioned in Chapter 1, the migration of ions during PSC aging is likely driven by multiple stress factors, including light exposure. According to Li et al., light-generated carriers can provide enough energy for Cs^+ cation migration, leading to the formation of a non-photoactive Cs-rich phase [102]. However, other studies, such as the work by Pavlovtec et al., have suggested that voltage bias is also necessary to drive the migration of cations [98].

In this case, the inclusions were observed only in the active area of PSC where a voltage bias was applied during the aging (see Figure 5.8). They thus may require voltage bias to form.

In addition, local electric fields and strains induced by halide segregation may also play a role in driving Cs migration [101, 111, 283]. In fact, first-principle calculations by Schelhas et al. have shown that halide demixed perovskites are more favorable to cation migration and segregation [266].

The role of PbI_2 clusters photolysis

The absence of PbI_2 clusters in the region near the inclusion suggests that they play a role in the formation of the red-shifted region and the inclusion. Figure 5.17(b) illustrates a second proposed mechanism based on the photo-decomposition PbI_2. This process is triggered by incoming light, which has been shown to decompose PbI_2 into metallic Pb^0 and volatile iodine I_2 through trap-assisted redox reactions (vacancies $V_I{}^+$ and $V_{Pb}{}^{2-}$) [256]. In this case, rather than forming I_2, it is proposed that the I^- ions may have moved and entered the CsMAFA lattice, replacing Br^- and $V_{Br}{}^+$ and resulting in enrichment in I concentration. This enrichment is then believed to be responsible for the red-shift of the area, as illustrated in stage (3) of Figure 5.17(b).

The enrichment of I may also have catalyzed the degradation of adjacent perovskite material by reducing the organic cations MA^+ and FA^+ (see the stage (4)), as reported by Donakowski et al. [284]. The resulting volatile species would be lost by the film as gases, leading to higher concentrations of Cs and Br in the inclusion. This hypothetical mechanism suggests that the red-shifted region is a temporary state of the CsMAFA perovskite degradation and will eventually turn into inclusion composition.

PbI_2 photo-decomposition also implies that metallic Pb^0 impurities remain where clusters were. Without the means to observe these Pb_0 impurities directly, we cannot definitively confirm that this mechanism is the one that occurs.

Both mechanisms described here raise several open questions. One is the whereabouts of the volatile species in the PSC. It has been reported in the literature that volatile species such as MAI, HI, or I_2 can escape from the CsMAFA film through Spiro-OMeTAD when the PSC is exposed to light [285], and voltage bias [286]. These species may corrode the gold contact layer, as mentioned in Chapter 1. A similar phenomenon may have occurred with PTAA in this case. Finally, it is highly probable that both mechanisms simultaneously formed the inclusions in the perovskite layer.

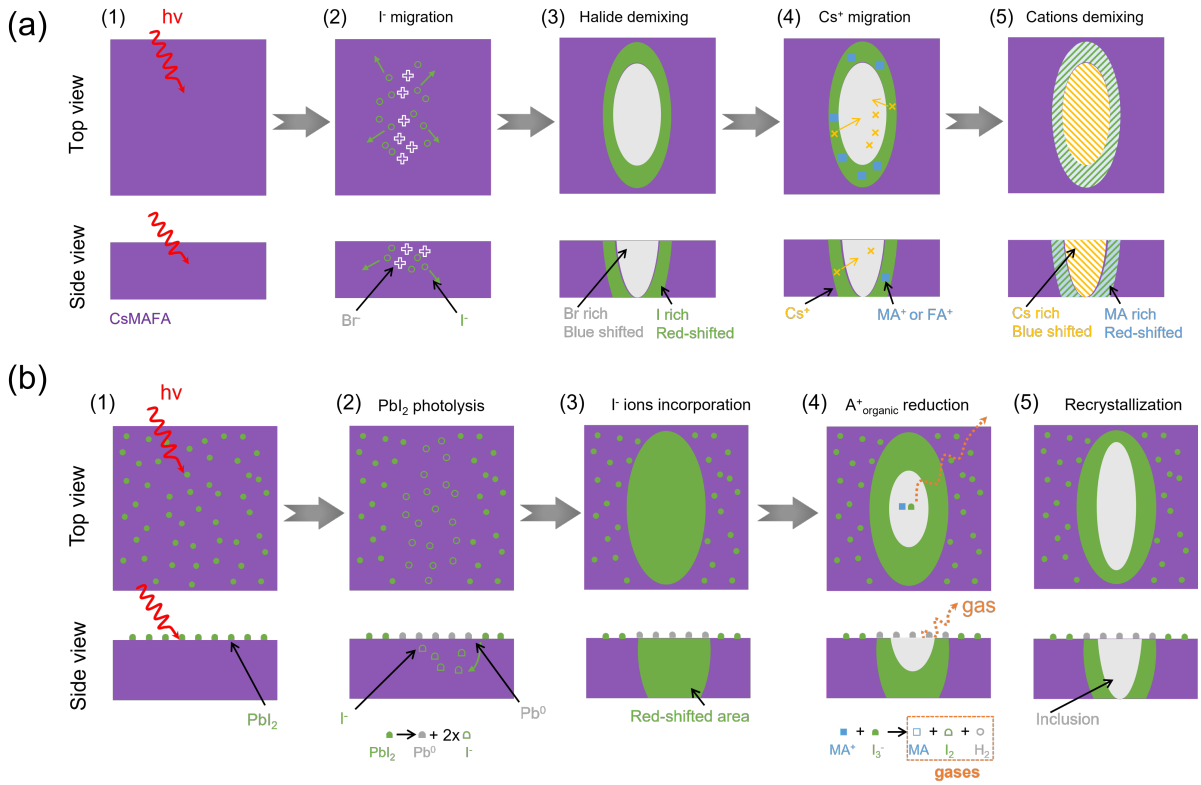

Figure 5.17: *Illustrations of photochemical mechanisms induced in CsMAFA perovskite films during operation. (a) Schematic showing the phase segregation supposed to form the photoinactive inclusion and the red-shifted area around. As the specimen is illuminated, I^- moves to form I-rich and Br-rich phases. These two phases are enough to explain the appearance of a red-shifted area in the vicinity of the inclusion but the high concentration of cesium within the inclusion. We propose the following mechanism based on cesium migration towards the Br-rich area. (b) PbI_2 photolysis generates atomic iodine, which reacts with mobile organic cations, MA^+ (or FA^+). The reaction indicated produces MA (or FA), I_2, and H_2 in gaseous form. It raises the question of how the gases could escape from the perovskite film encapsulated by PTAA and gold layers.*

The role of TiO_2

We observed and discussed in the previous section the decomposition of the perovskite into PbI_2 at TiO_2 interface in aged PSCs. The emergence of such degradation products at this location has been attributed to trapped charges promoting the deprotonation of perovskite organic cations [287]. The PbI_2 particles produced may promote further decomposition of the perovskite.

The role of the TiO_2 in the inclusion formation remains unclear. However, the poor filling of the m-TiO_2 under the inclusion, as shown in Figure 5.15, may suggest that they are related. It is possible that the poor filling of m-TiO_2 promotes the degradation of the capping perovskite layer.

5.3.2 Impact of changes in the perovskite film on the PSC performance

In Section 5.1, it was observed that the J_{MPP} of the heated PSC decreased by approximately 9% during 1000 hours of aging. This evolution is likely related to various changes in the PSCs and the perovskite film.

The presence of inclusions composed of a high bandgap Cs-rich phase is a possible explanation for this decline. Previous research has demonstrated that such phases can block current and be photo-inactive [102]. Our findings indicate that these inclusions occupy about 5% of the active area (see Figure 5.8), potentially reducing the output current of the PSC by a similar amount.

In the previous section, it was demonstrated that the mechanism of inclusion formation involves halide and cation segregation. These phenomena have been known to hinder optical absorption in perovskite films, as reported in the literature [28]. The reduction in EQE and the subsequent loss in output current observed in our study may therefore result from such segregation. Besides, it has been reported that phase segregation reduces the V_{oc} of PSCs due to the formation of low-bandgap regions [94, 171, 266].

The formation of heterogeneities in the film creates new boundaries and defects, which may also weaken the photo-generated carrier lifetime and thus the V_{oc}.

The presence of PbI_2 particles at the interface between the perovskite and TiO_2 likely harmed the performance of the PSC. As a photo-inactive material, PbI_2 may have reduced the photo-generated current of the PSC and inhibited the extraction of photo-generated electrons from the absorber. The instability caused by the use of TiO_2 highlights the need to explore more stable oxide alternatives, such as SnO_2 [99, 288].

5.4 Conclusions

In this chapter, we conducted an analysis of the stability of CsMAFA-based perovskite solar cells (PSCs) under operating conditions. The composition and deposition process of the perovskite film were optimized through the incorporation of SCN^- ions and a warm-up step of the precursor solution to enhance the long-term stability of the PSCs. The optimal devices were then evaluated under ISOS-L1 conditions, which consisted of maximum power point (MPP) measurements under illumination and a N_2 atmosphere, for over 1000 hours. Despite the remarkable stability of the MPP power output for both devices, with less than a 10% decline after 1000 hours, the results indicated a slight decrease in generated current over the aging period.

Subsequent nanoscale characterization of the aged PSCs using electron microscopy techniques, such as STEM-EDS, SEM-EDS, and CL, revealed the presence of non-luminescent inclusions within the perovskite film. These inclusions were identified as a potential cause for the observed decline in current over time. Through the analysis of these inclusions, we determined their composition to be $Cs_{0.28}FA_{0.72}Pb(I_{0.74}Br_{0.26})_3$. We also proposed potential mechanisms for their emergence in the perovskite films, including phenomena such as ion migration and PbI_2 cluster photolysis, which were driven by light exposure and voltage bias.

In conclusion, this study demonstrated that the interplay between PbI_2 cluster decomposition and ion migration within the perovskite film can have a significant impact on the performance of PSCs and must be mitigated to enhance their stability. One potential strategy to improve stability is to reduce the amount of PbI2 in the precursor solution. Additionally, methods suppressing cation and halide migration, such as reducing defect density in the perovskite film, can also be implemented to improve the stability of PSCs as discussed in Chapter 1.

This chapter also highlighted the benefits of combining J-V measurements of a PSC with nanoscale analysis of its absorber layer. The use of electron microscopy techniques provided valuable insights into the structural and compositional changes that occur within the perovskite film. This approach can be useful to identify the underlying causes of performance degradation and to develop strategies to improve the stability of PSCs.

In further studies, the same approach could be applied to CsMAFA-based PSC with reduced PbI_2 compositions to assess clearly the role of PbI_2 in inclusion formation. The same aging procedure is already implemented on various configuration developed at IPVF such as p-i-n PSCs, CsFA-based solar cells, to more stable devices.

The electron microscopy can also be correlated with other chemical analysis techniques, such as localized XPS measurements to provide an assessment of the composition of light elements such as C and N (constituents of MA^+ and FA^+) in the inclusions and their vicinity.

Additionally, high-level optical analysis techniques, such as Time-Resolved PL imaging (TRPL) can be employed to analyze the lifetime of charge carriers in the vicinity of the inclusions, thereby providing a direct link between the emergence of inclusions and the evolution of the PSC performance.

Further investigation of the role of PTAA on performance decline may be worthwhile. One potential approach would be to re-fabricate the solar cell after removing the PTAA and Au layers, similar to the method reported by Planes et al. [277] and compare the performance with the samples before re-fabrication. This could provide valuable insight into the specific role of PTAA in the degradation of PSC performance

General conclusion

Hybrid halide perovskite films such as CsMAFA hold immense potential for photovoltaic applications, but their instability is a major obstacle, hindering their commercialization. As discussed in Chapter 1, the instability of mixed-halide mixed-cation lead-based perovskites such as CsMAFA, manifests through phase segregations due to ion migration, phase transitions resulting in intrinsic instability, or species volatilization. These processes occur at the nano- and micro-scale within the film and significantly impact the performance of photovoltaic solar cells.

In this thesis, we aim to unveil the degradation mechanisms of CsMAFA perovskite films using correlative electron microscopy analytical techniques including energy dispersive X-ray spectroscopy (EDS), cathodoluminescence (CL), and selected area electron diffraction (SAED). In Chapter 2 we introduced the instruments used in this work, and we discussed their spatial resolution. The role of the electron dose in e-beam induced degradation was also addressed, and we outlined the conditions adopted to minimize damage. In addition, we presented in detail the calibration procedures performed for SEM-EDS (PhiroZ) and STEM-EDS (Cliff and Lorimer) measurements.

The unique aspect of our approach is the combination of these high-spatial resolution techniques, which allows the correlation of structural, chemical, and optoelectronic properties of the samples. We have first applied this approach to analyze inorganic cesium-based perovskites $CsPbBr_3$ and $CsPb_2Br_5$, then to study degradation products of aged CsMAFA perovskite films, and finally to investigate CsMAFA films inside a PSC operated for 1000 hours.

Analysis of $CsPbBr_3$ and $CsPb_2Br_5$ perovskite phases

In Chapter 3, we presented the results of SEM-EDS, PL, and CL measurements performed on a heterogeneous $CsPbBr_3$ film and $CsPb_2Br_5$ micro-crystals.

The $CsPbBr_3$ film composition was first confirmed by SEM-EDS measurements. Then, PL measurements revealed a green emission, which we attributed to the $CsPbBr_3$ tetragonal phase. Finally, CL measurements revealed two emission peaks: one at high energy, related to band-to-band recombination, and the second at lower energy, related to shallow defect-mediated recombination. Further CL measurements at low temperatures showed that the intensity of the high-energy peak is reduced by a thermal effect at room temperature. We determined the activation energy of this phenomenon, and we discussed its potential origins. These results are in good agreement with previous studies on $CsPbBr_3$ samples, especially regarding the evolution of the bandgap with temperature. In this study we provide one of the few reported studies of $CsPbBr_3$ perovskites with CL at low temperature.

We presented a similar study on $CsPb_2Br_5$ micro-crystals whose composition was also confirmed by SEM-EDS. PL measurements also revealed a green emission in these micro-crystals. This green emission in $CsPb_2Br_5$ causes a strong debate in the literature, since the theoretical bandgap is larger. CL measurements revealed two broad emission peaks: a low-energy peak that does not vary with temperature (attributed to a deep-defect recombination), a high-energy peak that varies with temperature (attributed to a band-to-band recombination). We noticed that the energy of the CL peak varies more with temperature than that of $CsPbBr_3$. Therefore, we assumed that the high-energy peak does not originate from residual $CsPbBr_3$ in $CsPb_2Br_5$

micro-crystals. Caicedo et al. observed a similar peak and attributed it to defects located at the $CsPbBr_3/CsPb_2Br_5$ interface [289]. Our SEM-EDS results showed that the micro-crystals have a homogeneous composition distribution excluding the hypothesis of Caicedo et al. in these samples.

Although we do not provide an explanation for the green luminescence in $CsPb_2Br_5$, this work feeds the ongoing debate on their optoelectronic properties with new experimental results.

Effect of moist air on CsMAFA perovskite thin films

In Chapter 4, we presented a study of the CsMAFA perovskite film degradation under air with high relative humidity (85% RH). We analyzed the degradation products formed through correlative high-resolution characterization techniques mentioned before (CL, SEM-EDS, STEM-EDS, and SAED). We identified three different compositions resulting from the interaction of CsMAFA perovskite with water molecules: PbI_2, $CsPb(I_{0.9}Br_{0.1})_3$, and $CsPb_2(I_{0.7}Br_{0.3})_5$.

A series of degradation pathways have been proposed to explain the formation of these phases. First, phase segregation may have occurred in the film, resulting in the formation of I-rich and Cs-rich regions. We assume that the I-rich regions have decomposed into pure PbI_2 crystals after volatilization of organic cations in gaseous form. We then suggest that the Cs-rich regions have also decomposed into $CsPb(I_{0.9}Br_{0.1})_3$ through volatilization of organic cations. Finally, we propose that this phase underwent a phase transition and transformed into $CsPb_2(I_{0.7}Br_{0.3})_5$ due to the action of water molecules.

In order to understand the impact of light on degradation, we also performed aging of CsMAFA perovskite films under coupled stress factors, including 1-sun illumination, heat (50°C), air, and humidity (55%). Our examination of the samples morphology indicated that light intensifies the degradation, which supports our hypothesis that phase segregation is the driving force behind degradation.

Furthermore, we analyzed the degradation products of a CsMAFA film exposed to N_2 and 85% RH. The small size of the degradation products, and their composition demonstrate the dramatic effect of oxygen in the degradation mechanisms described before.

Degradation of the perovskite thin film in a PSC operating during 1000 hours

In Chapter 5, we presented PSCs demonstrating a remarkable long-term stability with a T_{80} > 1000 hours under continuous 1-sun illumination and at MPP. After the stability test, the CsMAFA perovskite films that constitute the PSCs were analyzed by electron microscopy techniques, which revealed the presence of non-luminescent inclusions. We attributed the minor losses in the output current of the PSCs during the stability test to the formation of these inclusions. Through EDS measurements, the composition of these inclusions was estimated to be $Cs_{0.28}FA_{0.72}Pb(I_{0.74}Br_{0.26})_3$. We proposed pathways to explain their formation, including photolysis of PbI_2 clusters and the ion migration (halide and cation) in the film due to the illumination and the voltage bias.

Based on our findings, we provided strategies to prevent the formation of inclusions and subsequent losses in PSC performances. Reducing the amount of PbI_2 in the precursor solution can improve the stability of the PSC, although it may reduce the performance. Suppressing the cation and halide migration in the perovskite film would also be beneficial for PSC stability and can be achieved by reducing the defect density. In addition, exploring single cation or single halide perovskite compositions could also be beneficial for the device stability, as long as the phase stability of the photo-active perovskite is ensured.

This work demonstrated the benefits of combining J-V measurements and microscale characterizations for analyzing PSC degradation. We correlated variations in perovskite film composition and optoelectronic properties with variations in PSC electrical performance. The top-view measurements implemented in this work required the peeling of the PTAA contact layer and

the Au electrode. As we discuss in the Perspectives section, other methods could be used to prepare PSC cross-sections and perform in-depth measurements.

Perspectives

This thesis opens several perspectives regarding the characterization, the understanding, and the mitigation of hybrid perovskite film degradation. In the following paragraphs, we detail the future works that can be done to further develop the analytical techniques used and the understanding of the degradation mechanisms.

Characterization techniques

As a first perspective, we would propose to perform SEM-EDS and CL measurements on the same region of a PSC cross-section. These measurements would allow to examine the perovskite film in the solar cell architecture, i.e. between the charge transport layers. As the optoelectronic and structural properties as well as the degradation mechanisms of the perovskite film can be modified by the presence of adjacent layers, the characterization of such cross-sectional samples is particularly relevant. In addition, we could reveal the in-depth variations of the optical, chemical, and structural properties of the perovskite film. However, these measurements require a clean cross-section and therefore a specific sample preparation.

We attempted to prepare cross-sectional samples using an argon-based ion milling system from Hitachi (ArBlade 5000) to clean the cross-sectional surface of cleaved PSCs. Although the results were encouraging, further optimization is needed to prepare a wide, undamaged, and workable cross-section. Further optimization of the CL acquisition parameters is also required to collect sufficient CL signal to resolve spatial variations in the CL maps. With additional efforts, we believe that this approach will provide interesting insights into the in-depth distribution of optoelectronic properties.

Electron Beam Induced Current (EBIC) measurements could also be performed on these PSC cross sections using the capabilities of the Merlin SEM and the Chronos CL set-up. These measurements would provide valuable information on charge carrier transport and extraction in PSC devices.

In Chapter 4 we used an aging set-up that enables *in-situ* observations and measurements during the aging process. Moreover, both the Merlin SEM at IPVF and the Quanta[3] SEM at EDF Lab possess the capability for *in-situ* SEM imaging, as they can operate in a partial vacuum. This allows to modify the atmosphere inside the SEM chamber by adding of O_2, N_2 gases or water vapor, while monitoring the transformation of the film morphology.

Conducting *in-situ* measurements is a major perspective of this work, as it enables to study the kinetics of degradation mechanisms under specific stress factors. Through these measurements, we could also confirm the hypothesized lineage between degradation products such as needles and "flowers". These measurements would provide insight into the early stages of Cs-MAFA degradation and strengthen our current understanding of the degradation mechanisms.

When estimating the composition of samples using EDS, we encountered one of the major limitations of this technique, which is the detection of light elements contained in organic cations MA^+ and FA^+. Therefore, the incorporation of other techniques such as X-ray photoelectron spectroscopy (XPS), electron energy loss spectroscopy (EELS), solid-state NMR spectroscopy, or time-of-flight secondary ion mass spectrometry (TOF-SIMS) into our study could provide

[3]FEI Quanta 650 FEG

helpful information regarding the concentration in organic cations.

As mentioned in chapter 2, the CL instrument is equipped with a pulsed emission gun (pulsed e-beam mode), which enables time-resolved CL (TRCL) measurements. The latter allows the analysis of the charge carrier recombination dynamics in the investigated samples. In addition, according to Ferrer-Orri et al., operating in pulsed e-beam mode for steady-state analysis can help minimize e-beam-induced damage to CsMAFA perovskite films [184].

Working with this configuration of the CL instrument is particularly promising for the analysis of phases in the Cs-Pb-Br material system, which exhibited better e-beam stability. Nevertheless, these measurements require careful optimization of the acquisition parameters, as the CL intensity emitted by the sample is significantly reduced.

We have shown in this work that although electron microscopy is a powerful tool, precautions must be taken to avoid damaging hybrid perovskite materials. The recent development of more efficient detectors for analytical measurements, such as EDS and Scanning Electron Diffraction (SED) (similar to Orientation Imaging Microscopy), has allowed for low-dose acquisitions in TEM without sacrificing information [77]. These new technologies have already shown impressive results for high-resolution correlative composition and crystallographic mapping, and promise to further advance in our understanding of hybrid perovskite materials at the nanoscale.

Aging of innovative perovskite films

In the future, we plan to continue our investigation into the stability of hybrid perovskite films by aging other compositions using the methods outlined in Chapter 4. This will help us to gain a better understanding of the stability of these materials, which can be combined with the analysis of the stability of PSCs in operation, as described in Chapter 5. Our efforts will be focused on promising perovskite compositions, such as on $CsPbI_3$ (PhD project of Lauriane Scherrer) and 2D-capped CsMAFA perovskite (PhD project of Thomas Campos).

It is worth mentioning that we have already conducted aging experiments at 85% RH on $Cs_{0.17}FA_{0.83}Pb(I_{0.8}Br_{0.2})_3$ perovskite films deposited by a slot die process at IPVF (PhD project of Celia Aider). First observations showed the appearance of degradation products similar to those described for CsMAFA perovskite films.

In describing the results of this work, we have also highlighted a number of characterization tools that operate at high spatial resolution to probe perovskite properties. It is our hope that the methods and approaches outlined will be adopted and further developed by others to perform even more insightful investigations.

Resumé en français

Introduction

En août 2021, le Groupe d'experts intergouvernemental sur l'évolution du climat (GIEC) des Nations unies a publié la première partie de son sixième rapport d'évaluation, qui démontre sans équivoque la corrélation entre les activités humaines du siècle dernier et le réchauffement climatique [1]. Pour atténuer les effets du réchauffement climatique et éviter une augmentation des températures moyennes mondiales supérieure à 1,5°C par rapport aux niveaux préindustriels (objectif de l'accord de Paris sur le climat de 2015), il est nécessaire de réduire les émissions de gaz à effet de serre tels que le dioxyde de carbone, principalement généré par la consommation de combustibles fossiles comme le charbon, le gaz et le pétrole.

Les systèmes photovoltaïques sont un moyen de convertir directement l'énergie renouvelable du soleil en électricité utilisable. Le photovoltaïque représentait en 2021 3,6% de la production mondiale d'électricité (1002,9 TWh) avec 885 GW de capacité PV installée. Afin d'atteindre les niveaux d'émissions de gaz à effet de serre impliqués par l'objectif de 1,5°C, on estime qu'environ 600 GW de capacité PV doivent être installés chaque année d'ici 2030 [3].

La baisse des coûts de l'électricité photovoltaïque due à l'augmentation des rendements de conversion énergétiques, rend cette énergie de plus en plus attractive. Alors que les cellules solaires en silicium dominent actuellement le marché du photovoltaïque (95% de la production mondiale), elles s'approchent de façon critique de leur limite théorique d'efficacité qui s'élève à 30%. Les chercheurs se tournent vers de nouvelles technologies photovoltaïques susceptibles d'offrir un meilleur rendement ou de réduire les coûts de production afin de continuer à faire baisser le coût de l'électricité photovoltaïque.

L'utilisation de matériaux semi-conducteurs à bande interdite direct conjointement avec des cellules solaires silicium offre la possibilité de créer des cellules à jonction multiples comme les tandems (double jonction), qui peuvent récolter efficacement une plus grande partie du spectre solaire et ainsi dépasser la limite théorique des cellules à simple jonction.

Dans ce contexte, les matériaux pérovskites hybrides organique-inorganique à base de plomb sont devenus le fer de lance de la recherche sur le photovoltaïque. Les cellules solaires pérovskite (CSP) ont atteint en un temps record des rendements compétitifs avec les cellules solaires silicium (en simple jonction 25.7%) et au delà (en tandem sur silicium 32.5% [5]). De plus, elles bénéficient d'un faible coût de production.

Cependant, les CSPs présentent le défaut majeur d'être particulièrement instable, car elles sont affectés affectées par l'instabilité intrinsèque de la couche de pérovskite. Surmonter leur instabilité est un défi critique pour la commercialisation de cette technologie.

Les pérovskites hybrides sont particulièrement sujettes à la dégradation lorsqu'elles sont exposées à l'humidité, à l'oxygène, à la chaleur, au courant appliqué et à la lumière. Ces facteurs peuvent affecter considérablement la durée de vie des CSPs, ce qui les rend inadaptés aux applications photovoltaïques. Actuellement, d'importants travaux de recherche sont consacrés à la résolution de ces problèmes et les CSPs commencent à faire preuve d'une meilleure stabilité. Cependant, des efforts supplémentaires sont nécessaires pour atteindre le niveau de stabilité requis à la commercialisation de cette technologie.

Afin de développer des CSPs efficaces, peu coûteuses et stables, il est crucial de comprendre les mécanismes par lesquels les facteurs de stress externes affectent les matériaux pérovskites hybrides. L'objectif de ce travail est de mieux comprendre ces mécanismes en analysant les produits de dégradation formés dans des films de pérovskite vieillis. Pour ce faire, nous avons appliqué des techniques de microscopie électronique telles que la cathodoluminescence et la microanalyse de rayons X (EDS) dans un microscope électronique à balayage (MEB) et un microscope électronique à transmission (TEM) sur des films de pérovskite $Cs_{0.05}(MA_{0.15}FA_{0.85})_{0.95}Pb(I_{0.83}Br_{0.17})_3$ (CsMAFA) et des cellules solaires tout deux vieillis. En couplant ces méthodes de caractérisation locale et en corrélant les résultats obtenus, nous visons à identifier les causes sous-jacentes de la dégradation et à proposer des stratégies pour le développement de CSPs plus stables.

Optimisation des techniques de microscopies électroniques pour l'analyse de film de pérovskite hybrides

Dans cette thèse, nous visons à dévoiler les mécanismes de dégradation des films de pérovskite CsMAFA en utilisant des techniques analytiques corrélatives de microscopie électronique.

Dans le chapitre 2, nous avons présenté les instruments utilisés dans ce travail, et nous avons discuté de leur résolution spatiale. Le rôle de la dose d'électrons dans la dégradation induite par le faisceau d'électrons a également été abordé, et nous avons décrit les conditions adoptées pour minimiser les dommages.

La dégradation induite par le faisceau d'électrons des matériaux hybrides en pérovskite a été étudiée en utilisant l'imagerie MEB et la cartographie CL. L'analyse a révélé que la dégradation était principalement due à la radiolyse, indiquant que la réduction de la dose d'électrons peut atténuer cette dégradation. D'autres expériences ont été menées avec différentes tensions d'accélération et de basses températures pour étudier l'effet de ces paramètres sur la dégradation. Les résultats ont montré qu'une tension d'accélération de 3 keV était la plus appropriée pour l'étude des pérovskites CsMAFA. De plus, des températures inférieures à 300 K ont été trouvées pour augmenter la dégradation de la pérovskite.

De plus, la dégradation de la pérovskite hybride en STEM a été discutée, et un critère basé sur la comparaison des images HAADF acquises avant et après chaque cartographie EDS a été établi pour évaluer la dégradation.

En outre, nous avons présenté en détail les procédures d'étalonnage effectuées pour les mesures SEM-EDS (PhiroZ) et STEM-EDS (Cliff et Lorimer).

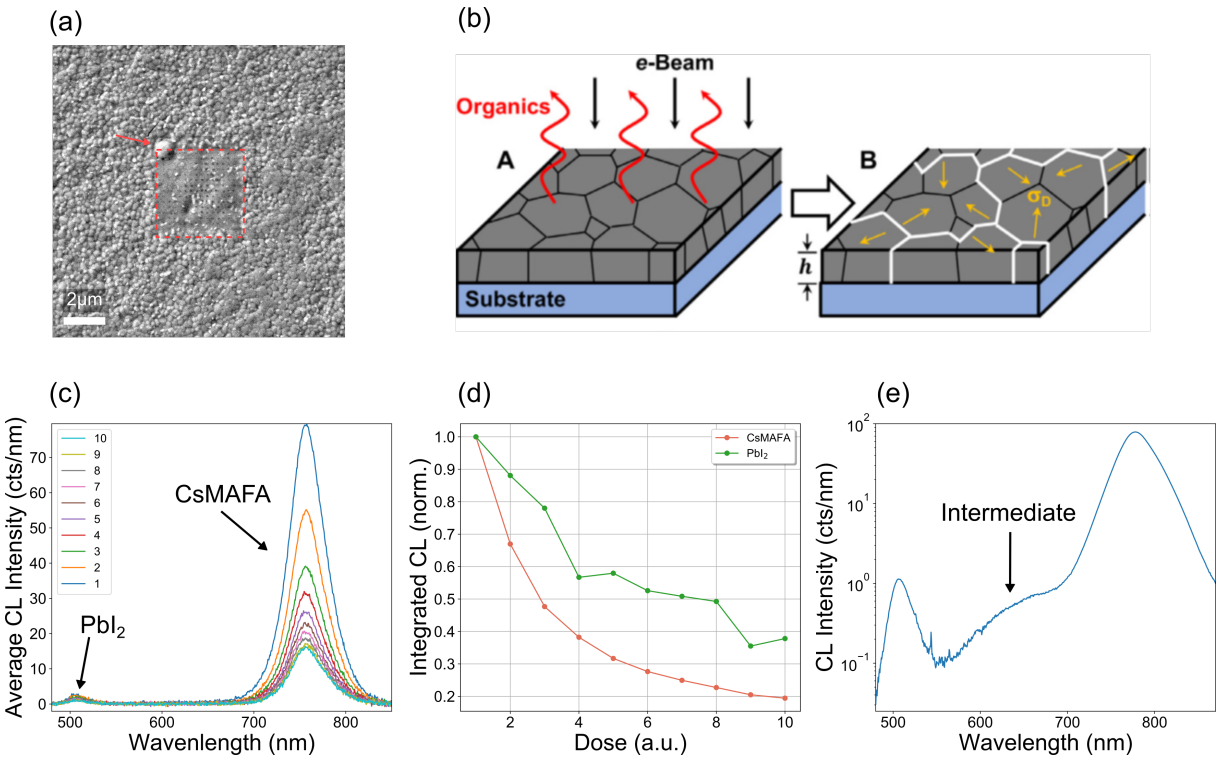

Figure 18: *(a) Image MEB d'un film de CsMAFA où dix cartes de CL ont été réalisées dans la zone délimitée par le carré pointillé rouge. (b) Représentation schématique des mécanismes responsables de la génération de fractures aux limites des grains dans les films minces hybrides lors de l'exposition à un faisceau d'électrons. Reproduit de [176]. (c) Spectres CL acquis successivement sur la même zone d'un film de pérovskite CsMAFA. Chaque acquisition est équivalente à une dose de 5,5 $e^-/Å^2$. Le signal est intégré sur le domaine spectral 775 ±75 nm, et les valeurs obtenues sont normalisées par la première et tracées en fonction de la dose d'exposition (de 1 à 10) en (d). La même procédure d'intégration est effectuée sur la contribution de PbI_2 (500 ±10 nm) et tracée en vert. (e) Spectre CL acquis avec un temps d'intégration plus long de 20 ms sur un film CsMAFA et tracé dans une échelle semi-logarithmique. L'émergence d'un large pic d'émission ("intermédiaire") à 660 nm est frappante.*

Analyse de pérovskites inorganiques : $CsPbBr_3$ et $CsPbBr_2Br_5$

Dans le chapitre 3, nous avons présenté les résultats des mesures SEM-EDS, PL et CL effectuées sur un film hétérogène de $CsPbBr_3$ et sur des microcristaux de $CsPb_2Br_5$.

La composition du film de $CsPbBr_3$ a d'abord été confirmée par des mesures SEM-EDS. Ensuite, les mesures PL ont révélé une émission verte, que nous avons attribuée à la phase tétragonale du $CsPbBr_3$. Enfin, les mesures CL ont révélé deux pics d'émission : l'un à haute énergie, lié à la recombinaison bande à bande, et le second à plus basse énergie, lié à la recombinaison médiée par des défauts peu profonds. D'autres mesures CL à basse température ont montré que l'intensité du pic à haute énergie est réduite par un effet thermique à température ambiante.Nous avons déterminé l'énergie d'activation de ce phénomène, et nous avons discuté de ses origines potentielles. Ces résultats sont en bon accord avec les études précédentes sur les échantillons de $CsPbBr_3$, notamment en ce qui concerne l'évolution de la bande interdite avec la température. Dans cette étude, nous fournissons l'une des rares études rapportées sur les pérovskites $CsPbBr_3$ avec des mesures CL à basse température.

Nous avons présenté une étude similaire sur des microcristaux de $CsPb_2Br_5$ dont la composition a également été confirmée par SEM-EDS. Les mesures PL ont également révélé une émission verte dans ces microcristaux. Cette émission verte dans $CsPb_2Br_5$ provoque un fort débat dans la littérature, puisque la bande interdite théorique est plus grande. Les mesures de

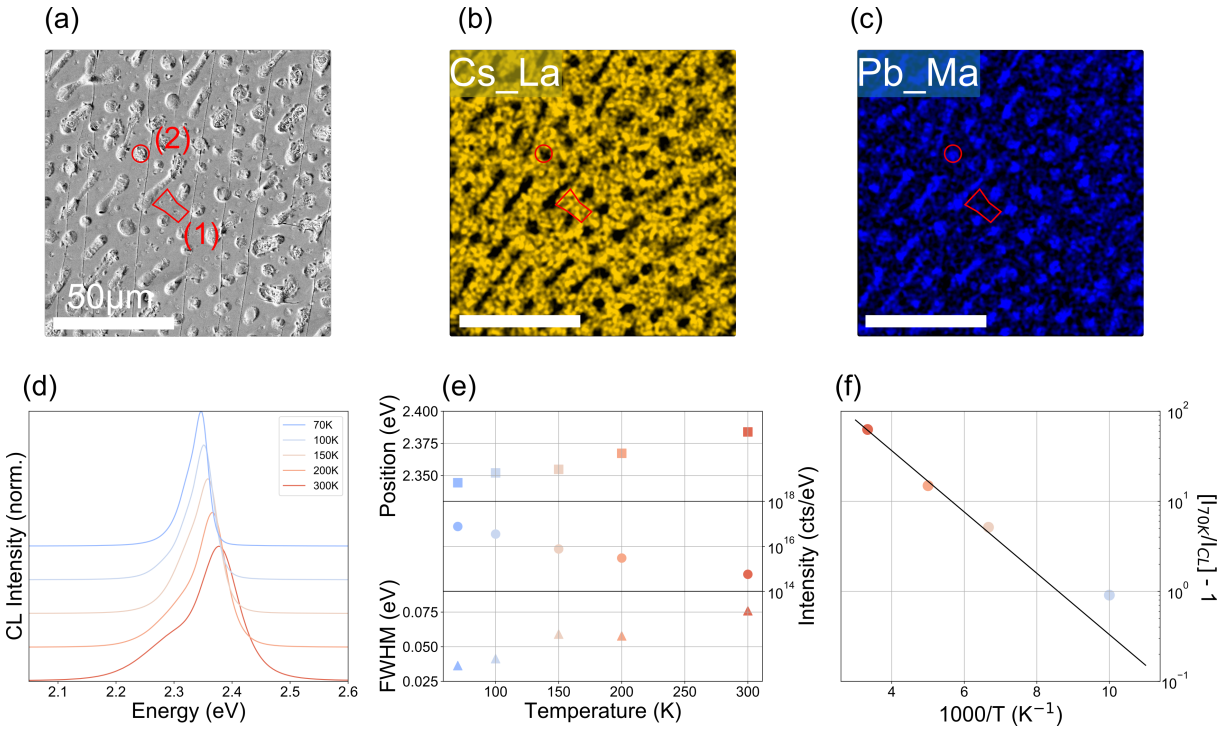

Figure 19: *(a) Image MEB et cartes élémentaires correspondantes de (b) Cs et (c) Pb déterminées par SEM-EDS. (d) Spectres CL normalisés à moyenne spatiale pour différentes températures. (e) Evolution de la position, de l'intensité et de la largeur de bande du pic principal de CL (positionné à 2.38 eV à 300 K) avec la température. (f) Le pic principal de CL positionné à 2.38 eV à 300 K a été intégré à chaque température. Les données ont été normalisées par la valeur à 70 K, et l'inverse a été calculé. On trace* $(I_{70K} - I_T) - 1$. *La fonction d'Arrhenius a été utilisée pour approcher les données.*

CL ont révélé deux larges pics d'émission : un pic de faible énergie qui ne varie pas avec la température (attribué à une recombinaison de défauts profonds), un pic de haute énergie qui varie avec la température (attribué à une recombinaison de bande à bande). Nous avons remarqué que l'énergie du pic CL varie davantage avec la température que celle du $CsPbBr_3$. Par conséquent, nous avons supposé que le pic à haute énergie ne provient pas de $CsPbBr_3$ résiduel dans les microcristaux de $CsPb_2Br_5$. Caicedo et al. ont observé un pic similaire et l'ont attribué à des défauts situés à l'interface $CsPbBr_3/CsPb_2Br_5$ [289]. Nos résultats SEM-EDS ont montré que les microcristaux ont une distribution de composition homogène excluant l'hypothèse de Caicedo et al. dans ces échantillons.

Bien que nous ne fournissions pas d'explication à la luminescence verte de $CsPb_2Br_5$, ce travail alimente le débat en cours sur leurs propriétés optoélectroniques avec de nouveaux résultats expérimentaux.

Effet de l'air humide sur les films minces de pérovskite CsMAFA

Dans le chapitre 4, nous avons présenté une étude de la dégradation du film de pérovskite CsMAFA sous air avec une humidité relative élevée (85% RH). Nous avons analysé les produits de dégradation formés grâce aux techniques corrélatives de caractérisation à haute résolution mentionnées précédemment (CL, SEM-EDS, STEM-EDS et SAED). Nous avons identifié trois compositions différentes résultant de l'interaction de la pérovskite CsMAFA avec les molécules d'eau : PbI_2, $CsPb(I_{0.9}Br_{0.1})_3$, and $CsPb_2(I_{0.7}Br_{0.3})_5$.

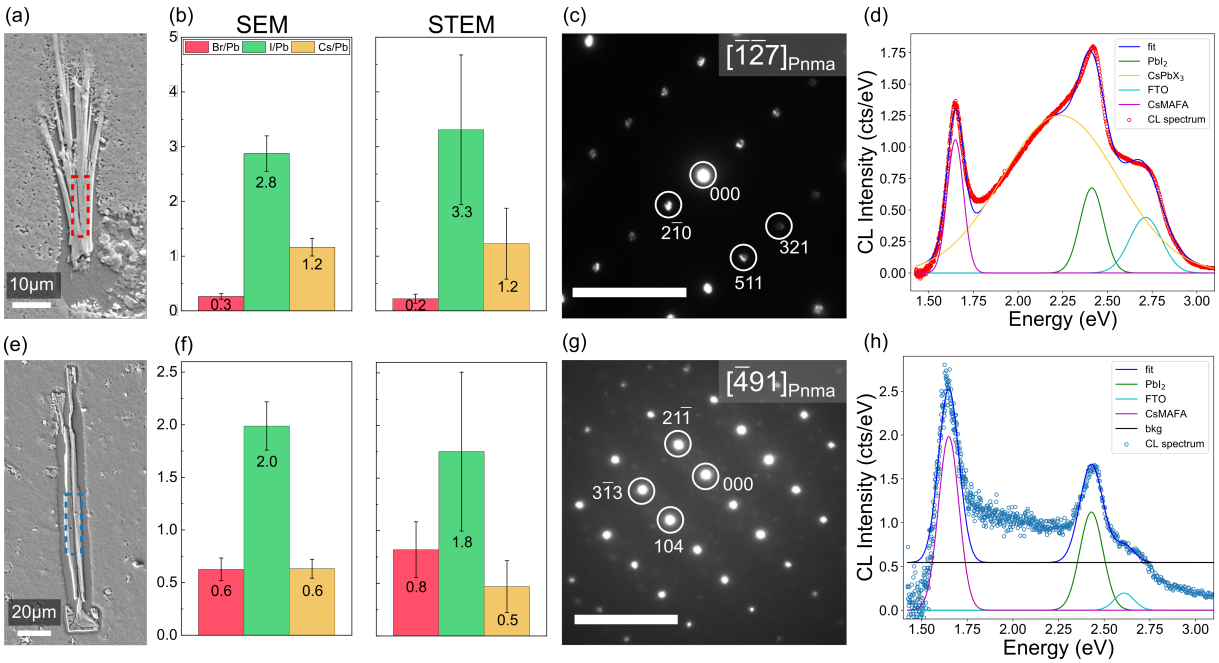

Figure 20: *Analyse corrélative des aiguilles (a,e) Images SEM des deux aiguilles étudiées. (b,f) Rapports correspondants de I/Pb, Br/Pb et Cs/Pb déterminés par quantification des mesures SEM-EDS et STEM-EDS, présentés dans un diagramme à barres. La composition de l'aiguille (a) et (e) est égale à : $CsPb(I_{0,9}Br_{0,1})_3$ et $CsPb_2(I_{0,7}Br_{0,3})_5$, respectivement. (c,g) Diffractogramme obtenu par des mesures de diffraction en zone sélectionnée (SAED) réalisées sur le même type d'aiguilles que celui présenté en (a) et (e). L'indexation montre que le diagramme de diffraction de l'aiguille $CsPb(I_{0,9}Br_{0,1})_3$ est orienté le long de l'axe de la zone $[1\bar{2}\bar{7}]$ et $CsPb_2(I_{0,7}Br_{0,3})_5$ le long de l'axe de la zone $[4\bar{9}1]$. (d-h) Spectres CL moyennés dans l'espace dans l'aiguille présentée en (a) et (e). Le spectre CL (d) est ajusté avec 4 fonctions gaussiennes correspondant aux contributions de CsMAFA (en violet), $CsPb(I_{0,9}Br_{0,1})_3$ (en jaune), PbI2 (en vert) et FTO (en bleu) à 1,65, 2,25, 2,41 et 2,71 eV, respectivement. Le spectre CL (h) est ajusté avec 3 fonctions gaussiennes correspondant aux contributions de CsMAFA (en violet), FTO (en bleu), PbI_2 (en vert) à 1.68, 2.41, et 2.71 eV, respectivement. Le bruit de fond "bkg" est tracé en noir.*

Une série de mécanismes de dégradation ont été proposées pour expliquer la formation de ces phases. Premièrement, une ségrégation de phase a pu se produire dans le film, entraînant la formation de régions riches en I et en Cs. Nous supposons que les régions riches en I se sont décomposées en cristaux de PbI_2 purs après volatilisation des cations organiques sous forme gazeuse. Nous suggérons ensuite que les régions riches en Cs se sont également décomposées en $CsPb(I_{0,9}Br_{0,1})_3$ par volatilisation de cations organiques. Enfin, nous proposons que cette phase a subi une transition de phase et s'est transformée en $CsPb_2(I_{0,7}Br_{0,3})_5$ sous l'action des molécules d'eau.

Afin de comprendre l'impact de la lumière sur la dégradation, nous avons également effectué le vieillissement des films de pérovskite CsMAFA sous des facteurs de stress couplés, incluant l'illumination par un soleil, la chaleur (50°C), l'air et l'humidité (55%). Notre examen de la morphologie des échantillons a indiqué que la lumière intensifie la dégradation, ce qui confirme notre hypothèse selon laquelle la ségrégation de phase est la force motrice de la dégradation.

De plus, nous avons analysé les produits de dégradation d'un film de CsMAFA exposé à N_2 et 85% RH. La petite taille des produits de dégradation, et leur composition démontrent l'effet dramatique de l'oxygène dans les mécanismes de dégradation décrits précédemment.

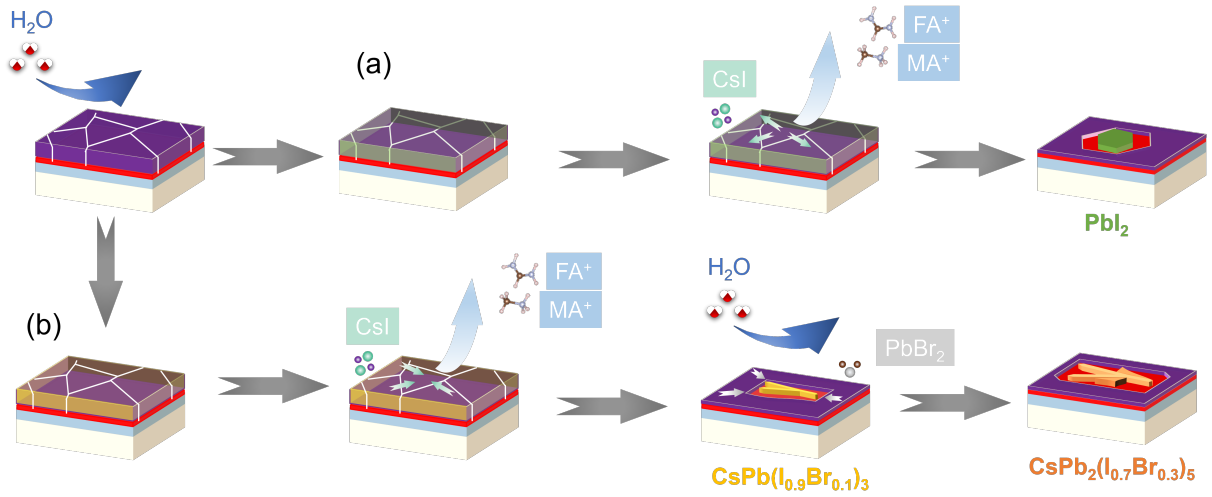

Figure 21: *Mécanismes de décomposition proposés pour le film de pérovskite CsMAFA sous une humidité relative élevée. Les molécules d'eau augmentent la mobilité des ions, ce qui conduit à la démixtion du film de CsMAFA. Deux mécanismes de dégradation distincts sont proposés à partir de ces films démixés. (a) Les cations organiques et les halogénures se volatilisent sous la forme de MAI → MA↑ + HI↑ (ou FAI → FA↑ + HI↑). Les cations Cs+ migrent vers le film environnant en laissant derrière eux du PbI_2, formant des produits de dégradation hexagonaux. (b) Les mêmes espèces volatiles sont extraites du matériau, laissant les éléments restants former des aiguilles de $CsPb(I_{0,9}Br_{0,1})_3$. Après une nouvelle exposition à l'air humide, ces dernières se transforment en aiguilles de $CsPb_2(I_{0,7}Br_{0,3})_5$ plus grosses en réagissant avec les produits de décomposition, c'est-à-dire PbI_2 et $PbBr_2$, du matériau environnant.*

Dégradation de la couche de pérovskite dans une cellule solaire pérovskite fonctionnant pendant 1000 heures

Dans le chapitre 5, nous avons présenté des PSCs démontrant une remarquable stabilité à long terme avec une $T_{80} > 1000$ heures sous un éclairage continu d'un soleil et à MPP. Après le test de stabilité, les films de pérovskite CsMAFA qui constituent les PSCs ont été analysés par des techniques de microscopie électronique, qui ont révélé la présence d'inclusions non luminescentes. Nous avons attribué les pertes mineures du courant de sortie des PSCs pendant le test de stabilité à la formation de ces inclusions. Grâce aux mesures EDS, la composition de ces inclusions a été estimée à $Cs_{0,28}FA_{0,72}Pb(I_{0,74}Br_{0,26})_3$. Nous avons proposé des voies pour expliquer leur formation, notamment la photolyse des clusters de PbI_2 et la migration des ions (halogénures et cations) dans le film sous l'effet de l'éclairage et de la tension de polarisation.

Sur la base de nos résultats, nous avons proposé des stratégies pour prévenir la formation d'inclusions et les pertes subséquentes des performances du PSC. La réduction de la quantité de PbI_2 dans la solution précurseur peut améliorer la stabilité du PSC, bien qu'elle puisse réduire les performances. La suppression de la migration des cations et des halogénures dans le film de pérovskite serait également bénéfique pour la stabilité du PSC et peut être obtenue en réduisant la densité des défauts. En outre, l'exploration de compositions de pérovskite à cation unique ou à halogénure unique pourrait également être bénéfique pour la stabilité du dispositif, tant que la stabilité de phase de la pérovskite photo-active est assurée.

Ce travail a démontré les avantages de la combinaison des mesures J-V et des caractérisations à l'échelle microscopique pour analyser la dégradation des PSC. Nous avons corrélé les variations de la composition du film de pérovskite et des propriétés optoélectroniques avec les variations des performances électriques du PSC. Les mesures en vue de dessus mises en œuvre dans ce travail ont nécessité le décollement de la couche de contact PTAA et de l'électrode Au. Comme

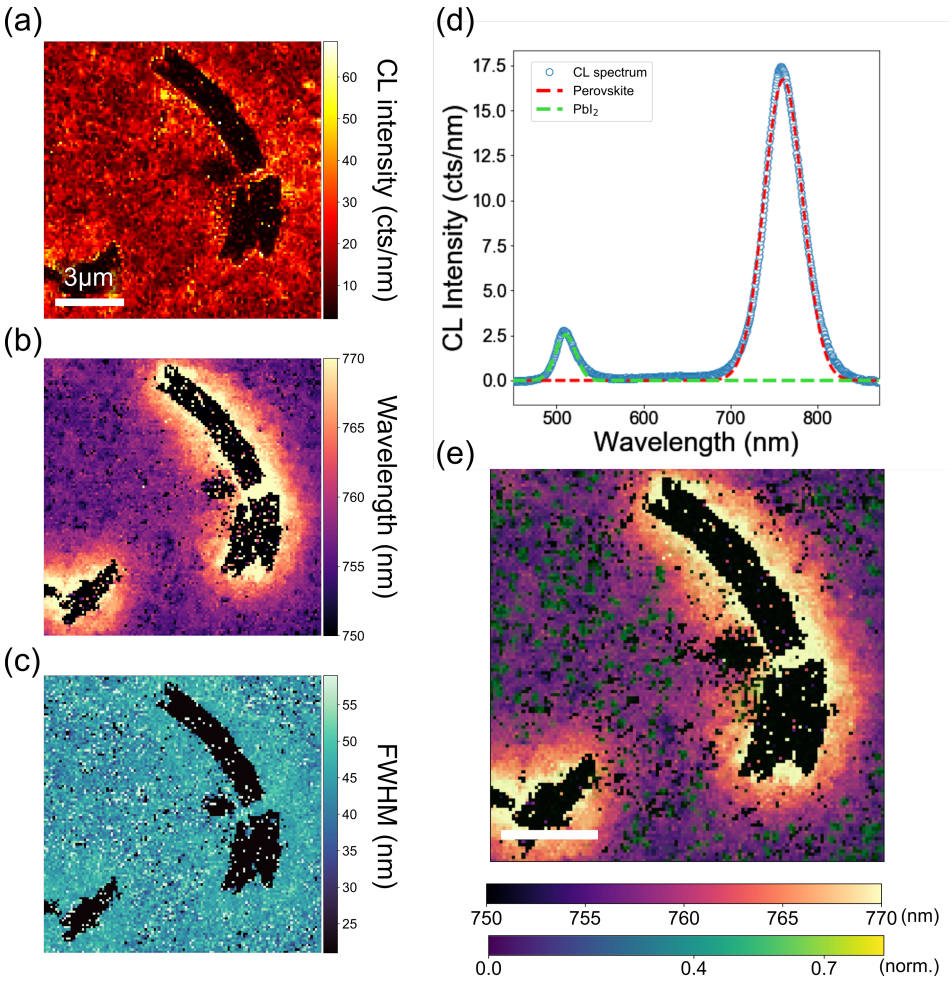

Figure 22: *Le pic d'émission de la pérovskite est ajusté avec une fonction gaussienne pour chaque pixel. (a) Carte d'intensité du pic de CL ; (b) Carte de longueur d'onde du pic de CL ; (c) Carte de FWHM du pic de CL. (d) Spectre CL moyenné (cercles bleus) ajusté avec une fonction bi-gaussienne correspondant à l'émission de la pérovskite (ligne rouge pointillée) et du PbI_2 (ligne verte pointillée). (e) Carte des pics de longueur d'onde de la pérovskite superposée à la carte de CL filtrée sur 500 µm, révélant la présence d'amas de PbIsbs2.*

nous le discutons dans la section Perspectives, d'autres méthodes pourraient être utilisées pour préparer des sections transversales de PSC et effectuer des mesures approfondies.

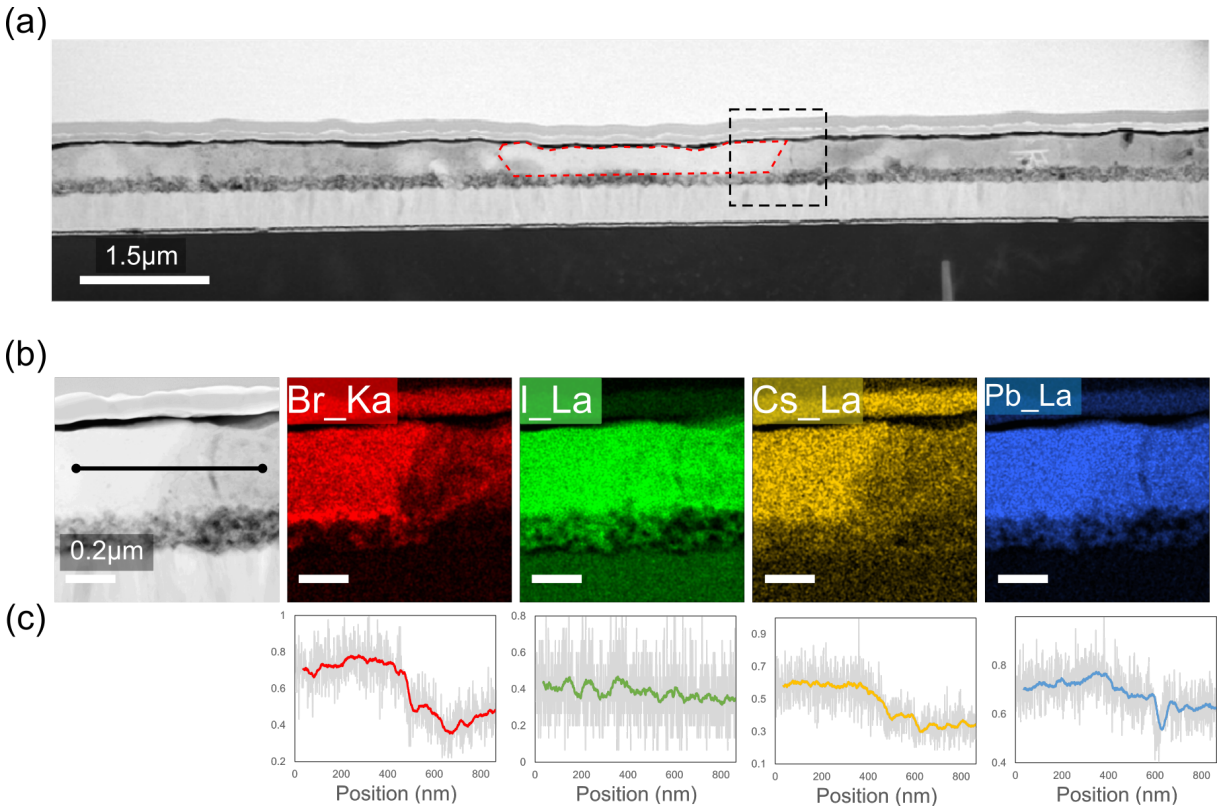

Figure 23: *(a) Image STEM-HAADF de la lamelle étudiée. Les couches constitutives de la CSP sont précisées ainsi que la position de la carte EDS suivante (carré pointillé).(b) Image HAADF montrant le chemin utilisé pour obtenir le balayage linéaire EDS en (c), et les cartes élémentaires correspondantes montrant la distribution des rayons X $Br_{K\alpha}$, $I_{L\alpha}$, $Cs_{L\alpha}$, et $Pb_{L\alpha}$ en (b).*

Conclusion

L'aspect unique de notre approche est la combinaison de ces techniques à haute résolution spatiale, qui permet la corrélation des propriétés structurelles, chimiques et optoélectroniques des échantillons.

En décrivant les résultats de ce travail, nous avons également mis en évidence un certain nombre d'outils de caractérisation qui fonctionnent à haute résolution spatiale pour sonder les propriétés des pérovskites. Nous espérons que les méthodes et les approches décrites seront adoptées et développées par d'autres afin de réaliser des études encore plus approfondies.

La réalisation de mesures *in-situ* est une perspective majeure de ce travail, car elle permet d'étudier la cinétique des mécanismes de dégradation sous des facteurs de contrainte spécifiques. Grâce à ces mesures, nous pourrions également confirmer la lignée hypothétique entre les produits de dégradation tels que les aiguilles et les "fleurs". Ces mesures permettraient de mieux comprendre les premières étapes de la dégradation du CsMAFA et de renforcer notre compréhension actuelle des mécanismes de dégradation.

À l'avenir, nous prévoyons de poursuivre notre étude de la stabilité des films de pérovskite hybride en vieillissant d'autres compositions à l'aide des méthodes décrites au chapitre 4. Cela nous aidera à mieux comprendre la stabilité de ces matériaux, qui pourra être combinée à l'analyse de la stabilité des PSC en fonctionnement, comme décrit au chapitre 5. Nos efforts se concentreront sur des compositions de pérovskite prometteuses, telles que la pérovskite $CsPbI_3$ (projet de thèse de Lauriane Scherrer) et la pérovskite CsMAFA coiffée en 2D (projet de thèse de Thomas Campos).

Appendix

Additional figures

Figure 24 shows the EDS spectrum averaged over the perovskite layer of a PSC lamella. The composition was estimated with two sets of calibrated k-factors and the results are shown in Table 2.4. The $Cs_{L\beta}$ line intensity is too low to estimate the composition of Cs.

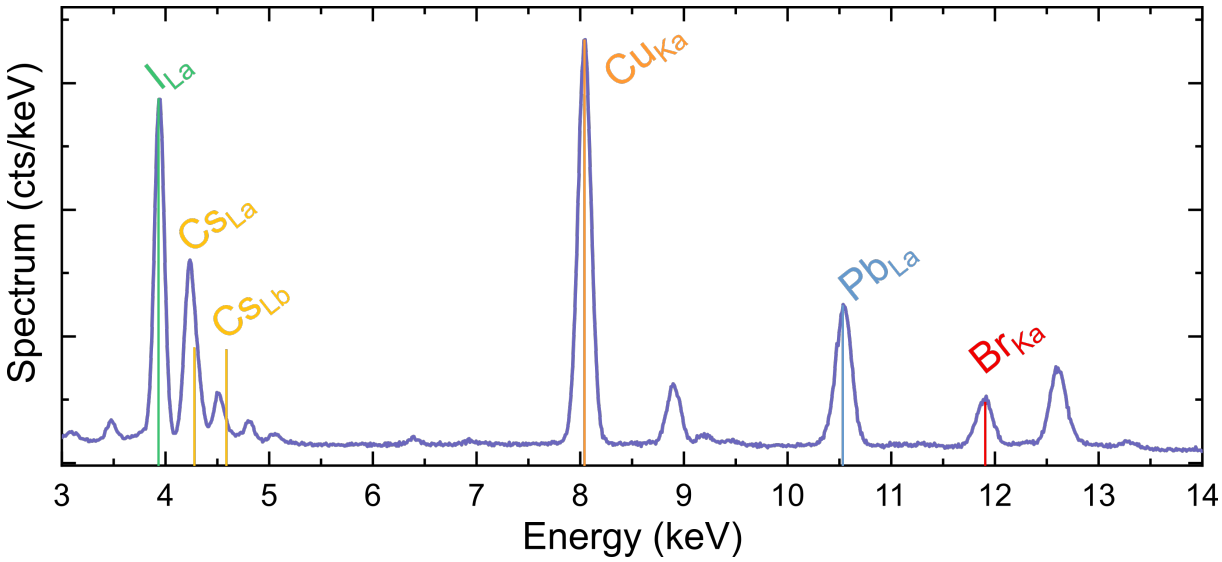

Figure 24: *STEM-EDS spectrum averaged over pixels included in a CsMAFA film. The X-ray lines $I_{L\alpha}$, $Cs_{L\alpha}$, $Cs_{L\beta}$, $Cu_{K\alpha}$, $Pb_{L\alpha}$, and $Br_{K\alpha}$ are represented. The $Cs_{L\beta}$ line is too low to estimate the composition of Cs.*

Figure 25(a) shows the SEM image of the disc-like degradation product analyzed by SEM-EDS. The EDS spectra plotted in (b) were averaged in the regions indicated by circles in the SEM image. The composition of these regions was estimated and the results are shown in Table 4.2.

Figures 26 show SEM images and corresponding elemental maps of the needles used to prepare the lamellae with the FIB miller. Their composition is similar to that of the needles analyzed in Figure 4.8.

Figure 27 shows STEM-EDS spectra averaged over the regions indicated in the HAADF images (1,2,3) in Figure 5.5(b). The $Cs_{L\beta}$ line is more prominent in the third EDS spectrum.

SEM images

Figures 28 show SEM images of a CsMAFA perovskite film from the same batch as the one aged at 85% RH and N_2 studied in section 4.5.2. This film was aged in air at 85% RH and shows the same degradation products observed in the previous study. By comparing the morphology of

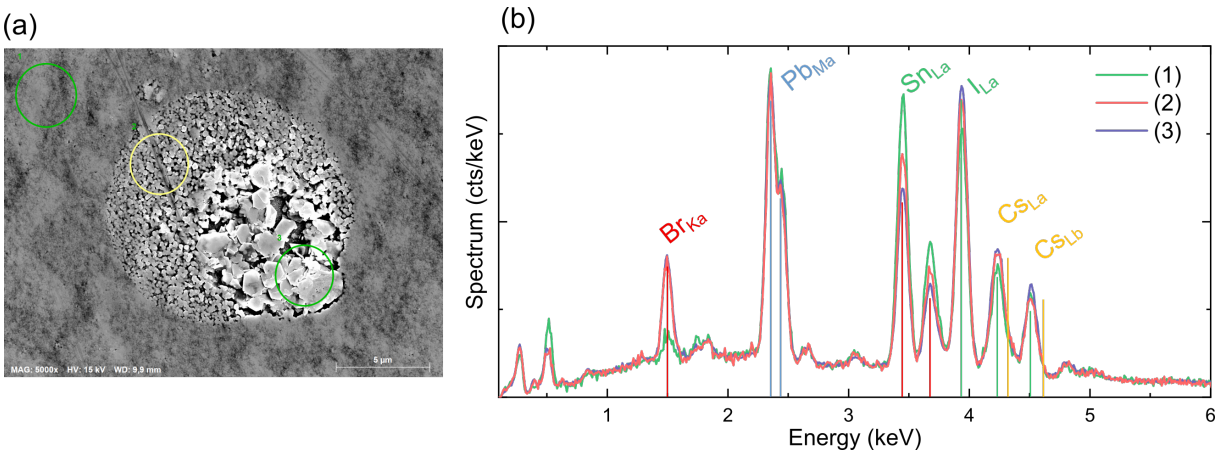

Figure 25: *(a) SEM image of the disc-like degradation product analyzed with EDS. The regions over which the EDS spectra were averaged are indicated by circles.(b) Corresponding SEM-EDS spectra. The X-ray lines $I_{L\alpha}$,$Cs_{L\alpha}$,$Cs_{L\beta}$,Pb_{M},and $Br_{L\alpha}$ are represented. The intensity of $Cs_{L\alpha}$ and $Cs_{L\beta}$ lines is too low to estimate the composition of Cs.*

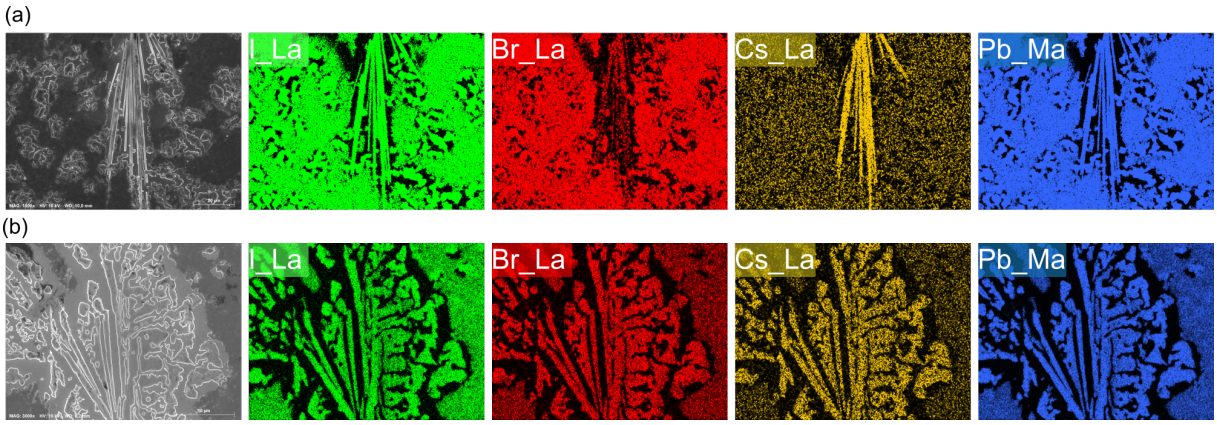

Figure 26: *(a) SEM image and corresponding SEM-EDS elemental maps (I, Br, Cs, and Pb) of the $CsPb(I_{0.9}Br_{0.1})_3$ needle from which a FIB lamella was prepared as shown in Figure 4.9. (b) Same images of the $CsPb_2(I_{0.7}Br_{0.3})_5$ needle.*

this film with the morphology of the film aged in N_2, we observe that the degradation mechanism is different in air and in N_2.

CL measurements at low temperature

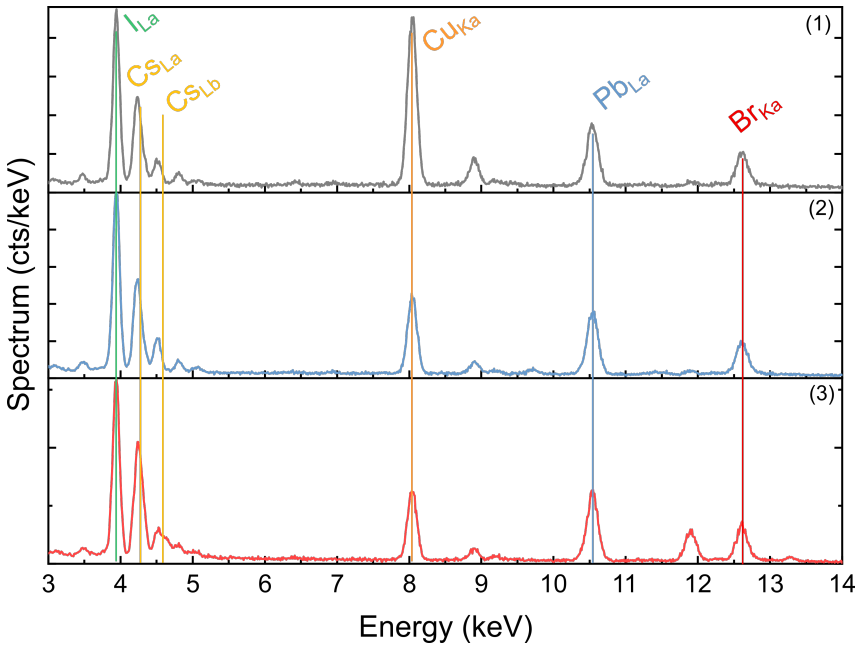

Figure 27: *STEM-EDS spectrum averaged over pixels included in the delimited regions of the HAADF images (1,2,3) in Figure 5.5(b). The X-ray lines* $I_{L\alpha}$, $Cs_{L\alpha}$, $Cs_{L\beta}$, $Cu_{K\alpha}$, $Pb_{L\alpha}$, *and* $Br_{K\alpha}$ *are represented. While in (1) and (2) the intensity of the* $Cs_{L\beta}$ *line is too low to estimate the Cs composition, it is significant in (3).*

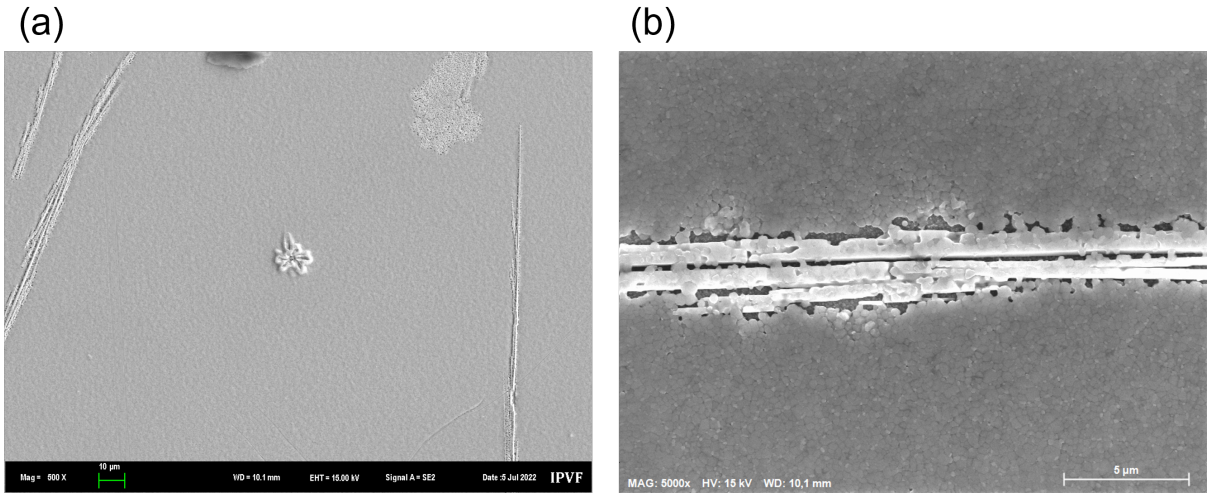

Figure 28: *SEM images of a CsMAFA perovskite film aged under air at 85% RH. (a) Needle and flower degradation products. (b) Needle.*

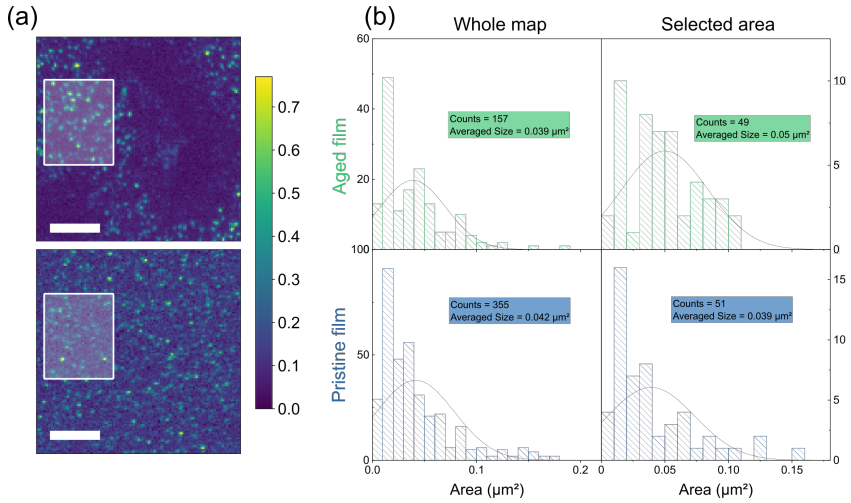

Figure 29: *(a) CL filtered maps on 500±10 nm revealing PbI_2 clusters presence. (b) Corresponding cluster histograms count as a function of their size in μm^2 in the selected areas shown in (a) and the whole map.*

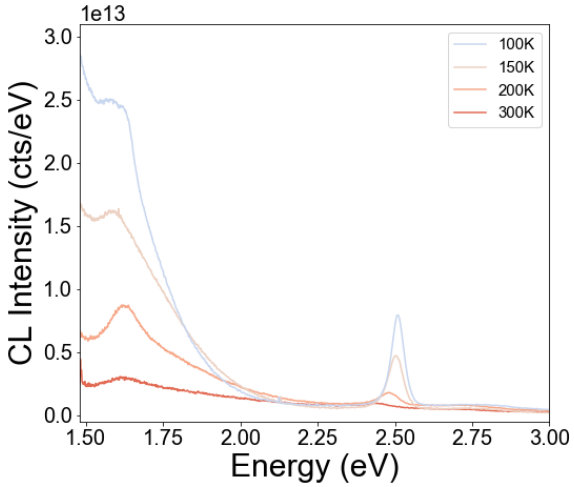

Figure 30: *CL spectra acquired at 300, 200, 150, and 100 K on the "flower" degradation product. Similarly to $CsPb_2(I_{0.7}Br_{0.3})_5$ needle, the CL signal at low energy (< 1.75 eV) is increasing at low temperatures.*

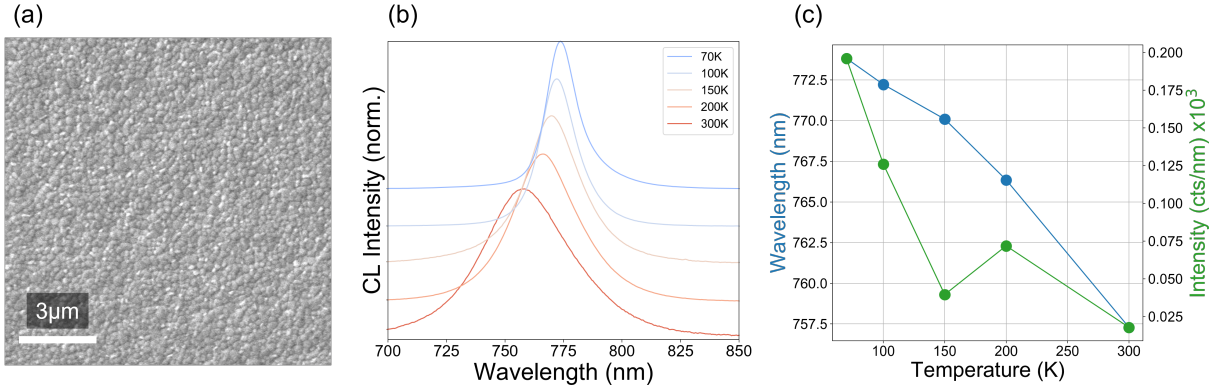

Figure 31: *(a) SEM image of the CsMAFA perovskite film studied with CL measurements at low temperatures. (b) Spatially averaged CL spectra for several temperatures ranging from 300 K down to 70 K. (b) Evolution of the perovskite peak intensity and position as a function of temperature.*

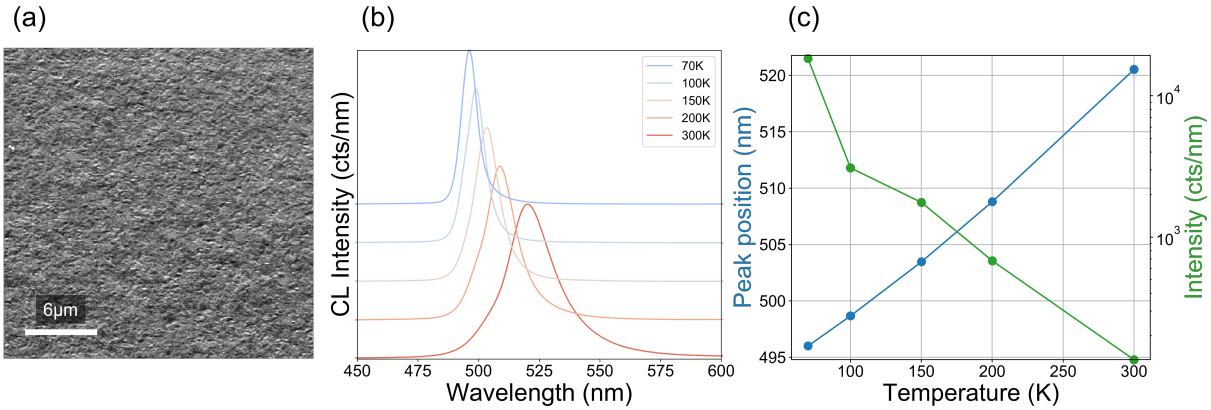

Figure 32: *(a) SEM image of the PbI_2 film studied with CL measurements at low temperatures. (b) Spatially averaged CL spectra for several temperatures ranging from 300 K down to 70 K. (b) Evolution of the PbI_2 emission peak intensity and position as a function of temperature.*

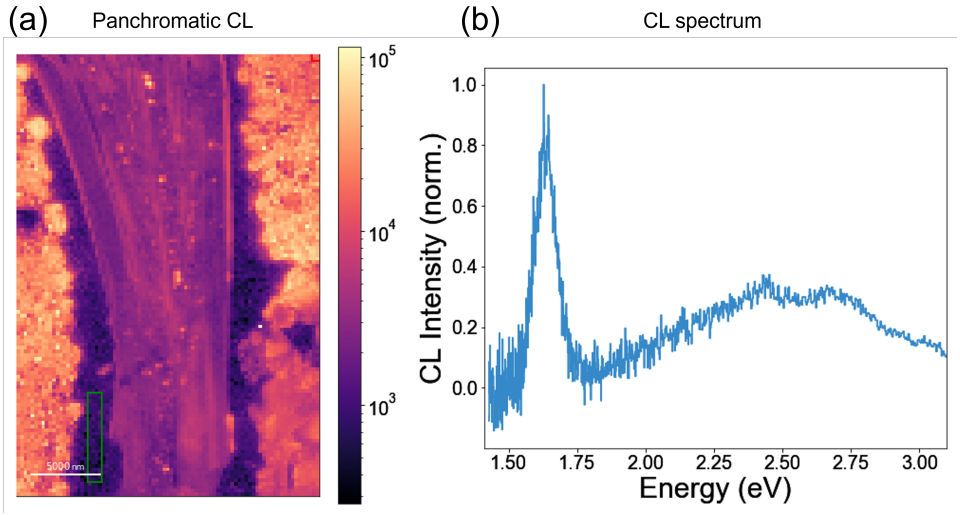

Figure 33: *(a) Panchromatic CL map with the colorbar in logarithmic scale. The CL signal in the green square is averaged and plot in (b).*

Appendix

Additional theory and methods

Characteristics of a solar cell

In the absence of illumination, a solar cell operates as a diode, generating current only when exposed to light. This current is generated through the process of electron-hole pair generation, separation, and extraction. As depicted in the equivalent electrical circuit shown in Figure 34, the device also possesses parasitic resistances, including series resistance (Rs) and parallel resistance (Rp).

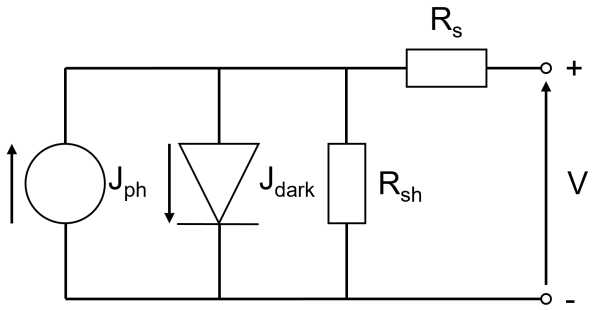

Figure 34: *The one-diode model equivalent electrical circuit of a solar cell.*

The $J(V)$ characteristic of the solar cell follows the equation:

$$J(V) = J_0 \left[\exp\left(\frac{q(V + SJR_s}{kT}\right) - 1\right] + \frac{V - SJR_s}{SR_{sh}} - J_{ph} \tag{1}$$

with J_0 the saturation current density, S the area of the solar cell, and J_{ph} the photo-generated current density.

Computational method

The calculations have been performed with the periodic CRYSTAL code [290–292]. Within CRYSTAL, both the Hartree–Fock (HF) equations and the Kohn–Sham equations of the density functional theory (DFT), as well as hybrid schemes where the exchange operator is a linear combination of the HF and DFT ones, can be solved self-consistently. Basis sets suited for both pseudopotential and all-electron types of calculation, in the form of Gaussian-type functions (GTFs), can be used.

For this work, a hybrid exchange-correlation functional optimized to yield description of the structural, electronic, and dynamic properties of $CsPbX_3$ (X = Cl, Br and I) perovskites in good agreement with experiment, has been used [206]: the Hamiltonian combines 16% of HF exact exchange with the PBEsol exchange-correlation functional [293]. The used basis-sets for Cs, Pb and I are also described in Ref. [206].

For the evaluation of the Coulomb and exchange series within CRYSTAL, the truncation thresholds for the bielectronic integrals, as defined in the CRYSTAL manual [290], were set to 10^{-8}, 10^{-8}, 10^{-8}, 10^{-8}, and 10^{-16} a.u. The calculations have been performed with 14 × 14 ×

14 Monkhorst–Pack k-point meshes [294] for the bulk materials, respectively. The convergence criteria on total energies (and for frequencies determination) were 10-9 (10-12) Ha. Atomic displacements and forces thresholds were 1.8×10^{-3} Bohr and 4.5×10^{-4} Ha/Bohr, respectively. With these computational conditions, the obtained data can be considered as fully converged.

To obtain the atomic structure of the measured compositions for each type of perovskite in this work, a supercell approach was used:

(1) For each "commensurate" concentration, all nonidentical substitution patterns have been considered. For each of them, the lattice parameters and internal coordinates have been optimized, maintaining the symmetry imposed by composition in question.

(2) For the configuration minimizing the total energy, the calculation of Γ phonons was performed in order to verify the dynamic stability.

(3) In the case of the existence of unstable modes (those with imaginary frequency), the symmetry was correspondingly reduced and the structure optimization was redone to enable displacements corresponding to the phonon eigenvector of such an unstable mode.

(4) For each concentration, the most stable configuration was retained for subsequent structural optimization, followed by the calculation of vibrational frequencies (see the previous step) for the ultimate stability analysis. The phonon contribution (zero-point energy) was then taken into account for the ultimate assessment of the relative stability of configurations.

This method was used for determining the different phases subgroup of the cubic ($Pm\bar{3}m$) of $CsPb(I_{0.97}Br_{0.03})_3$; 7 different atomic configurations of a 135 atoms supercell corresponding to the obtained phases have been explored. Since the disordered and ordered *Pnma* phases of this compound is not a subgroup of the cubic phase, it was treated separately: a 180 atoms supercell was used in order to respect the *Pnma* symmetry and the composition; for the disordered and ordered phases 10 and 39 atomic configurations have been optimized. For $CsPb_2(I_{0.7}Br_{0.3})_5$, in order to respect the composition, a 64 atoms supercell was used reducing the symmetry of the system from I4/mcm to P4/m, the described method was applied on this final system; in total 23 different atomic configurations have been probed. Table 6 summarizes the obtained final atomic structure for each composition and symmetry of each perovskites studied in this work.

Hyperspectral photoluminescence imaging

Photoluminescence (PL) is a technique that relies on the same principles as cathodoluminescence (CL), as discussed in Chapter 2. The sample under investigation is excited by an energy source and, as a result, emits light of a specific wavelength, known as luminescence, through radiative recombination of the generated carriers. In PL, the energy source is a light source, here, a LED with a wavelength of 405 nm. The emitted luminescence is collected by a camera and used to generate an image of the sample. Each pixel of the image contains a PL spectrum that is resolved in wavelength. The image obtained from this technique reveals the distribution of luminescence within the sample. The objective used during this thesis was x10, allowing for the acquisition of images with a field-of-view of approximately 700x900μm. Further details on the set-up and its utilization can be found in the published studies from the research groups of IPVF [260, 262].

X-ray diffraction spectroscopy

XRD is a technique used to study the atomic and molecular structure of materials. It involves shining X-rays onto a sample and measuring the diffraction patterns produced, which can be used to determine the crystal structure of the material. XRD is advantageous for investigating perovskite materials due to the close relationship between their optical properties and their structural arrangement.

Table 6: *Calculated lattice parameters (a, b and c in Å, and angles in °) and band gaps (in eV) for the different compounds identified in this work. A selection of experimental data are given for comparison.*

Compounds	Space group	Lattice parameters		Band gaps	
		Calc	Exp.	Calc.	Exp.
$CsPbI_3$	Pm-3m	a 6.196	6.189a, 6.198b	1.61	1.73a, 1.76c
$CsPb(I_{0.93}Br_{0.07})_3$	Pm-3m	a 6.192		2.06	
	P4mm	a 6.176 c 6.124		2.15	
	P-1	a 6.134 b 6.099 c 6.110 a 87.93 b 90.80 g 89.47		2.26	
	Pnma ord.	a 9.055 b 12.395 c 8.052		2.18	
	Pnma disord.	a 10.207 b 4.744 c 17.620		3.49	
$CsPbBr_3$	Pm-3m	a 5,884	5.883b, 5.870g	2.20	2.25d,
$CsPb_2I_5$	I4/mcm	a 8.914 c 15.567	9.060f 15.901f	2.83	2.40f
$CsPb_2(I_{0.7}Br_{0.3})_5$	P4/m	a 8.768 c 15.525		2.99	
	P11m	a 8.778 b 8.779 c 15.514 a 90. b 90. g 90.03		2.99	
$CsPb_2Br_5$	I4/mcm	a 8.417 c 15.479	8.450g , 8.483h 15.070g , 15.250h	3.98	3.87g

References: a [49]; b[50]; c[51]; d [52]; e[53]; f[54]; g[55]; h [56]

Selected area electron diffraction

SAED is a technique used to study the crystalline structure of materials at the nanoscale. It is a TEM technique involving a focused electron beam to probe the crystalline structure of a sample's small (selected) area. In SAED measurements, this area is placed in the path of the electron beam, and the diffraction patterns produced by the beam as it passes through the sample are measured. These diffraction patterns are unique to the particular arrangement of atoms within the sample and can be used to determine the material crystalline structure.

Articles and communications

Articles

1. S. Bernard, S. Jutteau, ***S. Mejaouri***, S. Cacovich, I. Zimmermann, A. Yaiche, S. Gbegnon, D. Loisnard, S. Collin, A. Duchatelet, F. Sauvage, J. Rousset, Solar RRL, *One-Step Slot-Die Coating Deposition of Wide-Bandgap Perovskite Absorber for Highly Efficient Solar Cells*, Solar RRL, vol. 5, no. 9, p. 2100391, 2021.

2. A. Singh, F. Matteoci, H. Zhu, D. Rossi, ***S. Mejaouri***, S. Cacovich, M. Auf Der Maur, F. Sauvage, A. Gagliardi, M. Gratzel, A. Di Carlo, *Methylamine Gas Treatment Affords Improving Semitransparency, Efficiency, and Stability of $CH_3NH_3PbBr_3$-Based Perovskite Solar Cells*, Solar RRL, vol. 5, no. 9, p. 2100277, 2021.

3. F. Matteocci, D. Rossi, L. A. Castriotta, D. Ory, ***S. Mejaouri***, M. A. der Maur, F. Sauvage, S. Cacovich, A. Di Carlo, *Wide bandgap halide perovskite absorbers for semitransparent photovoltaics: From theoretical design to modules*, Nano Energy 2022, 101, 107560.

4. I. Zimmermann, M. Provost, ***S. Mejaouri***, M. Al Atem, A. Blaizot, A. Duchatelet, S. Collin, J. Rousset, *Industrially Compatible Fabrication Process of Perovskite-Based Mini-Modules Coupling Sequential Slot-Die Coating and Chemical Bath Deposition*, ACS Appl. Mater. Interfaces 2022, 14, 11636.

5. ***S. Mejaouri***, S. Cacovich, P. Baranek, B. Bérenguier, I. Zimmermann, A. Yaiche, D. Loisnard, J. Rousset, S. Collin *Humidity-induced degradation processes of halide perovskites unveiled by correlative analytical electron microscopy*, to be submitted at Advanced Functional Materials.

Communications

1. ***S. Mejaouri***, S. Bernard, D. Loisnard, J. Rousset, and S. Collin, *Exploring degradation mechanisms in perovskite solar cells using extensive electron microscope techniques, JNPV (Dourdan, 2021).*

2. ***S. Mejaouri****, S. Cacovich, M. Ali Kazemi, F. Sauvage, D. Loisnard, J. Rousset and S. Collin, Correlative analysis of perovskite thin-films aged under humidity and lead-rich inorganic perovskites, EMRS Fall 2021 (Warsaw, 2021)*

3. ***S. Mejaouri****, S. Cacovich, I. Zimmermann, F. Sauvage, A. Yaiche, D. Loisnard, J. Rousset and S. Collin, Correlative analysis of perovskite solar cells aged under humidity, Photonic West - SPIE (San Fransisco, 2022)*

4. ***S. Mejaouri****, S. Cacovich, I. Zimmermann, F. Sauvage, A. Yaiche, D. Loisnard, P. Baranek, J. Rousset and S. Collin,Analysis of the degradation products of hybrid perovskite by correlative electron microscopy, HOPV22 (Valencia, 2022).*

References for Chapter : General introduction

[1] P. A. Arias et al. “Techincal summary”. In: *Climate Change 2021: The Physical Science Basis. Contribution of Working Group I to the Sixth Assessment Report of the Intergovernmental Panel on Climate Change*. Ed. by V. Masson-Delmotte et al. Cambridge University Press, 2021, pp. 33–144. DOI: 10.1017/9781009157896.002 *Cited on pages 1, 133.*

[2] Hannah Ritchie, Max Roser, and Pablo Rosado. “Energy”. In: *Our World in Data* (2022). https://ourworldindata.org/energy *Cited on page 1.*

[3] International Energy Agency (IEA). *Solar PV*. en-GB. Tech. rep. 2022 *Cited on pages 1, 2, 133.*

[4] Martin A. Green et al. “Solar cell efficiency tables (Version 60)”. en. In: *Progress in Photovoltaics: Research and Applications* 30.7 (2022), pp. 687–701. ISSN: 1099-159X. DOI: 10.1002/pip.3595 *Cited on page 1.*

[5] NREL. *Best Research-Cell Efficiency Chart*. en. 2022 *Cited on pages 2, 133.*

[6] Lisa Anna Zafoschnig, Sebastian Nold, and Jan Christoph Goldschmidt. “The Race for Lowest Costs of Electricity Production: Techno-Economic Analysis of Silicon, Perovskite and Tandem Solar Cells”. In: *IEEE Journal of Photovoltaics* 10.6 (Nov. 2020). Conference Name: IEEE Journal of Photovoltaics, pp. 1632–1641. ISSN: 2156-3403. DOI: 10.1109/JPHOTOV.2020.3024739 *Cited on pages 2, 15.*

[7] Leiping Duan et al. “Stability challenges for the commercialization of perovskite–silicon tandem solar cells”. en. In: *Nature Reviews Materials* (Jan. 2023). Publisher: Nature Publishing Group, pp. 1–21. ISSN: 2058-8437. DOI: 10.1038/s41578-022-00521-1 *Cited on pages 2, 16.*

[8] Randi Azmi et al. “Damp heat–stable perovskite solar cells with tailored-dimensionality 2D/3D heterojunctions”. In: *Science* 376.6588 (Apr. 2022). Publisher: American Association for the Advancement of Science, pp. 73–77. DOI: 10.1126/science.abm5784 *Cited on pages 2, 26.*

[9] Iwan Zimmermann et al. “Industrially Compatible Fabrication Process of Perovskite-Based Mini-Modules Coupling Sequential Slot-Die Coating and Chemical Bath Deposition”. In: *ACS Applied Materials & Interfaces* 14.9 (Mar. 2022). Publisher: American Chemical Society, pp. 11636–11644. ISSN: 1944-8244. DOI: 10.1021/acsami.1c24558 *Cited on pages 4, 18.*

References for Chapter 1: Stability of perovskite material in solar cells

[6] Lisa Anna Zafoschnig, Sebastian Nold, and Jan Christoph Goldschmidt. “The Race for Lowest Costs of Electricity Production: Techno-Economic Analysis of Silicon, Perovskite and Tandem Solar Cells”. In: *IEEE Journal of Photovoltaics* 10.6 (Nov. 2020). Conference Name: IEEE Journal of Photovoltaics, pp. 1632–1641. ISSN: 2156-3403. DOI: 10.1109/JPHOTOV.2020.3024739 *Cited on pages 2, 15.*

[7] Leiping Duan et al. “Stability challenges for the commercialization of perovskite–silicon tandem solar cells”. en. In: *Nature Reviews Materials* (Jan. 2023). Publisher: Nature Publishing Group, pp. 1–21. ISSN: 2058-8437. DOI: 10.1038/s41578-022-00521-1 *Cited on pages 2, 16.*

[8] Randi Azmi et al. “Damp heat–stable perovskite solar cells with tailored-dimensionality 2D/3D heterojunctions”. In: *Science* 376.6588 (Apr. 2022). Publisher: American Association for the Advancement of Science, pp. 73–77. DOI: 10.1126/science.abm5784 *Cited on pages 2, 26.*

[9] Iwan Zimmermann et al. “Industrially Compatible Fabrication Process of Perovskite-Based Mini-Modules Coupling Sequential Slot-Die Coating and Chemical Bath Deposition”. In: *ACS Applied Materials & Interfaces* 14.9 (Mar. 2022). Publisher: American Chemical Society, pp. 11636–11644. ISSN: 1944-8244. DOI: 10.1021/acsami.1c24558 *Cited on pages 4, 18.*

[10] V. M. Goldschmidt. “Die Gesetze der Krystallochemie”. de. In: *Naturwissenschaften* 14.21 (May 1926), pp. 477–485. ISSN: 1432-1904. DOI: 10.1007/BF01507527 *Cited on page 6.*

[11] Gregor Kieslich, Shijing Sun, and Anthony K. Cheetham. “An extended Tolerance Factor approach for organic–inorganic perovskites”. en. In: *Chemical Science* 6.6 (May 2015). Publisher: The Royal Society of Chemistry, pp. 3430–3433. ISSN: 2041-6539. DOI: 10.1039/C5SC00961H *Cited on page 6.*

[12] C. Li et al. “Formability of ABX3 (X = F, Cl, Br, I) halide perovskites”. en. In: *Acta Crystallographica Section B: Structural Science* 64.6 (Dec. 2008). Number: 6 Publisher: International Union of Crystallography, pp. 702–707. ISSN: 0108-7681. DOI: 10.1107/S0108768108032734 *Cited on page 6.*

[13] Akihiro Kojima et al. “Organometal Halide Perovskites as Visible-Light Sensitizers for Photovoltaic Cells”. In: *Journal of the American Chemical Society* 131.17 (May 2009). Publisher: American Chemical Society, pp. 6050–6051. ISSN: 0002-7863. DOI: 10.1021/ja809598r *Cited on pages 7, 8, 15.*

[14] Bumseop Kim, Jeongwoo Kim, and Noejung Park. “First-principles identification of the charge-shifting mechanism and ferroelectricity in hybrid halide perovskites”. en. In: *Scientific Reports* 10.1 (Nov. 2020). Number: 1 Publisher: Nature Publishing Group, p. 19635. ISSN: 2045-2322. DOI: 10.1038/s41598-020-76742-7 *Cited on pages 7, 18.*

[15] Meng Ren et al. “Potential lead toxicity and leakage issues on lead halide perovskite photovoltaics”. en. In: *Journal of Hazardous Materials* 426 (Mar. 2022), p. 127848. ISSN: 0304-3894. DOI: 10.1016/j.jhazmat.2021.127848 *Cited on page 7.*

[16] Weijun Ke and Mercouri G. Kanatzidis. “Prospects for low-toxicity lead-free perovskite solar cells”. en. In: *Nature Communications* 10.1 (Feb. 2019). Number: 1 Publisher: Nature Publishing Group, p. 965. ISSN: 2041-1723. DOI: 10.1038/s41467-019-08918-3 *Cited on pages 7, 22.*

[17] Giorgio Schileo and Giulia Grancini. “Lead or no lead? Availability, toxicity, sustainability and environmental impact of lead-free perovskite solar cells”. en. In: *Journal of Materials Chemistry C* 9.1 (2021). Publisher: Royal Society of Chemistry, pp. 67–76. DOI: 10.1039/D0TC04552G *Cited on pages 7, 22.*

[18] Jin-Wook Lee et al. “High-Efficiency Perovskite Solar Cells Based on the Black Polymorph of HC(NH2)2PbI3”. In: *Advanced Materials* 26.29 (2014), pp. 4991–4998. ISSN: 1521-4095. DOI: https://doi.org/10.1002/adma.201401137 *Cited on page 8.*

[19] Michael Kulbak et al. “Cesium Enhances Long-Term Stability of Lead Bromide Perovskite-Based Solar Cells”. In: *The Journal of Physical Chemistry Letters* 7.1 (Jan. 2016). Publisher: American Chemical Society, pp. 167–172. DOI: 10.1021/acs.jpclett.5b02597 *Cited on page 8.*

[20] Zhen Li et al. "Stabilizing Perovskite Structures by Tuning Tolerance Factor: Formation of Formamidinium and Cesium Lead Iodide Solid-State Alloys". en. In: *Chemistry of Materials* 28.1 (Jan. 2016), pp. 284–292. ISSN: 0897-4756, 1520-5002. DOI: 10.1021/acs.chemmater.5b04107 *Cited on pages 8, 12, 122.*

[21] Juan-Pablo Correa-Baena et al. "Promises and challenges of perovskite solar cells". In: *Science* 358.6364 (Nov. 2017). Publisher: American Association for the Advancement of Science, pp. 739–744. DOI: 10.1126/science.aam6323 *Cited on page 8.*

[22] Michael Saliba et al. "Incorporation of rubidium cations into perovskite solar cells improves photovoltaic performance". In: *Science* 354.6309 (Oct. 2016). Publisher: American Association for the Advancement of Science, pp. 206–209. DOI: 10.1126/science.aah5557 *Cited on page 8.*

[23] Dominic W. Ferdani et al. "Partial cation substitution reduces iodide ion transport in lead iodide perovskite solar cells". en. In: *Energy & Environmental Science* 12.7 (2019). Publisher: Royal Society of Chemistry, pp. 2264–2272. DOI: 10.1039/C9EE00476A *Cited on page 8.*

[24] Wan-Jian Yin, Tingting Shi, and Yanfa Yan. "Superior Photovoltaic Properties of Lead Halide Perovskites: Insights from First-Principles Theory". In: *The Journal of Physical Chemistry C* 119.10 (Mar. 2015). Publisher: American Chemical Society, pp. 5253–5264. ISSN: 1932-7447. DOI: 10.1021/jp512077m *Cited on page 8.*

[25] Eva L. Unger et al. "CHAPTER 4:Solution-processed Solar Cells: Perovskite Solar Cells". en. In: *Solar Energy Capture Materials*. Aug. 2019, pp. 153–192. DOI: 10.1039/9781788013512-00153 *Cited on page 8.*

[26] Keith T. Butler, Jarvist M. Frost, and Aron Walsh. "Band alignment of the hybrid halide perovskites CH 3 NH 3 PbCl 3 , CH 3 NH 3 PbBr 3 and CH 3 NH 3 PbI 3". en. In: *Materials Horizons* 2.2 (2015). Publisher: Royal Society of Chemistry, pp. 228–231. DOI: 10.1039/C4MH00174E *Cited on page 8.*

[27] Riley E. Brandt et al. "Searching for "Defect-Tolerant" Photovoltaic Materials: Combined Theoretical and Experimental Screening". In: *Chemistry of Materials* 29.11 (June 2017). Publisher: American Chemical Society, pp. 4667–4674. ISSN: 0897-4756. DOI: 10.1021/acs.chemmater.6b05496 *Cited on page 9.*

[28] Eric T. Hoke et al. "Reversible photo-induced trap formation in mixed-halide hybrid perovskites for photovoltaics". en. In: *Chemical Science* 6.1 (2015), pp. 613–617. ISSN: 2041-6520, 2041-6539. DOI: 10.1039/C4SC03141E *Cited on pages 9, 20, 127.*

[29] Michael C. Brennan et al. "Photoinduced Anion Segregation in Mixed Halide Perovskites". en. In: *Trends in Chemistry* 2.4 (Apr. 2020), pp. 282–301. ISSN: 25895974. DOI: 10.1016/j.trechm.2020.01.010 *Cited on pages 9, 20, 21, 122.*

[30] G. Murtaza and Iftikhar Ahmad. "First principle study of the structural and optoelectronic properties of cubic perovskites CsPbM3 (M=Cl, Br, I)". en. In: *Physica B: Condensed Matter* 406.17 (Sept. 2011), pp. 3222–3229. ISSN: 0921-4526. DOI: 10.1016/j.physb.2011.05.028 *Cited on page 9.*

[31] Samuel D. Stranks et al. "Electron-Hole Diffusion Lengths Exceeding 1 Micrometer in an Organometal Trihalide Perovskite Absorber". In: *Science* 342.6156 (Oct. 2013). Publisher: American Association for the Advancement of Science, pp. 341–344. DOI: 10.1126/science.1243982 *Cited on page 9.*

[32] Giacomo Giorgi and Koichi Yamashita. "Organic–inorganic halide perovskites: an ambipolar class of materials with enhanced photovoltaic performances". en. In: *Journal of Materials Chemistry A* 3.17 (Apr. 2015). Publisher: The Royal Society of Chemistry, pp. 8981–8991. ISSN: 2050-7496. DOI: 10.1039/C4TA05046K *Cited on page 9.*

[33] Qingfeng Dong et al. “Electron-hole diffusion lengths > 175 um in solution-grown CH3NH3PbI3 single crystals”. In: *Science* 347.6225 (Feb. 2015). Publisher: American Association for the Advancement of Science, pp. 967–970. DOI: 10.1126/science.aaa5760 *Cited on page 9.*

[34] Qianqian Lin et al. “Hybrid Perovskites: Prospects for Concentrator Solar Cells”. en. In: *Advanced Science* 5.4 (2018), p. 1700792. ISSN: 2198-3844. DOI: 10.1002/advs.201700792 *Cited on pages 10, 15, 43.*

[35] Dane W. deQuilettes et al. “Charge-Carrier Recombination in Halide Perovskites: Focus Review”. en. In: *Chemical Reviews* 119.20 (Oct. 2019), pp. 11007–11019. ISSN: 0009-2665, 1520-6890. DOI: 10.1021/acs.chemrev.9b00169 *Cited on pages 10, 43.*

[36] Laura M. Herz. “Charge-Carrier Dynamics in Organic-Inorganic Metal Halide Perovskites”. en. In: *Annual Review of Physical Chemistry* 67.1 (May 2016), pp. 65–89. ISSN: 0066-426X, 1545-1593. DOI: 10.1146/annurev-physchem-040215-112222 *Cited on pages 10, 71, 93.*

[37] Samuel D. Stranks et al. “Recombination Kinetics in Organic-Inorganic Perovskites: Excitons, Free Charge, and Subgap States”. In: *Physical Review Applied* 2.3 (Sept. 2014). Publisher: American Physical Society, p. 034007. DOI: 10.1103/PhysRevApplied.2.034007 *Cited on page 10.*

[38] Handong Jin et al. “It’s a trap! On the nature of localised states and charge trapping in lead halide perovskites”. en. In: *Materials Horizons* 7.2 (2020). Publisher: Royal Society of Chemistry, pp. 397–410. DOI: 10.1039/C9MH00500E *Cited on page 11.*

[39] Luis K. Ono, Shengzhong (Frank) Liu, and Yabing Qi. “Reducing Detrimental Defects for High-Performance Metal Halide Perovskite Solar Cells”. en. In: *Angewandte Chemie International Edition* 59.17 (2020), pp. 6676–6698. ISSN: 1521-3773. DOI: 10.1002/anie.201905521 *Cited on page 11.*

[40] Quinten A. Akkerman et al. “Genesis, challenges and opportunities for colloidal lead halide perovskite nanocrystals”. en. In: *Nature Materials* 17.5 (May 2018). Number: 5 Publisher: Nature Publishing Group, pp. 394–405. ISSN: 1476-4660. DOI: 10.1038/s41563-018-0018-4 *Cited on page 11.*

[41] Hiroki Uratani and Koichi Yamashita. “Charge Carrier Trapping at Surface Defects of Perovskite Solar Cell Absorbers: A First-Principles Study”. In: *The Journal of Physical Chemistry Letters* 8.4 (Feb. 2017). Publisher: American Chemical Society, pp. 742–746. DOI: 10.1021/acs.jpclett.7b00055 *Cited on page 11.*

[42] James M. Ball and Annamaria Petrozza. “Defects in perovskite-halides and their effects in solar cells”. en. In: *Nature Energy* 1.11 (Oct. 2016). Number: 11 Publisher: Nature Publishing Group, pp. 1–13. ISSN: 2058-7546. DOI: 10.1038/nenergy.2016.149 *Cited on page 11.*

[43] Daniele Meggiolaro et al. “Iodine chemistry determines the defect tolerance of lead-halide perovskites”. en. In: *Energy & Environmental Science* 11.3 (Mar. 2018). Publisher: The Royal Society of Chemistry, pp. 702–713. ISSN: 1754-5706. DOI: 10.1039/C8EE00124C *Cited on page 11.*

[44] Stuart Macpherson et al. “Local nanoscale phase impurities are degradation sites in halide perovskites”. In: *Nature* 607.7918 (2022), pp. 294–300 *Cited on page 11.*

[45] Teng Zhang et al. “Understanding the relationship between ion migration and the anomalous hysteresis in high-efficiency perovskite solar cells: A fresh perspective from halide substitution”. en. In: *Nano Energy* 26 (Aug. 2016), pp. 620–630. ISSN: 2211-2855. DOI: 10.1016/j.nanoen.2016.05.052 *Cited on page 11.*

[46] Daniele Meggiolaro, Edoardo Mosconi, and Filippo De Angelis. "Formation of Surface Defects Dominates Ion Migration in Lead-Halide Perovskites". In: *ACS Energy Letters* 4.3 (Mar. 2019). Publisher: American Chemical Society, pp. 779–785. DOI: 10.1021/acsenergylett.9b00247 *Cited on page 11.*

[47] Yucheng Liu et al. "Two-Inch-Sized Perovskite CH3NH3PbX3 (X = Cl, Br, I) Crystals: Growth and Characterization". In: *Advanced Materials* 27.35 (Sept. 2015). Publisher: John Wiley & Sons, Ltd, pp. 5176–5183. ISSN: 0935-9648. DOI: 10.1002/adma.201502597 *Cited on page 12.*

[48] Fabian Ruf et al. "Temperature-dependent studies of exciton binding energy and phase-transition suppression in (Cs,FA,MA)Pb(I,Br) 3 perovskites". en. In: *APL Materials* 7.3 (Mar. 2019), p. 031113. ISSN: 2166-532X. DOI: 10.1063/1.5083792 *Cited on pages 12, 18.*

[49] Congcong Wu et al. "All Electrospray Printing of Carbon-Based Cost-Effective Perovskite Solar Cells". en. In: *Advanced Functional Materials* 31.6 (2021), p. 2006803. ISSN: 1616-3028. DOI: 10.1002/adfm.202006803 *Cited on page 13.*

[50] Like Huang and Ziyi Ge. "Simple, Robust, and Going More Efficient: Recent Advance on Electron Transport Layer-Free Perovskite Solar Cells". en. In: *Advanced Energy Materials* 9.24 (2019), p. 1900248. ISSN: 1614-6840. DOI: 10.1002/aenm.201900248 *Cited on page 13.*

[51] Jin-Feng Liao et al. "Understanding of carrier dynamics, heterojunction merits and device physics: towards designing efficient carrier transport layer-free perovskite solar cells". en. In: *Chemical Society Reviews* 49.2 (2020). Publisher: Royal Society of Chemistry, pp. 354–381. DOI: 10.1039/C8CS01012A *Cited on page 13.*

[52] E. L. Unger et al. "Hysteresis and transient behavior in current–voltage measurements of hybrid-perovskite absorber solar cells". en. In: *Energy & Environmental Science* 7.11 (Oct. 2014). Publisher: The Royal Society of Chemistry, pp. 3690–3698. ISSN: 1754-5706. DOI: 10.1039/C4EE02465F *Cited on page 14.*

[53] Henry J. Snaith et al. "Anomalous Hysteresis in Perovskite Solar Cells". In: *The Journal of Physical Chemistry Letters* 5.9 (May 2014). Publisher: American Chemical Society, pp. 1511–1515. DOI: 10.1021/jz500113x *Cited on page 14.*

[54] Tomas Leijtens et al. "Mapping Electric Field-Induced Switchable Poling and Structural Degradation in Hybrid Lead Halide Perovskite Thin Films". en. In: *Advanced Energy Materials* 5.20 (2015), p. 1500962. ISSN: 1614-6840. DOI: 10.1002/aenm.201500962 *Cited on pages 14, 23.*

[55] Rebecca A. Belisle et al. "Interpretation of inverted photocurrent transients in organic lead halide perovskite solar cells: proof of the field screening by mobile ions and determination of the space charge layer widths". en. In: *Energy & Environmental Science* 10.1 (2017). Publisher: Royal Society of Chemistry, pp. 192–204. DOI: 10.1039/C6EE02914K *Cited on page 14.*

[56] William Shockley and Hans J. Queisser. "Detailed Balance Limit of Efficiency of p-n Junction Solar Cells". In: *Journal of Applied Physics* 32.3 (Mar. 1961). Publisher: American Institute of Physics, pp. 510–519. ISSN: 0021-8979. DOI: 10.1063/1.1736034 *Cited on page 15.*

[57] Jean-Francois Guillemoles et al. "Guide for the perplexed to the Shockley–Queisser model for solar cells". en. In: *Nature Photonics* 13.8 (Aug. 2019), pp. 501–505. ISSN: 1749-4885, 1749-4893. DOI: 10.1038/s41566-019-0479-2 *Cited on page 15.*

[58] Ahmed Hasan, Jawad Sarwar, and Ali Hasan Shah. "Concentrated photovoltaic: A review of thermal aspects, challenges and opportunities". en. In: *Renewable and Sustainable Energy Reviews* 94 (Oct. 2018), pp. 835–852. ISSN: 1364-0321. DOI: 10.1016/j.rser.2018.06.014 *Cited on page 15.*

[59] Robert T. Ross and Arthur J. Nozik. "Efficiency of hot-carrier solar energy converters". In: *Journal of Applied Physics* 53.5 (May 1982). Publisher: American Institute of Physics, pp. 3813–3818. ISSN: 0021-8979. DOI: 10.1063/1.331124 *Cited on page 15.*

[60] A. De Vos. "Detailed balance limit of the efficiency of tandem solar cells". en. In: *Journal of Physics D: Applied Physics* 13.5 (May 1980), p. 839. ISSN: 0022-3727. DOI: 10.1088/0022-3727/13/5/018 *Cited on page 15.*

[61] Simon Kahmann and Maria A. Loi. "Hot carrier solar cells and the potential of perovskites for breaking the Shockley–Queisser limit". en. In: *Journal of Materials Chemistry C* 7.9 (Feb. 2019). Publisher: The Royal Society of Chemistry, pp. 2471–2486. ISSN: 2050-7534. DOI: 10.1039/C8TC04641G *Cited on page 15.*

[62] Bruno Ehrler et al. "Photovoltaics Reaching for the Shockley–Queisser Limit". In: *ACS Energy Letters* 5.9 (Sept. 2020). Publisher: American Chemical Society, pp. 3029–3033. DOI: 10.1021/acsenergylett.0c01790 *Cited on page 15.*

[63] Yana Vaynzof. "The Future of Perovskite Photovoltaics—Thermal Evaporation or Solution Processing?" en. In: *Advanced Energy Materials* 10.48 (2020), p. 2003073. ISSN: 1614-6840. DOI: 10.1002/aenm.202003073 *Cited on page 15.*

[64] Nam-Gyu Park and Kai Zhu. "Scalable fabrication and coating methods for perovskite solar cells and solar modules". en. In: *Nature Reviews Materials* 5.5 (May 2020). Number: 5 Publisher: Nature Publishing Group, pp. 333–350. ISSN: 2058-8437. DOI: 10.1038/s41578-019-0176-2 *Cited on page 15.*

[65] Rosario Vidal et al. "Assessing health and environmental impacts of solvents for producing perovskite solar cells". en. In: *Nature Sustainability* (Dec. 2020). ISSN: 2398-9629. DOI: 10.1038/s41893-020-00645-8 *Cited on page 16.*

[66] Nam-Gyu Park. "Research Direction toward Scalable, Stable, and High Efficiency Perovskite Solar Cells". en. In: *Advanced Energy Materials* 10.13 (Apr. 2020), p. 1903106. ISSN: 1614-6832, 1614-6840. DOI: 10.1002/aenm.201903106 *Cited on page 16.*

[67] Zhen Li et al. "Scalable fabrication of perovskite solar cells". en. In: *Nature Reviews Materials* 3.4 (Mar. 2018). Number: 4 Publisher: Nature Publishing Group, pp. 1–20. ISSN: 2058-8437. DOI: 10.1038/natrevmats.2018.17 *Cited on page 16.*

[68] Sarah E. Sofia et al. "Roadmap for cost-effective, commercially-viable perovskite silicon tandems for the current and future PV market". en. In: *Sustainable Energy & Fuels* 4.2 (2020). Publisher: Royal Society of Chemistry, pp. 852–862. DOI: 10.1039/C9SE00948E *Cited on page 16.*

[69] Marko Jošt et al. "Monolithic Perovskite Tandem Solar Cells: A Review of the Present Status and Advanced Characterization Methods Toward 30% Efficiency". en. In: *Advanced Energy Materials* 10.26 (2020), p. 1904102. ISSN: 1614-6840. DOI: 10.1002/aenm.201904102 *Cited on page 16.*

[70] Lei Meng, Jingbi You, and Yang Yang. "Addressing the stability issue of perovskite solar cells for commercial applications". en. In: *Nature Communications* 9.1 (Dec. 2018), p. 5265. ISSN: 2041-1723. DOI: 10.1038/s41467-018-07255-1 *Cited on page 16.*

[71] T. Jesper Jacobsson et al. "An open-access database and analysis tool for perovskite solar cells based on the FAIR data principles". en. In: *Nature Energy* 7.1 (Jan. 2022). Number: 1 Publisher: Nature Publishing Group, pp. 107–115. ISSN: 2058-7546. DOI: 10.1038/s41560-021-00941-3 *Cited on page 17.*

[72] Julian Burschka et al. “Sequential deposition as a route to high-performance perovskite-sensitized solar cells”. en. In: *Nature* 499.7458 (July 2013). Number: 7458 Publisher: Nature Publishing Group, pp. 316–319. ISSN: 1476-4687. DOI: 10.1038/nature12340 *Cited on page 17.*

[73] Iwan Zimmermann et al. “Sequentially Slot-Die-Coated Perovskite for Efficient and Scalable Solar Cells”. en. In: *Advanced Materials Interfaces* 8.18 (2021), p. 2100743. ISSN: 2196-7350. DOI: 10.1002/admi.202100743 *Cited on page 17.*

[74] Michael Koehl et al. “Modeling of the nominal operating cell temperature based on outdoor weathering”. en. In: *Solar Energy Materials and Solar Cells* 95.7 (July 2011), pp. 1638–1646. ISSN: 0927-0248. DOI: 10.1016/j.solmat.2011.01.020 *Cited on page 18.*

[75] Yu An et al. “Structural Stability of Formamidinium- and Cesium-Based Halide Perovskites”. In: *ACS Energy Letters* 6.5 (May 2021). Publisher: American Chemical Society, pp. 1942–1969. DOI: 10.1021/acsenergylett.1c00354 *Cited on pages 18, 22, 63, 89.*

[76] Caleb C. Boyd et al. “Understanding Degradation Mechanisms and Improving Stability of Perovskite Photovoltaics”. en. In: *Chemical Reviews* 119.5 (Mar. 2019), pp. 3418–3451. ISSN: 0009-2665, 1520-6890. DOI: 10.1021/acs.chemrev.8b00336 *Cited on pages 18, 19, 22–25, 45, 82.*

[77] Tiarnan A. S. Doherty et al. “Stabilized tilted-octahedra halide perovskites inhibit local formation of performance-limiting phases”. In: *Science* 374.6575 (Dec. 2021). Publisher: American Association for the Advancement of Science, pp. 1598–1605. DOI: 10.1126/science.abl4890 *Cited on pages 18, 123, 132.*

[78] Emilio J. Juarez-Perez, Luis K. Ono, and Yabing Qi. “Thermal degradation of formamidinium based lead halide perovskites into sym-triazine and hydrogen cyanide observed by coupled thermogravimetry-mass spectrometry analysis”. en. In: *Journal of Materials Chemistry A* 7.28 (July 2019). Publisher: The Royal Society of Chemistry, pp. 16912–16919. ISSN: 2050-7496. DOI: 10.1039/C9TA06058H *Cited on page 18.*

[79] Emilio J. Juarez-Perez et al. “Photodecomposition and thermal decomposition in methylammonium halide lead perovskites and inferred design principles to increase photovoltaic device stability”. en. In: *Journal of Materials Chemistry A* 6.20 (2018), pp. 9604–9612. ISSN: 2050-7488, 2050-7496. DOI: 10.1039/C8TA03501F *Cited on pages 18, 23.*

[80] Lin Ma et al. “Temperature-Dependent Thermal Decomposition Pathway of Organic–Inorganic Halide Perovskite Materials”. en. In: *Chemistry of Materials* 31.20 (Oct. 2019), pp. 8515–8522. ISSN: 0897-4756, 1520-5002. DOI: 10.1021/acs.chemmater.9b03190 *Cited on pages 18, 45, 70.*

[81] Amalie Dualeh et al. “Thermal Behavior of Methylammonium Lead-Trihalide Perovskite Photovoltaic Light Harvesters”. In: *Chemistry of Materials* 26.21 (Nov. 2014). Publisher: American Chemical Society, pp. 6160–6164. ISSN: 0897-4756. DOI: 10.1021/cm502468k *Cited on page 19.*

[82] Rongrong Cheacharoen et al. “Design and understanding of encapsulated perovskite solar cells to withstand temperature cycling”. en. In: *Energy & Environmental Science* 11.1 (2018). Publisher: Royal Society of Chemistry, pp. 144–150. DOI: 10.1039/C7EE02564E *Cited on page 19.*

[83] Md Arafat Mahmud et al. “Origin of Efficiency and Stability Enhancement in High-Performing Mixed Dimensional 2D-3D Perovskite Solar Cells: A Review”. en. In: *Advanced Functional Materials* 32.3 (Jan. 2022), p. 2009164. ISSN: 1616-301X, 1616-3028. DOI: 10.1002/adfm.202009164 *Cited on pages 19, 21.*

[84] Yun Lin et al. “Enhanced Thermal Stability in Perovskite Solar Cells by Assembling 2D/3D Stacking Structures”. In: *The Journal of Physical Chemistry Letters* 9.3 (Feb. 2018). Publisher: American Chemical Society, pp. 654–658. DOI: 10.1021/acs.jpclett.7b02679 *Cited on page 19.*

[85] Jiale Li et al. “Encapsulation of perovskite solar cells for enhanced stability: Structures, materials and characterization”. en. In: *Journal of Power Sources* 485 (Feb. 2021), p. 229313. ISSN: 0378-7753. DOI: 10.1016/j.jpowsour.2020.229313 *Cited on page 19.*

[86] Dane W. deQuilettes et al. “Photo-induced halide redistribution in organic–inorganic perovskite films”. en. In: *Nature Communications* 7.1 (May 2016). Number: 1 Publisher: Nature Publishing Group, p. 11683. ISSN: 2041-1723. DOI: 10.1038/ncomms11683 *Cited on pages 19, 42.*

[87] Shaun Tan et al. “Shallow Iodine Defects Accelerate the Degradation of α-Phase Formamidinium Perovskite”. en. In: *Joule* 4.11 (Nov. 2020), pp. 2426–2442. ISSN: 2542-4351. DOI: 10.1016/j.joule.2020.08.016 *Cited on page 19.*

[88] Nga Phung et al. “The Role of Grain Boundaries on Ionic Defect Migration in Metal Halide Perovskites”. en. In: *Advanced Energy Materials* 10.20 (2020), p. 1903735. ISSN: 1614-6840. DOI: 10.1002/aenm.201903735 *Cited on pages 19, 21.*

[89] Yuze Lin et al. “Excess charge-carrier induced instability of hybrid perovskites”. en. In: *Nature Communications* 9.1 (Nov. 2018). Number: 1 Publisher: Nature Publishing Group, p. 4981. ISSN: 2041-1723. DOI: 10.1038/s41467-018-07438-w *Cited on page 19.*

[90] Roberto Brenes et al. “Metal Halide Perovskite Polycrystalline Films Exhibiting Properties of Single Crystals”. en. In: *Joule* 1.1 (Sept. 2017), pp. 155–167. ISSN: 2542-4351. DOI: 10.1016/j.joule.2017.08.006 *Cited on page 19.*

[91] Seog Joon Yoon et al. “Tracking Iodide and Bromide Ion Segregation in Mixed Halide Lead Perovskites during Photoirradiation”. en. In: *ACS Energy Letters* 1.1 (July 2016), pp. 290–296. ISSN: 2380-8195, 2380-8195. DOI: 10.1021/acsenergylett.6b00158 *Cited on pages 19, 20.*

[92] Vikas Kumar et al. “Nanoscale Mapping of Bromide Segregation on the Cross Sections of Complex Hybrid Perovskite Photovoltaic Films Using Secondary Electron Hyperspectral Imaging in a Scanning Electron Microscope”. en. In: *ACS Omega* 2.5 (May 2017), pp. 2126–2133. ISSN: 2470-1343, 2470-1343. DOI: 10.1021/acsomega.7b00265 *Cited on page 19.*

[93] The Duong et al. “Light and Electrically Induced Phase Segregation and Its Impact on the Stability of Quadruple Cation High Bandgap Perovskite Solar Cells”. en. In: *ACS Applied Materials & Interfaces* 9.32 (Aug. 2017), pp. 26859–26866. ISSN: 1944-8244, 1944-8252. DOI: 10.1021/acsami.7b06816 *Cited on page 19.*

[94] Kevin A. Bush et al. “Compositional Engineering for Efficient Wide Band Gap Perovskites with Improved Stability to Photoinduced Phase Segregation”. en. In: *ACS Energy Letters* 3.2 (Feb. 2018), pp. 428–435. ISSN: 2380-8195, 2380-8195. DOI: 10.1021/acsenergylett.7b01255 *Cited on pages 19, 117, 122, 127.*

[95] E. L. Unger et al. “Roadmap and roadblocks for the band gap tunability of metal halide perovskites”. en. In: *Journal of Materials Chemistry A* 5.23 (2017), pp. 11401–11409. ISSN: 2050-7488, 2050-7496. DOI: 10.1039/C7TA00404D *Cited on page 20.*

[96] Connor G. Bischak et al. “Origin of Reversible Photoinduced Phase Separation in Hybrid Perovskites”. en. In: *Nano Letters* 17.2 (Feb. 2017), pp. 1028–1033. ISSN: 1530-6984, 1530-6992. DOI: 10.1021/acs.nanolett.6b04453 *Cited on page 20.*

[97] Moritz H. Futscher et al. “Quantification of ion migration in CH3NH3PbI3 perovskite solar cells by transient capacitance measurements”. en. In: *Materials Horizons* 6.7 (Aug. 2019). Publisher: The Royal Society of Chemistry, pp. 1497–1503. ISSN: 2051-6355. DOI: 10.1039/C9MH00445A *Cited on page 21.*

[98] Ilia M. Pavlovetc et al. “Suppressing Cation Migration in Triple-Cation Lead Halide Perovskites”. In: *ACS Energy Letters* 5.9 (Sept. 2020). Publisher: American Chemical Society, pp. 2802–2810. DOI: 10.1021/acsenergylett.0c01207 *Cited on pages 21, 98, 125.*

[99] Jeffrey A. Christians et al. “Tailored interfaces of unencapsulated perovskite solar cells for >1,000 hour operational stability”. en. In: *Nature Energy* 3.1 (Jan. 2018). Number: 1 Publisher: Nature Publishing Group, pp. 68–74. ISSN: 2058-7546. DOI: 10.1038/s41560-017-0067-y *Cited on pages 21, 127.*

[100] Konrad Domanski et al. “Migration of cations induces reversible performance losses over day/night cycling in perovskite solar cells”. en. In: *Energy & Environmental Science* 10.2 (Feb. 2017). Publisher: The Royal Society of Chemistry, pp. 604–613. ISSN: 1754-5706. DOI: 10.1039/C6EE03352K *Cited on page 21.*

[101] Rusha Chatterjee et al. “Subdiffraction Infrared Imaging of Mixed Cation Perovskites: Probing Local Cation Heterogeneities”. In: *ACS Energy Letters* 3.2 (Feb. 2018). Publisher: American Chemical Society, pp. 469–475. DOI: 10.1021/acsenergylett.7b01306 *Cited on pages 21, 125.*

[102] Nengxu Li et al. “Microscopic Degradation in Formamidinium-Cesium Lead Iodide Perovskite Solar Cells under Operational Stressors”. en. In: *Joule* (July 2020). ISSN: 25424351. DOI: 10.1016/j.joule.2020.06.005 *Cited on pages 21, 98, 111, 125, 127.*

[103] Gee Yeong Kim et al. “Large tunable photoeffect on ion conduction in halide perovskites and implications for photodecomposition”. en. In: *Nature Materials* 17.5 (May 2018). Number: 5 Publisher: Nature Publishing Group, pp. 445–449. ISSN: 1476-4660. DOI: 10.1038/s41563-018-0038-0 *Cited on page 21.*

[104] Alexander J. Knight and Laura M. Herz. “Preventing phase segregation in mixed-halide perovskites: a perspective”. en. In: *Energy & Environmental Science* 13.7 (2020). Publisher: Royal Society of Chemistry, pp. 2024–2046. DOI: 10.1039/D0EE00788A *Cited on page 21.*

[105] Bo Chen et al. “Imperfections and their passivation in halide perovskite solar cells”. en. In: *Chemical Society Reviews* 48.14 (July 2019). Publisher: The Royal Society of Chemistry, pp. 3842–3867. ISSN: 1460-4744. DOI: 10.1039/C8CS00853A *Cited on page 21.*

[106] Furkan H. Isikgor et al. “Molecular engineering of contact interfaces for high-performance perovskite solar cells”. en. In: *Nature Reviews Materials* (Nov. 2022). Publisher: Nature Publishing Group, pp. 1–20. ISSN: 2058-8437. DOI: 10.1038/s41578-022-00503-3 *Cited on page 21.*

[107] Efrain Ochoa-Martinez et al. “Physical Passivation of Grain Boundaries and Defects in Perovskite Solar Cells by an Isolating Thin Polymer”. In: *ACS Energy Letters* 6.7 (July 2021). Publisher: American Chemical Society, pp. 2626–2634. DOI: 10.1021/acsenergylett.1c01187 *Cited on page 21.*

[108] Zahra Andaji-Garmaroudi et al. “Photobrightening in Lead Halide Perovskites: Observations, Mechanisms, and Future Potential”. en. In: *Advanced Energy Materials* 10.13 (2020), p. 1903109. ISSN: 1614-6840. DOI: 10.1002/aenm.201903109 *Cited on page 21.*

[109] Shun-Chang Liu et al. “Investigation of Oxygen Passivation for High-Performance All-Inorganic Perovskite Solar Cells”. In: *Journal of the American Chemical Society* 141.45 (Nov. 2019). Publisher: American Chemical Society, pp. 18075–18082. ISSN: 0002-7863. DOI: 10.1021/jacs.9b07182 *Cited on pages 21, 22, 98.*

[110] Lucie McGovern et al. “Grain Size Influences Activation Energy and Migration Pathways in MAPbBr3 Perovskite Solar Cells”. In: *The Journal of Physical Chemistry Letters* 12.9 (Mar. 2021). Publisher: American Chemical Society, pp. 2423–2428. DOI: 10.1021/acs.jpclett.1c00205 *Cited on page 21.*

[111] Loreta A. Muscarella et al. “Lattice Compression Increases the Activation Barrier for Phase Segregation in Mixed-Halide Perovskites”. In: *ACS Energy Letters* 5.10 (Oct. 2020). Publisher: American Chemical Society, pp. 3152–3158. DOI: 10.1021/acsenergylett.0c01474 *Cited on pages 21, 125.*

[112] Yuanyuan Zhou and Yixin Zhao. “Chemical stability and instability of inorganic halide perovskites”. en. In: *Energy & Environmental Science* 12.5 (May 2019). Publisher: The Royal Society of Chemistry, pp. 1495–1511. ISSN: 1754-5706. DOI: 10.1039/C8EE03559H *Cited on page 22.*

[113] Jinli Yang et al. “Investigation of CH3NH3PbI3 Degradation Rates and Mechanisms in Controlled Humidity Environments Using in Situ Techniques”. In: *ACS Nano* 9.2 (Feb. 2015). Publisher: American Chemical Society, pp. 1955–1963. ISSN: 1936-0851. DOI: 10.1021/nn506864k *Cited on pages 22, 81.*

[114] Zhaoning Song et al. “Perovskite Solar Cell Stability in Humid Air: Partially Reversible Phase Transitions in the PbI2-CH3NH3I-H2O System”. en. In: *Advanced Energy Materials* 6.19 (2016), p. 1600846. ISSN: 1614-6840. DOI: 10.1002/aenm.201600846 *Cited on page 23.*

[115] Jae Sung Yun et al. “Humidity-Induced Degradation via Grain Boundaries of HC(NH2)2PbI3 Planar Perovskite Solar Cells”. en. In: *Advanced Functional Materials* 28.11 (2018), p. 1705363. ISSN: 1616-3028. DOI: 10.1002/adfm.201705363 *Cited on pages 22, 23.*

[116] Parth Raval et al. “Understanding Instability in Formamidinium Lead Halide Perovskites: Kinetics of Transformative Reactions at Grain and Subgrain Boundaries”. In: *ACS Energy Letters* 7.4 (Apr. 2022). Publisher: American Chemical Society, pp. 1534–1543. DOI: 10.1021/acsenergylett.2c00140 *Cited on pages 22, 23.*

[117] Johannes Schlipf et al. “In Situ Monitoring the Uptake of Moisture into Hybrid Perovskite Thin Films”. en. In: *The Journal of Physical Chemistry Letters* 9.8 (Apr. 2018), pp. 2015–2021. ISSN: 1948-7185, 1948-7185. DOI: 10.1021/acs.jpclett.8b00687 *Cited on page 23.*

[118] Aurélien M. A. Leguy et al. “Reversible Hydration of CH3NH3PbI3 in Films, Single Crystals, and Solar Cells”. In: *Chemistry of Materials* 27.9 (May 2015). Publisher: American Chemical Society, pp. 3397–3407. ISSN: 0897-4756. DOI: 10.1021/acs.chemmater.5b00660 *Cited on page 22.*

[119] John M. Howard et al. “Humidity-Induced Photoluminescence Hysteresis in Variable Cs/Br Ratio Hybrid Perovskites”. en. In: *The Journal of Physical Chemistry Letters* 9.12 (June 2018), pp. 3463–3469. ISSN: 1948-7185. DOI: 10.1021/acs.jpclett.8b01357 *Cited on pages 22, 82, 83.*

[120] Yinghong Hu et al. “Impact of Rubidium and Cesium Cations on the Moisture Stability of Multiple-Cation Mixed-Halide Perovskites”. en. In: *ACS Energy Letters* 2.10 (Oct. 2017), pp. 2212–2218. ISSN: 2380-8195, 2380-8195. DOI: 10.1021/acsenergylett.7b00731 *Cited on pages 22, 82.*

[121] Paulo Ernesto Marchezi et al. "Degradation mechanisms in mixed-cation and mixed-halide CsxFA1-xPb(BryI1-y)3 perovskite films under ambient conditions". en. In: *Journal of Materials Chemistry A* 8.18 (May 2020). Publisher: The Royal Society of Chemistry, pp. 9302–9312. ISSN: 2050-7496. DOI: 10.1039/D0TA01201G *Cited on pages 22, 81, 99.*

[122] Kevin Ho et al. "Grain Transformation and Degradation Mechanism of Formamidinium and Cesium Lead Iodide Perovskite under Humidity and Light". en. In: *ACS Energy Letters* 6.3 (Mar. 2021), pp. 934–940. ISSN: 2380-8195, 2380-8195. DOI: 10.1021/acsenergylett.0c02247 *Cited on pages 23, 81.*

[123] Qi Wang et al. "Scaling behavior of moisture-induced grain degradation in polycrystalline hybrid perovskite thin films". en. In: *Energy & Environmental Science* 10.2 (2017). Publisher: Royal Society of Chemistry, pp. 516–522. DOI: 10.1039/C6EE02941H *Cited on page 23.*

[124] William R. Mateker and Michael D. McGehee. "Progress in Understanding Degradation Mechanisms and Improving Stability in Organic Photovoltaics". en. In: *Advanced Materials* 29.10 (2017), p. 1603940. ISSN: 1521-4095. DOI: 10.1002/adma.201603940 *Cited on page 24.*

[125] Jun Ji et al. "Two-Stage Ultraviolet Degradation of Perovskite Solar Cells Induced by the Oxygen Vacancy-Ti4+ States". en. In: *iScience* 23.4 (Apr. 2020), p. 101013. ISSN: 2589-0042. DOI: 10.1016/j.isci.2020.101013 *Cited on page 24.*

[126] Tian Chen, Jiangsheng Xie, and Pingqi Gao. "Ultraviolet Photocatalytic Degradation of Perovskite Solar Cells: Progress, Challenges, and Strategies". en. In: *Advanced Energy and Sustainability Research* 3.6 (2022), p. 2100218. ISSN: 2699-9412. DOI: 10.1002/aesr.202100218 *Cited on page 24.*

[127] Yiguo Yao et al. "Organic Hole-Transport Layers for Efficient, Stable, and Scalable Inverted Perovskite Solar Cells". en. In: *Advanced Materials* 34.44 (2022), p. 2203794. ISSN: 1521-4095. DOI: 10.1002/adma.202203794 *Cited on page 24.*

[128] Faming Li and Mingzhen Liu. "Recent efficient strategies for improving the moisture stability of perovskite solar cells". en. In: *Journal of Materials Chemistry A* 5.30 (2017). Publisher: Royal Society of Chemistry, pp. 15447–15459. DOI: 10.1039/C7TA01325F *Cited on page 24.*

[129] Lukasz Przypis et al. "Designing New Indene-Fullerene Derivatives as Electron-Transporting Materials for Flexible Perovskite Solar Cells". In: *The Journal of Physical Chemistry C* 125.49 (Dec. 2021). Publisher: American Chemical Society, pp. 27344–27353. ISSN: 1932-7447. DOI: 10.1021/acs.jpcc.1c07189 *Cited on page 24.*

[130] Ganbaatar Tumen-Ulzii et al. "Understanding the Degradation of Spiro-OMeTAD-Based Perovskite Solar Cells at High Temperature". en. In: *Solar RRL* 4.10 (2020), p. 2000305. ISSN: 2367-198X. DOI: https://doi.org/10.1002/solr.202000305 *Cited on page 24.*

[131] Wenya Song et al. "Improving the Morphology Stability of Spiro-OMeTAD Films for Enhanced Thermal Stability of Perovskite Solar Cells". In: *ACS Applied Materials & Interfaces* 13.37 (Sept. 2021). Publisher: American Chemical Society, pp. 44294–44301. ISSN: 1944-8244. DOI: 10.1021/acsami.1c11227 *Cited on pages 24, 25, 111.*

[132] Mikkel Jørgensen et al. "Stability of Polymer Solar Cells". en. In: *Advanced Materials* 24.5 (2012), pp. 580–612. ISSN: 1521-4095. DOI: 10.1002/adma.201104187 *Cited on page 24.*

[133] Colin D. Bailie et al. “Melt-infiltration of spiro-OMeTAD and thermal instability of solid-state dye-sensitized solar cells”. en. In: *Physical Chemistry Chemical Physics* 16.10 (2014). Publisher: Royal Society of Chemistry, pp. 4864–4870. DOI: 10.1039/C4CP00116H *Cited on page 24.*

[134] Guan-Woo Kim et al. “Hole Transport Materials in Conventional Structural (n–i–p) Perovskite Solar Cells: From Past to the Future”. en. In: *Advanced Energy Materials* 10.8 (2020), p. 1903403. ISSN: 1614-6840. DOI: 10.1002/aenm.201903403 *Cited on page 25.*

[135] Yuichi Kato et al. “Silver Iodide Formation in Methyl Ammonium Lead Iodide Perovskite Solar Cells with Silver Top Electrodes”. en. In: *Advanced Materials Interfaces* 2.13 (2015), p. 1500195. ISSN: 2196-7350. DOI: 10.1002/admi.201500195 *Cited on page 25.*

[136] S. Cacovich et al. “Gold and iodine diffusion in large area perovskite solar cells under illumination”. en. In: *Nanoscale* 9.14 (2017), pp. 4700–4706. ISSN: 2040-3364, 2040-3372. DOI: 10.1039/C7NR00784A *Cited on page 25.*

[137] Konrad Domanski et al. “Not All That Glitters Is Gold: Metal-Migration-Induced Degradation in Perovskite Solar Cells”. In: *ACS Nano* 10.6 (June 2016). Publisher: American Chemical Society, pp. 6306–6314. ISSN: 1936-0851. DOI: 10.1021/acsnano.6b02613 *Cited on page 25.*

[138] Lianfeng Zhao et al. “Redox Chemistry Dominates the Degradation and Decomposition of Metal Halide Perovskite Optoelectronic Devices”. In: *ACS Energy Letters* 1.3 (Sept. 2016). Publisher: American Chemical Society, pp. 595–602. DOI: 10.1021/acsenergylett.6b00320 *Cited on page 25.*

[139] Caleb C. Boyd et al. “Barrier Design to Prevent Metal-Induced Degradation and Improve Thermal Stability in Perovskite Solar Cells”. In: *ACS Energy Letters* 3.7 (July 2018). Publisher: American Chemical Society, pp. 1772–1778. DOI: 10.1021/acsenergylett.8b00926 *Cited on page 25.*

[140] Sikai Mei et al. “Improved Operational Stability of Perovskite Solar Cells via Au Barrier Layer Incorporation”. In: *ACS Applied Energy Materials* 4.10 (Oct. 2021). Publisher: American Chemical Society, pp. 11062–11068. DOI: 10.1021/acsaem.1c01993 *Cited on page 25.*

[141] G. Grancini et al. “One-Year stable perovskite solar cells by 2D/3D interface engineering”. en. In: *Nature Communications* 8.1 (June 2017). Number: 1 Publisher: Nature Publishing Group, p. 15684. ISSN: 2041-1723. DOI: 10.1038/ncomms15684 *Cited on page 26.*

[142] Joseph M. Luther and Laura T. Schelhas. “Perovskite solar cells can take the heat”. In: *Science* 376.6588 (Apr. 2022). Publisher: American Association for the Advancement of Science, pp. 28–29. DOI: 10.1126/science.abo3368 *Cited on page 26.*

[143] Mark V. Khenkin et al. “Consensus statement for stability assessment and reporting for perovskite photovoltaics based on ISOS procedures”. en. In: *Nature Energy* 5.1 (Jan. 2020), pp. 35–49. ISSN: 2058-7546. DOI: 10.1038/s41560-019-0529-5 *Cited on pages 26, 106.*

References for Chapter 2: Electron Microscopy techniques: theory and experimental methods

[34] Qianqian Lin et al. “Hybrid Perovskites: Prospects for Concentrator Solar Cells”. en. In: *Advanced Science* 5.4 (2018), p. 1700792. ISSN: 2198-3844. DOI: 10.1002/advs.201700792 *Cited on pages 10, 15, 43.*

[35] Dane W. deQuilettes et al. “Charge-Carrier Recombination in Halide Perovskites: Focus Review”. en. In: *Chemical Reviews* 119.20 (Oct. 2019), pp. 11007–11019. ISSN: 0009-2665, 1520-6890. DOI: 10.1021/acs.chemrev.9b00169 *Cited on pages 10, 43.*

[76] Caleb C. Boyd et al. “Understanding Degradation Mechanisms and Improving Stability of Perovskite Photovoltaics”. en. In: *Chemical Reviews* 119.5 (Mar. 2019), pp. 3418–3451. ISSN: 0009-2665, 1520-6890. DOI: 10.1021/acs.chemrev.8b00336 *Cited on pages 18, 19, 22–25, 45, 82.*

[80] Lin Ma et al. “Temperature-Dependent Thermal Decomposition Pathway of Organic–Inorganic Halide Perovskite Materials”. en. In: *Chemistry of Materials* 31.20 (Oct. 2019), pp. 8515–8522. ISSN: 0897-4756, 1520-5002. DOI: 10.1021/acs.chemmater.9b03190 *Cited on pages 18, 45, 70.*

[86] Dane W. deQuilettes et al. “Photo-induced halide redistribution in organic–inorganic perovskite films”. en. In: *Nature Communications* 7.1 (May 2016). Number: 1 Publisher: Nature Publishing Group, p. 11683. ISSN: 2041-1723. DOI: 10.1038/ncomms11683 *Cited on pages 19, 42.*

[144] Tim Palucka. *History of electron microscopy, 1931-2000*. Dec. 2002 *Cited on page 29.*

[145] Gerhard Huebschen et al. *Materials Characterization Using Nondestructive Evaluation (NDE) Methods*. en. Google-Books-ID: ZR1rBgAAQBAJ. Woodhead Publishing, Mar. 2016. ISBN: 978-0-08-100057-1 *Cited on pages 31, 34, 51.*

[146] B. G. Yacobi and D. B. Holt. *Cathodoluminescence Microscopy of Inorganic Solids*. en. Google-Books-ID: QbHhBwAAQBAJ. Springer Science & Business Media, June 2013. ISBN: 978-1-4757-9595-0 *Cited on pages 30, 42.*

[147] T. E. Everhart and P. H. Hoff. “Determination of Kilovolt Electron Energy Dissipation vs Penetration Distance in Solid Materials”. In: *Journal of Applied Physics* 42.13 (Dec. 1971). Publisher: American Institute of Physics, pp. 5837–5846. ISSN: 0021-8979. DOI: 10.1063/1.1660019 *Cited on page 31.*

[148] Hendrix Demers et al. “Three-dimensional electron microscopy simulation with the CASINO Monte Carlo software”. en. In: *Scanning* 33.3 (May 2011), pp. 135–146. ISSN: 01610457. DOI: 10.1002/sca.20262 *Cited on page 31.*

[149] Jordi Ferrer Orri et al. “Unveiling the Interaction Mechanisms of Electron and X-ray Radiation with Halide Perovskite Semiconductors using Scanning Nanoprobe Diffraction”. In: *Advanced Materials* 34.18 (2022), p. 2200383 *Cited on pages 31, 124.*

[150] R.F. Egerton. “Dose measurement in the TEM and STEM”. en. In: *Ultramicroscopy* 229 (Oct. 2021), p. 113363. ISSN: 03043991. DOI: 10.1016/j.ultramic.2021.113363 *Cited on page 32.*

[151] R.F. Egerton. “Radiation damage to organic and inorganic specimens in the TEM”. en. In: *Micron* 119 (Apr. 2019), pp. 72–87. ISSN: 09684328. DOI: 10.1016/j.micron.2019.01.005 *Cited on pages 32, 57.*

[152] Shulin Chen and Peng Gao. “Challenges, myths, and opportunities of electron microscopy on halide perovskites”. In: *Journal of Applied Physics* 128.1 (July 2020). Publisher: American Institute of Physics, p. 010901. ISSN: 0021-8979. DOI: 10.1063/5.0012310 *Cited on pages 33, 44, 48, 49, 57, 58.*

[153] Yu-Hao Deng and Leon Georg Nest. “Analysis of misidentifications in TEM characterisation of organic-inorganic hybrid perovskite material”. en. In: *Journal of Microscopy* (Feb. 2021), jmi.13000. ISSN: 0022-2720, 1365-2818. DOI: 10.1111/jmi.13000 *Cited on page 33.*

[154] Mathias Uller Rothmann et al. “Microstructural Characterisations of Perovskite Solar Cells - From Grains to Interfaces: Techniques, Features, and Challenges”. en. In: *Advanced Energy Materials* 7.23 (Dec. 2017), p. 1700912. ISSN: 16146832. DOI: 10.1002/aenm.201700912 *Cited on page 33.*

[155] Yuanyuan Zhou, Hadas Sternlicht, and Nitin P. Padture. “Transmission Electron Microscopy of Halide Perovskite Materials and Devices”. en. In: *Joule* 3.3 (Mar. 2019), pp. 641–661. ISSN: 25424351. DOI: 10.1016/j.joule.2018.12.011 *Cited on pages 33, 49.*

[156] Zhiya Dang et al. “Transformation and degradation of metal halide perovskites induced by energetic electrons and their practical implications”. en. In: *Nano Futures* 5.3 (July 2021). Publisher: IOP Publishing, p. 032001. ISSN: 2399-1984. DOI: 10.1088/2399-1984/ac0c24 *Cited on page 33.*

[157] R F Egerton and Y Zhu. “Spatial resolution in secondary-electron microscopy”. en. In: *Microscopy* (May 2022), dfac022. ISSN: 2050-5698, 2050-5701. DOI: 10.1093/jmicro/dfac022 *Cited on page 34.*

[158] R. F. Egerton. *Physical principles of electron microscopy: an introduction to TEM, SEM, and AEM*. en. OCLC: ocm61714990. New York, NY: Springer, 2005. ISBN: 978-0-387-25800-3 *Cited on pages 34, 35, 37, 52.*

[159] Daniel Abou-Ras et al. “Electron Microscopy on Thin Films for Solar Cells”. en. In: *Advanced Characterization Techniques for Thin Film Solar Cells*. John Wiley & Sons, Ltd, 2011, pp. 299–345. ISBN: 978-3-527-63628-0 *Cited on page 36.*

[160] Joseph I. Goldstein et al. *Scanning Electron Microscopy and X-Ray Microanalysis*. en. New York, NY: Springer, 2018. ISBN: 978-1-4939-6674-5 978-1-4939-6676-9. DOI: 10.1007/978-1-4939-6676-9 *Cited on pages 36, 37.*

[161] François Brisset et al. *Microscopie électronique à balayage et microanalyses*. EDP sciences, 2012 *Cited on page 37.*

[162] David B. Williams and C. Barry Carter. *Transmission electron microscopy: a textbook for materials science*. en. 2nd ed. New York: Springer, 2008. ISBN: 978-0-387-76500-6 *Cited on pages 38, 52, 55, 56, 89, 90, 124.*

[163] Attolight AG. *Allalin 4027 Chronos User Guide*. Feb. 2016 *Cited on page 40.*

[164] Connor G. Bischak et al. “Heterogeneous Charge Carrier Dynamics in Organic–Inorganic Hybrid Materials: Nanoscale Lateral and Depth-Dependent Variation of Recombination Rates in Methylammonium Lead Halide Perovskite Thin Films”. en. In: *Nano Letters* 15.7 (July 2015), pp. 4799–4807. ISSN: 1530-6984, 1530-6992. DOI: 10.1021/acs.nanolett.5b01917 *Cited on page 40.*

[165] Daniel Abou-Ras et al. “No Evidence for Passivation Effects of Na and K at Grain Boundaries in Polycrystalline Cu(In,Ga)Se2 Thin Films for Solar Cells”. en. In: *Solar RRL* 3.8 (2019), p. 1900095. ISSN: 2367-198X. DOI: https://doi.org/10.1002/solr.201900095 *Cited on page 40.*

[166] The Duong et al. “Structural engineering using rubidium iodide as a dopant under excess lead iodide conditions for high efficiency and stable perovskites”. en. In: *Nano Energy* 30 (Dec. 2016), pp. 330–340. ISSN: 22112855. DOI: 10.1016/j.nanoen.2016.10.027 *Cited on page 40.*

[167] Thomas Bidaud. “Characterization of nanomaterials by cathodoluminescence for photovoltaic applications”. These de doctorat. université Paris-Saclay, Jan. 2021 *Cited on page 40.*

[168] Harvey Guthrey and John Moseley. "A Review and Perspective on Cathodoluminescence Analysis of Halide Perovskites". en. In: *Advanced Energy Materials* (Feb. 2020), p. 1903840. ISSN: 1614-6832, 1614-6840. DOI: 10.1002/aenm.201903840 *Cited on pages 41, 42, 46.*

[169] Rebecca L. Milot et al. "Temperature-Dependent Charge-Carrier Dynamics in CH $_3$ NH $_3$ PbI $_3$ Perovskite Thin Films". en. In: *Advanced Functional Materials* 25.39 (Oct. 2015), pp. 6218–6227. ISSN: 1616-301X, 1616-3028. DOI: 10.1002/adfm.201502340 *Cited on page 42.*

[170] Jongchul Lim et al. "Elucidating the long-range charge carrier mobility in metal halide perovskite thin films". en. In: *Energy & Environmental Science* 12.1 (2019). Publisher: Royal Society of Chemistry, pp. 169–176. DOI: 10.1039/C8EE03395A *Cited on page 42.*

[171] Pietro Caprioglio et al. "Nano-emitting Heterostructures Violate Optical Reciprocity and Enable Efficient Photoluminescence in Halide-Segregated Methylammonium-Free Wide Bandgap Perovskites". en. In: *ACS Energy Letters* (Jan. 2021), pp. 419–428. ISSN: 2380-8195, 2380-8195. DOI: 10.1021/acsenergylett.0c02270 *Cited on pages 42, 43, 92, 127.*

[172] Sebastián Caicedo-Dávila et al. "Spatial Phase Distributions in Solution-Based and Evaporated Cs–Pb–Br Thin Films". en. In: *The Journal of Physical Chemistry C* 123.29 (July 2019), pp. 17666–17677. ISSN: 1932-7447, 1932-7455. DOI: 10.1021/acs.jpcc.9b02567 *Cited on pages 42, 64, 66.*

[173] Jonas Lähnemann et al. *LumiSpy/lumispy: v0.2.1*. Nov. 2022. DOI: 10.5281/zenodo.7274897 *Cited on page 43.*

[174] Francisco de la Peña et al. *hyperspy/hyperspy: Release v1.7.3*. Oct. 2022. DOI: 10.5281/zenodo.7263263 *Cited on page 43.*

[175] Nir Klein-Kedem, David Cahen, and Gary Hodes. "Effects of Light and Electron Beam Irradiation on Halide Perovskites and Their Solar Cells". en. In: *Accounts of Chemical Research* 49.2 (Feb. 2016), pp. 347–354. ISSN: 0001-4842, 1520-4898. DOI: 10.1021/acs.accounts.5b00469 *Cited on pages 44, 45, 48.*

[176] Srinivas K. Yadavalli et al. "Electron-beam-induced cracking in organic-inorganic halide Perovskite thin films". en. In: *Scripta Materialia* 187 (Oct. 2020), pp. 88–92. ISSN: 13596462. DOI: 10.1016/j.scriptamat.2020.05.062 *Cited on pages 44–46, 135.*

[177] Zenghua Cai, Yuning Wu, and Shiyou Chen. "Energy-dependent knock-on damage of organic–inorganic hybrid perovskites under electron beam irradiation: First-principles insights". en. In: *Applied Physics Letters* 119.12 (Sept. 2021), p. 123901. ISSN: 0003-6951, 1077-3118. DOI: 10.1063/5.0065849 *Cited on page 45.*

[178] Shulin Chen et al. "Transmission electron microscopy of organic-inorganic hybrid perovskites: myths and truths". en. In: *Science Bulletin* 65.19 (Oct. 2020), pp. 1643–1649. ISSN: 2095-9273. DOI: 10.1016/j.scib.2020.05.020 *Cited on page 45.*

[179] Chuanxiao Xiao et al. "Mechanisms of Electron-Beam-Induced Damage in Perovskite Thin Films Revealed by Cathodoluminescence Spectroscopy". en. In: *The Journal of Physical Chemistry C* 119.48 (Dec. 2015), pp. 26904–26911. ISSN: 1932-7447, 1932-7455. DOI: 10.1021/acs.jpcc.5b09698 *Cited on pages 45–48.*

[180] R.F. Egerton, P. Li, and M. Malac. "Radiation damage in the TEM and SEM". en. In: *Micron* 35.6 (Aug. 2004), pp. 399–409. ISSN: 09684328. DOI: 10.1016/j.micron.2004.02.003 *Cited on pages 45, 58.*

[181] Zhelu Hu et al. “Thermal conductivity and diffusivity of triple-cation perovskite halide materials for solar cells”. In: *Journal of Applied Physics* 127.12 (Mar. 2020). Publisher: American Institute of Physics, p. 125113. ISSN: 0021-8979. DOI: 10.1063/1.5138480 *Cited on page 45.*

[182] Shulin Chen et al. “General Decomposition Pathway of Organic–Inorganic Hybrid Perovskites through an Intermediate Superstructure and its Suppression Mechanism”. en. In: *Advanced Materials* (May 2020), p. 2001107. ISSN: 0935-9648, 1521-4095. DOI: 10.1002/adma.202001107 *Cited on pages 45, 57.*

[183] Aleksandar R. Milosavljević et al. “Low-Energy Electron-Induced Transformations in Organolead Halide Perovskite”. en. In: *Angewandte Chemie International Edition* 55.34 (Aug. 2016), pp. 10083–10087. ISSN: 14337851. DOI: 10.1002/anie.201605013 *Cited on page 45.*

[184] Jordi Ferrer Orri. “Using pulsed mode scanning electron microscopy for cathodoluminescence studies on hybrid perovskite films”. en. In: (2021), p. 11 *Cited on pages 47, 132.*

[185] Olivia Hentz, Zhibo Zhao, and Silvija Gradečak. “Impacts of Ion Segregation on Local Optical Properties in Mixed Halide Perovskite Films”. en. In: *Nano Letters* 16.2 (Feb. 2016), pp. 1485–1490. ISSN: 1530-6984, 1530-6992. DOI: 10.1021/acs.nanolett.5b05181 *Cited on page 47.*

[186] Shulin Chen et al. “Atomic scale insights into structure instability and decomposition pathway of methylammonium lead iodide perovskite”. en. In: *Nature Communications* 9.1 (Dec. 2018), p. 4807. ISSN: 2041-1723. DOI: 10.1038/s41467-018-07177-y *Cited on pages 48, 57.*

[187] Mathias Uller Rothmann et al. “Structural and Chemical Changes to $CH_3NH_3PbI_3$ Induced by Electron and Gallium Ion Beams”. en. In: *Advanced Materials* 30.25 (June 2018), p. 1800629. ISSN: 0935-9648, 1521-4095. DOI: 10.1002/adma.201800629 *Cited on pages 48, 49, 57.*

[188] Sebastián Caicedo-Dávila et al. “Effects of postdeposition annealing on the luminescence of mixed-phase CsPb2Br5/CsPbBr3 thin films”. In: *The Journal of Physical Chemistry C* 124.36 (2020), pp. 19514–19521 *Cited on page 48.*

[189] C. Kisielowski et al. “Detection of Single Atoms and Buried Defects in Three Dimensions by Aberration-Corrected Electron Microscope with 0.5-Å Information Limit”. en. In: *Microscopy and Microanalysis* 14.5 (Oct. 2008). Publisher: Cambridge University Press, pp. 469–477. ISSN: 1435-8115, 1431-9276. DOI: 10.1017/S1431927608080902 *Cited on page 49.*

[190] Junhui Ran et al. “Electron-Beam-Related Studies of Halide Perovskites: Challenges and Opportunities”. en. In: *Advanced Energy Materials* (Feb. 2020), p. 1903191. ISSN: 1614-6832, 1614-6840. DOI: 10.1002/aenm.201903191 *Cited on page 49.*

[191] P.R. Munroe. “The application of focused ion beam microscopy in the material sciences”. en. In: *Materials Characterization* 60.1 (Jan. 2009), pp. 2–13. ISSN: 10445803. DOI: 10.1016/j.matchar.2008.11.014 *Cited on page 49.*

[192] Tae Woong Kim and Satoshi Uchida. “Role of FIB and TEM in Organo-Halide Perovskite Solar Cell Observations”. en. In: (2019), p. 7 *Cited on page 49.*

[193] Miroslava Schaffer, Bernhard Schaffer, and Quentin Ramasse. “Sample preparation for atomic-resolution STEM at low voltages by FIB”. en. In: *Ultramicroscopy* 114 (Mar. 2012), pp. 62–71. ISSN: 03043991. DOI: 10.1016/j.ultramic.2012.01.005 *Cited on page 50.*

[194] Quentin Jeangros et al. "In Situ TEM Analysis of Organic–Inorganic Metal-Halide Perovskite Solar Cells under Electrical Bias". en. In: *Nano Letters* 16.11 (Nov. 2016), pp. 7013–7018. ISSN: 1530-6984, 1530-6992. DOI: 10.1021/acs.nanolett.6b03158 *Cited on page 50.*

[195] Felix Utama Kosasih et al. "Nanometric Chemical Analysis of Beam-Sensitive Materials: A Case Study of STEM-EDX on Perovskite Solar Cells". en. In: *Small Methods* (Nov. 2020), p. 2000835. ISSN: 2366-9608, 2366-9608. DOI: 10.1002/smtd.202000835 *Cited on pages 52, 54, 58.*

[196] P. Hartel, H. Rose, and C. Dinges. "Conditions and reasons for incoherent imaging in STEM". en. In: *Ultramicroscopy* 63.2 (June 1996), pp. 93–114. ISSN: 0304-3991. DOI: 10.1016/0304-3991(96)00020-4 *Cited on page 53.*

[197] Sebastián Caicedo-Dávila et al. "Effects of Postdeposition Annealing on the Luminescence of Mixed-Phase $CsPb_2Br_5$ /$CsPbBr_3$ Thin Films". en. In: *The Journal of Physical Chemistry C* 124.36 (Sept. 2020), pp. 19514–19521. ISSN: 1932-7447, 1932-7455. DOI: 10.1021/acs.jpcc.0c06955 *Cited on pages 54, 64, 72, 73, 75, 76.*

[198] P. Schlossmacher et al. "Enhanced Detection Sensitivity with a New Windowless XEDS System for AEM Based on Silicon Drift Detector Technology". en. In: *Microscopy Today* 18.4 (July 2010), pp. 14–20. ISSN: 1551-9295, 2150-3583. DOI: 10.1017/S1551929510000404 *Cited on page 54.*

[199] Masashi Watanabe. "Practical Aspects and Advanced Applications of XEDS". en. In: *Transmission Electron Microscopy*. Ed. by C. Barry Carter and David B. Williams. Cham: Springer International Publishing, 2016, pp. 467–503. ISBN: 978-3-319-26649-7 978-3-319-26651-0. DOI: 10.1007/978-3-319-26651-0_17 *Cited on page 55.*

[200] Zhiya Dang et al. "*In Situ* Transmission Electron Microscopy Study of Electron Beam-Induced Transformations in Colloidal Cesium Lead Halide Perovskite Nanocrystals". en. In: *ACS Nano* 11.2 (Feb. 2017), pp. 2124–2132. ISSN: 1936-0851, 1936-086X. DOI: 10.1021/acsnano.6b08324 *Cited on page 57.*

[201] Mathias Uller Rothmann et al. "Direct observation of intrinsic twin domains in tetragonal CH3NH3PbI3". en. In: *Nature Communications* 8.1 (Apr. 2017), p. 14547. ISSN: 2041-1723. DOI: 10.1038/ncomms14547 *Cited on page 57.*

[202] Xinlei Zhang et al. "Orientational Dependence of Electron Beam Irradiation Damage in Lead-Free Halide Double Perovskite Cs2AgBiBr6". In: *The Journal of Physical Chemistry C* 125.23 (June 2021). Publisher: American Chemical Society, pp. 13033–13040. ISSN: 1932-7447. DOI: 10.1021/acs.jpcc.1c03049 *Cited on page 57.*

[203] Mathias Uller Rothmann et al. "Atomic-scale microstructure of metal halide perovskite". en. In: *Science* 370.6516 (Oct. 2020), eabb5940. ISSN: 0036-8075, 1095-9203. DOI: 10.1126/science.abb5940 *Cited on page 58.*

[204] Felix Utama Kosasih. "Low Dose Analytical Electron Microscopy of Hybrid Perovskite Photovoltaic Devices". en. PhD thesis. 2022 *Cited on page 58.*

References for Chapter 3: Analysis of cesium, lead, and bromide-based perovskite

[36] Laura M. Herz. "Charge-Carrier Dynamics in Organic-Inorganic Metal Halide Perovskites". en. In: *Annual Review of Physical Chemistry* 67.1 (May 2016), pp. 65–89. ISSN: 0066-426X, 1545-1593. DOI: 10.1146/annurev-physchem-040215-112222 *Cited on pages 10, 71, 93.*

[75] Yu An et al. “Structural Stability of Formamidinium- and Cesium-Based Halide Perovskites”. In: *ACS Energy Letters* 6.5 (May 2021). Publisher: American Chemical Society, pp. 1942–1969. DOI: 10.1021/acsenergylett.1c00354 *Cited on pages 18, 22, 63, 89.*

[80] Lin Ma et al. “Temperature-Dependent Thermal Decomposition Pathway of Organic–Inorganic Halide Perovskite Materials”. en. In: *Chemistry of Materials* 31.20 (Oct. 2019), pp. 8515–8522. ISSN: 0897-4756, 1520-5002. DOI: 10.1021/acs.chemmater.9b03190 *Cited on pages 18, 45, 70.*

[172] Sebastián Caicedo-Dávila et al. “Spatial Phase Distributions in Solution-Based and Evaporated Cs–Pb–Br Thin Films”. en. In: *The Journal of Physical Chemistry C* 123.29 (July 2019), pp. 17666–17677. ISSN: 1932-7447, 1932-7455. DOI: 10.1021/acs.jpcc.9b02567 *Cited on pages 42, 64, 66.*

[197] Sebastián Caicedo-Dávila et al. “Effects of Postdeposition Annealing on the Luminescence of Mixed-Phase $CsPb_2Br_5$ /$CsPbBr_3$ Thin Films”. en. In: *The Journal of Physical Chemistry C* 124.36 (Sept. 2020), pp. 19514–19521. ISSN: 1932-7447, 1932-7455. DOI: 10.1021/acs.jpcc.0c06955 *Cited on pages 54, 64, 72, 73, 75, 76.*

[205] Julian A. Steele et al. “Thermal unequilibrium of strained black CsPbI3 thin films”. en. In: *Science* 365.6454 (Aug. 2019). Publisher: American Association for the Advancement of Science Section: Report, pp. 679–684. ISSN: 0036-8075, 1095-9203. DOI: 10.1126/science.aax3878 *Cited on page 63.*

[206] Arpit Mishra, Philippe Baranek, and Andrei Postnikov. “First-principles investigation of CO2, CO, and O2 adsorptions on the (001)-reconstructed surfaces of CsPbX3 (X = Cl, Br, and I) perovskites”. en. In: *Surfaces and Interfaces* 25 (Aug. 2021), p. 101264. ISSN: 2468-0230. DOI: 10.1016/j.surfin.2021.101264 *Cited on pages 63, 64, 89, 147.*

[207] T. Paul et al. “Tunable cathodoluminescence over the entire visible window from all-inorganic perovskite $CsPbX_3$ 1D architecture”. en. In: *Journal of Materials Chemistry C* 6.13 (2018), pp. 3322–3333. ISSN: 2050-7526, 2050-7534. DOI: 10.1039/C7TC05703B *Cited on pages 64, 66.*

[208] Ji-Hyun Cha et al. “Photoresponse of CsPbBr3 and Cs4PbBr6 Perovskite Single Crystals”. en. In: *J. Phys. Chem. Lett.* (2017), p. 6 *Cited on page 64.*

[209] Peng Xiao et al. “Emergence of Nanoplatelet Light-Emitting Diodes”. en. In: *Materials* 11.8 (Aug. 2018), p. 1376. ISSN: 1996-1944. DOI: 10.3390/ma11081376 *Cited on page 64.*

[210] Xiaosheng Tang et al. “Perovskite CsPb2Br5 Microplate Laser with Enhanced Stability and Tunable Properties”. en. In: *Advanced Optical Materials* 5.3 (2017), p. 1600788. ISSN: 2195-1071. DOI: 10.1002/adom.201600788 *Cited on pages 64, 71, 75, 82.*

[211] Guopeng Li et al. “Shape and phase evolution from CsPbBr 3 perovskite nanocubes to tetragonal CsPb 2 Br 5 nanosheets with an indirect bandgap”. en. In: *Chemical Communications* 52.75 (2016). Publisher: Royal Society of Chemistry, pp. 11296–11299. DOI: 10.1039/C6CC05877A *Cited on pages 64, 71, 72, 75, 98.*

[212] Zhaojun Zhang et al. “Growth, characterization and optoelectronic applications of pure-phase large-area $CsPb_2Br_5$ flake single crystals”. en. In: *Journal of Materials Chemistry C* 6.3 (2018), pp. 446–451. ISSN: 2050-7526, 2050-7534. DOI: 10.1039/C7TC04834C *Cited on pages 64, 98.*

[213] Giovanni Mannino et al. “Temperature-Dependent Optical Band Gap in CsPbBr3, MAPbBr3, and FAPbBr3 Single Crystals”. In: *The Journal of Physical Chemistry Letters* 11.7 (Apr. 2020). Publisher: American Chemical Society, pp. 2490–2496. DOI: 10.1021/acs.jpclett.0c00295 *Cited on pages 64, 66.*

[214] H. Näsström et al. “Dependence of phase transitions on halide ratio in inorganic CsPb(Br $_{x}$ I $_{1-x}$) $_{3}$ perovskite thin films obtained from high-throughput experimentation”. en. In: *Journal of Materials Chemistry A* 8.43 (2020), pp. 22626–22631. ISSN: 2050-7488, 2050-7496. DOI: 10.1039/D0TA08067E *Cited on page 64.*

[215] Muhan Cao et al. “Low-Dimensional-Networked Cesium Lead Halide Perovskites: Properties, Fabrication, and Applications”. en. In: *Small Methods* 4.12 (Dec. 2020), p. 2000303. ISSN: 2366-9608, 2366-9608. DOI: 10.1002/smtd.202000303 *Cited on pages 64, 71.*

[216] Yeshu Tan et al. “Ultrastable and Reversible Fluorescent Perovskite Films Used for Flexible Instantaneous Display”. en. In: *Advanced Functional Materials* 29.23 (2019), p. 1900730. ISSN: 1616-3028. DOI: 10.1002/adfm.201900730 *Cited on page 64.*

[217] Diego Di Girolamo et al. “Dual effect of humidity on cesium lead bromide: enhancement and degradation of perovskite films”. en. In: *Journal of Materials Chemistry A* 7.19 (2019), pp. 12292–12302. ISSN: 2050-7488, 2050-7496. DOI: 10.1039/C9TA00715F *Cited on pages 64, 83, 97, 98.*

[218] Xisheng Zhang et al. “All-Ambient Processed Binary CsPbBr3–CsPb2Br5 Perovskites with Synergistic Enhancement for High-Efficiency Cs–Pb–Br-Based Solar Cells”. en. In: *ACS Appl. Mater. Interfaces* (2018), p. 10 *Cited on page 64.*

[219] Bo Qiao et al. “Water-resistant, monodispersed and stably luminescent CsPbBr $_{3}$ /CsPb $_{2}$ Br $_{5}$ core–shell-like structure lead halide perovskite nanocrystals”. en. In: *Nanotechnology* 28.44 (Nov. 2017), p. 445602. ISSN: 0957-4484, 1361-6528. DOI: 10.1088/1361-6528/aa892e *Cited on page 64.*

[220] Xiaoli Zhang et al. “All-Inorganic Perovskite Nanocrystals for High-Efficiency Light Emitting Diodes: Dual-Phase CsPbBr $_{3}$ -CsPb $_{2}$ Br $_{5}$ Composites”. en. In: *Advanced Functional Materials* 26.25 (July 2016), pp. 4595–4600. ISSN: 1616301X. DOI: 10.1002/adfm.201600958 *Cited on page 64.*

[221] Guoqing Tong et al. “Dual-Phase CsPbBr3–CsPb2Br5 Perovskite Thin Films via Vapor Deposition for High-Performance Rigid and Flexible Photodetectors”. en. In: *Small* 14.7 (2018), p. 1702523. ISSN: 1613-6829. DOI: 10.1002/smll.201702523 *Cited on page 64.*

[222] Mei Liu et al. “Unveiling Solvent-Related Effect on Phase Transformations in CsBr–PbBr $_{2}$ System: Coordination and Ratio of Precursors”. en. In: *Chemistry of Materials* 30.17 (Sept. 2018), pp. 5846–5852. ISSN: 0897-4756, 1520-5002. DOI: 10.1021/acs.chemmater.8b00537 *Cited on pages 65, 98, 99.*

[223] Libo Fan et al. “Research Progress on the Stability of Organic–Inorganic Halide Perovskite Photodetectors in a Humid Environment Through the Modification of Perovskite Layers”. en. In: *Journal of Electronic Materials* 51.6 (June 2022), pp. 2801–2818. ISSN: 1543-186X. DOI: 10.1007/s11664-022-09548-0 *Cited on page 65.*

[224] Xianhao Zhao et al. “First-principles study on the electronic and optical properties of the orthorhombic CsPbBr3 and CsPbI3 with Cmcm space group”. en. In: *New Journal of Chemistry* 45.35 (Sept. 2021). Publisher: The Royal Society of Chemistry, pp. 15857–15862. ISSN: 1369-9261. DOI: 10.1039/D1NJ02216D *Cited on page 66.*

[225] Ioannis Petousis et al. “High-throughput screening of inorganic compounds for the discovery of novel dielectric and optical materials”. en. In: *Scientific Data* 4.1 (Jan. 2017). Number: 1 Publisher: Nature Publishing Group, p. 160134. ISSN: 2052-4463. DOI: 10.1038/sdata.2016.134 *Cited on page 66.*

[226] Yanan Li et al. “Lattice Modulation of Alkali Metal Cations Doped Cs1-xRxPbBr3 Halides for Inorganic Perovskite Solar Cells”. en. In: *Solar RRL* 2.10 (2018), p. 1800164. ISSN: 2367-198X. DOI: 10.1002/solr.201800164 *Cited on page 66.*

[227] M. Sebastian et al. “Excitonic emissions and above-band-gap luminescence in the single-crystal perovskite semiconductors CsPbBr3 and CsPbCl3”. In: *Physical Review B* 92.23 (Dec. 2015). Publisher: American Physical Society, p. 235210. DOI: 10.1103/PhysRevB.92.235210 *Cited on page 66.*

[228] Benjamin T. Diroll, Hua Zhou, and Richard D. Schaller. “Low-Temperature Absorption, Photoluminescence, and Lifetime of CsPbX3 (X = Cl, Br, I) Nanocrystals”. en. In: *Advanced Functional Materials* 28.30 (2018), p. 1800945. ISSN: 1616-3028. DOI: 10.1002/adfm.201800945 *Cited on pages 66, 70, 93.*

[229] Jia-Yue Yang and Ming Hu. “Temperature-Induced Large Broadening and Blue Shift in the Electronic Band Structure and Optical Absorption of Methylammonium Lead Iodide Perovskite”. In: *The Journal of Physical Chemistry Letters* 8.16 (Aug. 2017). Publisher: American Chemical Society, pp. 3720–3725. DOI: 10.1021/acs.jpclett.7b01719 *Cited on page 66.*

[230] M. Smith et al. “Free excitonic transitions in GaN, grown by metal-organic chemical-vapor deposition”. In: *Journal of Applied Physics* 79.9 (May 1996). Publisher: American Institute of Physics, pp. 7001–7004. ISSN: 0021-8979. DOI: 10.1063/1.362448 *Cited on page 66.*

[231] Eyal Cohen et al. “Nonheteroepitaxial CsPbBr $_3$ /Cs $_4$ PbBr $_6$ Interfaces Result in Non-passivated Bright Bromide Vacancies”. en. In: *Chemistry of Materials* 34.12 (June 2022), pp. 5377–5385. ISSN: 0897-4756, 1520-5002. DOI: 10.1021/acs.chemmater.2c00098 *Cited on pages 68, 69.*

[232] *Materials Data on PbBr2 by Materials Project*. English. Tech. rep. mp-862868. Lawrence Berkeley National Lab. (LBNL), Berkeley, CA (United States). LBNL Materials Project, July 2020. DOI: 10.17188/1309683 *Cited on page 69.*

[233] Xiaoman Ma et al. “Mechanism of Single-Photon Upconversion Photoluminescence in All-Inorganic Perovskite Nanocrystals: The Role of Self-Trapped Excitons”. In: *The Journal of Physical Chemistry Letters* 10.20 (Oct. 2019). Publisher: American Chemical Society, pp. 5989–5996. DOI: 10.1021/acs.jpclett.9b02289 *Cited on page 70.*

[234] Zhen Liu et al. “Temperature-dependent photoluminescence and lasing properties of CsPbBr3 nanowires”. In: *Applied Physics Letters* 114.10 (Mar. 2019). Publisher: American Institute of Physics, p. 101902. ISSN: 0003-6951. DOI: 10.1063/1.5082759 *Cited on pages 70, 93.*

[235] Hee Chul Woo et al. “Temperature-Dependent Photoluminescence of CH3NH3PbBr3 Perovskite Quantum Dots and Bulk Counterparts”. en. In: *J. Phys. Chem. Lett.* (2018), p. 9 *Cited on pages 70, 93.*

[236] Taiping Lu et al. “Temperature-dependent photoluminescence in light-emitting diodes”. en. In: *Scientific Reports* 4.1 (May 2015), p. 6131. ISSN: 2045-2322. DOI: 10.1038/srep06131 *Cited on page 70.*

[237] Brenden A. Magill et al. “Probe of the excitonic transitions and lifetimes in quasi-2D organic–inorganic halide perovskites”. In: *AIP Advances* 12.1 (Jan. 2022). Publisher: American Institute of Physics, p. 015114. DOI: 10.1063/5.0072566 *Cited on page 70.*

[238] Katelyn P. Goetz et al. “Shining Light on the Photoluminescence Properties of Metal Halide Perovskites”. en. In: *Advanced Functional Materials* 30.23 (2020), p. 1910004. ISSN: 1616-3028. DOI: 10.1002/adfm.201910004 *Cited on page 70.*

[239] Yuqing Cao et al. “The photothermal stability study of silica-coated CsPbBr3 perovskite nanocrystals”. en. In: *Journal of Solid State Chemistry* 311 (July 2022), p. 123086. ISSN: 0022-4596. DOI: 10.1016/j.jssc.2022.123086 *Cited on pages 71, 93.*

[240] Jun Yi et al. "The correlation between phase transition and photoluminescence properties of CsPbX3 (X = Cl, Br, I) perovskite nanocrystals". en. In: *Nanoscale Advances* 2.10 (Oct. 2020). Publisher: RSC, pp. 4390–4394. ISSN: 2516-0230. DOI: 10.1039/D0NA00545B *Cited on pages 71, 93.*

[241] Qi Wang et al. "Improved thermal stability of photoluminescence in Cs4PbBr6 microcrystals/CsPbBr3 nanocrystals". en. In: *Journal of Colloid and Interface Science* 554 (Oct. 2019), pp. 133–141. ISSN: 0021-9797. DOI: 10.1016/j.jcis.2019.06.083 *Cited on page 71.*

[242] Yu-Qian Zhou et al. "Green Emission Induced by Intrinsic Defects in All-Inorganic Perovskite CsPb $_2$ Br $_5$". en. In: *The Journal of Physical Chemistry Letters* 10.20 (Oct. 2019), pp. 6118–6123. ISSN: 1948-7185, 1948-7185. DOI: 10.1021/acs.jpclett.9b02367 *Cited on pages 71, 72.*

[243] Chuanjiang Qin et al. "Centrifugal-Coated Quasi-Two-Dimensional Perovskite CsPb2Br5 Films for Efficient and Stable Light-Emitting Diodes". In: *The Journal of Physical Chemistry Letters* 8.21 (Nov. 2017). Publisher: American Chemical Society, pp. 5415–5421. DOI: 10.1021/acs.jpclett.7b02371 *Cited on pages 71, 72, 75, 96.*

[244] Kun-Hua Wang et al. "Large-Scale Synthesis of Highly Luminescent Perovskite-Related CsPb2Br5 Nanoplatelets and Their Fast Anion Exchange". en. In: *Angewandte Chemie* 128.29 (2016), pp. 8468–8472. ISSN: 1521-3757. DOI: 10.1002/ange.201602787 *Cited on pages 71, 75, 95.*

[245] Jing Li et al. "Synthesis of all-inorganic CsPb $_2$ Br $_5$ perovskite and determination of its luminescence mechanism". en. In: *RSC Advances* 7.85 (2017), pp. 54002–54007. ISSN: 2046-2069. DOI: 10.1039/C7RA10693A *Cited on page 71.*

[246] Sebastián Caicedo Dávila. "Influence of mixed phases on the optoelectronic properties of Cs-Pb-Br compounds". PhD thesis. Sept. 2020 *Cited on pages 72, 76.*

[247] Chong Wang et al. "Extrinsic Green Photoluminescence from the Edges of 2D Cesium Lead Halides". en. In: *Advanced Materials* 31.33 (Aug. 2019), p. 1902492. ISSN: 0935-9648, 1521-4095. DOI: 10.1002/adma.201902492 *Cited on page 72.*

[248] Peng Shen et al. "Extrinsic Photoluminescence and Resonant Raman Spectra of CsPb2Br5 Microspheres". In: *The Journal of Physical Chemistry C* 125.12 (Apr. 2021). Publisher: American Chemical Society, pp. 6767–6772. ISSN: 1932-7447. DOI: 10.1021/acs.jpcc.0c11301 *Cited on pages 72, 73, 75, 95.*

[249] Mohammad Ali Akhavan Kazemi et al. "Moisture-Induced Non-Equilibrium Phase Segregation in Triple Cation Mixed Halide Perovskite Monitored by In Situ Characterization Techniques and Solid-State NMR". In: *Energy & Environmental Materials* (2022) *Cited on pages 73, 82.*

[250] Jun Yin et al. "Point Defects and Green Emission in Zero-Dimensional Perovskites". eng. In: *The Journal of Physical Chemistry Letters* 9.18 (Sept. 2018), pp. 5490–5495. ISSN: 1948-7185. DOI: 10.1021/acs.jpclett.8b02477 *Cited on page 76.*

[251] Dan Han et al. "Unraveling luminescence mechanisms in zero-dimensional halide perovskites". en. In: *Journal of Materials Chemistry C* 6.24 (2018). Publisher: Royal Society of Chemistry, pp. 6398–6405. DOI: 10.1039/C8TC01291A *Cited on page 76.*

References for Chapter 4: Analysis of CsMAFA perovskite degradation products

[36] Laura M. Herz. "Charge-Carrier Dynamics in Organic-Inorganic Metal Halide Perovskites". en. In: *Annual Review of Physical Chemistry* 67.1 (May 2016), pp. 65–89. ISSN: 0066-426X, 1545-1593. DOI: 10.1146/annurev-physchem-040215-112222 *Cited on pages 10, 71, 93.*

[75] Yu An et al. "Structural Stability of Formamidinium- and Cesium-Based Halide Perovskites". In: *ACS Energy Letters* 6.5 (May 2021). Publisher: American Chemical Society, pp. 1942–1969. DOI: 10.1021/acsenergylett.1c00354 *Cited on pages 18, 22, 63, 89.*

[76] Caleb C. Boyd et al. "Understanding Degradation Mechanisms and Improving Stability of Perovskite Photovoltaics". en. In: *Chemical Reviews* 119.5 (Mar. 2019), pp. 3418–3451. ISSN: 0009-2665, 1520-6890. DOI: 10.1021/acs.chemrev.8b00336 *Cited on pages 18, 19, 22–25, 45, 82.*

[98] Ilia M. Pavlovetc et al. "Suppressing Cation Migration in Triple-Cation Lead Halide Perovskites". In: *ACS Energy Letters* 5.9 (Sept. 2020). Publisher: American Chemical Society, pp. 2802–2810. DOI: 10.1021/acsenergylett.0c01207 *Cited on pages 21, 98, 125.*

[102] Nengxu Li et al. "Microscopic Degradation in Formamidinium-Cesium Lead Iodide Perovskite Solar Cells under Operational Stressors". en. In: *Joule* (July 2020). ISSN: 25424351. DOI: 10.1016/j.joule.2020.06.005 *Cited on pages 21, 98, 111, 125, 127.*

[109] Shun-Chang Liu et al. "Investigation of Oxygen Passivation for High-Performance All-Inorganic Perovskite Solar Cells". In: *Journal of the American Chemical Society* 141.45 (Nov. 2019). Publisher: American Chemical Society, pp. 18075–18082. ISSN: 0002-7863. DOI: 10.1021/jacs.9b07182 *Cited on pages 21, 22, 98.*

[113] Jinli Yang et al. "Investigation of CH3NH3PbI3 Degradation Rates and Mechanisms in Controlled Humidity Environments Using in Situ Techniques". In: *ACS Nano* 9.2 (Feb. 2015). Publisher: American Chemical Society, pp. 1955–1963. ISSN: 1936-0851. DOI: 10.1021/nn506864k *Cited on pages 22, 81.*

[119] John M. Howard et al. "Humidity-Induced Photoluminescence Hysteresis in Variable Cs/Br Ratio Hybrid Perovskites". en. In: *The Journal of Physical Chemistry Letters* 9.12 (June 2018), pp. 3463–3469. ISSN: 1948-7185. DOI: 10.1021/acs.jpclett.8b01357 *Cited on pages 22, 82, 83.*

[120] Yinghong Hu et al. "Impact of Rubidium and Cesium Cations on the Moisture Stability of Multiple-Cation Mixed-Halide Perovskites". en. In: *ACS Energy Letters* 2.10 (Oct. 2017), pp. 2212–2218. ISSN: 2380-8195, 2380-8195. DOI: 10.1021/acsenergylett.7b00731 *Cited on pages 22, 82.*

[121] Paulo Ernesto Marchezi et al. "Degradation mechanisms in mixed-cation and mixed-halide CsxFA1-xPb(BryI1-y)3 perovskite films under ambient conditions". en. In: *Journal of Materials Chemistry A* 8.18 (May 2020). Publisher: The Royal Society of Chemistry, pp. 9302–9312. ISSN: 2050-7496. DOI: 10.1039/D0TA01201G *Cited on pages 22, 81, 99.*

[122] Kevin Ho et al. "Grain Transformation and Degradation Mechanism of Formamidinium and Cesium Lead Iodide Perovskite under Humidity and Light". en. In: *ACS Energy Letters* 6.3 (Mar. 2021), pp. 934–940. ISSN: 2380-8195, 2380-8195. DOI: 10.1021/acsenergylett.0c02247 *Cited on pages 23, 81.*

[162] David B. Williams and C. Barry Carter. *Transmission electron microscopy: a textbook for materials science*. en. 2nd ed. New York: Springer, 2008. ISBN: 978-0-387-76500-6 *Cited on pages 38, 52, 55, 56, 89, 90, 124.*

[171] Pietro Caprioglio et al. “Nano-emitting Heterostructures Violate Optical Reciprocity and Enable Efficient Photoluminescence in Halide-Segregated Methylammonium-Free Wide Bandgap Perovskites”. en. In: *ACS Energy Letters* (Jan. 2021), pp. 419–428. ISSN: 2380-8195, 2380-8195. DOI: 10.1021/acsenergylett.0c02270 *Cited on pages 42, 43, 92, 127.*

[206] Arpit Mishra, Philippe Baranek, and Andrei Postnikov. “First-principles investigation of CO2, CO, and O2 adsorptions on the (001)-reconstructed surfaces of CsPbX3 (X = Cl, Br, and I) perovskites”. en. In: *Surfaces and Interfaces* 25 (Aug. 2021), p. 101264. ISSN: 2468-0230. DOI: 10.1016/j.surfin.2021.101264 *Cited on pages 63, 64, 89, 147.*

[210] Xiaosheng Tang et al. “Perovskite CsPb2Br5 Microplate Laser with Enhanced Stability and Tunable Properties”. en. In: *Advanced Optical Materials* 5.3 (2017), p. 1600788. ISSN: 2195-1071. DOI: 10.1002/adom.201600788 *Cited on pages 64, 71, 75, 82.*

[211] Guopeng Li et al. “Shape and phase evolution from CsPbBr 3 perovskite nanocubes to tetragonal CsPb 2 Br 5 nanosheets with an indirect bandgap”. en. In: *Chemical Communications* 52.75 (2016). Publisher: Royal Society of Chemistry, pp. 11296–11299. DOI: 10.1039/C6CC05877A *Cited on pages 64, 71, 72, 75, 98.*

[212] Zhaojun Zhang et al. “Growth, characterization and optoelectronic applications of pure-phase large-area CsPb $_2$ Br $_5$ flake single crystals”. en. In: *Journal of Materials Chemistry C* 6.3 (2018), pp. 446–451. ISSN: 2050-7526, 2050-7534. DOI: 10.1039/C7TC04834C *Cited on pages 64, 98.*

[217] Diego Di Girolamo et al. “Dual effect of humidity on cesium lead bromide: enhancement and degradation of perovskite films”. en. In: *Journal of Materials Chemistry A* 7.19 (2019), pp. 12292–12302. ISSN: 2050-7488, 2050-7496. DOI: 10.1039/C9TA00715F *Cited on pages 64, 83, 97, 98.*

[222] Mei Liu et al. “Unveiling Solvent-Related Effect on Phase Transformations in CsBr–PbBr $_2$ System: Coordination and Ratio of Precursors”. en. In: *Chemistry of Materials* 30.17 (Sept. 2018), pp. 5846–5852. ISSN: 0897-4756, 1520-5002. DOI: 10.1021/acs.chemmater.8b00537 *Cited on pages 65, 98, 99.*

[228] Benjamin T. Diroll, Hua Zhou, and Richard D. Schaller. “Low-Temperature Absorption, Photoluminescence, and Lifetime of CsPbX3 (X = Cl, Br, I) Nanocrystals”. en. In: *Advanced Functional Materials* 28.30 (2018), p. 1800945. ISSN: 1616-3028. DOI: 10.1002/adfm.201800945 *Cited on pages 66, 70, 93.*

[234] Zhen Liu et al. “Temperature-dependent photoluminescence and lasing properties of CsPbBr3 nanowires”. In: *Applied Physics Letters* 114.10 (Mar. 2019). Publisher: American Institute of Physics, p. 101902. ISSN: 0003-6951. DOI: 10.1063/1.5082759 *Cited on pages 70, 93.*

[235] Hee Chul Woo et al. “Temperature-Dependent Photoluminescence of CH3NH3PbBr3 Perovskite Quantum Dots and Bulk Counterparts”. en. In: *J. Phys. Chem. Lett.* (2018), p. 9 *Cited on pages 70, 93.*

[239] Yuqing Cao et al. “The photothermal stability study of silica-coated CsPbBr3 perovskite nanocrystals”. en. In: *Journal of Solid State Chemistry* 311 (July 2022), p. 123086. ISSN: 0022-4596. DOI: 10.1016/j.jssc.2022.123086 *Cited on pages 71, 93.*

[240] Jun Yi et al. “The correlation between phase transition and photoluminescence properties of CsPbX3 (X = Cl, Br, I) perovskite nanocrystals”. en. In: *Nanoscale Advances* 2.10 (Oct. 2020). Publisher: RSC, pp. 4390–4394. ISSN: 2516-0230. DOI: 10.1039/D0NA00545B *Cited on pages 71, 93.*

[243] Chuanjiang Qin et al. “Centrifugal-Coated Quasi-Two-Dimensional Perovskite CsPb2Br5 Films for Efficient and Stable Light-Emitting Diodes”. In: *The Journal of Physical Chemistry Letters* 8.21 (Nov. 2017). Publisher: American Chemical Society, pp. 5415–5421. DOI: 10.1021/acs.jpclett.7b02371 *Cited on pages 71, 72, 75, 96.*

[244] Kun-Hua Wang et al. “Large-Scale Synthesis of Highly Luminescent Perovskite-Related CsPb2Br5 Nanoplatelets and Their Fast Anion Exchange”. en. In: *Angewandte Chemie* 128.29 (2016), pp. 8468–8472. ISSN: 1521-3757. DOI: 10.1002/ange.201602787 *Cited on pages 71, 75, 95.*

[248] Peng Shen et al. “Extrinsic Photoluminescence and Resonant Raman Spectra of CsPb2Br5 Microspheres”. In: *The Journal of Physical Chemistry C* 125.12 (Apr. 2021). Publisher: American Chemical Society, pp. 6767–6772. ISSN: 1932-7447. DOI: 10.1021/acs.jpcc.0c11301 *Cited on pages 72, 73, 75, 95.*

[249] Mohammad Ali Akhavan Kazemi et al. “Moisture-Induced Non-Equilibrium Phase Segregation in Triple Cation Mixed Halide Perovskite Monitored by In Situ Characterization Techniques and Solid-State NMR”. In: *Energy & Environmental Materials* (2022) *Cited on pages 73, 82.*

[252] Taehyun Hwang et al. “Methylammonium-chloride post-treatment on perovskite surface and its correlation to photovoltaic performance in the aspect of electronic traps”. In: *Journal of Applied Physics* 126.2 (July 2019). Publisher: American Institute of Physics, p. 023101. ISSN: 0021-8979. DOI: 10.1063/1.5098336 *Cited on page 81.*

[253] Feng Hao et al. “Controllable Perovskite Crystallization at a Gas–Solid Interface for Hole Conductor-Free Solar Cells with Steady Power Conversion Efficiency over 10%”. en. In: *Journal of the American Chemical Society* 136.46 (Nov. 2014), pp. 16411–16419. ISSN: 0002-7863, 1520-5126. DOI: 10.1021/ja509245x *Cited on page 81.*

[254] Ryan Taoran Wang et al. “Moisture-Stable FAPbI $_3$ Perovskite Achieved by Atomic Structure Negotiation”. en. In: *The Journal of Physical Chemistry Letters* 12.22 (June 2021), pp. 5332–5338. ISSN: 1948-7185, 1948-7185. DOI: 10.1021/acs.jpclett.1c01482 *Cited on page 81.*

[255] Jun Nishida et al. “Heterogeneous Cation–Lattice Interaction and Dynamics in Triple-Cation Perovskites Revealed by Infrared Vibrational Nanoscopy”. en. In: *ACS Energy Letters* 5.5 (May 2020), pp. 1636–1643. ISSN: 2380-8195, 2380-8195. DOI: 10.1021/acsenergylett.0c00522 *Cited on pages 81, 99.*

[256] Bart Roose et al. “Critical Assessment of the Use of Excess Lead Iodide in Lead Halide Perovskite Solar Cells”. en. In: *The Journal of Physical Chemistry Letters* 11.16 (Aug. 2020), pp. 6505–6512. ISSN: 1948-7185, 1948-7185. DOI: 10.1021/acs.jpclett.0c01820 *Cited on pages 82, 117, 125.*

[257] Ibrahim Dursun et al. “CsPb $_2$ Br $_5$ Single Crystals: Synthesis and Characterization”. en. In: *ChemSusChem* 10.19 (Oct. 2017), pp. 3746–3749. ISSN: 18645631. DOI: 10.1002/cssc.201701131 *Cited on page 82.*

[258] Jeffrey A. Christians, Pierre A. Miranda Herrera, and Prashant V. Kamat. “Transformation of the Excited State and Photovoltaic Efficiency of CH3NH3PbI3 Perovskite upon Controlled Exposure to Humidified Air”. In: *Journal of the American Chemical Society* 137.4 (Feb. 2015). Publisher: American Chemical Society, pp. 1530–1538. ISSN: 0002-7863. DOI: 10.1021/ja511132a *Cited on page 82.*

[259] Sebastian Svanström et al. “Degradation Mechanism of Silver Metal Deposited on Lead Halide Perovskites”. In: *ACS Applied Materials & Interfaces* 12.6 (Feb. 2020). Publisher: American Chemical Society, pp. 7212–7221. ISSN: 1944-8244. DOI: 10.1021/acsami.9b20315 *Cited on pages 82, 95.*

[260] Amaury Delamarre, Laurent Lombez, and Jean-François Guillemoles. "Contactless mapping of saturation currents of solar cells by photoluminescence". In: *Applied Physics Letters* 100.13 (Mar. 2012). Publisher: American Institute of Physics, p. 131108. ISSN: 0003-6951. DOI: 10.1063/1.3697704 *Cited on pages 83, 148.*

[261] Zhaoning Song et al. "Impact of Moisture on Photoexcited Charge Carrier Dynamics in Methylammonium Lead Halide Perovskites". en. In: *The Journal of Physical Chemistry Letters* 9.21 (Nov. 2018), pp. 6312–6320. ISSN: 1948-7185, 1948-7185. DOI: 10.1021/acs.jpclett.8b02595 *Cited on pages 83, 95.*

[262] Stefania Cacovich et al. "Light Induced Passivation in Triple Cation Mixed Halide Perovskites: Interplay between Transport Properties and Surface Chemistry". en. In: *ACS Applied Materials & Interfaces* (July 2020), acsami.0c06844. ISSN: 1944-8244, 1944-8252. DOI: 10.1021/acsami.0c06844 *Cited on pages 83, 148.*

[263] Rebecca J. Sutton et al. "Cubic or Orthorhombic? Revealing the Crystal Structure of Metastable Black-Phase CsPbI $_3$ by Theory and Experiment". en. In: *ACS Energy Letters* 3.8 (Aug. 2018), pp. 1787–1794. ISSN: 2380-8195, 2380-8195. DOI: 10.1021/acsenergylett.8b00672 *Cited on page 89.*

[264] Di Yang et al. "All-inorganic cesium lead halide perovskite nanocrystals: synthesis, surface engineering and applications". en. In: *Journal of Materials Chemistry C* 7.4 (Jan. 2019). Publisher: The Royal Society of Chemistry, pp. 757–789. ISSN: 2050-7534. DOI: 10.1039/C8TC04381G *Cited on page 96.*

[265] Lang Liu et al. "A-site phase segregation in mixed cation perovskite". en. In: *Materials Reports: Energy*. Printable Solar Cells: From Materials to Devices 1.4 (Nov. 2021), p. 100064. ISSN: 2666-9358. DOI: 10.1016/j.matre.2021.100064 *Cited on page 98.*

[266] Laura T. Schelhas et al. "Insights into operational stability and processing of halide perovskite active layers". en. In: *Energy & Environmental Science* 12.4 (2019). Publisher: Royal Society of Chemistry, pp. 1341–1348. DOI: 10.1039/C8EE03051K *Cited on pages 98, 125, 127.*

[267] Mingzhu Long et al. "Abnormal Synergetic Effect of Organic and Halide Ions on the Stability and Optoelectronic Properties of a Mixed Perovskite via In Situ Characterizations". en. In: *Advanced Materials* 30.28 (2018), p. 1801562. ISSN: 1521-4095. DOI: 10.1002/adma.201801562 *Cited on page 98.*

[268] Wanliang Tan et al. "Thermal Stability of Mixed Cation Metal Halide Perovskites in Air". In: *ACS Applied Materials & Interfaces* 10.6 (Feb. 2018). Publisher: American Chemical Society, pp. 5485–5491. ISSN: 1944-8244. DOI: 10.1021/acsami.7b15263 *Cited on page 98.*

[269] Bekir Turedi et al. "Water-Induced Dimensionality Reduction in Metal-Halide Perovskites". In: *The Journal of Physical Chemistry C* 122.25 (June 2018). Publisher: American Chemical Society, pp. 14128–14134. ISSN: 1932-7447. DOI: 10.1021/acs.jpcc.8b01343 *Cited on page 98.*

[270] Jakub Holovský et al. "Lead Halide Residue as a Source of Light-Induced Reversible Defects in Hybrid Perovskite Layers and Solar Cells". In: *ACS Energy Letters* 4.12 (Dec. 2019). Publisher: American Chemical Society, pp. 3011–3017. DOI: 10.1021/acsenergylett.9b02080 *Cited on page 99.*

[271] Ganbaatar Tumen-Ulzii et al. "Detrimental Effect of Unreacted PbI2 on the Long-Term Stability of Perovskite Solar Cells". en. In: *Advanced Materials* 32.16 (2020), p. 1905035. ISSN: 1521-4095. DOI: 10.1002/adma.201905035 *Cited on pages 99, 117.*

[272] Huanhuan Wang et al. “Ligand-Modulated Excess PbI2 Nanosheets for Highly Efficient and Stable Perovskite Solar Cells”. en. In: *Advanced Materials* 32.21 (2020), p. 2000865. ISSN: 1521-4095. DOI: 10.1002/adma.202000865 *Cited on pages 99, 117.*

References for Chapter 5: Analysis of the degradation products in PSC aged under operation conditions

[20] Zhen Li et al. “Stabilizing Perovskite Structures by Tuning Tolerance Factor: Formation of Formamidinium and Cesium Lead Iodide Solid-State Alloys”. en. In: *Chemistry of Materials* 28.1 (Jan. 2016), pp. 284–292. ISSN: 0897-4756, 1520-5002. DOI: 10.1021/acs.chemmater.5b04107 *Cited on pages 8, 12, 122.*

[28] Eric T. Hoke et al. “Reversible photo-induced trap formation in mixed-halide hybrid perovskites for photovoltaics”. en. In: *Chemical Science* 6.1 (2015), pp. 613–617. ISSN: 2041-6520, 2041-6539. DOI: 10.1039/C4SC03141E *Cited on pages 9, 20, 127.*

[29] Michael C. Brennan et al. “Photoinduced Anion Segregation in Mixed Halide Perovskites”. en. In: *Trends in Chemistry* 2.4 (Apr. 2020), pp. 282–301. ISSN: 25895974. DOI: 10.1016/j.trechm.2020.01.010 *Cited on pages 9, 20, 21, 122.*

[77] Tiarnan A. S. Doherty et al. “Stabilized tilted-octahedra halide perovskites inhibit local formation of performance-limiting phases”. In: *Science* 374.6575 (Dec. 2021). Publisher: American Association for the Advancement of Science, pp. 1598–1605. DOI: 10.1126/science.abl4890 *Cited on pages 18, 123, 132.*

[94] Kevin A. Bush et al. “Compositional Engineering for Efficient Wide Band Gap Perovskites with Improved Stability to Photoinduced Phase Segregation”. en. In: *ACS Energy Letters* 3.2 (Feb. 2018), pp. 428–435. ISSN: 2380-8195, 2380-8195. DOI: 10.1021/acsenergylett.7b01255 *Cited on pages 19, 117, 122, 127.*

[98] Ilia M. Pavlovetc et al. “Suppressing Cation Migration in Triple-Cation Lead Halide Perovskites”. In: *ACS Energy Letters* 5.9 (Sept. 2020). Publisher: American Chemical Society, pp. 2802–2810. DOI: 10.1021/acsenergylett.0c01207 *Cited on pages 21, 98, 125.*

[99] Jeffrey A. Christians et al. “Tailored interfaces of unencapsulated perovskite solar cells for >1,000 hour operational stability”. en. In: *Nature Energy* 3.1 (Jan. 2018). Number: 1 Publisher: Nature Publishing Group, pp. 68–74. ISSN: 2058-7546. DOI: 10.1038/s41560-017-0067-y *Cited on pages 21, 127.*

[101] Rusha Chatterjee et al. “Subdiffraction Infrared Imaging of Mixed Cation Perovskites: Probing Local Cation Heterogeneities”. In: *ACS Energy Letters* 3.2 (Feb. 2018). Publisher: American Chemical Society, pp. 469–475. DOI: 10.1021/acsenergylett.7b01306 *Cited on pages 21, 125.*

[102] Nengxu Li et al. “Microscopic Degradation in Formamidinium-Cesium Lead Iodide Perovskite Solar Cells under Operational Stressors”. en. In: *Joule* (July 2020). ISSN: 25424351. DOI: 10.1016/j.joule.2020.06.005 *Cited on pages 21, 98, 111, 125, 127.*

[111] Loreta A. Muscarella et al. “Lattice Compression Increases the Activation Barrier for Phase Segregation in Mixed-Halide Perovskites”. In: *ACS Energy Letters* 5.10 (Oct. 2020). Publisher: American Chemical Society, pp. 3152–3158. DOI: 10.1021/acsenergylett.0c01474 *Cited on pages 21, 125.*

[131] Wenya Song et al. “Improving the Morphology Stability of Spiro-OMeTAD Films for Enhanced Thermal Stability of Perovskite Solar Cells”. In: *ACS Applied Materials & Interfaces* 13.37 (Sept. 2021). Publisher: American Chemical Society, pp. 44294–44301. ISSN: 1944-8244. DOI: 10.1021/acsami.1c11227 *Cited on pages 24, 25, 111.*

[143] Mark V. Khenkin et al. “Consensus statement for stability assessment and reporting for perovskite photovoltaics based on ISOS procedures”. en. In: *Nature Energy* 5.1 (Jan. 2020), pp. 35–49. ISSN: 2058-7546. DOI: 10.1038/s41560-019-0529-5 *Cited on pages 26, 106.*

[149] Jordi Ferrer Orri et al. “Unveiling the Interaction Mechanisms of Electron and X-ray Radiation with Halide Perovskite Semiconductors using Scanning Nanoprobe Diffraction”. In: *Advanced Materials* 34.18 (2022), p. 2200383 *Cited on pages 31, 124.*

[162] David B. Williams and C. Barry Carter. *Transmission electron microscopy: a textbook for materials science*. en. 2nd ed. New York: Springer, 2008. ISBN: 978-0-387-76500-6 *Cited on pages 38, 52, 55, 56, 89, 90, 124.*

[171] Pietro Caprioglio et al. “Nano-emitting Heterostructures Violate Optical Reciprocity and Enable Efficient Photoluminescence in Halide-Segregated Methylammonium-Free Wide Bandgap Perovskites”. en. In: *ACS Energy Letters* (Jan. 2021), pp. 419–428. ISSN: 2380-8195, 2380-8195. DOI: 10.1021/acsenergylett.0c02270 *Cited on pages 42, 43, 92, 127.*

[256] Bart Roose et al. “Critical Assessment of the Use of Excess Lead Iodide in Lead Halide Perovskite Solar Cells”. en. In: *The Journal of Physical Chemistry Letters* 11.16 (Aug. 2020), pp. 6505–6512. ISSN: 1948-7185, 1948-7185. DOI: 10.1021/acs.jpclett.0c01820 *Cited on pages 82, 117, 125.*

[266] Laura T. Schelhas et al. “Insights into operational stability and processing of halide perovskite active layers”. en. In: *Energy & Environmental Science* 12.4 (2019). Publisher: Royal Society of Chemistry, pp. 1341–1348. DOI: 10.1039/C8EE03051K *Cited on pages 98, 125, 127.*

[271] Ganbaatar Tumen-Ulzii et al. “Detrimental Effect of Unreacted PbI2 on the Long-Term Stability of Perovskite Solar Cells”. en. In: *Advanced Materials* 32.16 (2020), p. 1905035. ISSN: 1521-4095. DOI: 10.1002/adma.201905035 *Cited on pages 99, 117.*

[272] Huanhuan Wang et al. “Ligand-Modulated Excess PbI2 Nanosheets for Highly Efficient and Stable Perovskite Solar Cells”. en. In: *Advanced Materials* 32.21 (2020), p. 2000865. ISSN: 1521-4095. DOI: 10.1002/adma.202000865 *Cited on pages 99, 117.*

[273] Weijun Ke et al. “Employing Lead Thiocyanate Additive to Reduce the Hysteresis and Boost the Fill Factor of Planar Perovskite Solar Cells”. In: *Advanced Materials* 28.26 (2016), pp. 5214–5221. ISSN: 1521-4095. DOI: 10.1002/adma.201600594 *Cited on page 106.*

[274] Apurba Mahapatra et al. “A review of aspects of additive engineering in perovskite solar cells”. en. In: *Journal of Materials Chemistry A* 8.1 (2020). Publisher: Royal Society of Chemistry, pp. 27–54. DOI: 10.1039/C9TA07657C *Cited on page 106.*

[275] Jayita Dutta et al. “An inherent instability study using ab initio computational methods and experimental validation of Pb(SCN)2 based perovskites for solar cell applications”. en. In: *Scientific Reports* 10.1 (Sept. 2020). Number: 1 Publisher: Nature Publishing Group, p. 15241. ISSN: 2045-2322. DOI: 10.1038/s41598-020-72210-4 *Cited on page 107.*

[276] Ji-Youn Seo et al. “Dopant Engineering for Spiro-OMeTAD Hole-Transporting Materials towards Efficient Perovskite Solar Cells”. en. In: *Advanced Functional Materials* 31.45 (2021), p. 2102124. ISSN: 1616-3028. DOI: 10.1002/adfm.202102124 *Cited on page 107.*

[277] Emilie Planes et al. “Degradation Mechanisms in a Mixed Cations and Anions Perovskite Solar Cell: Mitigation Effect of the Gold Electrode”. en. In: *ACS Applied Energy Materials* 4.2 (Feb. 2021), pp. 1365–1376. ISSN: 2574-0962, 2574-0962. DOI: 10.1021/acsaem.0c02613 *Cited on pages 111, 128.*

[278] Carolin M. Sutter-Fella et al. "Cation-Dependent Light-Induced Halide Demixing in Hybrid Organic–Inorganic Perovskites". en. In: *Nano Letters* 18.6 (June 2018), pp. 3473–3480. ISSN: 1530-6984, 1530-6992. DOI: 10.1021/acs.nanolett.8b00541 *Cited on page 117.*

[279] F. Cordero et al. "Cation reorientation and octahedral tilting in the metal-organic perovskites MAPI and FAPI". en. In: *Journal of Alloys and Compounds* 867 (June 2021), p. 158210. ISSN: 0925-8388. DOI: 10.1016/j.jallcom.2020.158210 *Cited on page 122.*

[280] Waqaas Rehman. "Photovoltaic mixed-cation lead mixed-halide perovskites: links between crystallinity, photo-stability and electronic properties". en. In: *Environmental Science* (2017), p. 9 *Cited on page 122.*

[281] Paul Gratia et al. "The Many Faces of Mixed Ion Perovskites: Unraveling and Understanding the Crystallization Process". en. In: *ACS Energy Letters* 2.12 (Dec. 2017), pp. 2686–2693. ISSN: 2380-8195, 2380-8195. DOI: 10.1021/acsenergylett.7b00981 *Cited on page 124.*

[282] Yue Lu et al. "In CH $_3$ NH $_3$ PbI $_3$ Perovskite Film, the Surface Termination Layer Dominates the Moisture Degradation Pathway". en. In: *Chemistry – A European Journal* 27.11 (Feb. 2021), pp. 3729–3736. ISSN: 0947-6539, 1521-3765. DOI: 10.1002/chem.202003121 *Cited on page 125.*

[283] Hui-Seon Kim and Nam-Gyu Park. "Importance of tailoring lattice strain in halide perovskite crystals". en. In: *NPG Asia Materials* 12.1 (Dec. 2020), p. 78. ISSN: 1884-4049, 1884-4057. DOI: 10.1038/s41427-020-00265-w *Cited on page 125.*

[284] Anthony Donakowski et al. "Improving Photostability of Cesium-Doped Formamidinium Lead Triiodide Perovskite". In: *ACS Energy Letters* 6.2 (Feb. 2021). Publisher: American Chemical Society, pp. 574–580. DOI: 10.1021/acsenergylett.0c02339 *Cited on page 125.*

[285] Ross A. Kerner et al. "Low Threshold Voltages Electrochemically Drive Gold Migration in Halide Perovskite Devices". In: *ACS Energy Letters* 5.11 (Nov. 2020). Publisher: American Chemical Society, pp. 3352–3356. DOI: 10.1021/acsenergylett.0c01805 *Cited on page 126.*

[286] Cristina Besleaga et al. "Iodine Migration and Degradation of Perovskite Solar Cells Enhanced by Metallic Electrodes". In: *The Journal of Physical Chemistry Letters* 7.24 (Dec. 2016). Publisher: American Chemical Society, pp. 5168–5175. DOI: 10.1021/acs.jpclett.6b02375 *Cited on page 126.*

[287] Namyoung Ahn et al. "Trapped charge-driven degradation of perovskite solar cells". en. In: *Nature Communications* 7.1 (Nov. 2016). Bandiera_abtest: a Cc_license_type: cc_by Cg_type: Nature Research Journals Number: 1 Primary_atype: Research Publisher: Nature Publishing Group Subject_term: Materials for devices;Solar cells Subject_term_id: materials-for-devices;solar-cells, p. 13422. ISSN: 2041-1723. DOI: 10.1038/ncomms13422 *Cited on page 126.*

[288] Konrad Wojciechowski et al. "C60 as an Efficient n-Type Compact Layer in Perovskite Solar Cells". In: *The Journal of Physical Chemistry Letters* 6.12 (June 2015). Publisher: American Chemical Society, pp. 2399–2405. DOI: 10.1021/acs.jpclett.5b00902 *Cited on page 127.*

References for Chapter 5.4: General conclusion

[77] Tiarnan A. S. Doherty et al. "Stabilized tilted-octahedra halide perovskites inhibit local formation of performance-limiting phases". In: *Science* 374.6575 (Dec. 2021). Publisher: American Association for the Advancement of Science, pp. 1598–1605. DOI: 10.1126/science.abl4890 *Cited on pages 18, 123, 132.*

[184] Jordi Ferrer Orri. "Using pulsed mode scanning electron microscopy for cathodoluminescence studies on hybrid perovskite films". en. In: (2021), p. 11 *Cited on pages 47, 132.*

[289] Sebastián Caicedo-Dávila et al. "Effect of Post-deposition Annealing on the Luminescence of Mixed-phase CsPb2Br5/CsPbBr3 Thin Films". en. In: (), p. 15 *Cited on pages 130, 136.*

References for Chapter 5.4: Resumé en français

[1] P. A. Arias et al. "Techincal summary". In: *Climate Change 2021: The Physical Science Basis. Contribution of Working Group I to the Sixth Assessment Report of the Intergovernmental Panel on Climate Change*. Ed. by V. Masson-Delmotte et al. Cambridge University Press, 2021, pp. 33–144. DOI: 10.1017/9781009157896.002 *Cited on pages 1, 133.*

[3] International Energy Agency (IEA). *Solar PV*. en-GB. Tech. rep. 2022 *Cited on pages 1, 2, 133.*

[5] NREL. *Best Research-Cell Efficiency Chart*. en. 2022 *Cited on pages 2, 133.*

[176] Srinivas K. Yadavalli et al. "Electron-beam-induced cracking in organic-inorganic halide Perovskite thin films". en. In: *Scripta Materialia* 187 (Oct. 2020), pp. 88–92. ISSN: 13596462. DOI: 10.1016/j.scriptamat.2020.05.062 *Cited on pages 44–46, 135.*

[289] Sebastián Caicedo-Dávila et al. "Effect of Post-deposition Annealing on the Luminescence of Mixed-phase CsPb2Br5/CsPbBr3 Thin Films". en. In: (), p. 15 *Cited on pages 130, 136.*

References for Chapter 5.4: Additional theory and methods

[206] Arpit Mishra, Philippe Baranek, and Andrei Postnikov. "First-principles investigation of CO2, CO, and O2 adsorptions on the (001)-reconstructed surfaces of CsPbX3 (X = Cl, Br, and I) perovskites". en. In: *Surfaces and Interfaces* 25 (Aug. 2021), p. 101264. ISSN: 2468-0230. DOI: 10.1016/j.surfin.2021.101264 *Cited on pages 63, 64, 89, 147.*

[260] Amaury Delamarre, Laurent Lombez, and Jean-François Guillemoles. "Contactless mapping of saturation currents of solar cells by photoluminescence". In: *Applied Physics Letters* 100.13 (Mar. 2012). Publisher: American Institute of Physics, p. 131108. ISSN: 0003-6951. DOI: 10.1063/1.3697704 *Cited on pages 83, 148.*

[262] Stefania Cacovich et al. "Light Induced Passivation in Triple Cation Mixed Halide Perovskites: Interplay between Transport Properties and Surface Chemistry". en. In: *ACS Applied Materials & Interfaces* (July 2020), acsami.0c06844. ISSN: 1944-8244, 1944-8252. DOI: 10.1021/acsami.0c06844 *Cited on pages 83, 148.*

[290] Roberto Dovesi et al. "The CRYSTAL code, 1976–2020 and beyond, a long story". In: *The Journal of Chemical Physics* 152.20 (May 2020). Publisher: American Institute of Physics, p. 204111. ISSN: 0021-9606. DOI: 10.1063/5.0004892 *Cited on page 147.*

[291] Roberto Dovesi et al. “Quantum-mechanical condensed matter simulations with CRYSTAL”. en. In: *WIREs Computational Molecular Science* 8.4 (2018), e1360. ISSN: 1759-0884. DOI: 10.1002/wcms.1360 *Cited on page 147.*

[292] A. Erba et al. “Large-Scale Condensed Matter DFT Simulations: Performance and Capabilities of the CRYSTAL Code”. eng. In: *Journal of Chemical Theory and Computation* 13.10 (Oct. 2017), pp. 5019–5027. ISSN: 1549-9626. DOI: 10.1021/acs.jctc.7b00687 *Cited on page 147.*

[293] John P. Perdew et al. “Restoring the Density-Gradient Expansion for Exchange in Solids and Surfaces”. In: *Physical Review Letters* 100.13 (Apr. 2008). Publisher: American Physical Society, p. 136406. DOI: 10.1103/PhysRevLett.100.136406 *Cited on page 147.*

[294] Hendrik J. Monkhorst and James D. Pack. “Special points for Brillouin-zone integrations”. In: *Physical Review B* 13.12 (June 1976). Publisher: American Physical Society, pp. 5188–5192. DOI: 10.1103/PhysRevB.13.5188 *Cited on page 148.*